Perovskite/Silicon Tandem Solar Cells: Toward Affordable Ultra-High Efficiency Photovoltaics ?

PAR

Jérémie WERNER

ÉCOLE POLYTECHNIQUE
FÉDÉRALE DE LAUSANNE

Suisse
2018

"I'd put my money on the sun and solar energy,
what a source of power. I hope we don't have to
wait until oil and coal run out, before we tackle that."
— Thomas Edison, 1931

Abstract

Nowadays the photovoltaics market is dominated by crystalline silicon solar cells. As their efficiency approaches the theoretical efficiency limit, novel solutions have to be found for photovoltaics to further enhance its competitiveness with other energy sources, in particular the fossil fuels. One of the most promising approaches lies in combining market-proven silicon solar cell technology, having a low optical band gap, with an efficient near-infrared transparent wide-band gap top cell to form a tandem cell, as a mechanically stacked or monolithically integrated device. This strategy will enable ultra-high performance photovoltaic energy harvesting systems with low additional costs. Organic-inorganic halide perovskite solar cells are promising candidates for top cells, showing high efficiencies with simple and potential cost-effective device fabrication.

In this thesis, we develop perovskite solar cells specifically for tandem applications. We develop and optimize an hybrid sequential deposition method combining thermal evaporation and solution processing to fabricate perovskite absorber materials with specifically tailored optoelectronic properties. These materials are systematically investigated for their optical, structural and electronic properties, including their complex refractive indices which can be used for optical simulations. We then apply these absorbers in perovskite solar cells both in n-i-p and p-i-n configurations, for which we show several charge transport materials combinations.

As a replacement for the standard metal opaque rear electrode of perovskite cells, we describe the development of a TCO-based transparent electrode, for which sputtered IZO is presented as a good candidate thanks to its high carrier mobility and broadband transparency. Sputtering-induced damages are reduced by the introduction of a buffer layer: molybdenum oxide (MoO_x) for cells in n-i-p configuration and tin oxide (SnO_2) for cells in p-i-n configuration. The parasitic absorption losses in the MoO_x are described in details, including a solution to minimize these losses with a carbon dioxide (CO_2) plasma treatment. We then discuss the parasitic absorption losses in charge transport layers and TCOs, with experimental comparison of various materials. The optimisation of the perovskite absorber deposition method and the improvement of the charge transport layers and transparent electrode allows the fabrication 1 cm^2 area semitransparent perovskite solar cells with >16% efficiency.

We then integrate the semitransparent perovskite cells in mechanically stacked 4-terminal tandem solar cells. The challenges in reducing the strong parasitic absorption and reflection losses are first discussed, including solutions with the introduction of optical coupling liquid, antireflective foils and less absorbing TCOs. With these improvements, we demonstrate

4-terminal tandem measurements with >25% total efficiency with a small area top cell. With larger 1 cm^2 area top cells, we fabricate integrated 4-terminal tandem devices with both sub-cellshaving similar size and total efficiency >23%.

The integration of perovskite solar cells in 2-terminal monolithically connected tandem solar cells with silicon heterojunction bottom cells is finally presented. This configuration is the most promising architecture for a future commercialization. First, we show the development of a transparent conductive oxide (TCO)-based recombination layer. Then, the important reflection losses and interference effects observed in all-flat devices are discussed, including solutions to these issues. The origins of parasitic absorption losses in monolithic tandem are then explained and, supported by optical simulations, new architectures and materials are investigated. We then replace the polished wafers by fully textured silicon bottom cells for better light management: an attempt of planarization with LPCVD ZnO is first described with its inherent technical difficulties; then the development of a tandem device with the top cell conformally coated onto the textured bottom cell is explained, leading to >25% certified power conversion efficiency. Finally, the end of the thesis presents preliminary but promising results on the up-scalability and light soaking stability of the developed textured tandems, as well as a proof-of-concept of a first perovskite/perovskite/silicon triple junction solar cell on textured wafers.

Key words: tandem solar cells, silicon, perovskite, high-efficiency, monolithic interconnection, 2-terminal, 4-terminal, sputtering, evaporation, spin-coating, transparent conductive oxide, transition metal oxide, light management, optical losses, parasitic absorption.

Résumé

Le marché du photovoltaïque est largement dominé par les cellules en silicium cristallin. Cependant, comme leur rendement approche la limite théorique, de nouvelles solutions doivent être envisagées pour continuer à améliorer la compétitivité du photovoltaïque envers les autres sources d'énergie. Une des solutions les plus prometteuses est de combiner les technologies du silicium, largement éprouvées par le marché industriel et ayant une énergie de bande interdite faible, avec une cellule solaire à large bande interdite et transparente dans le spectre des infrarouges pour former une cellule solaire tandem. Les deux cellules absorbent chacune une partie spécifique du spectre de la lumière et la cellule tandem peut être construite soit en empilant mécaniquement les deux cellules connectées alors en configuration 4-terminaux, ou en faisant croître la cellule à large bande interdite directement sur la cellule silicium. La cellule tandem avec intégration monolithique est alors connectée en 2-terminaux. Cette stratégie pourrait permettre la fabrication de systèmes photovoltaïques à très haut rendement, avec peu de coûts additionnels. Les cellules photovoltaïques hybrides organique-inorganique à pérovskites sont d'excellentes candidates pour une application en tandem avec le silicium cristallin, grâce à leur haut rendement et leurs techniques de fabrication simples et à bas coûts.

Dans cette thèse, nous développons des cellules à pérovskites spécifiquement pour des applications en tandem. Pour la couche absorbante, nous adaptons et optimisons une méthode de croissance hybride, combinant une étape d'évaporation thermique d'halogénures de plomb et de césium suivie par un dépôt par centrifugation d'une solution d'halogénure organique. Cette méthode permet la fabrication de couches en pérovskites avec des propriétés optoélectroniques adaptées, et facilement adaptables aux nécessités spécifiques des applications en tandem. Ces matériaux avec des bandes interdites d'énergies variable entre 1.5 et 1.8 eV sont étudiés systématiquement pour leur propriétés optiques, structurelles et électroniques, avec en particulier la mesure de leur indice de réfraction utile pour la modélisation optique de cellules solaires. Nous fabriquons ensuite des cellules solaires avec ces nouveaux matériaux pérovskites, soit en polarité n-i-p ou p-i-n. Des matériaux de transport de charges sont spécifiquement choisis et testés pour chacune des configurations, afin d'obtenir des cellules solaires pérovskites opaques ayant un rendement suffisant.

En lieu et place du contact arrière typiquement en métal, nous présentons une électrode transparente à base d'un oxyde transparent et conducteur déposé par pulvérisation cathodique. Les dommages engendrés par cette méthode de dépôt sont limités par l'introduction d'une couche tampon, en oxyde de molybdène pour les cellules n-i-p et en oxyde d'étain pour les

cellules p-i-n. Nous discutons ensuite les pertes en absorption parasitique dans les couches de transport de charges et dans l'électrode transparente. Après optimisation du processus de fabrication et des diverses couches, des cellules semitransparente à pérovskites sont démontrées avec des rendements >16% sur une taille de cellule >1 cm^2.

Nous intégrons ensuite ces cellules semitransparentes dans des tandems en 4-terminaux. Après une étude systématique des pertes optiques liées à cette configuration et une re-optimisation du procédé, nous pouvons démontrer des tandems en mesure 4-terminaux avec des rendements totaux >25%, avec une cellule à pérovskites de petite taille, et jusqu'à 23% avec une surface de 1 cm^2.

Finalement, nous présentons l'intégration monolithique en tandem 2-terminaux, l'architecture la plus prometteuse en vue d'une future commercialisation. Nous montrons l'utilisation d'un oxyde conducteur et transparent pour le contact intermédiaire de recombinaison de charge. Les importantes pertes optiques dues aux réflexions engendrées par l'utilisation de surfaces polies sont discutées, ainsi que des solutions pour les atténuer. L'origine des pertes par absorption parasitique est ensuite expliquée et soutenues par une combinaison de simulations optiques et de mesures expérimentales. Les plaquettes de silicium polies sont ensuite remplacées par des plaquettes texturisées, pour une meilleure gestion de la lumière en minimisant les pertes par réflexion. Le développement d'une cellule tandem monolithique 2-terminaux ayant une cellule à pérovskites déposée de manière conforme sur la surface des pyramides de silicium permet enfin la démonstration de rendements certifiés >25%, établissant un nouveau record du monde pour la technologie. La fin de la thèse présente des résultats préliminaires pour des cellules tandem plus larges, pour leur stabilité sous lumière et pour une première démonstration d'une cellule à triple jonctions : pérovskites/pérovskites/silicium sur substrats texturisés.

Mots-clés : cellules solaires en tandem, silicium, perovskite, haute efficacité, interconnection monolithique, 2-terminaux, 4-terminaux, pulverisation cathodique, évaporation, dépôt par centrifugation, oxyde transparent conducteur, oxyde de métaux de transition, gestion de la lumière, pertes optiques, absorption parasitique.

Contents

Contents

1 Introduction

1.1 Photovoltaics: a clean sustainable energy?

The world energy demand has constantly increased over history and is predicted to continue to climb in the coming years, with a 30% expansion by 2040 as compared to today [2]. The pollution created by the use of fossil fuels is undeniably impacting the climate of our planet and our everyday life through the increasing number of smog days, natural disasters, geopolitical conflicts for access to resources... The development of a clean and sustainable energy system is therefore one of the most important challenges of our time. The access to energy is a trigger for economic growth and often the key to expand the education and health systems, particularly in under-developed and isolated regions [1].

What are the options? There are currently several renewable energy technologies under development, from which the top three are: wind, hydro and solar. These energy resources are intermittent but also complementary. Indeed, wind does not blow all the time, neither does the sun shine all the time. But combined in a smart electricity grid including storage capability (batteries, fuel production, pumped-storage hydro), they can be largely sufficient to provide all energy we need, whenever we need.

Solar energy is particularly interesting, as it provides an inexhaustible and universal source of energy, available everywhere on Earth with typically around 1000 W/m^2 on the ground and 1367 W/m^2 in space for satellites powering. If we consider the total energy consumption in Switzerland in 2016 as reported by the Swiss Federal Office of Energy [3], 854'300 TJ, ≈1200 kWh/m^2 average solar radiation per annum[2] in Switzerland and 15% efficient pho-

---

Parts of this introduction Chapter are based on a review paper published in Advanced Materials Interfaces and adapted with permission from [1]. The Sections taken in part or fully from this publication are marked with an asterisk *.

[1] *e.g.* https://lighteducationdevelopment.org/solar-lights/ or in Ladakh: http://www.ghe.co.in/
[2] ≈1450 kWh/m^2 in South roof orientation, ≈850 kWh/m^2 in North roof orientation, according to https://www.uvek-gis.admin.ch/BFE/sonnendach/?lang=en

tovoltaic modules, we can calculate that it would require only ≈3.2% of Switzerland surface to fully cover its energy needs. This number drops to 2.2% if we use the best photovoltaic commercial module currently available with a module efficiency of 22% [4] and down to 1.6% if the efficiency can be increased to 30%, which is the practical target of the technology studied in this thesis. This corresponds roughly to three times the size of the Lake of Neuchâtel, which could be then disseminated on building roofs and facades, transportation vehicles, electronic wearables, roadsides, hydropower dam lakes... and free-up all the space currently used by other polluting power generation systems such as gas thermal power plants or nuclear plants. Furthermore, these calculated required surfaces might well be in reality much smaller, as currently around 75% of the total energy consumption in Switzerland is in the form of fuels. The near-future wide-spread introduction of electrical vehicles or fuel cells cars should considerably reduce the total energy consumption and therefore the required photovoltaic surface.

Solar energy has therefore an enormous potential and will largely contribute to our electrified and sustainable future society. In the rest of this thesis, only solar photovoltaics (PV) – direct conversion of solar energy to electricity – will be considered and the following Sections of this introduction will enter more into details on the challenges faced by this technology and the possible solutions proposed by this thesis work.

1.2 The limitations of PV: Physics and Economics

1.2.1 Fundamental limits

Sunlight is composed of photons with in the spectral range from the infrared to the visible and ultraviolet (see Figure 1.1a). Indeed, the irradiation spectrum of the sun is close to a black body with a temperature of 5778 K. When this light passes through the Earth's atmosphere, it is attenuated through interactions with among others O_2, H_2O and CO_2 molecules. Therefore, part of the light is scattered and reflected back and part is absorbed by these molecules, which can be clearly seen in the irradiation spectrum measured on the ground. The irradiation spectrum outside the atmosphere is usually called AM0 and the spectrum on the ground with the sun directly perpendicular (shortest path from space to ground) is called AM1. In order to take into account the additional distance of the light travelled in the atmosphere, the spectrum AM1.5 describes the situation when the sun is at 48.2° zenith angle, which is a good representation of the light seen by most of Europe and the United States of America. This spectrum is therefore adopted as the standard for photovoltaic device testing [5].

A photovoltaic device absorbs this incident light and directly converts it into a usable electrical power, via the photovoltaic effect discovered already in 1839 by Edmond Becquerel. However, the first actual solar cell made out of silicon was developed only in 1954 at Bell laboratories and showed a photoconversion efficiency of 6%. After over 60 years of research, the record efficiency for silicon solar cells has reached 26.7% [6] and the single-junction solar cell record is held by a GaAs cell with 28.8% efficiency [7]. These photoconversion efficiencies (PCE) – ratio of the extracted power at maximum power point to the incident light power – can still
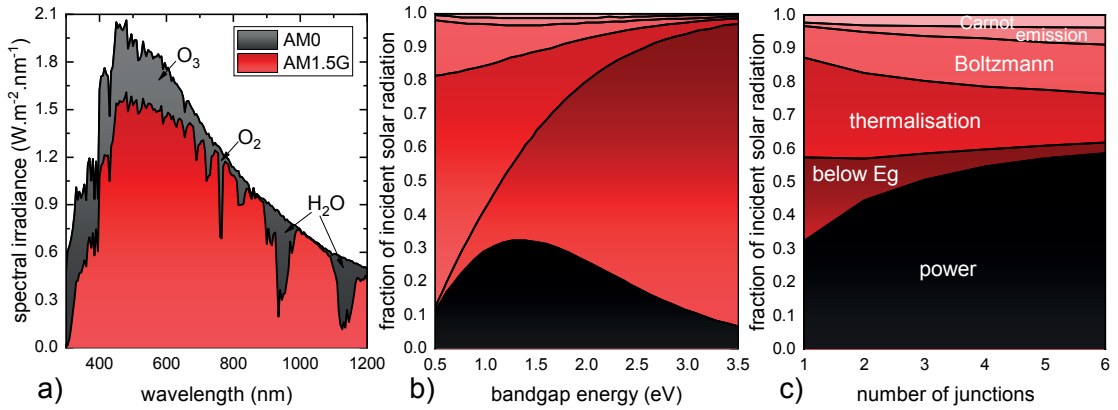
Figure 1.1 – a) Solar spectrum; b) Fundamental losses limiting the power output of a solar cell; c) Reduction of impact of the losses by increasing the number of junction, considering optimized band gap combinations. Adapted from reference [8].

appear low, when we try to compare them to for example commercial Diesel engines with energy conversion efficiencies about 40%.

To understand the fundamental limits of photovoltaic devices, we need first to describe a typical solar cell. Similarly to all photovoltaic technologies, a solar cell is composed of an absorber material, usually a semiconductor. When a photon is absorbed in such material, it will excite an electron from a lower energy state (*i.e.* the valence band) to a higher energy state (*i.e.* the conduction band), creating a so-called electron-hole pair. These negative and positive charge carriers need then to be separated and extracted to flow through an external load. This can be done by selective contacts, applied on either side of the absorber layer, which will preferentially extract one kind of carrier. The device efficiency is then limited by losses during those processes of absorption, charge excitation, separation and extraction. This can be observed by their effect on either reducing the device voltage or photogenerated current [8].

An important property of a semiconductor material is its optical bandgap (E_g), which refers to an energy range without electronic states. A photon will then be absorbed only if its energy is larger than E_g, so that an electron from the valence band can effectively be excited across the band gap and to the conduction band. The absorber material will then be transparent to all photons with energies below E_g, *i.e.* they will pass through without interacting and be lost. If the excited electrons received more energy than E_g, they will be excited to electronic states above the conduction band and will quickly lose this excess energy by thermalisation to return to the states with lowest energy in the conduction band. Thermalisation of charges by photons with energies above E_g and transparency for photon energies below E_g are the most important losses. Additional losses can be separated in emission losses, due to spontaneous emission as the cell also acts as a blackbody, Carnot losses for the heat loss to the environment necessary for the energy conversion, and Boltzmann losses describing the entropy generation due to unbalanced absorption and emission [8]. Those losses can be qualified as intrinsic, as they cannot be overcome by device and material optimization in a high performing device, and lead to a fundamental efficiency limit of 33.7%, formulated in 1961 by Shockley and Queisser

[9] for single-junction solar cells. A semiconductor material with a band gap of 1.34 eV offers then the best compromise between current reduction due to below-E_g and emission losses and voltage reduction due to thermalisation and the entropic losses.

Practically, a solar cell is not perfect and is subject to extrinsic losses, which are limiting the real device record performance to values below this limit. These losses can be carrier recombinations in the bulk (radiative, Auger or Shockley-Read-Hall [10]) or at the surfaces or interfaces through defect states, limiting the achievable voltage. They can also be optical, such as reflection losses or parasitic absorption in non-active layers such as the charge carrier transporting layers or contacts, limiting the current. Finally, ohmic losses can further decrease the device performance, through low shunt resistance (alternative current path contacting the front and back electrodes) and high series resistance (transport losses). Extrinsic losses can be minimized by improving the material optoelectronic quality and by optimizing both the device design and fabrication process.

However, the efficiency limit of 33.7% is defined only for a single-junction solar cell, *i.e.* the cell is composed of only one absorber having a defined band gap energy. A promising approach to overcome this single junction limit is then to use multiple materials with different band gap energies arranged in a multijunction solar cell so that they all absorb a specific part of the spectrum. This concept is fundamental for this thesis and will be further developed in Chapter 1.3.
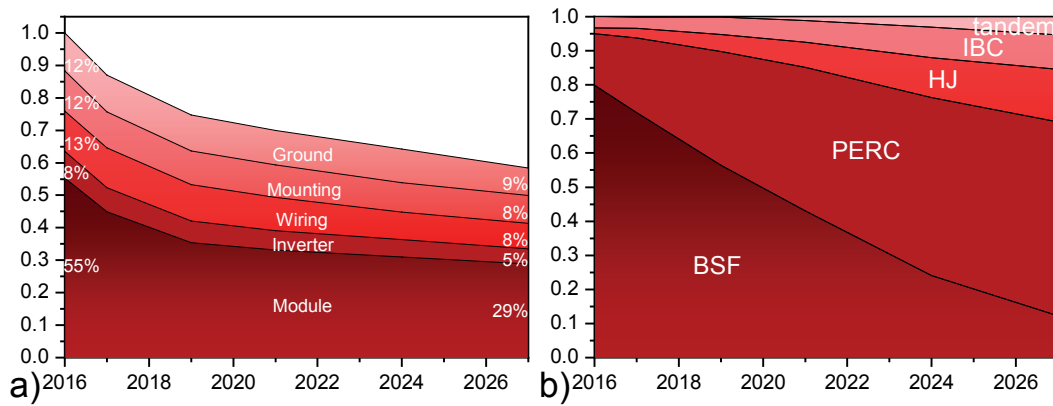
Figure 1.2 – International technological roadmap for photovoltaics between 2016 and 2027: a) Cost elements of PV system in US and Europe for systems >100kW; b) Expected technological transitions in silicon industry, evolving from BSF to PERC and SHJ, and finally to Si-based tandems after 2020. Adapted from reference [11].

1.2.2 It all comes down to costs *

In recent years, the costs of PV systems has decreased drastically while installations have soared, making PV economically competitive with conventional energy resources, *e.g.* coal, in many areas. As prices are falling, wholesale and retail grid parity should be reached in most countries within a few years [12]. For a PV system, the levelized cost of electricity (LCOE) is dominated by the balance of system (BOS) cost, including inverter, construction, connection, and mounting structure, with a share of typically 50 to 60% of the total costs. Therefore, a

straightforward approach to reduce the LCOE is to raise cell efficiency, which directly lowers the area-related BOS costs (except for the inverter, all other BOS costs are area-related), if implemented without significant additional processing costs [11]. As illustrated by Figure 1.2a, the costs of PV systems are expected to continue to decrease in the coming decade, supported by the replacement of older aluminum back surface field (Al-BSF) solar cells with more recent and more efficient technologies such as passivated emitter rear contact (PERC) or amorphous-silicon/crystalline-silicon heterojunction solar cell (SHJ), as shown in Figure 1.2b. Any new photovoltaic technology needs therefore to compete directly with the mass-produced silicon cells, in terms of production costs, market price and trust from customers, industry and investors (bank loan). Consequently, most thin-film companies could not survive this competition and the whole photovoltaic industry has a large inertia to implement innovative approaches, *e.g.* the PERC concept. However, further efficiency improvement of silicon photovoltaics will soon become difficult by small technological variations and, in order to continue to lower the price of PV electricity, new concepts will have to be developed and adopted by the industry. The most promising one of them is going for multijunction solar cells.

1.3 Multijunction solar cells

1.3.1 The concept

As illustrated in Figure 1.1c, the most effective solution to reduce the intrinsic fundamental losses described in a previous Section is to combine several absorber materials with different band gaps in a multijunction solar cell. Each material's band gap is tuned to effectively harvest a specific part of the spectrum. The stack is arranged with the widest band gap material facing the sun, letting through the sub-band gap photons which can be absorbed in the following absorbers with decreasing band gap energies from top to bottom. This strategy serves to both reduce the thermalisation losses, as the band gap better matches the photon energy, and the below-E_g losses, as the photons not absorbed in one material can be transmitted to the next one and still be absorbed. The simplest multijunction configuration is the so-called tandem solar cell combining two subcells. However, theoretically an infinite number of junctions could be made, each of them matching one photon energy. This idealistic device could reach efficiencies as high as 86.8% under concentrated light [13]. Practically, 46% efficiency is the maximum demonstrated performance for a quadruple junction III-V solar cell under concentration and around 38% under 1 sun illumination [7]. The most efficient tandem device (2 junctions) at 1 sun illumination is currently a GaAs//Si 4-terminal tandem with 32.8% efficiency by Essig *et al.* [14].

The main problem is the cost/efficiency trade-off. Highly efficient multijunction solar cells are fabricated with III-V semiconductor materials, which are complex and expensive both in terms of the materials and the required processing methods [15]. Therefore, they can be used only for concentration applications or niche applications where energy density is more important than absolute cost (*e.g.* space, sensors). On the other hand, multijunction solar cells can also be made very cheap with the example of the micromorph silicon solar cells, using a
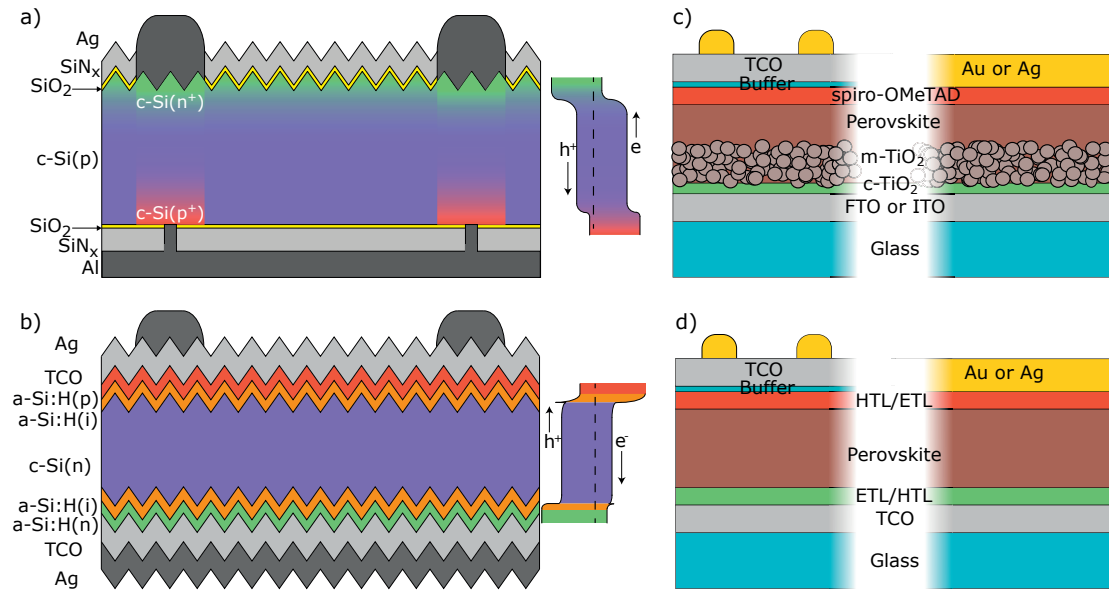
Figure 1.3 – Single-junction solar cell schematics: a) passivated emitter rear contact (PERC) solar cell; b) amorphous-silicon/crystalline-silicon heterojunction solar cell (SHJ); c) mesoporous perovskite solar cell, semitransparent (TCO-based) and opaque (Au or Ag), using a TiO$_2$-based electron contact; d) planar perovskite solar cell, semi-transparent (TCO-based) and opaque (Au or Ag), which can be in either polarities: p-i-n (hole transporting layer deposited on the glass/ITO substrate) or n-i-p (electron transporting layer deposited on the glass/ITO substrate).

stack of amorphous and microcrystalline silicon thin films [16, 17]. They were however not efficient enough to find a market and most companies producing these cells unfortunately went bankrupt or stopped production.

In order to apply the multijunction concept to utility scale PV systems, it must rely on simple and cost-effective technologies and still provide significantly improved performance so that it become actually worth choosing them instead of a well-established silicon technology. The following Section presents the two best candidates currently available to reach this challenging target.

1.3.2 Which are the perfect candidates?

1.3.2.1 A long-lasting market leader: Silicon *

Crystalline silicon-based technologies have been dominating the PV market for decades (>90% in 2017 [11]), thanks to their low fabrication costs and high reliability of their material and fabrication processes [18]. Silicon is a widely abundant element on Earth, a stable, low cost, non-toxic and well-known and studied material, after decades of research and applications in microtechnologies. Typical crystalline silicon (c-Si) module efficiencies are now about 17-18%, with a record commercial product efficiency of 22.2% [19, 4]. Research cell record efficiencies are approaching 27% with the latest certified record of Kaneka at 26.7% [20, 6]. Therefore, only marginal improvements in performance are still possible, considering the 29.4% theoretical

limit for c-Si single junction solar cells [21], imposed by Auger recombination.

For tandem applications, c-Si solar cells are nearly ideal in the role of the low band gap bottom cell due to their suitable band gap of 1.1 eV, high open circuit voltage (V_{oc}) of up to 750 mV [22], high infrared response [23], cost-competitive manufacturing based on their market dominance, and high efficiency [6]. Silicon solar cells have become mass-production products, fabricated in a highly competitive industry system. This competition is however at the cost of innovation and reactiveness: it is nowadays extremely difficult for any new technology to enter the photovoltaic market and sustain the competition with c-Si. Therefore, innovation and disruption has a better chance to succeed in a collaborative manner: developing strategies to further improve the efficiency or reduce the cost of c-Si solar cells by adding or changing some steps in the production line, rather than trying to replace it entirely.

1.3.2.2 A disrupting newcomer: Perovskites *

Finding the ideal wide-band gap partner for c-Si is considerably more difficult. III-V solar cells have been proposed for their high efficiency and tunable band gap, and mechanically stacked 4-terminal tandem cells with >32% efficiency were recently demonstrated [14]. However, the high manufacturing costs of III-V solar cells hinders their large-scale deployment for terrestrial applications. Also, epitaxial growth of high-quality III-V layers on silicon substrates for monolithic tandem cells remains challenging [24]. A possible answer to this quest for high efficiency and low cost came with the emergence of perovskite solar cells [25, 26].

Perovskite is the name given to materials having the ABX$_3$ crystal structure, as illustrated in Figure 1.4. The A-site is filled with cations such as methylammonium, CH_3NH_3 (MA), formamidinium, $[R_2N - CH = NR_2]^+$ (FA), or Cs, either alone or mixed. The B-site contains the metal element, usually Pb, Sn or a mix of both. And the X-site has the halide elements, *e.g.* I, Br, Cl.

Organic-inorganic lead halide perovskite solar cells present several advantages that make them highly interesting for their use as a top cell in silicon-based tandem solar cells. The performance of perovskite cells has been rapidly raised to >22% [7], with an increasing number of research groups showing >20% efficient cells [27, 28, 29, 30, 31, 32]. Their exceptional optoelectronic properties are also well suited for tandem applications, including a high absorption coefficient, low sub-band gap absorption, and a steep absorption edge [33]. Moreover, perovskite solar cells offer band gap tunability throughout a wide spectral range [34], high V_{oc} with low potential loss [35], high defect tolerance, long charge carrier diffusion lengths [36], and photon recycling [37]. Importantly, perovskite solar cells combine high efficiencies and excellent optoelectronic properties with the potential for low-cost processing and abundant availability of the constituent elements [38, 39]. Reported fabrication protocols for perovskite solar cells include a variety of deposition techniques based on solution processes, such as spin coating [29] or slot-die coating [40], as well as vacuum-based methods, such as thermal evaporation [?] or chemical vapor deposition [41].
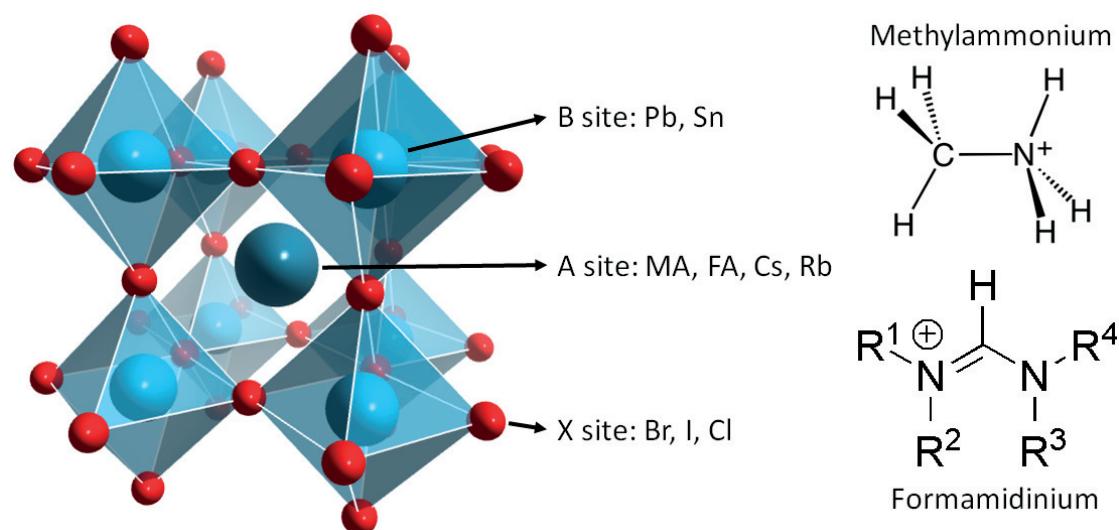
Figure 1.4 – ABX$_3$ crystal structure of perovskite materials and chemical structure of the two most used A-site cations: methylammonium and formamidinium. Adapted from https://chemicalstructure.net/portfolio/perovskite/

1.3.3 Tandem architectures *

A tandem solar cell can be made in several configurations, each of them having specific advantages and disadvantages, which will hereafter shortly be introduced and compared.

The most simple tandem device architecture from a process development point of view is the mechanically stacked 4TT (Figure 1.5a). The two subcells are fabricated independently, stacked on top of each other and contacted individually. This has the obvious advantage of process simplicity, allowing for the use of the optimal fabrication conditions specific to each subcell, *e.g.* concerning cell polarity, substrate roughness, process temperature, and solvents. This configuration requires four electrodes, with at least three of them showing high transparency in a wide spectral range for the front window electrode and at least in the infrared spectral region for the other two. Minimizing parasitic absorption and manufacturing costs for these electrodes is therefore crucial for the viability of this tandem configuration. During operation, the two subcells can be independently kept at their maximum power points, with separate tracking systems. This in particular reduces the constraints on the choice of the top cell band gap and makes the system less sensitive to spectral variations. As a result, 4TT cells can reach high efficiencies with a broad range of top cell band gaps ranging from 1.6-2 eV, with an optimum at 1.81 eV when using a crystalline silicon bottom cell [42]. However, using 4 terminals implies also doubling all the power electronics, *e.g.* inverters, which comes at a cost. As a possible solution to this problem, mechanically stacked voltage-matched tandem modules have been proposed, using only 2 terminals and arranging the cells in sub-modules connected in parallel [43, 44]. As the open-circuit voltage varies logarithmically with light intensity, a voltage-matched connection can be more resilient toward spectral variations compared to a current-matched connection.

Other 4TT concepts were demonstrated, such as spectral splitting systems [45, 46, 47] or
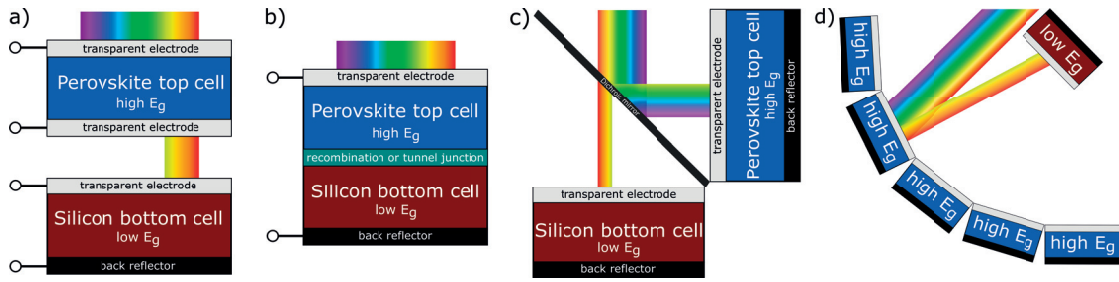
Figure 1.5 – Schematics of several perovskite/silicon tandem architectures: a) 4-terminal mechanically stacked; b) 2-terminal monolithically integrated; c) 4-terminal optical spectral splitting; d) 4-terminal reflective tandem. For all these configurations, the perovskite top cell has a higher band gap (E_g) than the crystalline silicon bottom cell with E_g = 1.1 eV. Reproduced with permission [1]. Copyright 2017, John Wiley and Sons.

reflective tandems [48, 49]. A 4-terminal spectral splitting tandem device consists of a dichroic mirror, which splits the light toward the high and low band gap cells, as illustrated in Figure 1.5c. This has the advantage that standard cells can be used without any specific adaptation, particularly without the need for additional transparent electrodes. However, the optical components are usually expensive, limiting the economic viability of this tandem architecture for non-concentrated photovoltaic systems. Reflective tandems could be an interesting alternative. The PVMirror concept, introduced recently by Holman *et al.* [49], consists of placing the cheapest subcell in a curved arrangement and use either a short-pass or a long-pass dichroic mirror to reflect and concentrate respectively the long or short wavelengths of light onto the more expensive subcell. The concept therefore offers high flexibility in terms of manufacturing and system integration, as it can be combined with other solar energy harvesting technologies, *e.g.* solar thermal collectors. However, such approaches, which require solar tracking, will be poor at collecting the diffuse light present in the solar spectrum, and their performance might strongly be impacted by module soiling.

Due to the limitations and the rather complex system integration for spectral splitting and reflective tandem cells, the focus of the rest of this Section will be set on 2-terminal and 4-terminal planar modules.

Figure 1.5b presents a monolithically integrated 2-terminal perovskite/silicon tandem solar cell. This architecture consists of a perovskite top cell, which is deposited onto the silicon bottom cell. The two subcells are then electrically connected in series, through a recombination layer or tunnel junction. Compared to the 4-terminal mechanically stacked tandem, this architecture therefore requires only one transparent electrode, lowering the manufacturing costs due to reduced material usage and fewer deposition steps. The reduced number of electrodes also leads to less parasitic absorption in the non-active layers, which is why 2-terminal tandems have a high practical efficiency potential. Following Kirchhoff's law, a monolithic tandem will have a voltage equal to the sum of the ones of the two subcells, which is beneficial as high voltages result in reduced resistive losses in PV systems. However, 2-terminal tandem cells also have some constraints: The two subcells must be designed to generate similar photocurrent under operation, as the tandem current will be limited by the subcell with the lower current. This current matching requirement limits the ideal top cell band gap to a narrow

range of 1.7-1.8 eV and makes the system also more sensitive to spectral variations, requiring for optimal operation a specific design for a specific geographic location. Finally, as the top cell layers are deposited onto the bottom cell, the top cell processing has to be performed such that the bottom cell performance is not affected. In addition, the bottom cell has to act as a suitable substrate, which is especially challenging for cells with textured surfaces, as it is typically the case for crystalline silicon cells.

Using detailed-balance calculations, including Auger recombination limiting the silicon single junction cells to 29.4% [21], the theoretically achievable efficiency for perovskite/silicon tandem cells in the 2-terminal and 4-terminal configurations can be calculated [50, 51, 52]. An efficiency limit of about 43% was found for both configurations, with steeply falling values for non-ideal top cell band gaps in case of the 2-terminal tandem due to the current matching restriction. The optimal top cell band gap is considerably broader for the 4-terminal configuration as the subcell currents do not have to be matched.

Perovskite solar cells are suitable partners not only for crystalline silicon but also for emerging thin film technologies, such as chalcogenides [53, 54, 55], kesterites [56] or polymer solar cells [57]. Clear efficiency gains have already been demonstrated, compared to the individual subcell performances, with a 4TT measurements over 23% with CIGS bottom cells [55]. All-perovskite tandems were also already demonstrated. With the recent development of low-band gap perovskite materials, their performance was rapidly raised to >20% [58, **?**, 59, 60, 61]. On the other hand, silicon solar cells can also be combined with other top cell technologies, such as III-V cells [14]. This type of cells has been successfully applied in satellites and terrestrial concentration systems, and allows for high efficiencies with material compositions having ideal top cell band gaps of 1.7-1.8 eV. However, the bottleneck for III-V/silicon tandem cells is the production costs of the top cell: For one-sun terrestrial applications these tandem cells become economically viable only if the GaAs or InGaP cells can be manufactured at a similar price as the silicon cell [15], a cost target which has so far not been reached. Nevertheless, III-V/silicon tandems might find usefulness in applications where space constraints (*e.g.* small roofs) and/or weight saving and power density are more important than achieving the lowest cost.

1.4 The childhood of perovskite/silicon tandem solar cells *

Even though perovskites have already been studied in the 1990s for light emitting diodes in particular by Mitzi et al. [62], the first publication showing a solar cell with a perovskite absorber material was published only in 2009 by Miyasaka's group [63]. The efficiency was only 3.8% with a device life time in the range of minutes due to the use of a liquid electrolyte. However, this launched an incredible competition in the photovoltaics research community, leading to 22.7% certified efficiency in 2018. A dedicated review was published elsewhere, providing more in-depth historical details on the birth of the perovskite solar cell [25].

Perovskite materials quickly triggered interest for multijunction solar cells. Already in his original paper [63], Miyasaka demonstrated high band gap materials showing high photovoltage

and band gap tunability in the range 1.5-2.1 eV. Later, the possibility to make planar thin film solid-state devices [64] and to use vacuum-based techniques [65] confirmed the potential of this technology to partner with silicon for low-cost tandem cells [66].

In 2014, De Wolf et al used photothermal deflection and photocurrent spectroscopy techniques to measure the absorption spectrum of methylammonium lead triiodide (MAPbI$_3$), the most wide-spread perovskite composition [33]. Remarkably, this study showed that this composition has a very large absorption coefficient, with sharp absorption edge and low sub-band gap absorption, typical of direct semiconductors, such as III-V materials. These optoelectronic properties are essential for a top cell in a tandem solar cell, as they allow for the use of relatively thin absorber layers and lead to minimal parasitic absorption in the sub-band gap spectral region where the light has to be transmitted to the bottom cell.

At the same time, several publications presented simulations based on optical modelling [50, 51, 67, 68, 69], establishing the requirements and challenges to reach efficiencies beyond 30%. Light management and parasitic absorption were already early identified as major challenges, which will be discussed in more detail in the following Chapters.

The development of any flat plate tandem solar cell in the 4-terminal or 2-terminal configuration involves replacing the opaque metal rear contact used in single-junction perovskite solar cells with a transparent electrode. The first reports of semitransparent perovskite solar cells and mechanically stacked tandem cells were published at the end of 2014 by Löper *et al.* [70] and by Bailie *et al.* [71], showing 13.4% and 17% 4-terminal tandem efficiencies, respectively. Löper *et al.* used a sputtered indium tin oxide (ITO) transparent electrode, which
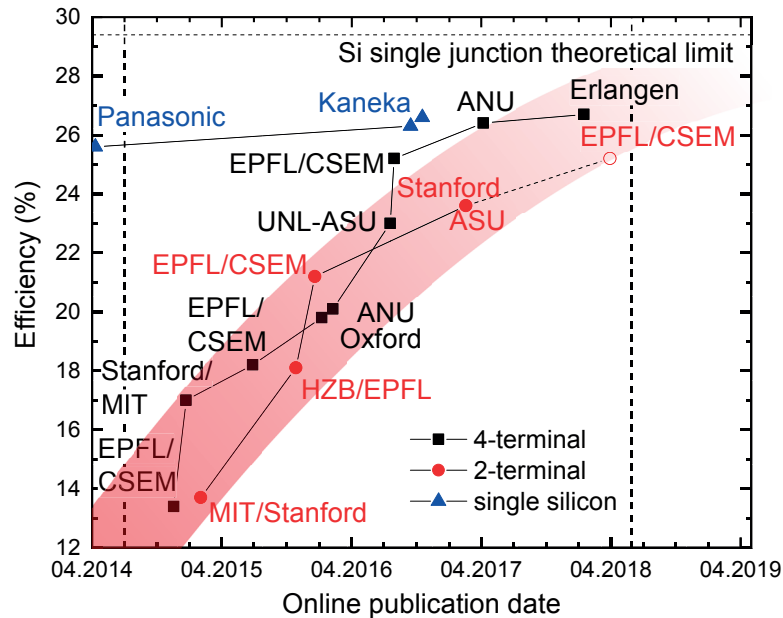
Figure 1.6 – Monolithic 2-terminal and mechanically stacked 4-terminal perovskite/silicon tandem efficiency record evolution, according to the online publication date. The vertical dashed lines indicate the starting date and defence date of this thesis. The horizontal dashed line at 29.4% indicates the theoretical efficiency limit for single-junction silicon solar cells. Adapted with permission [1]. Copyright 2017, John Wiley and Sons.

had however suboptimal electronic properties, as the high-temperature treatment normally necessary to reach a low sheet-resistance would have severely damaged the perovskite cell. The same group showed later that using an amorphous TCO, in this case indium zinc oxide (IZO), instead of ITO can solve this issue as it can be used as-deposited and still has a high carrier mobility and low sheet resistance [72]. Bailie *et al.* used a silver nanowire mesh, which was first formed by spray coating on a polymer foil and then mechanically transferred onto the perovskite cell layer stack. They could show high transparency and low sheet resistance, but the reproducibility due to the mechanical transfer was still challenging [71].

Soon after that, this same group collaborated with the Buonassisi group at MIT to fabricate the first perovskite/silicon monolithic tandem using the same silver nanowire electrode [81]. Using a mesoporous perovskite top cell and a diffused junction silicon bottom cell with a silicon tunnel junction, they showed a 13.7% efficient monolithic tandem with still modest V_{oc} of 1.58 V. Parasitic absorption in the charge transporting layers was drastically limiting

Table 1.1 – Evolution of 4-terminal and 2-terminal perovskite/silicon tandem efficiency. * designates steady state efficiencies. SHJ: silicon heterojunction solar cell; PERL: passivated emitter with rear locally diffused solar cell; IBC: interdigitated back contact solar cell; nc-Si: nanocrystalline silicon [70, 71, 72, 73, 74, 75, 76, 77, 78, 79, 80, 81, 82, 83, 84, 85, 86, 87, 88]. Note that EPFL LPI is the laboratory for photonic interfaces of Prof. Michael Graetzel, and EPFL otherwise designates EPFL PV-Lab, the laboratory of photovoltaics of Prof. Christophe Ballif.

Mechanically stacked 4-terminal						
Perovskite	Eg, eV	Silicon	Area, cm^2 top; bottom	PCE % top + bottom = total	Institute	Year
MAPbI$_3$	1.55	SHJ	0.25; 4	6.2+7.2=13.4	EPFL/CSEM	2014
MAPbI$_3$	1.55	Multi-Si	0.39; 0.39	12.7+4.3=17.0	Stanford/MIT/EPFL	2014
MAPbI$_3$	1.55	SHJ	0.25; 4	10.4+7.8=18.2	EPFL/CSEM	2015
FACsPbI$_{3-x}$Br$_x$	1.74	SHJ	0.09; na	12.5+7.3=19.8*	Oxford/HZB	2016
MAPbI$_3$	1.55	PERL	0.25; 4	12.2+7.9=20.1*	ANU	2016
MAPbI$_3$	1.55	SHJ	0.075; 4	16.5+6.5=23.0	UNL/ASU	2016
MAPbI$_3$	1.55	SHJ	0.25; 4	16.4+8.8=25.2*	EPFL/CSEM	2016
MAPbI$_3$	1.55	SHJ	1; 4	14.5+8.5=23.0*	EPFL/CSEM	2016
CsMAFAPbI$_{3-x}$Br$_x$	1.63	IBC-SHJ	0.36; 4	16.6+7.9=24.5*	ANU	2016
RbCsMAFAPbI$_{3-x}$Br$_x$	1.74	IBC	0.16; 4	16.0+10.4=26.4*	ANU	2017
MAPbI$_3$ (module)	1.55	IBC	4; 4	12.0+8.2=20.2	IMEC	2017
MAPbI$_3$	1.55	PERL	0.1; 1	17.1+9.6=26.7	Erlangen	2018
MAPbI$_3$	1.55	IBC	0.1; 1	17.1+8.1=25.2	Erlangen	2018
CsFAPbIBr	1.56	IBC	4; 4	15.3+8.6=23.9*	IMEC	2018

Monolithically integrated 2-terminal							
Perovskite	Eg, eV	Silicon	Recomb. layer	Area, cm^2	PCE %	Institute	Year
MAPbI$_3$	1.55	Homojunction	n^{++}/p^{++} Si tunnel	1	13.7	MIT/Stanford	2015
FAMAPbI$_{3-x}$Br$_x$	1.56	SHJ	ITO	0.12	18.1*	HZB/EPFL	2015
MAPbI$_3$	1.55	SHJ	IZO	0.17	21.2*	EPFL/CSEM	2015
MAPbI$_3$	1.55	SHJ	IZO	1.43	20.5*	EPFL/CSEM	2016
MAPbI$_3$	1.55	Homojunction	ZTO	1.43	16.0*	EPFL/CSEM	2016
CsFAPbI$_{3-x}$Br$_x$	1.63	SHJ	ITO	1	23.6*	Stanford/ASU	2017
CsFAPbI$_{3-x}$Br$_x$	1.63	SHJ	nc-Si tunnel	0.25	22.8	EPFL/CSEM	2017
CsFAPbIBr	1.63	SHJ	nc-Si tunnel	12.93	18.0*	EPFL/CSEM	2017
CsRbFAMAPbIBr	1.6	Homojunction	ITO/Cr/Pd/Ag	1	22.5*	ANU	2018

the performance of this monolithic tandem device. These first publications launched an efficiency race, as illustrated in Figure 1.6 and summarized in Table 1.1, showing the main perovskite/silicon tandem experimental results published in the years 2014-2018.

At the end of 2015, Albrecht *et al.* used a silicon heterojunction solar cell as the bottom cell for a monolithic tandem with 18.1% efficiency [82], exploiting their high near-infrared spectral response and high voltage. It was also the first demonstration of a low-temperature planar perovskite solar cell using an atomic layer deposition (ALD)-grown SnO_2 layer as the electron transporting layer. The monolithic tandem efficiency record was improved two months later by Werner *et al.* with a PCBM-based planar perovskite top cell and an IZO intermediate recombination layer, reaching 21.2% steady-state efficiency [83]. This cell was limited by the bottom cell current, due to the use of a double-side polished silicon wafer. In August 2016, the bottom cell current was improved with the introduction of rear-side textured silicon wafers, and an efficiency of 20.5% was demonstrated on a 1.4 cm^2 monolithic tandem cell, as compared to the previous monolithic tandem cells demonstrated on sizes <0.3 cm^2 [76].

In the meantime, progress was made on the development of perovskite materials with wider band gaps containing cesium (Cs) cations, resulting in improved device stability and higher reproducibility [89]. McMeekin *et al.* then used a Cs-FA double cation perovskite material to open the band gap to ≈1.74 eV, the ideal value for a top cell absorber material [73].

Device stability is a major challenge for the development of perovskite solar cells and particularly for their implementation in tandem solar cells with silicon technologies. Thermal stability is necessary for the cell to survive conventional encapsulation with >100°C annealing temperature and to pass damp-heat testing protocols. Bush *et al.* demonstrated that perovskite solar cells featuring TCO front and rear electrodes (and thus suitable for tandem integration) show improved thermal stability as compared to cells with a metal rear electrode. The TCO rear electrode can act as an efficient barrier for moisture ingress and should prevent the loss of volatile organic compounds from the absorber layer [90].

In February 2017, the same group managed to pass a 1000-hour damp heat test at 85°C and 85% relative humidity with a semitransparent perovskite solar cell, using a p-i-n polarity and a CsFA double cation perovskite material. In the same publication, a 1 cm^2 monolithic tandem with 23.6% efficiency was demonstrated [85], the published record value for a perovskite/silicon monolithic tandem cell at the time of writing this thesis[3].

The performance of mechanically stacked 4-terminal tandem cells also gradually increased, mostly driven by the improved efficiency of single-junction semitransparent perovskite cells. Important progress was made in 2016 with the first experimental demonstration of >25% total efficiency [76]. The Catchpole group at ANU then pushed this performance to 26.4% by developing wide band gap multication perovskite absorber [78] and Brabec's group in Erlangen further improved it recently to 26.7% by better controlling electrical and optical losses [80]. These 4-terminal tandem measurements were combining small <0.2 cm^2 top cell with larger 1-4 cm^2 silicon bottom cell. Until now, this was the case for most published 4-terminal results, based on indirect performance measurements of the two subcells. However, first

---

[3]Tandem cells with >25% efficiencies were however announced by several groups in conferences between March and May 2018, including EPFL/PV-lab (see Section 5.4.3)

progress in up-scaling the perovskite top cell has already been made. 1 cm^2 semitransparent perovskite cells were demonstrated with 14.5% efficiency [76, 85]. When combined into a fully integrated 4-terminal tandem device with a silicon heterojunction bottom cell of the same size, an efficiency of 23.2% was reached [91]. Further up-scaling typically involves reducing resistive losses in the transparent electrodes and scribing of the layer stack to define segments and to interconnect them into a module. Semitransparent modules with an aperture area of 4 cm^2 were recently demonstrated, reaching an efficiency of 12%, which led to a module-on-cell 4-terminal tandem with 20.2% efficiency [79]. The same group then further improve this performance to 23.9% by reducing reflection losses with the introduction of a microtextured antireflective foil (ARF) and an intermediate optical coupling liquid [88].

1.5 Techno-economic considerations for tandem solar cells *

Several studies have addressed the economics of perovskite solar cells [92, 93, 94]. In this Section [4], we focus on monolithic 2-terminal tandem cells, guided by simple considerations of manufacturing processes in production lines, keeping in mind that no fully defined industrial manufacturing process for perovskite-based cells exists yet. For this analysis, we consider the number of process steps required in addition to those for the silicon bottom cell (which could be Al-BSF, PERC or SHJ). In particular, metallization costs of the front are not included, being already part of the silicon cells. Each process step specific to the perovskite top cell has related investments, costs of consumables, and operational costs (personal, facilities and maintenance). In Table 1.2 we assume that each process step has related investment costs in the range of 1-3 million €, allowing for the processing of 3000 wafers per hour or an equivalent of around 400'000 m^2 of panels per year. We make an assumption of 15% operational cost per year compared to investments, and of 1.5 €/m^2 of consumables per step. The proposed values are in the range of what is possible either for coating on c-Si wafers (*e.g.* SiN layer, or ultra-thin ALD films), or for thin film processes with low-cost materials (e.g. thin semiconductor layer, 70-100 nm TCO layer). Table 1.2 shows that, for instance, a 4% absolute efficiency increase, equal to the power output of an additional 40 W/m^2, would result in manufacturing costs of 26 €cts per additional watt of output power of the module in the case of 4 extra process steps, with 1.5 M€ investment per step. A similar cost can also be achieved with more steps, which would however require a higher increase in efficiency.

This represents a good target value, considering the roadmap of c-Si module costs, which are expected to reach 25-30 €cts/W within the next five to ten years [95]. It is also possible to make a rough estimation of the value related to the enhanced module efficiency. Assuming that the area-related costs are in the range of 27 €/m^2 for solar parks (all costs excluding inverter) and 63 €/m^2 for small rooftop systems, the efficiency gain translates into a saving in a range of a few cents (here 2.1 €cts/W to 2.7 €cts/W for solar parks and 6.4 to 7.6 €cts/W for rooftops). These values show that even though it will be challenging to reach considerably

---

[4]This Section is taken from a review paper that we published in Advanced Materials Interfaces [1] and was written by Prof. Christophe Ballif. It gives an important message for the future commercialization of the perovskite/silicon tandem technology developed during this thesis.

Table 1.2 – Guideline for estimating potential manufacturing costs of the perovskite top cell in a monolithic perovskite/silicon tandem cell. We consider only the extra-steps induced by the perovskite top cell deposition (and not the potential steps saved on the c-Si cell). The equipment is depreciated over 7 years. Consumable costs of 1.5 €/m^2 per step and 15% operational costs per year as fraction of CAPEx (including facilities, maintenance personals) are assumed. For the area related costs savings, 18% nominal module efficiency is considered. Reproduced with permission [1]. Copyright 2017, John Wiley and Sons.

Number of extra-steps	Investment [M€/step]	Depreciation [€/m^2]	Consumables [€/m^2]	Operational costs [€/m^2]	Total process costs [€/m^2]	Abs. Eff. Gain [%]	Manufacturing costs [€cts/W]	Area related BOS cost saving [€cts/Wp] Parks	Area related BOS cost saving [€cts/Wp] Roof top
3	1.5	1.61	4.5	1.69	7.79	4	19.5	2.7	6.4
4	1.5	2.14	6	2.25	10.39	4	26	2.7	6.4
5	1.5	2.68	7.5	2.81	12.99	4	32.5	2.7	6.4
3	3	3.21	4.5	3.38	11.09	4	27.7	2.7	6.4
4	3	4.29	6	4.5	14.79	4	37	2.7	6.4
5	3	5.36	7.5	5.63	18.48	4	46.2	2.7	6.4
4	2	2.86	6	3	11.86	3	39.5	2.1	5
4	2	2.86	6	3	11.86	5	23.7	3.3	7.6

lower module production costs per Watt compared to single-junction c-Si in the mid-term, perovskite/silicon tandem PV systems could be cost competitive as a result of their higher performance, especially for applications where surface area is limited. Then the higher we can increase the efficiency gain, the more BOS cost we can save.

The final production costs will include other possible positive factors (reduced costs of metallization thanks to the high-voltage, low-current device), and potentially also negative ones such as yield (possibility of shunting the top cell) or the requirement for edge sealants in modules. Similarly, the energy yield might be favored by the good temperature coefficient of the top cell, whereas spectral mismatch effects, long-term degradation and bankability (meaning higher cost of capital) might penalize the cost of electricity produced by such modules. As a general guideline, in addition to demonstrating real long term stability, the viability is ensured by two important factors: the increased efficiency gain compared to the original single-junction solar cells, and the reduction of the number of additional process steps (or of the costs associated with each step). Finally, this simple calculation also shows that all usage of expensive material (typically >10 €/m^2) will likely prevent any market penetration of this technology.

1.6   Objectives and structure of the thesis

1.6.1   Objectives

The objective of this thesis is to develop perovskite/crystalline silicon tandem solar cells, with efficiencies beyond the state-of-the-art single-junction silicon solar cells and cell size >1 cm^2. This requires the combination of two very different photovoltaic technologies in a single device, while maintaining their individual performances. The scientific challenges are in developing new perovskite absorber materials with appropriate optical band gap and stability, as well as the charge transporting layers and transparent contacts with minimized parasitic absorption. The technological challenges are the development of the device structure, the development of the absorber and contact material deposition processes and the practical demonstration of large size perovskite-based solar cells while using industrially compatible and available processing techniques that can be easily implemented into a standard silicon process line at low additional costs.

1.6.2   Structure

The structure of this thesis is as follows:

- **Chapter 2** presents the development of a low temperature hybrid sequential deposition technique for the perovskite absorber and the fabrication of single junction opaque perovskite solar cells with tunable band gap.

- **Chapter 3** investigates the replacement of the standard opaque metal electrode of perovskite cells by a broadband transparent electrode based on sputtered TCOs.

- **Chapter 4** presents the application of semitransparent perovskite cells in mechanically stacked 4-terminal tandem solar cells.

- **Chapter 5** investigates the integration of perovskite solar cells in monolithic tandem solar cells, from flat to fully textured devices.

- **Chapter 6** concludes this thesis by summarizing the work and providing a perspective outlook for future research on the topic.

1.7   Contribution to the field

The present work contributes to the fields of silicon photovoltaic devices and of perovskite solar cells as follows:

As a replacement to the gold opaque rear metallization of perovskite single junction cells, we demonstrated a broadband transparent electrode based on a sputtered amorphous indium zinc oxide [72]. We optimized the device performance by introducing a transition metal oxide

buffer layer to protect the sensitive organic layers from the plasma environment. In-depth investigations of these metal oxides revealed interesting interactions with temperature, Ar ion bombardment or plasma luminescence, which can be prevented by a CO_2 plasma treatment [96].

For the perovskite absorber layer, we developed an hybrid sequential deposition method involving a first co-evaporation of cesium-based compounds with lead iodide and then a transformation to the perovskite phase by spin coating the organo-halide solution followed by thermal annealing. With a systematic investigation of the optical, structural and electronic properties of perovskite materials with various optical band gaps, the performance of perovskite solar cells in both n-i-p and p-i-n configuration was improved and optimized for tandem integration. Also, refractive index and extinction coefficient were measured for perovskite materials with optical band gap between 1.5 and 1.8 eV, which is required for multijunction optical modelling [97].

We applied the semitransparent perovskite cells in mechanically stacked 4-terminal tandem cells and demonstrated up to 25.6% total efficiency with a top cell having 0.25 cm^2 area, and up to 23.2% with a 1 cm^2 area top cell. This last performance was measured in an integrated device where both subcells had the same size and were attached together with a PDMS optical coupling layer [76, 91]. This result is so far the only demonstration of perovskite/silicon 4TT integrated device, making it the most comparable with III-V/c-Si state-of-the-art 4TT devices.

Finally, we developed monolithically integrated tandem devices. By implementing the advancements in our perovskite single junction cells development, we showed high performance monolithic tandem cells first in n-i-p configuration with all flat surfaces and later in p-i-n configuration with fully textured bottom cells and conformal top cell coating. With this last close-to-optically optimal cell, record certified efficiencies up to 25.2% were demonstrated [83, 76, 84, 98].

These findings open the way for >30% efficient silicon-based photovoltaics, with low additional manufacturing cost and high potential for industrialization. Finally, this thesis work contributes to other related investigations on transition metal oxides [99, 100], on perovskite/perovskite tandem devices [101], and on studies toward a better understanding of perovskite materials and devices [102, 103, 104, 105, 106, 107, 108, 109, 86]

2 Toward a tandem-specific perovskite cell: method, materials and device development

Summary

This chapter presents first the requirements a perovskite top cell should meet for an optimal integration in a silicon-based tandem device. Then the method used throughout this thesis for the perovskite absorber deposition is described in detail. This method is based on an hybrid sequential deposition technique involving a thermal evaporation of PbI_2 followed by an organo-halide solution spin coating. Perovskite materials with various optical band gaps are fabricated and characterized through a large optical, structural and electronic study. In particular, their complex refractive indices are compared and discussed in function of their fabrication conditions. Finally, devices in both n-i-p and p-i-n polarities are presented using the various perovskite absorber materials.

2.1 Introduction *

Developing perovskite-based tandem solar cells necessarily requires an adaptation of the single-junction cell fabrication process. Historically, perovskite solar cells were first based on the dye-sensitized solar cell architecture, including a mesoporous titan dioxide (mp-TiO$_2$) scaffold layer requiring a sintering step at 500°C [72]. This relatively high temperature is not of concern for 4-terminal tandem cells, where both subcells are fabricated separately. For monolithic tandem cells, however, this process temperature limits the options for the silicon bottom cell to diffused-junction or "tunnel oxide" cells. Silicon heterojunction solar cells, currently the crystalline silicon technology with the highest performance and therefore especially interesting for high-efficiency silicon-based tandems, are only compatible with top cell processes up to ≈200°C. Above this temperature, the hydrogen from the amorphous silicon layers passivating the wafer surfaces starts effusing, which strongly affects passivation and hence leads to reduced V_{oc}[18].

After an initial phase, when mesoporous perovskite solar cells were dominating the field, planar, *i.e.* scaffold-free, cells started to catch up, driven by improvements of the perovskite material quality and better interface control [110]. The removal of the scaffold structure enabled the development of highly efficient perovskite cells, which are fully processed at low temperatures (<200°C) and compatible with silicon heterojunction bottom cells [76, 111, 112, 113]. Charge transporting layers deposited at low temperatures include p-type 2,2',7,7'-Tetrakis-(N,N-di-4-methoxyphenylamino)-9,9'-spirobifluorenes (spiro-OMeTAD), poly(3,4-ethylenedioxythiophene)-poly(styrenesulfonate) (PEDOT:PSS), poly(triarylamine) (PTAA) and NiO$_x$, as well as n-type titan dioxide (TiO$_2$), SnO$_2$, Buckminsterfullerene (C$_{60}$) and phenyl-C61-butyric-acid-methyl-ester (PCBM), among others [110, 114, 115].

The most widely used perovskite material composition is MAPbI$_3$ with a band gap of ≈1.55 eV, which is below the optimal value of ≈1.73 eV for an ideal top cell in monolithic tandems with silicon bottom cell. For 4-terminal tandem cells, the ideal band gap is slightly larger, even though high efficiencies can also be reached with non-ideal top cell band gaps due to the considerably less pronounced performance drop for lower band gaps [116]. Although MAPbI$_3$ top cells were well suited for initial proof-of-concept tandem devices, demonstrating efficiencies beyond the single-junction silicon record, especially for monolithic tandems, requires top cells with a ≈0.2 eV higher band gap. This increase in band gap has to be reached while still preserving material and interface quality, to obtain a corresponding increase in V_{oc}. The band gap of MA-based perovskites can easily be increased by substituting part of the iodine with bromine, yielding values between 1.55 eV and >2 eV [117]. However, the stability of these compounds has been found to be highly limited, subject to photo-induced phase segregation and phase separation [118, 119, 120, 121].

A breakthrough concerning phase stability was reached with the introduction of perovskite materials containing the Cs and FA cations, either partially or fully replacing MA [73, 89]. For example, using the $(FA_{0.83}Cs_{0.17}Pb(I_{0.6}Br_{0.4})_3)$ material with a band gap of 1.74 eV, perovskite cells with up to 17% efficiency were demonstrated, yielding a V_{oc} of 1.2 V with the theoretical potential of 1.42 V [73]. Moreover, Beal *et al.* showed that the MA cation is volatile and tends to

evaporate from the device under thermal stress during device operation, such that replacing it with Cs considerably improves the thermal stability [122]. The purely inorganic $CsPbBrI_2$ material showed a suitable band gap close to 1.9 eV. However, the cell performance was still very limited due to a non-optimized deposition process and too thin absorber layer. The $CsPbI_3$ composition would be highly suitable for tandem applications as well, with a band gap of 1.73 eV [123]. Unfortunately, its photoactive phase is unstable at room temperature [124]. Unger *et al.* compared reported data of perovskite cells with band gaps between 1.2 and 2.2 eV and found that most reported V_{oc} followed the expected monotonic increase for band gaps up to ≈1.7 eV. For larger band gaps, strong deviations were observed, which they attributed to a phase separation, resulting in a lower V_{oc} [34]. Further work will therefore be required to improve the crystallinity and ionic homogeneity in wide-band gap perovskite materials.

The charge extraction layers must also be adapted to these new compositions with higher band gaps as shown by Lin *et al.* [125]. Increasing the band gap typically shifts the conduction band toward higher energies (toward the vacuum energy level). Thus, adapting the energy levels of the electron transporting layer helped to increase the V_{oc} and reach efficiencies as high as 18.5% with a band gap of 1.71 eV.

Even though the optimal top cell band gap is 1.73 eV for ideal monolithic tandem cells, in state-of-the-art devices, current matching could be reached with band gaps of 1.6-1.65 eV, due to the parasitic absorption in the UV/visible spectral part in the transparent front electrode and the charge transporting layers. These devices did not reach ultimate performance, but further increasing the top cell band gap will also not be beneficial before the top cell spectral response is increased in that wavelength range. In addition, monolithic tandem cells typically show their highest performance at a slight current mismatch, when the subcell with the higher fill factor is current limiting [126]. Assuming that high-performance silicon bottom cells typically still exhibit higher fill factors, the ideal top cell band gap might be slightly below the above mentioned ideal values.

2.1.1 The requirements for tandem applications

We can therefore define the requirements for an ideal top cell in a silicon-based tandem:

- The entire cell layer stack must be processed at low temperature <200°C, in order to stay compatible with SHJ bottom cells.

- The usage of toxic solvents should be reduced as much as possible for environmental concerns and for the safety of the laboratory workers [127]. Examples of solvents with high health concerns include dimethylsulphoxide (DMSO),N, N-dimethylformamide (DMF) or chlorobenzene. The toxicity of the materials used in the device should also be considered, *e.g.* lead content.

- The processing techniques used for the perovskite absorber as well as for the charge transporting layer should be up-scalable, industrially compatible and highly reproducible.

- A planar architecture should be preferred, as it is simpler, leads to easier fabrication procedures and enhances direct optical coupling between the tandem subcells.

- The method for depositing the perovskite absorber should be compatible with rough substrate and yield conformal layers on silicon textured wafers.

- This method should be flexible enough to allow material compositional engineering, to easily tune the band gap and adapt the composition for optimal performance and stability.

- The perovskite material should have high optoelectronic quality, to allow high device performance. It should also be compact, pin-hole free, with low surface roughness in order to allow the use of thin charge transporting layers.

- The perovskite top cell must show minimal parasitic absorption losses over the entire spectral region, *i.e.* both in the low-wavelength region to minimize the losses in the top cell, and similarly in the longer wavelength region (sub-band gapregion of top cell) for the bottom cell, *i.e.* the device must feature broadband transparent electrodes and charge transporting layers.

- The materials used for the perovskite absorber, the charge transporting layers and electrodes should show a good chemical and environmental stability, ideally inert and non-volatile.

These requirements were the underlying motivations for the choices we made throughout this thesis, both for the methods and materials we used. The following Sections present the development of a perovskite cell toward the completion of these requirements. The development of transparent electrodes and near-infrared (NIR)-transparent perovskite cell will be the subject of the next Chapter 3.

2.2 A sequential 2-step hybrid deposition method

2.2.1 Presentation of the method

We chose to adopt and develop an interdiffusion method involving three important steps: first the inorganic components are deposited on the substrate, *e.g.* lead iodide (PbI_2), CsI, CsBr...; then an organo-halide-containing solution is spin coated; finally, the bilayer precursor is annealed on an hotplate to promote the interdiffusion of the organo-halide compounds into the PbI_2 layer and their chemical reaction leads to the formation of the final crystallised perovskite film.

The sequential method was first demonstrated in 2013 by Burschka *et al.* [128]. In this publication, the PbI_2/DMF solution was infiltrated in a mp-TiO_2 layer and then converted to $MAPbI_3$ by dipping the substrates into a 2-propanol solution of methylammonium iodide, CH_3NH_3I (MAI). Our early experimentation with this method revealed that the control of the
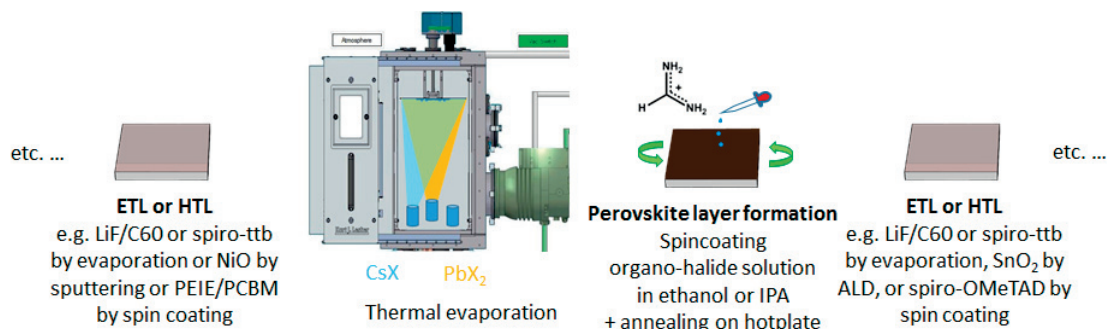
Figure 2.1 – Schematic description of the hybrid sequential 2-step deposition method.

concentration of MAI in the solution was difficult to keep constant and the dipping timing was crucial, impacting the reproducibility and yield. Other groups demonstrated that the solution-processed PbI_2 can be replaced by a thermally evaporated PbI_2 layer, then converted by spin coating a MAI in 2-propanol solution on this seed layer [112, 129].

We quickly adopted this strategy, schematically illustrated in Figure 2.1, using a Lesker mini-spectro thermal evaporator. This method was used for most devices presented in this thesis, as it was early-on foreseen as the most promising way to achieve high performance tandem solar cells on textured wafers, while allowing high freedom in the material composition development, the choice of charge transporting layers and up-scalability, satisfying many of the requirements stated in the previous Section.

2.2.2 Solvent engineering and perovskite morphology *

The perovskite layer morphology must be controlled to yield homogeneously distributed grain size, low surface roughness, compact layer with gains growing vertically throughout the layer and suppressed pin-holes formation. This can be achieved by controlling the evaporation conditions for the PbI_2 layer (shown in Figure 2.2) or by tuning the solvent during the solution processing step to deposit the organo-halide compounds. 2-propanol was first used as the solvent for MAI spin coating. It was however difficult to obtain a uniform layer on larger samples (*i.e.* 2.5x2.5 cm^2) without pin-holes. 20 mg/ml of 2-methoxyethanol were then added
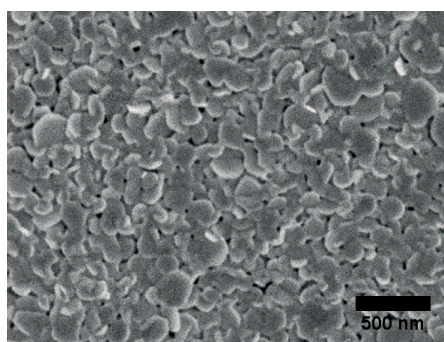
Figure 2.2 – SEM topview image of an evaporated PbI_2 layer on a glass/ITO substrate.
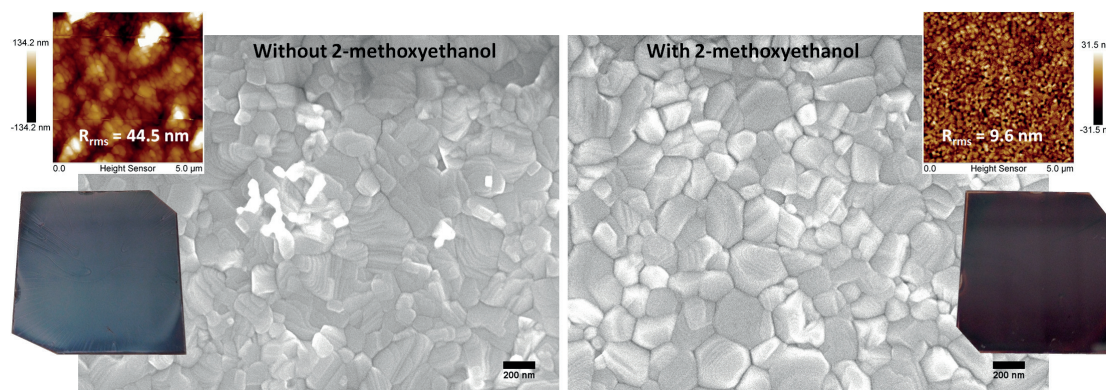
Figure 2.3 – SEM and AFM characterization of a MAPbI$_3$ perovskite layers grown without or with addition of 2-methoxyethanol in the MAI/2-propanol solution. The two pictures show 2.5x2.5 cm^2 substrates covered with the perovskite layer, illustrating the mirror-like appearance of the film when using the additive. Reproduced with permission [83]. Copyright 2016, American Chemical Society.

to the MAI solution. As shown in Figure 2.3, this helped to reduce the surface roughness of the perovskite layers from R$_{rms}$=44.5 nm down to 9.6 nm, as measured by atomic force microscope (AFM) [83]. The layers were then more homogeneous, more compact, contained less pin-holes and had a shiny appearance, as shown in the photographs in Figure 2.3. These observations were then confirmed by Ugur *et al.* in a larger study about glycol ether additives [130].

Further tests were carried out with other solvents, as shown in Figure 2.4. Pure ethanol was found to yield similar film morphology and device performance as the 2-propanol/2-methoxyethanol solution, with the advantage to be easier and more controllable. Also, increasing the annealing temperature of MAPbI$_3$ films from 100°C to 120°C allowed to increase the
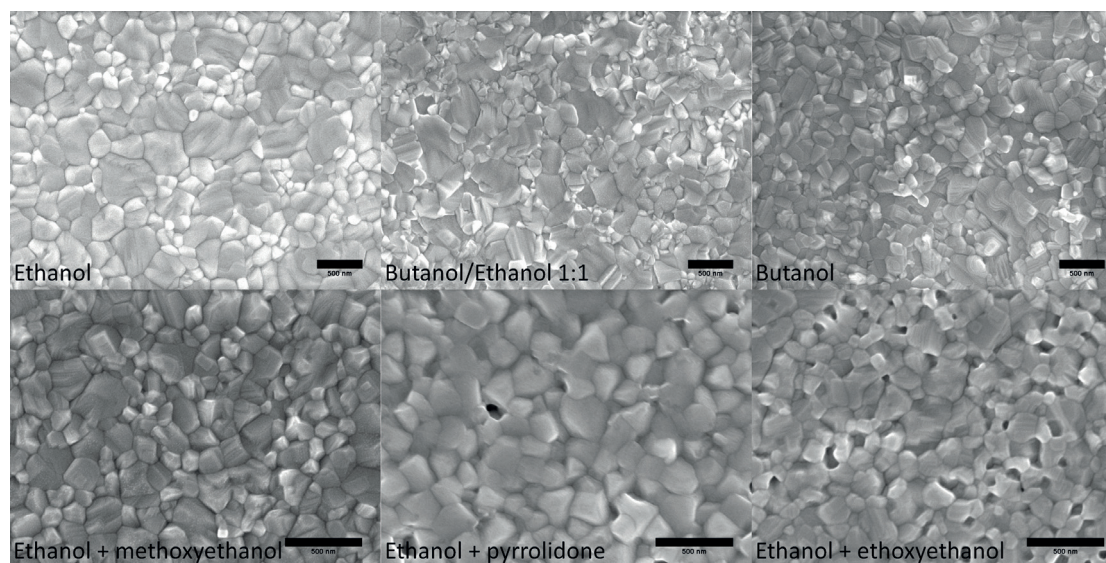
Figure 2.4 – SEM topview images of MAPbI$_3$ perovskite layers grown with various solvent mixture for the organo-halide solution, showing a solvent-dependent morphology.
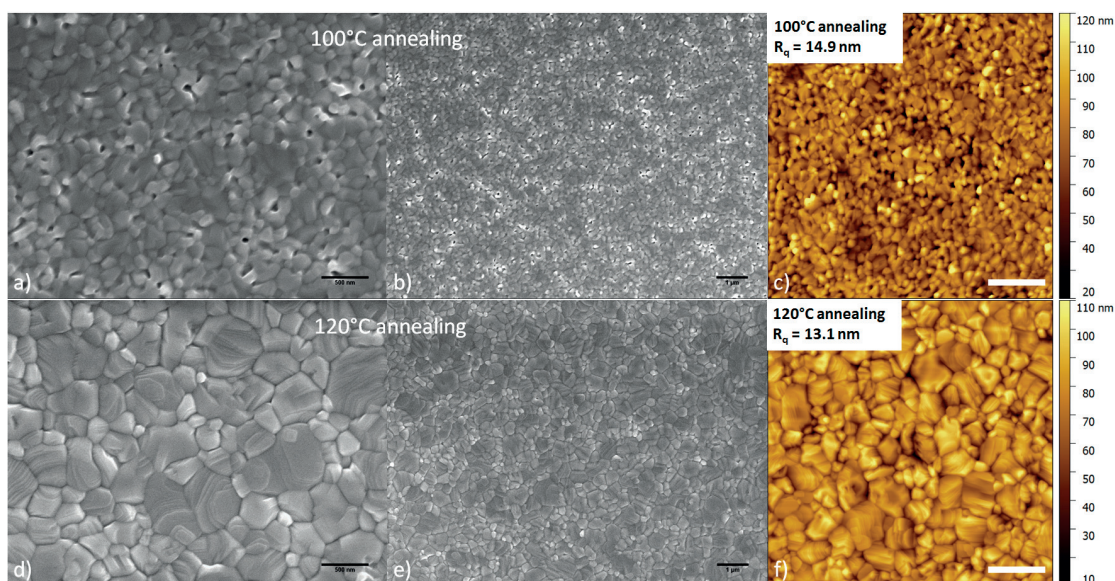
Figure 2.5 – Effect of the annealing temperature on the morphology and surface roughness of a MAPbI$_3$ perovskite layer grown with an ethanol solution: a), b), d) and e) scanning electron microscope (SEM) topview images. c) and f) AFM topographic images.

grain size and further reduce pin-holes formation (Figure 2.5). These empirical observations could unfortunately not be further studied and explained, due to time constraints imposed by the fast-moving field. For the rest of the thesis, pure ethanol was used for all devices, if not explicitly otherwise specified.

2.2.3 Perovskite material compositions with various band gaps*

The composition of the perovskite absorber, namely the cation (*e.g.* Cs, Rb, FA, MA and combinations thereof), the metal (*e.g.* Pb and/or Sn) and the halide (*e.g.* I, Cl, Br), can be modified to yield materials with absorption edges ranging from 1.2 eV up to >2 eV [34]. MAPbI$_3$ perovskites were the first widespread perovskite materials and was also therefore logically the first perovskite absorber used for this thesis. MAPbI$_3$ absorber layers however tend to be highly sensitive to environmental factors such as temperature, humidity, light [131, 132]... The MA cation was shown to become volatile at slightly elevated temperatures already around 85°C, leaving the layer decomposing back to PbI$_2$ [133]. Furthermore, tandem applications require materials with more optimized wider band gap energies in order to fine tune the current distribution in the tandem device. MAPbI$_3$ exhibits a band gap of only 1.55 eV, lower than the theoretically optimal band gap value of 1.72 eV for 2-terminal tandems [116]. In practice, we will see in Chapter 5 that the absorber material needs to be tuned rather between 1.6 and 1.7 eV to allow flexibility and to take into account parasitic absorption losses which reduces the theoretically optimal band gap to values <1.7 eV. Replacing the MA cation by Cs and FA was shown to yield more stable perovskite materials, while still preserving the high performance and band gap tunability [89, 122, 73, 134]. CsFA double cation perovskite materials were

also demonstrated with a sequential 2-step deposition method, using two spin coating steps [135, 136].

Based on these first demonstrations, we tried to fabricate these more promising compositions with the sequential 2-step hybrid deposition method described in the previous Section, comprising a co-evaporation step of a cesium halide compound and PbI_2, followed by spin coating of the FA halide solution [86, 97]. Three different cesium halides were used in this study: cesium iodide (CsI), cesium chloride (CsCl) and cesium bromide (CsBr), all co-evaporated with PbI_2. The final cesium content in the perovskite films was controlled by adjusting the evaporation rates of the Cs- and Pb-containing compounds. A mixture of formamidinium iodide (FAI) and formamidinium bromide (FABr) dissolved in ethanol was then spin-coated on this layer and subsequently annealed in air to form the final ≈320-nm-thick perovskite layer. Overall, the final perovskite composition and layer morphology were defined by the choice of the evaporated cesium halide compound, its evaporation rate with respect to the
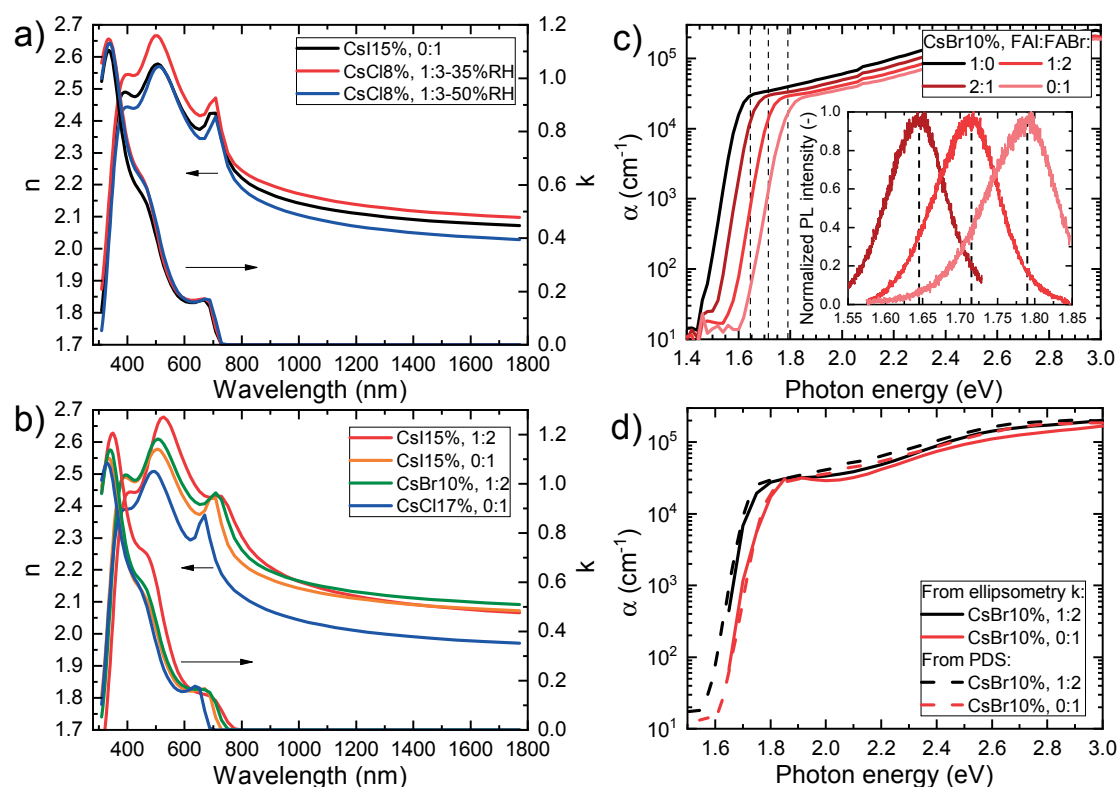
Figure 2.6 – Variable-angle spectroscopic ellipsometry measurements: a) Comparison of complex refractive indices of two CsFAPbIBr perovskite compositions yielding a similar absorption edge at ≈1.69 eV and effect of humidity level during perovskite annealing with ambient relative humidities of 35%RH or 50%RH; b) Comparison of complex refractive indices of perovskite materials made with CsI, CsCl or CsBr; c) Absorption coefficient (α) spectra of CsBr-based perovskite materials with absorption edges ranging from 1.54 eV to 1.74 eV, measured by photothermal deflection spectroscopy (PDS); d) Comparison of the absorption coefficient spectra measured by PDS or from ellipsometry measurements of k ($\alpha=4\pi k/\lambda$). The legends indicate the ratio between the Cs halide evaporation rate and the one of PbI_2 (percentage) and the mixing ratio of the FAI and FABr in the spin-coated solutions. Reproduced with permission [97]. Copyright 2018, American Chemical Society.
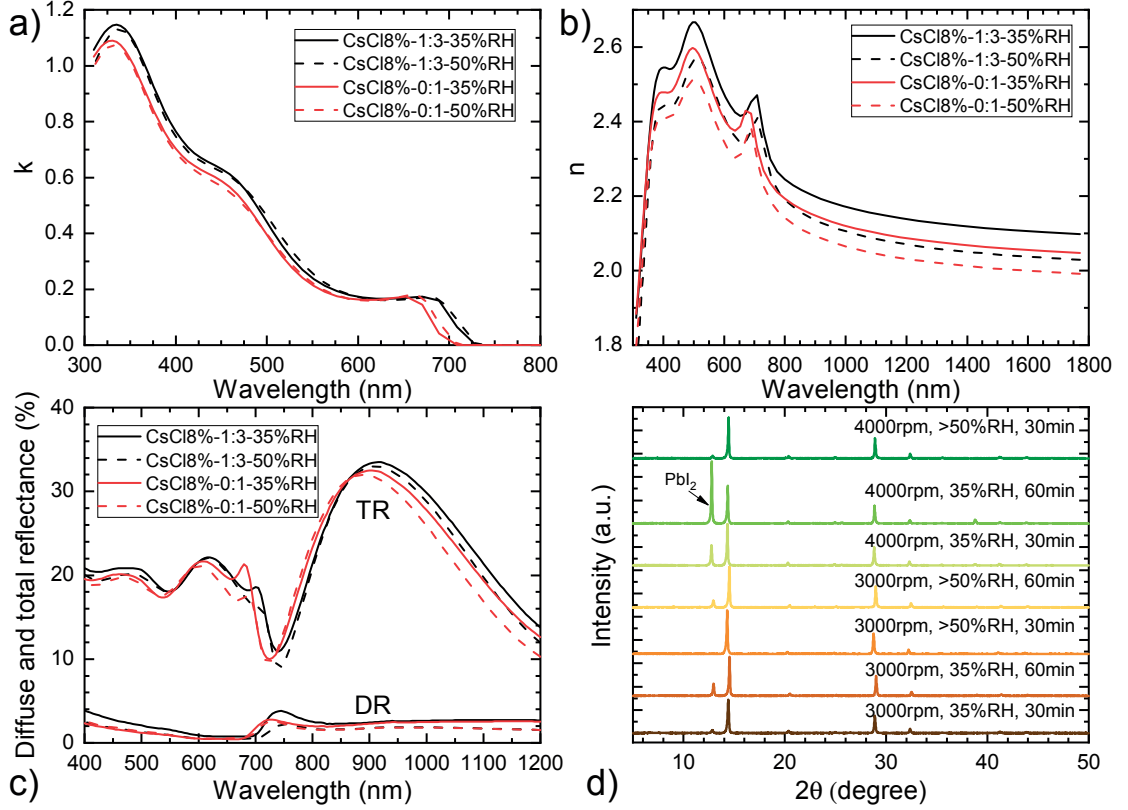
Figure 2.7 – Environmental effects on the fabrication of CsFAPbIBr perovskite materials and their optical and structural properties: a) & b) ellipsometry and c) reflectance measurements of perovskite materials annealed in either ≈35%RH or ≈50%RH; d) XRD patterns of CsCl8%-1:3 with various spin coating speed, relative humidity during layer annealing and annealing time. Reproduced with permission [97]. Copyright 2018, American Chemical Society.

one of PbI_2, and the composition of the FA-halide solution.

These perovskite films were characterized by variable-angle spectroscopic ellipsometry (VASE) and photospectrometry. The resulting complex refractive indices (n + ik) are shown in Figure 2.6. The characterization and modeling protocols are based on our previous work on methylammonium lead triiodide [103]. Figure 2.6a shows the complex refractive indices of two perovskite materials, which exhibit similar absorption edges but were deposited using either CsI or CsCl in the co-evaporation step. The differences in n and k values are a clear indication that ellipsometry measurement results, and more generally the optical properties of perovskite materials, are highly dependent on the exact composition and hence fabrication procedure. For example, environmental aspects such as the presence of humidity during the annealing step can drastically affect the optical properties, as shown in Figure 2.7 for CsCl-based perovskite films. The real part of the refractive index is found to significantly decrease with increasing ambient humidity levels. Note that the interdiffusion process is known to be accelerated in the presence of humidity during the annealing of the film [137]. Indeed, it enhances the diffusivity of organo-halides in the PbI_2-contaning layer, which in turn reduces the amount of unconverted PbI_2 residues in the final layer. This effect is also
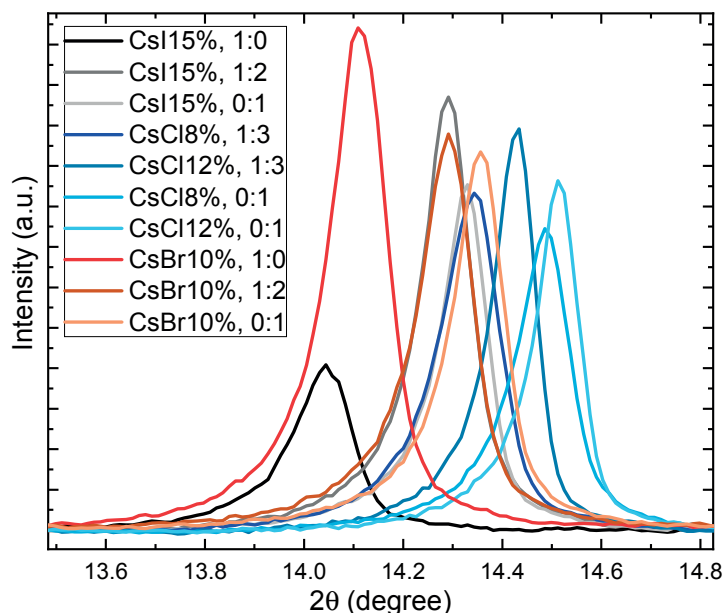
Figure 2.8 – XRD patterns of CsFAPbIBr perovskite layers with various compositions, illustrating the (100) peak shift to higher angles with increasing absorption onset energy. The legend indicates the ratio between the Cs halide evaporation rate and the one of PbI_2 (percentage) and the mixing ratio of the FAI and FABr in the spin-coated solutions. Reproduced with permission [97]. Copyright 2018, American Chemical Society.

clearly observed in the present experiment (Figure 2.7d), as illustrated by x-ray diffraction (XRD) spectra of CsCl-based perovskite films prepared with different humidity levels, spin speed during the FA-halide solution coating and annealing time. The amount of unconverted lead iodide increases when the amount of spin-coated FA-halides is not sufficient (spin speed too high or solute concentration too low), when the humidity level is too low or when the samples are annealed for too long.

Figure 2.6b shows n and k data corresponding to four perovskite compositions having dif-
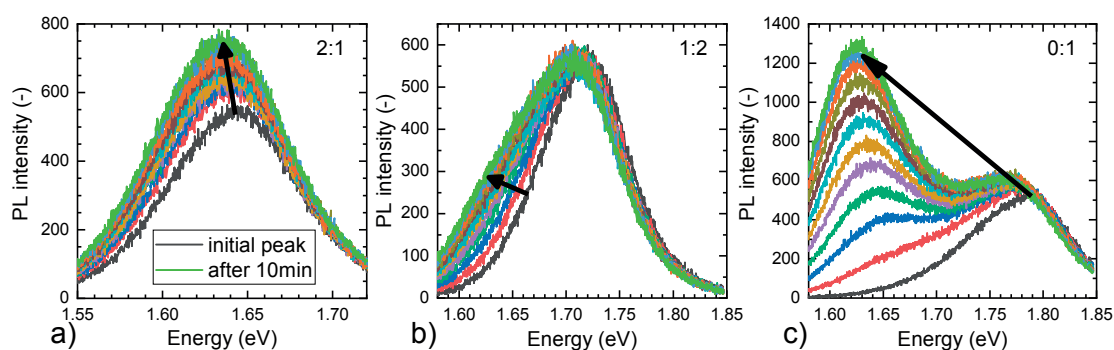
Figure 2.9 – Evolution of photoluminescence (PL) spectra recorded over 10 minutes for three CsFAPbIBr perovskite compositions made with 10% CsBr during co-evaporation with PbI_2 and FAI:FABr ratios of a) 2:1, b) 1:2 and c) 0:1 in the spin coated solution. PL was measured on perovskite layers on glass with a 514 nm laser with 10 mW power, 0.1 attenuation factor and 5 μm spot diameter, corresponding to an equivalent light intensity of ≈50 suns. The spectra were recorded for 10 minutes at 10 s increments at room temperature. Reproduced with permission [97]. Copyright 2018, American Chemical Society.
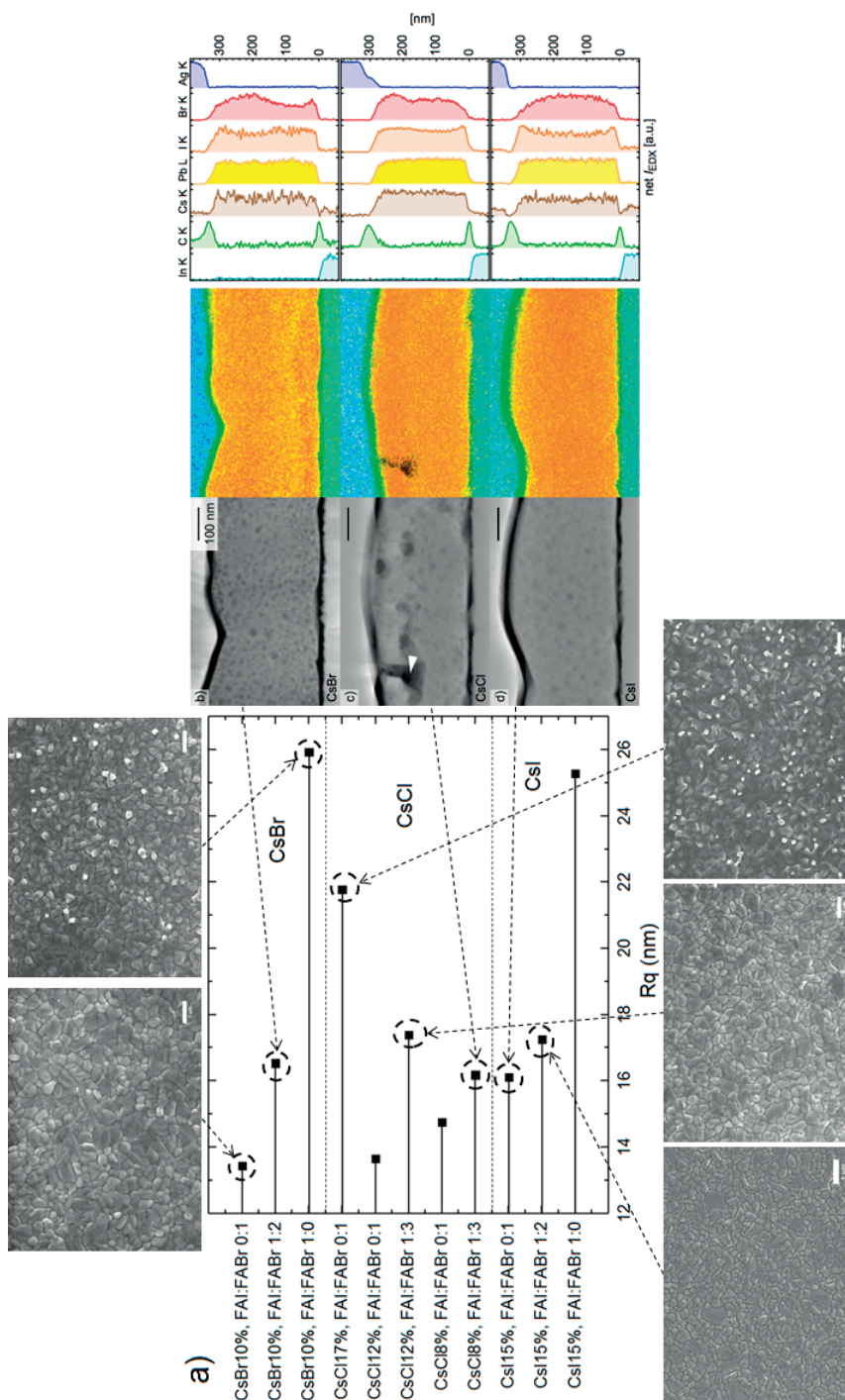
Figure 2.10 – Structural characterization: a) Surface roughness AFM measurements on glass substrates, as a function of the CsFAPbIBr perovskite layer composition, showing a lower surface roughness with higher bromide content; SEM top view images are given for some designated materials (scale bars represent 1μm); b)-d) STEM cross-section images of perovskite solar cells in p-i-n configuration, with their corresponding EDX maps showing the composition variation across the cell section. Reproduced with permission [97]. Copyright 2018, American Chemical Society.

ferent absorption onsets between ≈1.6 eV and ≈1.8 eV. In order to confirm the absorption onsets from ellipsometry data, photothermal deflection spectroscopy (PDS) measurements were carried out on selected samples and the resulting absorption coefficient (α) spectra are shown in Figure 2.6c. As illustrated in Figure 2.6d, ellipsometry and PDS measurements are well in agreement. The absorption onsets increase as expected with increasing Cs and/or with increasing concentration of smaller anions (Cl, Br), as also shown in Figure B.1 using Fourier-transform photocurrent spectroscopy (FTPS). This band gap widening is attributed to a decrease of the lattice constant, which is observed by XRD as a shift of the (100) reflection peak around 14° (Figure 2.8). The initial PL peaks of the CsBr-based perovskites are shown in the inset to Figure 2.6c. They are located at photon energies ≈50 meV higher when compared to the optical band gaps of these materials. As shown in Figure 2.9, recording PL spectra over 10 minutes revealed a drifting of the initial peak toward lower energies. This effect was the most pronounced with wide band gap materials containing larger amounts of Br and was previously attributed to light-induced halide segregation [119]. Abdi-Jalebi *et al.* recently demonstrated that the photoluminescence of wide band gap perovskite materials can be stabilized by passivating the absorber surface and grain boundaries with potassium halide layers [32]. Introducing alkali halides into the perovskite material composition is currently under investigation at PV-Lab by using triple co-evaporation with Cs-halides and Pb-halides. A detailed characterization by AFM, SEM and scanning transmission electron microscope (TEM) of the structural properties of these layers is shown in Figure 2.10. From energy-dispersive X-ray spectroscopy (EDX) chemical maps, the Cs:Pb atomic concentration ratio in the perovskite films could be estimated: 0.16 ± 0.03 with a 15% evaporation rate of CsI to PbI_2 and 0.18 ± 0.03 with a 10% evaporation rate of CsBr to PbI_2.

Figure 2.10 shows a STEM micrograph and corresponding EDX data of p-i-n perovskite cells (see Section 2.3.2). In this case based on a perovskite layer made with the CsI precursor deposited at a deposition rate of 15% relative to that of PbI_2 and using a pure FABr solution the perovskite layer exhibits a compact microstructure, without large voids. While its interfaces are slightly richer in I, Br still diffused down to the 2,2',7,7'-Tetra(N,N -di-p -tolyl)amino-9,9-spirobifluorene (spiro-TTB) interface during the annealing step. As shown in Figure 2.10, a CsBr-based perovskite cell shows a similar microstructure, while a CsCl-based composition features a top surface composed of smaller grains and pores (arrowhead in Figure 2.10). Interestingly, the surface roughness, as determined by AFM and shown in Figure 2.10, also tends to decrease with increasing bromide content. This effect can be explained by looking at the surface morphology of the perovskite film with a SEM. Excess iodide species tend to stay on top of the perovskite grains, visible as white spots on the SEM image of the sample with CsBr10% with pure FAI solution. Increasing too much the Cs content (higher rate ratio) produces a similar morphology, as seen *e.g.* on the sample with CsCl17%.

It is important to note that structural and morphological variations resulting from different compositions, deposition methods and environmental conditions, do affect ellipsometric data (*e.g.* see Figure 2.6a) and are at the origin of the large spread in published data [138, 139, 140, 141, 103]. While absolute values should be assessed with caution, the *n* and *k* data retrieved here enables reliable optical simulations and provides valuable insights to

optimize devices as discussed later in Section 5.3.3.

2.3 Low-temperature planar device development...

2.3.1 ... in *n-i-p* polarity

The n-i-p polarity is historically the standard configuration, as the first cells were based on TiO$_2$ n-type contacts deposited on fluorine doped tin oxide (FTO)-coated glass substrates already widespread for dye-sensitized solar cells. Spiro-OMeTAD was also the most common hole transporting layer (and still is, though at a lower extent). This polarity was therefore logically the first we adopted at the beginning of this thesis.

With the development of our 2-step hybrid deposition method and the use of only 2-propanol for the organohalide solution, it was then possible to replace the TiO$_2$ layers by thinner fullerene layers, *i.e.* PCBM. Fullerenes were shown to enable the fabrication of planar perovskite solar cells with low hysteresis and high efficiency [142, 143]. Spiro-OMeTAD was kept as the hole transporting layer. The ITO/PCBM interface was modified with polyethyleneimine (PEIE) spin coated layer, which helped to increase the yield and performance of the cells. PEIE reduces the work function of ITO and improves the charge extraction with the fullerene layer [111]. We used this device structure in references [83, 76]. Further development involved the replacement of the spin coating processes by thermal evaporation: the 20-nm-thick solution processed PCBM layer was replaced by 6-nm-thick thermally evaporated C$_{60}$ layer and the solution processed PEIE interlayer was replaced by a thermally evaporated 1-nm-thick lithium fluoride (LiF) layer.

The spiro-OMeTAD p-type charge transporting layer was more difficult to replace. This topic will be further discussed later in Section 3.3.2, about parasitic absorption reduction in charge transporting layers.

2.3.2 ... in *p-i-n* polarity *

P-i-n perovskite solar cells were developed in the second half of this thesis, in order to reduce parasitic absorption losses (see Sections 3.3.2 and 5.3) and to make the perovskite cell fabrication process compatible with textured silicon wafers (see Section 5.4). The following paragraphs present the application of the perovskite materials described in Section 2.2.3.

Perovskite solar cells were developed using a 17-nm-thick spiro-TTB [144] hole transporting layer thermally evaporated onto ITO-coated glass substrates. More details on the influence of interlayers and spiro-TTB thickness are shown in Figures 2.11. The perovskite absorber layer was then deposited with the 2-step method discussed above. The electron contact was made of an evaporated bilayer of 20-nm-thick C$_{60}$ and 5-nm-thick 1,3,5-Tri[(3-pyridyl) -phen-3-yl]benzene (TmPyPB) [145], followed by Ag metallization. For tandem applications, the opaque Ag electrode used for these cells would have to be replaced by a transparent electrode, as discussed in Section 3.2.3. The cell fabrication process had therefore only 1 solution pro-
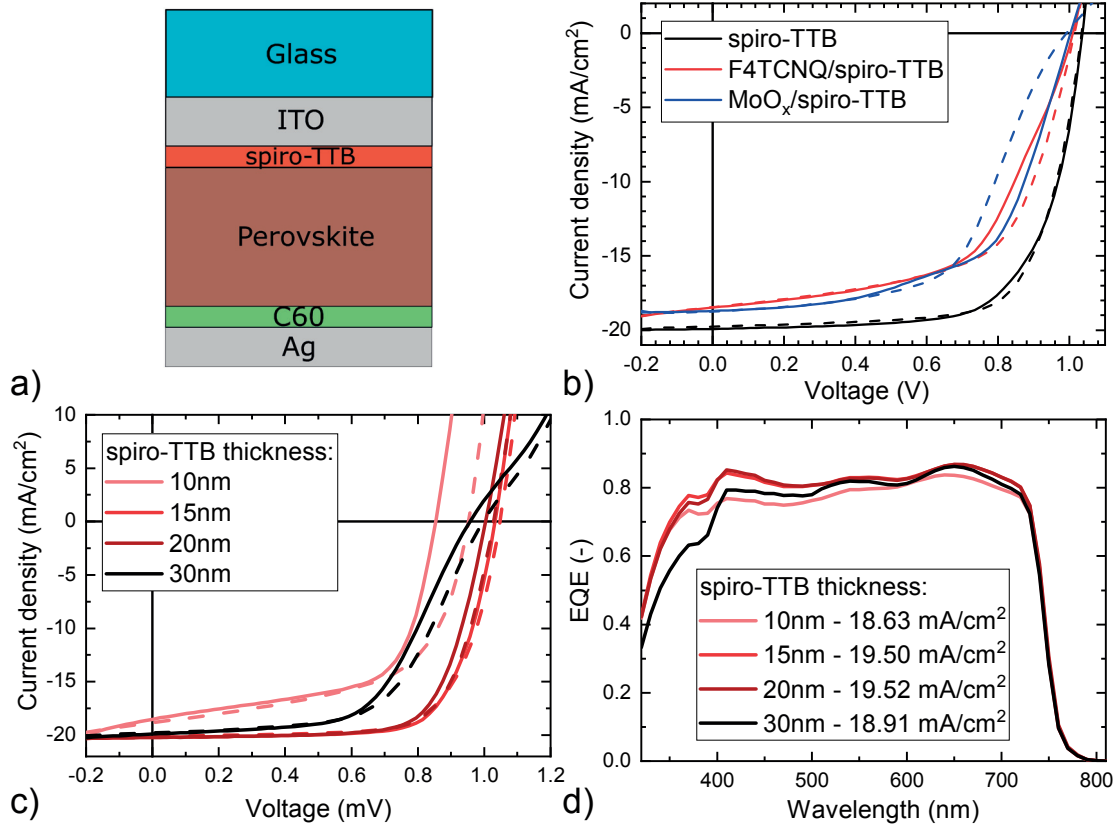
Figure 2.11 – a) Schematic of a p-i-n opaque CsFAPbIBr perovskite cell with spiro-TTB hole transporting layer and C_{60} electron transporting layer. b) current density/voltage (*J-V*) curves of opaque p-i-n perovskite cells on ITO/glass substrates with different hole contact stacks, showing that spiro-TTB alone was the best tested option. c) *J-V* and d) external quantum efficiency (EQE) curves showing the impact of the spiro-TTB layer thickness on the performance of an opaque p-i-n perovskite cell with structure as in a). An optimum can be found around 15-17 nm. The dashed lines in b-c) are reverse scans, whereas solid lines are forward scans.

cessing step left for the perovskite layer, which could in the future be replaced by a chemical vapor deposition (CVD) process, as already demonstrated elsewhere [146, 41, 147], or a full evaporation process [148]. The lead-compound, now evaporated, could also in the future be deposited by sputtering [149].

The EQE measurements shown in Figure 2.12 demonstrate that a high spectral response can be obtained with all the perovskite compositions investigated in Section 2.2.3. The photogenerated currents calculated from these spectra vary from $\approx$22 mA/ cm^2 for the narrowest optical band gap ($\approx$1.51 eV) to $\approx$15 mA/ cm^2 for the widest ($\approx$1.8 eV), following an expected parallel line to the maximum obtainable current for a given band gap and the AM1.5g spectrum, as shown in Figure 2.13b. Figure 2.13c summarizes the optical band gaps for all investigated perovskite compositions. This data, extracted from EQE curves, is confirmed by band gap values measured from FTPS (Figure B.1), PDS measurements (Figure 2.6c), as well as the k values determined from ellipsometry.

Additional current-voltage measurements can be found in the annexed Table B.1, showing, amongst others, the increase in open-circuit voltage with optical band gap. The best cells
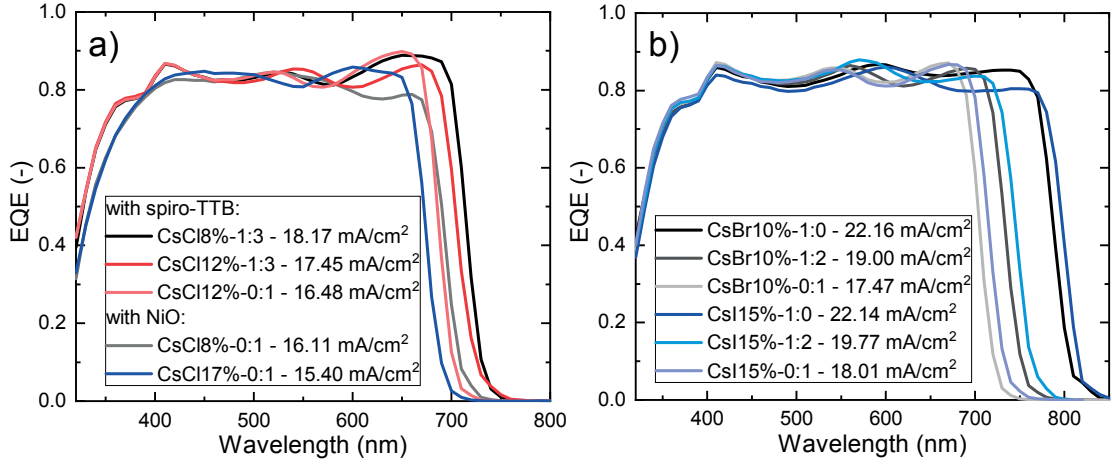
Figure 2.12 – External quantum efficiency spectra of single-junction perovskite cells with various compositions, indicated in the legends by their fabrication conditions, in a) using CsCl and b-c) CsBr and CsI. The legends indicate the ratio between the Cs halide evaporation rate and the one of PbI_2 (percentage) and the mixing ratio of the FAI and FABr in the spin-coated solutions. The structure of the cells was as follow: glass/ITO/spiro-TTB or NiO/CsFAPbIBr perovskite/C_{60}/TmPyPB/Ag. Reproduced with permission [97]. Copyright 2018, American Chemical Society.
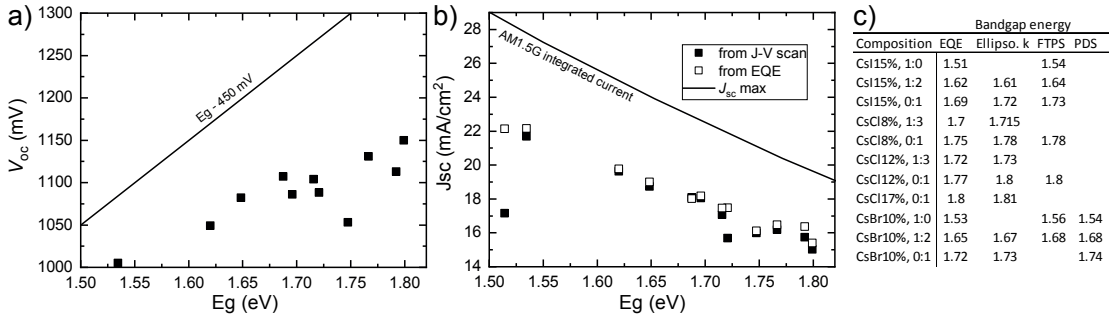
Figure 2.13 – Band gap dependent V_{oc} (a) and short circuit current density (J_{sc}) (b) of opaque p-i-n perovskite solar cells. c) Optical band gap energy values for the investigated CsFAPbIBr perovskite compositions, measured from EQE spectra, ellipsometric measurements of the extinction coefficient, FTPS and PDS measurements. EQE and FTPS are measured on full cells. VASE and PDS are carried out on glass substrates. Reproduced with permission [97]. Copyright 2018, American Chemical Society.

are found to have band gaps between 1.6 and 1.65 eV and demonstrate efficiencies of ≈15%, whereas the cell with the widest band gap of ≈1.8 eV had an efficiency of ≈12% at maximum power point, as shown in Figure 2.14b. This cell still suffered from significant losses in V_{oc}. This observation was also correct for all other devices (see Figure 2.13a). Such differences between the experimentally measured V_{oc} and the expected value corresponding to the optical band gap are known and frequently reported for perovskite solar cells, especially for increasingly wide optical band gaps [34]. This effect is now sometimes referred to as the Hoke effect, describing a photo-induced phase segregation [34, 119], and can also be observed in PL measurements by a shift of the peak over time (see Figure 2.9).

The fill factor (*FF*) of spiro-TTB-based p-i-n cells was limited by low shunt resistance and high interfacial series resistance. By replacing the thermally evaporated spiro-TTB layer by a
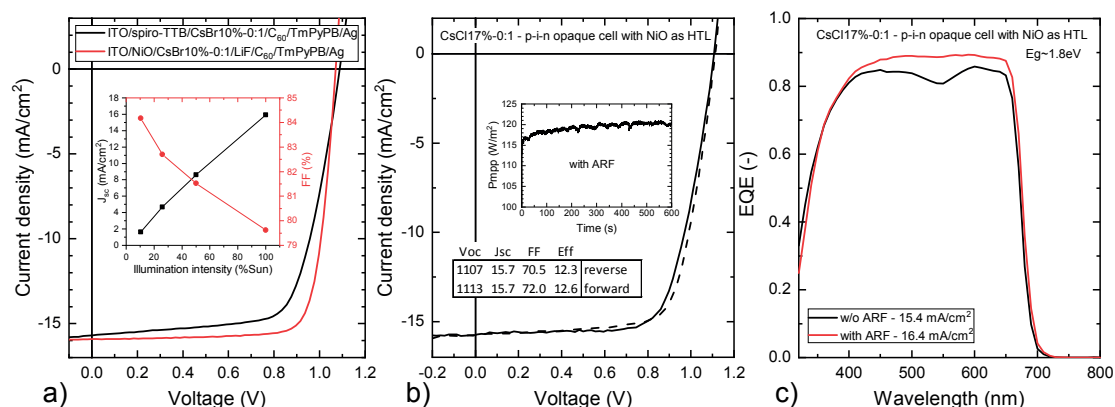
Figure 2.14 – a) Effect of interface modification in p-i-n CsFAPbIBr perovskite solar cells, with spiro-TTB or NiO on the p-side and C_{60}/TmPyPB or LiF/C_{60}/TmPyPB on the n-side. b) *J-V* characteristics of a p-i-n perovskite cell with 1.8 eV band gap, including ARF to reduce reflection losses, and c) its corresponding EQE curves. Reproduced with permission [97]. Copyright 2018, American Chemical Society.

sputtered nickel oxide (NiO$_x$) layer and changing the interface between the perovskite and C_{60} layers with LiF, the *FF* could be significantly increased up to 80% at 1-sun illumination, as shown in Figure 2.14a. This modification translated to an efficiency boost of >1%$_{abs}$ (details in Table B.1). Low illumination current-voltage measurements also show that if interfacial resistances could be further reduced, *FF*>80% could be achievable.

2.4   General conclusions on the chapter

In this chapter, we showed the development of a low temperature process for depositing the perovskite absorber, based on a sequential 2-step hybrid method. We systematically tuned the material composition and showed absorbers with optical band gap energies ranging from 1.5 to 1.8 eV. Their optical, structural and electronic properties were carefully studied, in order to gain more knowledge on their usability for tandem applications and on their weaknesses requiring further investigations.

We gradually modified the standard all-solution processed perovskite cell to a cell with fully evaporated charge transporting layers and only one remaining solution processed step, *i.e.* the organo-halide spin coating, which could in the near-future also be replaced by a CVD process. All these vapor-phase deposition techniques are industrially available and known to be up-scalable, either from Si industry or from OLEDs flat panel displays industry.

The device architecture was simplified from the mesoporous TiO$_2$-based cell including thick heavily doped spiro-OMeTAD, to an all planar device with thin, undoped evaporated charge transporting layers. Indeed the latest p-i-n cells can be composed of a 15-nm-thick hole transporting layer, the perovskite absorber and a 15-nm-thick electron transporting layer.

Also, no toxic solvents are used any more, as only ethanol is necessary in the developed method.

The next steps of this research should then be focused on further improving the optoelectronic properties of the absorber layer and the quality of its interfaces with the charge transporting layers to improve the single junction cell performance toward >20%. The main and crucial challenge is however to improve the material stability and device reliability, which is still largely unknown and could barely be addressed during this thesis.

3 Near-Infrared-transparent perovskite solar cell development

Summary

This chapter presents the development of semitransparent perovskite solar cells with high near-infrared transparency. First, the development of a TCO-based transparent electrode is described, as replacement for the standard metal opaque rear electrode of perovskite cells. IZO is presented as a good candidate thanks to its high carrier mobility and broadband transparency. Sputtering-induced damages are reduced by the introduction of a buffer layer: MoO_x for cells in n-i-p configuration and SnO_2 for cells in p-i-n configuration. The parasitic absorption losses in the MoO_x is described in details, including a solution to minimize these losses with a CO_2 plasma treatment. Parasitic absorption losses in charge transporting layers and TCOs are then discussed, with experimental comparison of various materials. Finally, 1 cm^2 area semitransparent n-i-p perovskite solar cells with >16% efficiency are presented.

3.1 Introduction*

3.1.1 Electrode requirements for tandem applications

In a tandem solar cell, the perovskite cell acts as the top cell, harvesting the visible light while letting red and NIR light pass through to be absorbed in the narrower band gap silicon bottom cell. However, perovskite solar cells typically feature a metal rear electrode, making the device opaque. Therefore, a large part of the initial effort on perovskite/silicon tandem cell development was dedicated to the search for an appropriate transparent electrode as replacement for the opaque metal rear contact. This electrode is a key feature of both 2- and 4-terminal tandems, and should be highly transparent in a wide spectrum range, including the NIR region to maximize the amount of light transmitted to the bottom cell [151].
The requirements for this transparent electrode can be formulated as follow:

- The transparent contact should have a low sheet resistance.

- The deposition of the transparent contact must be soft and should not damage the sensitive organic underlying layers, in order to preserve high device electrical characteristics.

- The materials of this contact must be stable and inert, to avoid any chemical reaction with the materials of the other layers present in the cell during its field operation. Possibly, it could also act as a diffusion barrier, keeping volatile species in the cell and preventing moisture ingress from the environment.

- The electrode must be highly transparent over the whole solar spectrum.

- The materials and deposition technique should be cost-effective and up-scalable.

3.1.2 Literature overview

Several types of electrodes were intestigated over the last 4 years. Silver nanowire mesh electrodes were demonstrated by several groups, usually deposited by spray coating and mechanical transfer [71, 152, 153]. Questions about stability were however rapidly raised, due to the formation of silver halide complexes through reaction with ions from the perovskite layer [85, 154]. Also, the complexity of the fabrication technique and the low reproducibility might severely limit the application of silver nanowires in larger scale tandem devices. Graphene oxide fabricated by chemical vapor deposition was shown to have a high transparency, however, with a high sheet resistance of up to 350 Ω/sq [155, 156]. Transparent electrodes based on thin evaporated metal layers were also demonstrated, *e.g.* Au [157], MoO_x/Au/MoO_x [158], and Cu/Au [75]. They have the advantage of process simplicity, however with the disadvantage of strong parasitic absorption, especially in the top cell sub-band gap spectral range. For example, the Cu/Au bilayer electrode as presented in reference [75] leads to a perovskite top cell sub-band gap absorption between 20 and 30% in the 800-1200 nm wavelength range

where the silicon bottom cell absorbs.

In contrast, TCOs are widely used materials in photovoltaics, combining high transparency, conductivity, process adaptability and reproducibility [151]. Sputtering systems are commonly used in industry and are compatible with large-area and high-throughput processing.

Figure 3.1 illustrates the state-of-the-art at the start of this thesis, as presented by Löper *et al.* [70]. The perovskite top cell in this example was using a non-optimised ITO electrode. The EQE measurement of the filtered bottom cell shows that the top cell was absorbing about 20-30% of the light in its sub-band gap spectral region, thus drastically limiting the possible performance of the bottom cell. The following Sections cover the development of a sputtered TCO-based electrode with broadband transparency, the related challenges in terms of sputtering damage and parasitic absorption losses, and the solutions developed though this thesis.
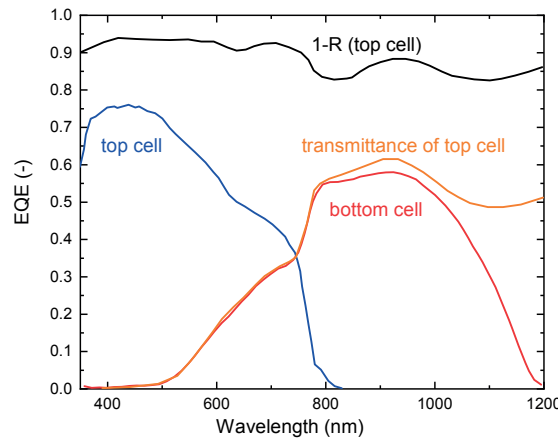
Figure 3.1 – EQE measurements of semitransparent MAPbI$_3$ perovskite cell and a silicon bottom cell in 4TT configuration, illustrating the state-of-the-art at the start of this thesis and the important optical losses in the >800 nm wavelength spectral region. The data is extracted from Löper *et al.* [70].

3.2 Sputtered transparent conductive oxide

3.2.1 Initial developments: minimizing sputter damage *

The first development of a sputtered transparent electrode started at EPFL/PV-lab a couple of months before the beginning of this thesis with one of the most commonly used TCO: ITO [70]. It has however the disadvantage that it generally requires relatively high deposition temperatures or post-deposition annealing to reach its crystalline structure with the lowest resistivity [159, 160]. Such thermal treatments would degrade organic materials such as spiro-OMeTAD. Therefore, the reported efficiency was limited due to the high resistivity of the non-annealed ITO layer [70]. Amorphous TCOs, such as IZO, are therefore advantageous as they can be deposited at low power, low temperature and without post-deposition thermal treatment, while maintaining excellent electrical and optical properties [161]. Deposited on glass substrates, IZO has already been applied as a front electrode in opaque perovskite [162]
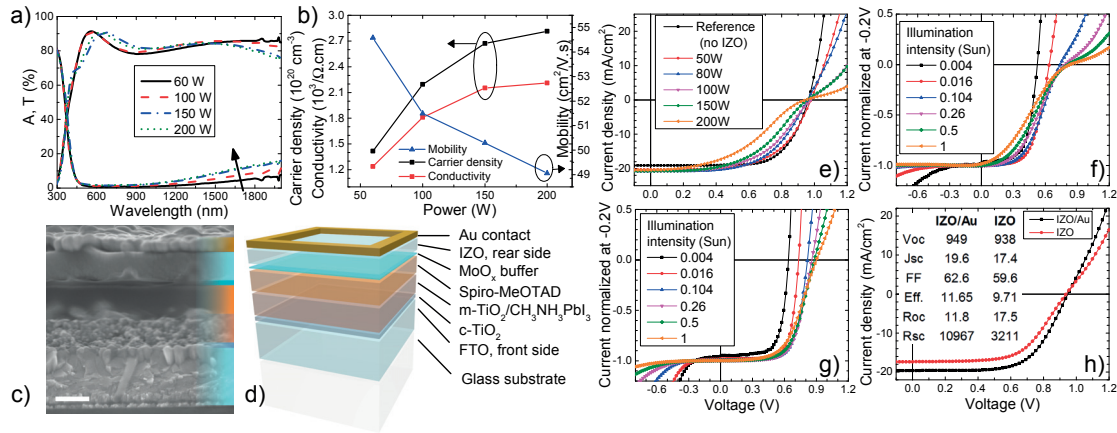
Figure 3.2 – a) Total transmittance (T) and absorptance (A) spectra of IZO layers deposited at several sputter powers while keeping other sputter parameters constant, measured by UV-vis spectrophotometry. b) The influence of sputter power on lateral conductivity, carrier density and electron mobility, determined by Hall effect measurements. c) SEM cross-sectional image (scale bar is 250 nm) and d) schematic illustration of a typical mesoporous MAPbI$_3$ perovskite solar cell structure with a transparent rear electrode and Au contact. *J-V* measurements: e) effect of sputter power variation. f) & g) *J-V* curves at several illumination intensities, from 0.004 to 1 sun, normalized at 0.2 V, for a cell with strong s-shaped *J-V* curve sputtered at 150 W (f) and one with moderate s-shaped *J-V* curve sputtered at 60 W (g). h) Best semitransparent cell with IZO rear electrode, compared to an opaque cell with IZO/Au electrode, the inset table provides the related *J-V* parameters. The IZO layers of these cells were deposited at 60 W sputter power. Reproduced with permission [72]. Copyright 2015, Elsevier.

and dye-sensitized solar cells [163, 164].

We therefore developed sputtered IZO layers with the aim to reach both high conductivity and high NIR transparency while minimizing sputter damage to the underlying layers. An RF magnetron sputtering system[1] was therefore chosen for its reduced physical impact compared to direct-current sputtering [165]. The substrate temperature during deposition was fixed at 60°C, as this was found to be a good compromise between enhancing the electrical properties of the IZO layer and avoiding thermal damage to the organic layers in the perovskite cells. For the process gas, we used pure argon, without the addition of oxygen, as this results in IZO layers with both better electrical properties and less sputter damage due to fewer negative ions in the plasma [166]. The as-deposited IZO layer was amorphous [161]. The sputter power was varied to study its effects on the electrical and optical properties of IZO layers on glass, as shown in Figure 3.2a and b. The absorptance of the IZO layer increases in the infrared with increasing sputter power. This can be explained by free-carrier absorption due to the increase in charge carrier density as seen in Figure 3.2b. Simultaneously, the Hall effect carrier mobility decreases with increasing power. Overall, the conductivity is then reduced at low power. The average absorptance of the IZO layer deposited at 60 W (0.76 W/ cm^2) was less than 3% in the 400–1200 nm wavelength range, which is below the limit of 5%, previously reported as a requirement for the top-cell electrode in a high-efficiency tandem device [51]. In comparison, transparent electrodes based on metals or metal nanowires typically show a considerably

---

[1]Note that for this early development, IZO layers were deposited in the Leybold Univex sputtering system. Later on, a new system (baptized "TheBigLebowski") was build in-house combining sputtering with an IZO target and thermal evaporation for organic charge transporting layers and metal oxides.

higher absorption [152].

These IZO layers were then applied as transparent rear electrodes in perovskite solar cells with a device architecture and layer morphology as shown in the scanning electron microscopy cross-sectional image in Figure 3.2c and the schematic illustration in Figure 3.2d. The perovskite cells were processed as mentioned in Section A.1.1 and the active area of the semitransparent cells was defined by a thermally evaporated Au frame.

To assess the sputter damage when depositing IZO directly onto the spiro-OMeTAD layer, we varied the sputter power from 50 W to 200 W. For this test, the rear electrode consisted of a 120-nm-thick IZO layer capped by a full-area evaporated Au contact to decouple the effect of sputter damage from the sheet resistance of the IZO layer. The resulting J-V curves are shown in Figure 3.2e. They show an inflection close to the V_{oc}, usually referred to as an s-shape. In organic solar cells, s-shaped J-V curves have been attributed to poor electrical properties or the presence of energetic barriers at one or more interfaces [165, 167, 168]. Increasing the sputter power resulted in an increasingly pronounced s-shape around the V_{oc}. However, the lowest power still showed an increased series resistance compared to the reference cell without IZO. To reveal the origin of this s-shape, we used the methodology described in [167]: a cell featuring an s-shaped J-V curve was illuminated at several intensities from 0.004 to 1 suns and the resulting J-V curves were then normalized at 0.2 V, where the current was saturated for all curves (see also Figure 3.2f). The increase in V_{oc} with light intensity, combined with the crossing of the curves in the fourth quadrant of the J-V graph, suggests that the s-shape can be attributed to the presence of an extraction barrier for holes in the device. As a comparison, the same method was used for a cell showing a less pronounced s-shape (see Figure 3.2g), whose J-V curves exhibited strongly reduced curve crossing. From these results and the variation of the s-shape with the sputter power, we attribute the extraction barrier to damage made to the spiro-OMeTAD layer during IZO deposition. Using the deposition parameters that resulted in the smallest extraction barrier (60 W sputter power), we made semitransparent cells with an IZO rear electrode (*i.e.* without a full-area Au layer) sputtered directly on the sensitive organic hole transporting layer and obtained a power conversion efficiency of up to 9.7%, with a J-V curve as shown in Figure 3.2h. This curve still shows a small s-shape indicating that sputter damage could not be entirely prevented by varying the deposition parameters. Note the increase in J_{sc} seen in Figure 3.2e, which is observed independent of the sputter power for cells with the IZO/Au rear electrode. This indicates that the IZO layer introduced between the organic layer and the Au contact acts as an optical spacer, modifying the interference pattern within the layer stack.

3.2.2 Transition metal oxides as buffer layers in *n-i-p* cells *

To eliminate the hole extraction barrier caused by sputter damage, we inserted a thin buffer layer between the spiro-OMeTAD hole transporting layer and the IZO rear electrode. This buffer should allow efficient hole extraction and be resilient to the energetic plasma particle bombardment during sputtering. Transition metal oxides have already proven to fulfil these requirements and have been applied in organic electronic devices [169], silicon solar cells

Table 3.1 – Cell parameters obtained from current density-voltage and external quantum efficiency measurements. The IZO layers were 120-nm-thick and deposited at 60 W. All measurements were done with illumination through the glass substrate.

Rear contact type	V_{oc} mV	J_{sc} mA/cm^2	FF %	Eff. %	R_{oc} Ohm.cm^2	R_{sc} Ohm.cm^2
spiro/Au	866	18.97	76.1	12.5	4.44	2108
spiro/MoO$_x$ 35 nm/Au	865	18.75	73.5	11.94	5.01	1957
spiro/MoO$_x$ 10 nm/IZO/Au	859	19.02	71.9	11.76	5.11	1360
spiro/MoO$_x$ 35 nm/IZO/Au	869	18.31	75.3	11.98	4.98	1918
spiro/MoO$_x$ 10 nm/IZO	870	17.51	68.0	10.36	7.06	7302
spiro/MoO$_x$ 35 nm/IZO	829	16.38	75.6	10.25	5.25	1861

[170, 99] and perovskite solar cells [171, 70].

We chose thermally evaporated MoO$_x$ as a buffer material and tested layers with a thickness of either 10 nm or 35 nm. Two IZO sputter powers, 60 W and 150 W, were chosen to compare
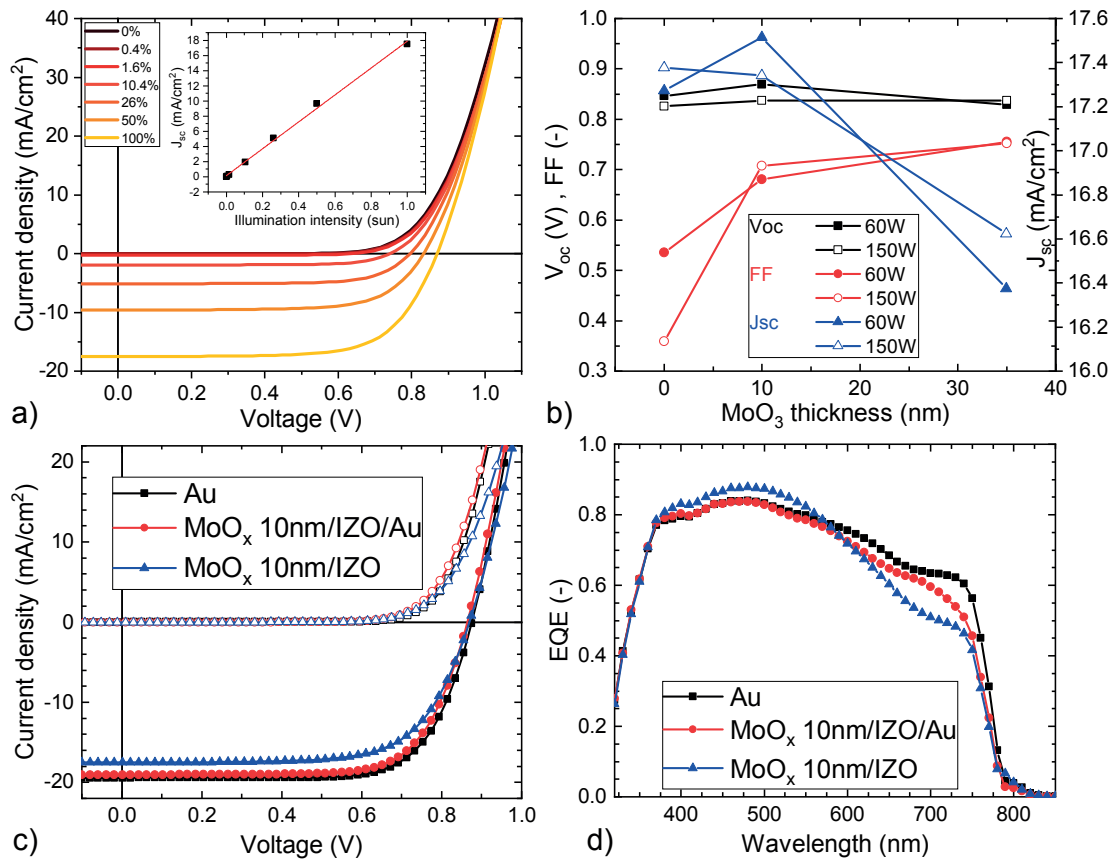
Figure 3.3 – a) Illumination dependent *J-V* measurements of a semitransparent MAPbI$_3$ perovskite cell with a 10-nm-thick MoO$_x$/IZO rear electrode. b) Effect of MoO$_x$ buffer layer thickness and sputtering power on *J-V* parameters of semitransparent cells with MoO$_x$/IZO rear electrode. c) *J-V* and d) EQE curves of the semitransparent cell with a 10-nm-thick MoO$_x$/IZO rear electrode compared to opaque cells with Au electrode. The cells were measured at 1 sun illumination (solid symbols) and in the dark (open symbols). All measurements were done with illumination through the glass substrate. Adapted with permission [72]. Copyright 2015, Elsevier.

the sputter damage and the capability of the buffer to protect the underlying layers. The J-V curves and EQE spectra of these cells are shown in Figure 3.3, and their device characteristics are summarized in Table 3.1. The IZO layers had a thickness of 120 nm and a sheet resistances of 49 Ω/sq and 35 Ω/sq for 60 W and 150 W of sputter power, respectively. Figure 3.3b shows the effect of the MoO_x buffer thickness on the J-V parameters of the semitransparent cells. The V_{oc} is not affected by the presence of the buffer layer or of the IZO layer. Introducing a thin layer of MoO_x has a strong effect on the FF, especially for the 150 W samples, where it improves from 36% to 70%. The FF continues to increase for the thicker buffer layer, but to a much smaller extent. This indicates that there is still a degree of sputter damage in the spiro-OMeTAD layer when capped with a 10-nm-thick MoO_x layer. This damage is completely eliminated only by the thicker buffer, as shown by FFs very similar to that of the reference cell with the Au rear electrode. The similar FF of the opaque and semitransparent cells also shows that the lateral conductivity of the IZO electrode was sufficiently high to not add strong losses due to additional series resistance to the cell. Therefore the only significant FF losses can be attributed to sputter damage for the cells with the thin buffer layer. However, as indicated by the missing s-shape, and confirmed by illumination-dependent J-V measurements (Figure 3.3a), the presence of the thin MoO_x layer already suffices to fully remove the extraction barrier that was observed in the cells lacking a MoO_x buffer. It is also interesting to note that the presence of a buffer layer strongly reduces the influence of the sputter power. A drawback of the thicker buffer layer is the reduced J_{sc}, as shown in Figure 3.3b. This is confirmed by the J_{sc} values obtained from EQE curves. Moreover, the significant discrepancy between J_{sc} values obtained from the J-V curves and the EQE spectra for the samples with the thicker MoO_x buffer layer indicates charge collection issues. This is also observed in the case of the opaque cell with a 35-nm-thick MoO_x/Au electrode. The J_{sc} values obtained from both techniques are however rather consistent for the Au reference cell and the semitransparent and opaque cells with a 10-nm-thick MoO_x buffer layer. The best semitransparent perovskite cell in this configuration and with 60 W sputter power exhibited a power conversion efficiency of 10.3% and a J-V curve without hysteresis. By comparing this semitransparent cell with opaque cells with either a Au or MoO_x/IZO/Au rear electrode, we can see that the main efficiency loss is due to reduced J_{sc} in the semitransparent cell. This can clearly be attributed to the lack of (internal) reflectivity of the IZO compared to the Au electrode, as shown by the optical losses at wavelengths above 600 nm (Figure 3.3d). Such optical losses could at least partially be compensated for by properly designed low-refractive index coatings on front and rear electrodes, *e.g.* lithium fluoride as demonstrated in reference [71]. However if the semitransparent cell is applied as top cell in a tandem configuration, the photons that are not absorbed in a single pass through the perovskite solar cell can still be harvested by the bottom cell, such that these optical losses become less critical.

3.2.3 Semitransparent *p-i-n* perovskite cells

Following the development of opaque p-i-n perovskite cells described in Section 2.3.2, similarly to the n-i-p cells, the rear metallization needs to be replaced by a transparent electrode.
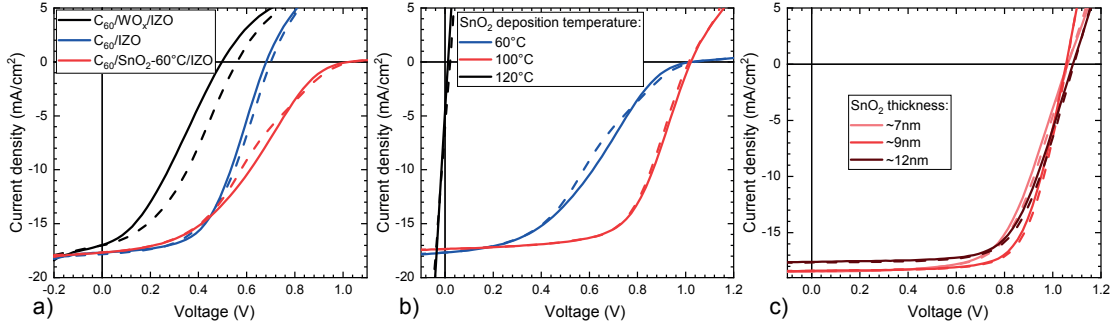
Figure 3.4 – *J-V* curves of semitransparent p-i-n CsFAPbIBr perovskite cells: a) comparison of buffer materials; b) effect of temperature during the deposition of SnO_2 by ALD; c) effect of SnO_2 thickness.

However, in this case, it has to be deposited on a C_{60} electron transporting layer, instead of spiro-OMeTAD hole transporting layer.

Zinc oxide nanoparticles were already used by other groups as a buffer layer protecting the C_{60} layer during sputtering [152, 172, 90, 80]. However, solution processes should be avoided for future integration on textured silicon wafers, as they are typically less conformal than vapor-based techniques. Additionally, stability concerns about chemical reaction between the perovskite elements and ZnO nanoparticles were raised by Cheng *et al.* [173]. We then tried to apply the low-power IZO sputtering recipe described in the previous sections, but unsuccessfully, as shown in Figure 3.4a with strong V_{oc} losses. As shown in the same Figure, using an evaporated tungsten oxide (WO_x) layer was not working either.

SnO_2 layers deposited by ALD looked in contrary more promising and were then also demonstrated by Bush *et al.* to be an effective buffer layer material for p-i-n semitransparent perovskite cells [85]. Other groups have also shown that such layer can in addition act as a moisture ingress barrier [174, 175].

A thermal ALD process was therefore developed jointly with the Swiss Center for Electronics and Microtechnology (CSEM). Figure 3.4b shows that the deposition temperature has a drastic effect on the device performance, with an optimal temperature around 100°C. Lower temperatures lead to the formation of *J-V* curves strongly s-shaped around V_{oc}. Higher temperatures, in conjunction with the water vapour necessary for the ALD process, tend to degrade the perovskite layer. Figure 3.4c shows the effect of thickness for SnO_2 layers deposited at 100°C. We can also observe an optimum around 9-10 nm, thick enough to avoid sputter damage without increasing series resistance and optical losses.

3.3 Parasitic absorption losses

3.3.1 In transition metal oxide buffer layers *

Transition metal oxides (TMOs) are susceptible materials which are sensitive to their environment, such as air or oxygen exposure [176], temperature [177, 178, 179, 180], UV-light [181], UV-ozone [182], or plasma treatments [183, 184, 185, 186, 187]. This is because many

TMOs readily undergo redox reactions. Evaporated metal oxides are especially sensitive, as they are often substoichiometric when as-deposited, due to an oxygen deficiency [188, 169]. The presence of oxygen vacancies creates positively charged structural defect states in the band gap, which enables the attractive hole injection properties of TMOs despite their n-type semiconductor character [188]. Some of the defect states also act as localized color centers, resulting in absorption in the visible/near-infrared spectrum, spread at different wavelengths around 800 nm depending on their oxidation states. This sensitivity and the associated coloration are desirable for some applications such as gas and chemical sensing. TMOs were for these reasons widely studied specifically for their photochromic [189, 190, 191] and electrochromic [192] properties. However, for optoelectronic applications, where high transparency is required in charge transporting layers, any color change could be detrimental and result in performance reduction.

In particular, it was recently pointed out that the optical properties of TMO layers are strongly affected during sputter deposition of a TCO overlayer, resulting in a more pronounced absorptance of the TMO/TCO stack than the expected sum of their individual absorptance values [72, 99]. If such a stack is used as a front window electrode in a solar cell, this increased absorptance directly translates into a decreased photocurrent and, as a result, reduced device performance.

It would therefore be highly interesting to find either a pretreatment method to prevent the appearance of this absorptance increase or a post-treatment to recover sputter damage (discoloration). Inspiration for this can be taken from an early study on photochromism of amorphous transition metal oxides by Colton *et al.* [189] They showed that TMO films can be bleached (decolored) by thermal annealing at 300°C in an oxidizing atmosphere, preventing simultaneously any further (post)coloration. However, high temperature annealing is not desirable for many applications due to the temperature sensitivity of underlying films, such as for perovskite solar cells [133], silicon heterojunction solar cells [18], or other organic opto-electronic devices [169]. To date though, an alternative bleaching method at low temperature has yet to be reported.

Here, we study the coloration of TMOs, induced by temperature, Ar plasma exposure, and TCO overlayer sputter deposition, and demonstrate a low-temperature bleaching treatment based on CO_2 plasma exposure. We show how this treatment can prevent and recover TMO layer coloration when applied respectively before or after Ar plasma exposure. To illustrate this method, we investigate and compare two commonly used substoichiometric metal oxides: molybdenum oxide (MoO_x, $x < 3$) and tungsten oxide (WO_x, $x < 3$). Their chemical and optical properties are characterized by UV-vis spectrophotometry and x-ray photoelectron spectroscopy (XPS), showing a larger resilience for WO_x to sputter damage. Finally, we apply the knowledge gained from these findings in semitransparent perovskite solar cells, showing how parasitic absorption can be strongly reduced in the transparent electrode.

Figure 3.5 shows the absorptance and optical band gap energies calculated from Tauc plots for three thermally evaporated TMOs: MoO_x, WO_x, and V_2O_5. These TMO layers had a device-relevant thickness ($\approx$8-12 nm), while keeping in mind that their coloration is a bulk effect and thus scales with thickness [190]. For application as a front window layer in solar cells, V_2O_5 is

not suitable because of its narrower optical band gap, causing a blue cutoff, and was therefore not further considered in this study. We chose to use MoO_x for most experiments presented here, as it is the most studied and widely used TMO and was already demonstrated to work well in several types of photovoltaic devices, including perovskite and silicon heterojunction solar cells [72, 193, 99].

Figure 3.6a shows the main subject investigated in this section: the synergistic absorptance effect observed in sequentially deposited TMO/TCO layer stacks, illustrated by the example of MoO_x. To demonstrate that this effect is not limited to MoO_x, we tested other TMOs, namely WO_x and V_2O_5, and observed a similar synergistic absorptance increase (see Figure S1 of reference [96]). By testing several types of TCO overlayers such as ITO, IZO, hydrogenated indium oxide (IO:H), and zinc oxide (ZnO), we found that their chemical composition does not seem to affect the observed absorptance effect (see Figure S2 of reference [96]). Moreover, when depositing the TMO onto the TCO layer, this effect was not observed (see Figure S1 of reference [96]). These findings confirm that the synergistic absorptance increase is exclusively due to a modification of the TMO layer during the TCO sputtering process. Comparing the observed color changes to optical spectra reported in the literature indicates that the TMO layer is reduced during TCO sputtering, resulting in the formation of additional oxygen vacancies, as evidenced by a broad sub-band gap absorption peak centered at a wavelength of ≈800 nm [169]. During TCO deposition by sputtering, the samples are in contact with a plasma, which will slightly heat the sample (<100°C) and lead to exposure with UV light as well as ion bombardment. In order to gain a better understanding of the TMO modifications, we assessed each of these factors individually.

The effect of thermal annealing on the absorption of a MoO_x film is shown in Figures 3.6b and 3.6c. When annealed in air, the MoO_x layer absorptance increases up to ≈200°C and then starts to bleach again at higher temperatures (Figure 3.6b). This trend can be explained by the competition between a reduction (Mo^{6+} to Mo^{5+}) reaction, dominant at low temperatures, and an oxidation (Mo^{5+} to Mo^{6+}) process at high temperatures in the oxygen-rich atmosphere,
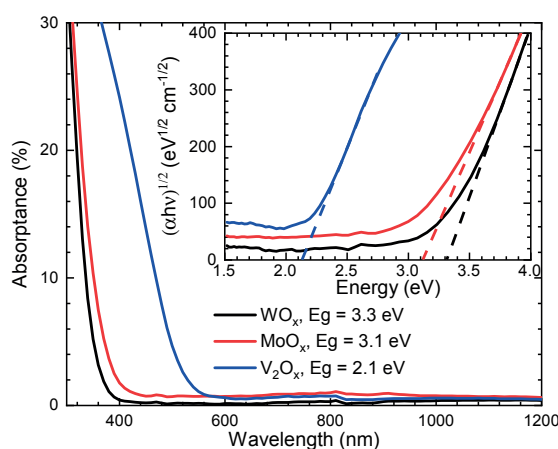
Figure 3.5 – Absorptance spectra and Tauc plots of ≈10 nm thick evaporated MoO_x, WO_x, and vanadium pentoxide (V_2O_5) layers on glass. Reproduced with permission [96]. Copyright 2016, American Chemical Society.
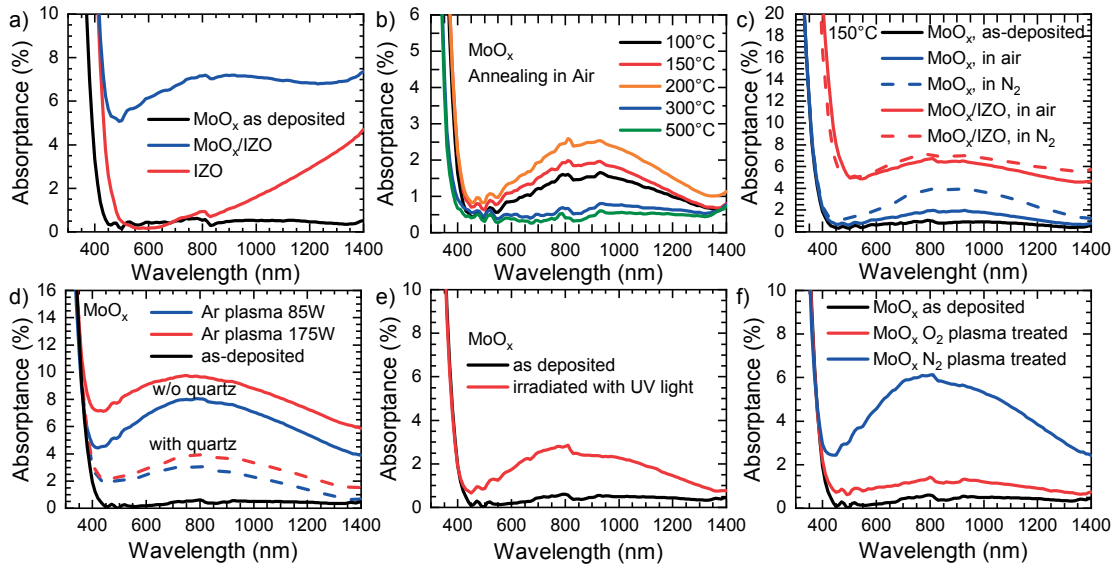
Figure 3.6 – Absorptance spectra of MoO$_x$ films: a) as a bare film, in a stack with an IZO overlayer, and compared to the absorptance of a bare IZO layer; b) annealed in air at temperatures ranging from 100 to 500°C; c) annealed in air and N$_2$ with and without IZO overlayer; d) Ar plasma treated for 5 min; e) irradiated with UV light for 10 min; f) O$_2$ and N$_2$ plasma treated. Reproduced with permission [96]. Copyright 2016, American Chemical Society.

confirming the observations reported by Colton *et al.* [189] As expected, in an inert atmosphere, such as nitrogen, the same annealing treatment results in a similar coloration at low temperatures (<200°C) (Figure 3.6c). Leftheriotis *et al.* showed similar coloration of metal oxide films when annealed in a vacuum [180]. They also demonstrated that bleaching the films by annealing in an oxygen-rich atmosphere at high temperature led to a polycrystalline film, losing its as-deposited amorphous nature. High-temperature reoxidation can therefore be excluded as a bleaching solution for temperature sensitive optoelectronic applications.

Figures 3.6d and 3.6e show the effect of full Ar plasma or only of UV-light irradiation on the optical absorptance of a MoO$_x$ layer. We observe that the coloration scales with the power of the plasma and therefore with bombardment energy [183]. The influence of Ar ion bombardment was already widely reported and known to reduce oxides to lower stoichiometry due to the preferential sputtering of oxygen [187]. Also, when removing the effect of ion bombardment by protecting the sample with a quartz plate, thus exposing the sample only to plasma luminescence, the layer is still affected. This effect is not specific for transition metal oxide; similar behavior was also observed for thin amorphous silicon passivation layers used in silicon heterojunction technology [194]. UV light can also result in coloration, as shown in Figure 3.6e and reported elsewhere [181].

After identifying that elevated temperature, UV light, and Ar ion bombardment all contribute to the coloration of TMO layers during TCO overlayer deposition, we assessed several approaches to prevent coloration or bleach colored TMO layers at low temperatures.

First, we explored oxygen plasma [184, 195, 196] and UV-ozone [197, 182] treatments, which are known to modify the work function and change the stoichiometry of metal oxide films. We therefore exposed TMO layers to UV-ozone and could completely bleach the colored films
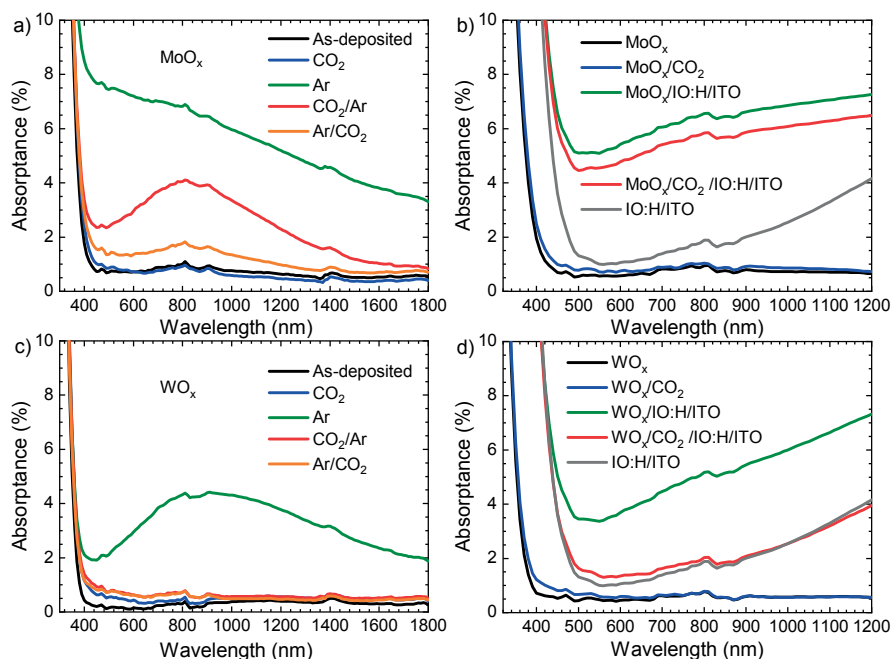
Figure 3.7 – Absorptance spectra of MoO_x and WO_x thin films after plasma treatments (a, c) and with a sputtered IO:H/ITO TCO bilayer deposited on top of the TMOs (b, d). The Ar and CO_2 plasma treatments were carried out for 10 and 20 min, respectively. Reproduced with permission [96]. Copyright 2016, American Chemical Society.

(see Figure S3 of reference [96]). However, when re-exposed to an Ar plasma, the coloration recovered to a large extent the initial intensity. Oxygen (O_2) plasma exposure was found to be inefficient as an oxidizing method (Figure 3.6f) due to the presence of ion bombardment having a reduction effect similar, but to a lower extent, to the one of an Ar plasma treatment [196]. This finding also suggests that introducing oxygen in the TCO sputtering gas mixture would not help to lower the reducing effect of the plasma.

To the best of our knowledge, the use of a CO_2 plasma has not yet been proposed to engineer the optical properties of TMOs. Figures 3.7a and 3.7c show the absorptance spectra for MoO_x and WO_x, when treated with CO_2 and Ar plasmas. The Ar plasma was used here to "mimic" the effect of a TCO deposition by sputtering on a TMO layer, without actual film deposition. For comparison, Figures 3.7b and 3.7d show the closer to-device cases with the full TMO/TCO stacks, with or without the CO_2 plasma treatment before TCO sputtering. From Figure 3.7, three main effects can be observed: (1) CO_2 plasma pretreating of as-deposited MoO_x or WO_x films considerably reduces the damage caused by a subsequent Ar plasma and thus can prevent, at least partially, the coloration observed in TMO/TCO stacks; (2) a CO_2 plasma can be used to effectively bleach a colored film, which has been treated with an Ar plasma, and thus recover the as-deposited optical properties; (3) compared to MoO_x, WO_x is inherently less affected by Ar plasma exposure and ion bombardment and can be completely bleached by CO_2 plasma exposure.

In order to better understand the chemical modifications induced to the MoO_x and WO_x films by the plasma treatments discussed above, XPS measurements were carried out on cotreated
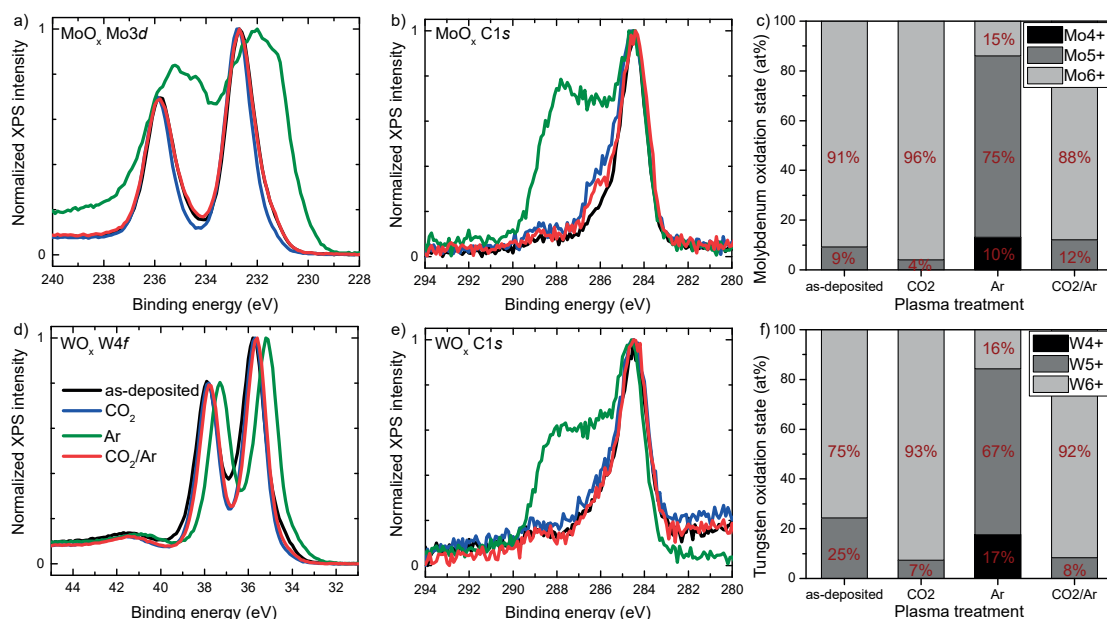
Figure 3.8 – XPS spectra of MoO_x and WO_x before and after several plasma treatments: for MoO_x, (a) Mo 3d, (b) C 1s, and (c) Mo oxidation states; and for WO_x (d) W 4f, (e) C 1s, and (f) W oxidation states. Panels c and f show the oxidation state distribution of Mo and W present in the TMO layers and are derived from the fitting of the curves in panels (a) and (d). The transition metal oxide layers for these XPS measurements were coevaporated with the layers used for spectrophotometry shown in Figure 3.7. Reproduced with permission [96]. Copyright 2016, American Chemical Society.

samples. The full set of XPS spectra are given in the Supplementary Information of reference [96]. We only focus on the Mo and W core levels and carbon peaks to draw conclusions on changes in the chemical states of these elements due to the plasma treatments.

Figure 3.8 shows the core levels of MoO_x and WO_x, their respective carbon peaks, and the fraction of their oxidation states measured by fitting the core level curves after the plasma treatments. Both Mo and W are known to have several stable oxidation states [169], and it is widely accepted that they can be identified from their binding energies. In addition, the impact of Ar plasma exposure on stoichiometric molybdenum oxide (MoO_3) and stoichiometric tungsten oxide (WO_3) (with Mo^{6+} and W^{6+} oxidation states) has been studied in the past, and it has been confirmed by XPS measurements that it leads to the appearance of lower oxidation states of the metal atoms [187].

Figure 3.8a shows the two characteristic core level peaks of Mo, at 232.7 eV for Mo 3d5/2 and at 235.8 eV for Mo 3d3/2, in the as-deposited MoO_x film, in good agreement with the literature [181]. This as-deposited MoO_x is largely composed of Mo in the 6+ oxidation state, and the fraction of Mo^{6+} even increases after CO_2 plasma treatment, proving the oxidizing effect of this treatment. The Ar plasma treatment carried out on as-deposited MoO_x dramatically reduces its oxygen content and causes the films to be largely composed of 5+ and 4+ oxidation states, which are at the origin of the large absorptance of this film, as shown in Figure 3.7a. Conversely, the CO_2 plasma-treated MoO_x is quite resilient to Ar plasma exposure and still contains 88 at.% Mo^{6+} oxidation states after going through the same Ar plasma treatment, resulting in the

lower optical absorptance compared to the sample without CO_2 plasma pretreatment.

The as-deposited WO_x has a large content ($\approx$25 at. %) of W^{5+} which is significantly larger than the Mo^{5+} content in as-deposited MoO_x layers. The effects of CO_2 and Ar plasma exposure follow the same trend as for the MoO_x layers: The content of Mo^{6+} increases after CO_2 plasma treatment, and the film becomes then resilient to subsequent Ar plasma treatment, resulting in a final W^{5+} content <10 at.%. This confirms the spectrophotometric observations in Figure 3.7c that a WO_x film can be totally bleached by a CO_2 plasma and that a CO_2 plasma pretreatment prevents further coloration. This pretreatment also prevents a valence band shift and the appearance of Mo d states in the band gap observed for the untreated samples after Ar plasma exposure.

Further investigations will be necessary to determine the origin of this resilience after CO_2 plasma treatment, as observed in our current set of measurements. We carried out a preliminary Raman spectroscopy measurement of MoO_x layers on glass to determine their structural properties (see Figure S7 of reference [96]). It clearly indicates that the as-deposited layer are amorphous, with very broad peaks around the expected position of the α-phase peaks. The Raman spectrum is not affected by the CO_2 plasma treatment, which indicates that the observed resilience dos not originate from structural changes. One possible explanation in the case of MoO_x could be the formation of Mo-O-C bonds that appears as a shoulder in the C 1s peak after the CO_2 plasma treatment. In fact, such a shoulder emerges in the C 1s core-level spectra of Ar plasma-treated samples relative to the as-deposited MoO_x (Figure 3.8b). However, the same effect of the CO_2 plasma is not visible in WO_x XPS spectra.

Furthermore, it is evident from the spectrophotometric measurements that WO_x is intrinsically more resilient to ion bombardment than MoO_x. A possible explanation for this difference was formulated by Meyer *et al.* [198] WO_x could form nanocrystalline clusters $(WO_3)n$, which offer large cross section for incoming particles such as Ar^+ ions. Another possible explanation involves the comparison of the standard reduction potentials of MoO_3 and WO_3, +0.075E°/V and -0.090E°/V, respectively [199]. The more positive the reduction potential of a material, the more readily it can be reduced. Therefore, MoO_3 is intrinsically more prone to reduction compared to WO_3.

As mentioned above, the coloration of TMO layers can induce optical losses when used for transparent electrodes of optoelectronic devices and could therefore be detrimental to device performance. On the basis of our present findings, we implemented different TMO/TCO stacks - untreated and exposed to CO_2 plasma - in solar cells, where they have recently found widespread application. Specifically for semitransparent perovskite solar cells for building integration or tandem applications, TMOs are used underneath the transparent top electrode to avoid sputter damage to the sensitive charge transporting and perovskite layers during TCO sputtering [72]. Until now, MoO_x has typically been used for these applications [193, 83, 74]. Duong *et al.* recently pointed out that a significant part of the sub-band gap absorptance of their mesoporous semitransparent perovskite solar cells originates from the MoO_x/ITO electrode [74]. Based on the results shown in Figure 3.7, it would be beneficial, at least in terms of optical properties, to replace MoO_x by WO_x and possibly to introduce a CO_2 plasma treatment between the TMO evaporation and the TCO sputtering processes. We therefore implemented
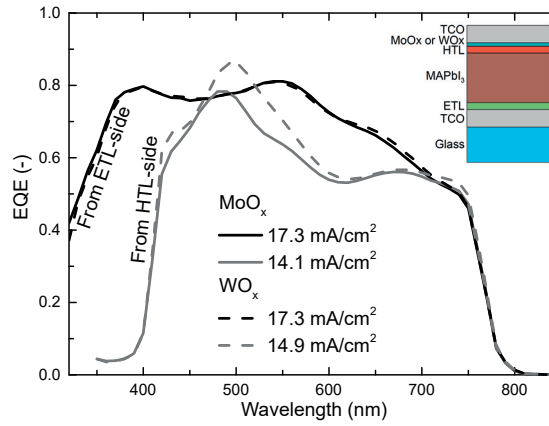
Figure 3.9 – External quantum efficiency of semitransparent MAPbI$_3$ perovskite solar cells with either MoO$_x$ or WO$_x$ as protective buffer layer. Illuminated from either hole-collecting (HTL) or electron-collecting (ETL) side, as defined in the schematic of the cell. Reproduced with permission [96]. Copyright 2016, American Chemical Society.

this absorption mitigation strategy to semitransparent perovskite solar cells, with a device architecture as shown in the inset to Figure 3.9, and obtained similar electrical performances with WO$_x$ and MoO$_x$ layers, with or without CO$_2$ plasma treatment (Figure 3.10), showing steady efficiencies between 11 and 13% during maximum power-point tracking. WO$_x$-based cells showed slightly increased series resistances, which we attribute to a non-optimized thickness. Further work will be necessary to optimize the electrical performance of these cells.

The optical gains of these cells due to the CO$_2$ plasma treatment and the use of WO$_x$ are illustrated in Figures 3.9 and 3.11. Figure 3.9 shows the EQE measurements of semitransparent perovskite cells with WO$_x$ and MoO$_x$ layers. Because of the reduced parasitic absorption losses, the WO$_x$-based cell has a higher spectral response compared to the MoO$_x$-based cell,
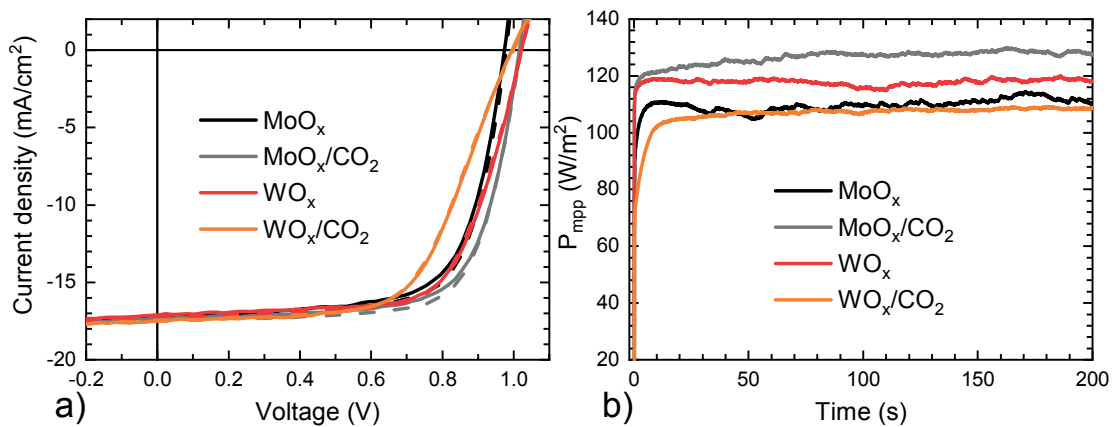
Figure 3.10 – a) J-V and b) maximum power point tracking curves for semitransparent MAPbI$_3$ perovskite solar cells with MoO$_x$ or WO$_x$ buffer layers (with or without CO$_2$ plasma pre-treatment). Dashed J-V curves are in forward (J_{sc} to V_{oc}) direction and solid J-V curves are in reverse (V_{oc} to J_{sc}) direction. Reproduced with permission [96]. Copyright 2016, American Chemical Society.
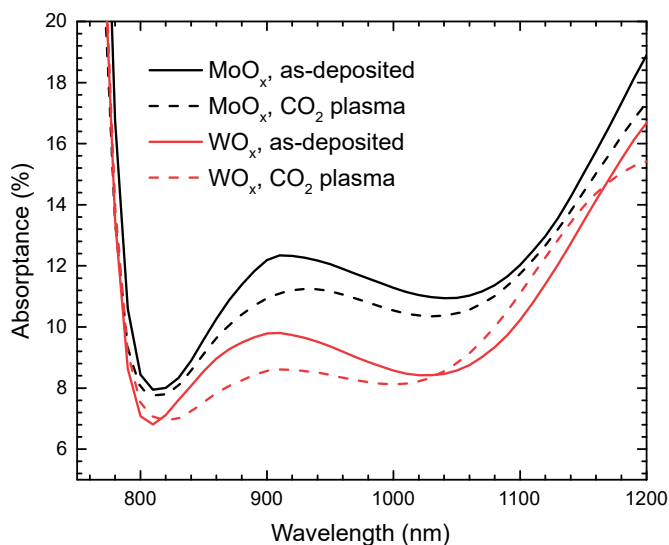
Figure 3.11 – Sub-band gap absorptance of semitransparent planar MAPbI$_3$perovskite cells with MoO$_x$ or WO$_x$ (CO$_2$ plasma treated or without treatment) as buffer layer in the rear transparent electrode. Reproduced with permission [96]. Copyright 2016, American Chemical Society.

when illuminated through the transparent electrode comprising the TMO/TCO stack. This configuration is particularly important for monolithic perovskite-based tandem cells (such as perovskite on silicon or perovskite on CIGS), where the perovskite top cell has to be illuminated through this electrode. When illuminated from the other side (glass substrate side), the two cells show similar EQE. This case is relevant for single-junction devices or for top cells in mechanically stacked 4-terminal tandems. However, a gain can be observed in the sub-band gap spectral region, as illustrated by Figure 3.11. Low values in this graph indicate high transmittance through the perovskite top cell. Previously reported semitransparent perovskite solar cells had over 20% sub-band gap absorptance due to the use of FTO-coated glass substrates and suboptimal layer stacks [72, 193]. After changing the substrates to ITO, the sub-band gap absorptance could be reduced to 10-12% [83, 74], corresponding to the MoO$_x$ as deposited case in Figure 3.11. Replacing this MoO$_x$ layer by a WO$_x$ layer with a CO$_2$ plasma treatment helped to further reduce these sub-band gap parasitic absorptions by 2-3%$_{abs}$. In a tandem configuration, where this near-infrared light is transmitted to a low-band gap bottom cell (*e.g.*, a wafer-based silicon solar cell), this would therefore lead to an improved bottom cell photocurrent. For monolithic perovskite/silicon heterojunction tandem solar cells, current gains in both top (+0.2 mA/cm^2) and bottom (+0.7 mA/cm^2) cells were observed when replacing MoO$_x$ by WO$_x$, demonstrating the benefit of using WO$_x$ in such tandem cells (see reference [96]). The remaining parasitic absorptance is then mostly due to the absorptance in the electron and hole transporting layers. These measurements clearly demonstrate that replacing MoO$_x$ by WO$_x$ and applying a CO$_2$ plasma pretreatment prior to TCO deposition can strongly reduce the parasitic absorption losses and increase photocurrent in both the top cell and the bottom cell of tandem devices.
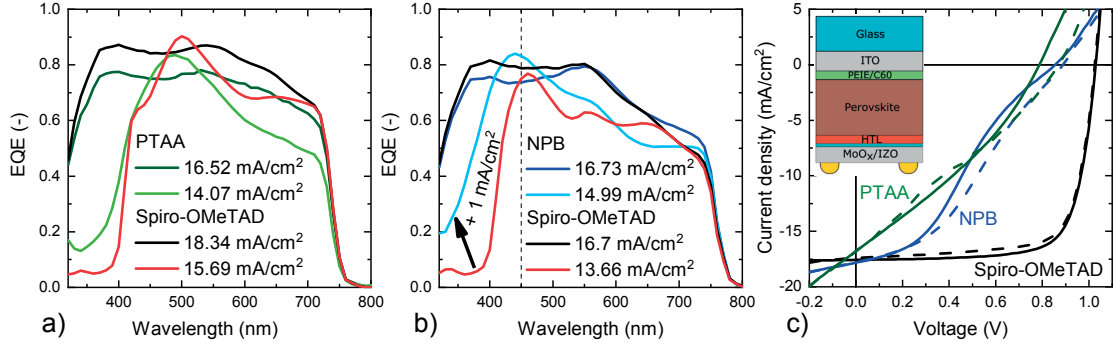
Figure 3.12 – EQE curves of semitransparent CsFAPbIBr perovskite solar cells with a) either N,N' -Bis(naphthalen-1-yl)-N,N' -bis(phenyl)-benzidine (NPB) or spiro-OMeTAD, and b) PTAA or spiro-OMeTAD as hole transporting layer and illuminated either in substrate (through the IZO) or superstrate configuration (through the glass), and c) their corresponding *J-V* curves for comparison of the electrical properties. All cells have a MoO$_x$/IZO transparent electrode.

3.3.2 In charge transporting layers

In a monolithic tandem, as it will be discussed later in Chapter 5, the semitransparent perovskite cell is illuminated in substrate configuration, *i.e.* through the transparent electrode instead of through the glass as in the more commonly used superstrate configuration. As shown in Figure 3.12 or B.2, spiro-OMeTAD absorbs strongly the light in the spectral range below 400 nm wavelength, which can be evaluated to >1 mA/cm^2 loss compared to the photocurrent when illuminated in the superstrate configuration. It is therefore important to find an alternative solution resulting in lower parasitic absorption losses.

PTAA was demonstrated as an efficient alternative to spiro-OMeTAD in opaque perovskite solar cells [200, 27]. Unfortunately, it also generates strong parasitic absorption losses when applied in semitransparent cells measured in substrate configuration, as shown from EQE measurements in Figure 3.12a.
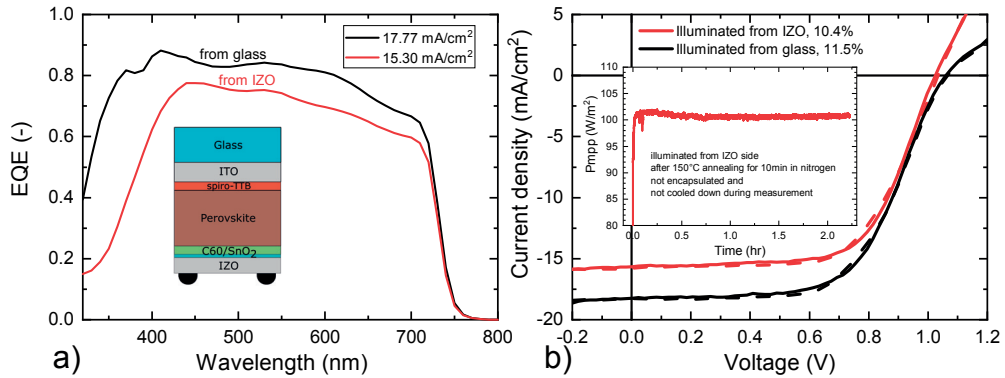
Figure 3.13 – a) EQE and b) *J-V* curves of semitransparent p-i-n CsFAPbIBr perovskite solar cells illuminated either in substrate (through the IZO) or superstrate configuration (through the glass). The schematic inset illustrates the device layer stack and the inset in b) shows the maximum power point tracking (MPPT) of the cell measured in substrate configuration in air without active cooling.

Thin thermally evaporated organic layers were more promising. Figure 3.12b shows that replacing a 150-nm-thick and heavily doped spiro-OMeTAD by a 15-nm-thick NPB layer helps to gain ≈ 1 mA/ cm^2 in the wavelength range below 450 nm. Unfortunately, the *J-V* characteristics of such cells were suffering from s-shapes, which indicate the presence of interfacial barriers. We only managed to overcome these electrical performance limitations when using thin undoped p-type evaporated layers by inverting the device polarity, from n-i-p to p-i-n (see Sections 2.3.1 and 2.3.2). This is in contrast to other laboratories, where such layers were successfully used in n-i-p cells [144]. As shown in Figure 3.13a, the spectral response in the low-wavelength region can then be high, while keeping correct electrical performance (Figure 3.13b). The remaining current difference between substrate and superstrate illumination, observed both in EQE and *J-V* measurements, can be attributed to non-optimal carrier extraction and parasitic absorption in the TCO, as discussed in the next Section.

3.3.3   In the transparent conductive oxide

As shown in Figure 3.14, choosing a wide band gap TCO can provide a slight increase in current due to higher transparency in the low-wavelength region. In their as-deposited conditions, IZrO showed the best spectral response in this region for the tested TCOs when measured in substrate configuration. For example, replacing IZO by IZrO allows to gain 0.15 mA/cm^2 in the <400 nm region, due to their different optical band gap. IO:H can have a very similar optical performance once annealed, here done at 150°C in nitrogen to not degrade the perovskite material. IZrO and annealed IO:H have also higher carrier mobilities >100 $cm^2V^{-1}s^{-1}$, compared to ≈ 55 $cm^2V^{-1}s^{-1}$ for IZO. High carrier mobility is important to minimize free carrier absorption losses in the longer wavelengths spectral region.
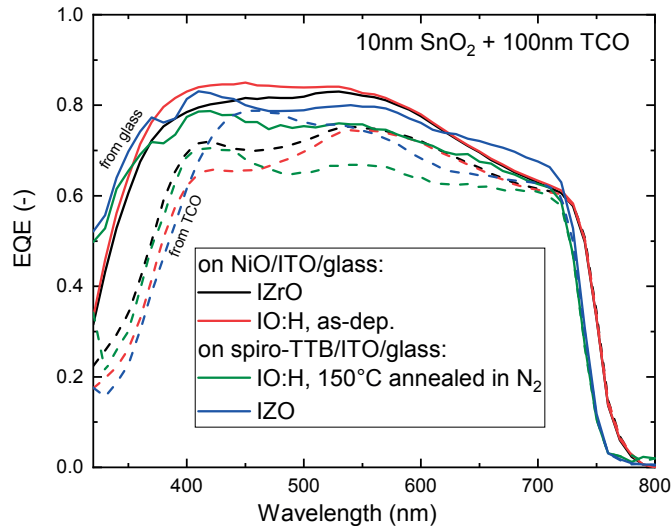
Figure 3.14 – EQE curves comparing IZO, indium zirconium oxide (IZrO) and IO:H as rear-side TCO in semitransparent p-i-n CsFAPbIBr perovskite cells. Solid lines show EQE measurements in superstrate configuration, whereas dashed lines show measurements in substrate configuration.

3.4 Toward efficient large area NIR-transparent perovskite cells

Figure 3.15 shows the highest performing semitransparent perovskite cells with 1 cm^2 area fabricated during this thesis. In the p-i-n configuration using spiro-TTB as hole transporting layer, C_{60} as electron transporting layer and SnO_2/IZO as transparent electrode, the cell had an efficiency of around 13% under maximum power point tracking and 13.5% from reverse *J-V* curve, without antireflective foil nor coating. In the n-i-p configuration using LiF/C_{60} as electron transporting bilayer, spiro-OMeTAD as hole transporting layer and MoO$_x$/IO:H/ITO as transparent electrode, the best cell had an efficiency of around 15.7% under maximum power point tracking without ARF (see Figure B.3). With ARF, the current density increased to >20 mA/ cm^2, which pushed the performance >16%. Both cells had still rather low *FF*, which can be attributed to interfacial series resistance losses, unoptimized thicknesses and charge transporting materials properties, including energy levels alignment with the used perovskite materials, as well as recombinations in the perovskite absorber and its interfaces. Also additional efforts in metallization design and TCO deposition processes will be needed to further improve *FF* and overall cell performance of the 1 cm^2 cell.
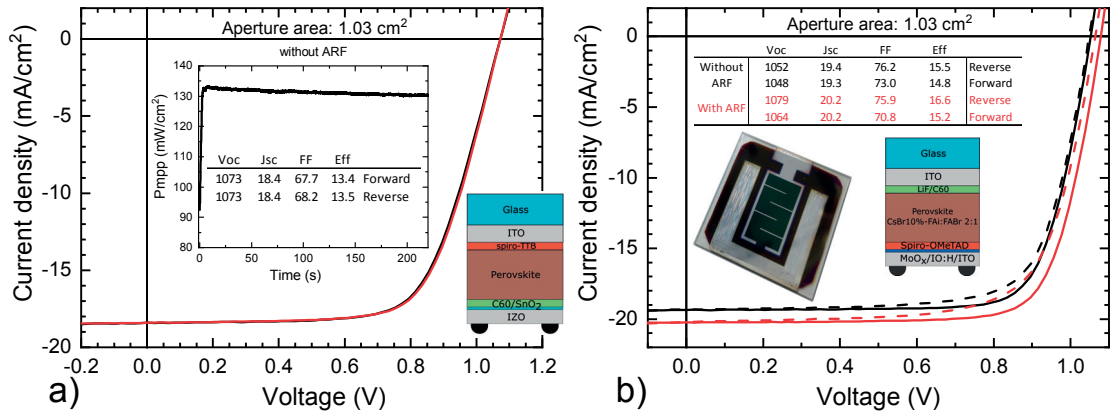
Figure 3.15 – Best 1 cm^2 area semitransparent CsFAPbIBr perovskite solar cell in a) p-i-n and b) n-i-p polarity. Device schematics are given in both subfigure, showing the materials used for the presented cells. The inset in a) shows the maximum power point tracking curve and *J-V* parameters table. A picture of the cell is shown in b), illustrating the cell design and metallization.

3.5 General conclusions on the chapter

In this chapter, the requirements for an optimal transparent electrode were defined and its initial development was described. As replacement for the opaque rear metal contact, a TCO-based electrode was developed using a high mobility amorphous TCO, namely IZO, absorbing <3% in the 400-1200 nm spectrum. Sputter damage was minimized by careful control of the deposition conditions and with the introduction of a transition metal oxide buffer layer, MoO$_x$ or WO$_x$, thermally evaporated on the spiro-OMeTAD hole transporting layer of n-i-p cells. Parasitic absorption losses in the buffer layer appeared to be important

and a more in-depth investigation revealed that transition metal oxides are sensitive to the sputtering plasma environment: light, temperature, argon bombardment... A method based on an oxidizing CO_2 plasma pre-treatment was developed to prevent the appearance of the absorption peak in the buffer layer after TCO deposition. It was also shown that WO_x is intrinsically more resilient to sputtering damage compared to MoO_x, and should provide better transparency to the electrode. Similarly to the n-i-p cells, a transparent electrode was developed for the p-i-n cells and the buffer layer was SnO_2 deposited by ALD. The deposition temperature was found to be an important parameter, with s-shaped J-V curves appearing with too low or too high temperatures. 100°C was found to give the best device performance. Parasitic absorption losses are also important in the charge transporting layers. It was rapidly found that spiro-OMeTAD was the source of strong parasitic absorption losses especially for semitransparent cells measured in substrate configuration with direct illumination through the spiro-OMeTAD electrode stack. Investigations were carried out to find a replacement that is undoped, thinner and thermally evaporated. Only p-i-n cells allowed the use of both electron and hole transporting layers satisfying these criteria. Finally, 1 cm^2 area semitransparent perovskite cells were demonstrated in both p-i-n and n-i-p configurations, with efficiencies up to ≈16%.

The semitransparent perovskite cells presented in this chapter are suitable for tandem applications, as they satisfy the requirements specified in the introduction. They were then applied in perovskite/silicon tandem solar cells in both 4-terminal and 2-terminal architectures, as presented in Chapter 4 and Chapter 5 respectively.

Future investigations on transparent electrodes for tandem applications should then focus on further reducing parasitic absorption losses, and also incorporate constraints linked to stability. Indeed, the electrode should also be designed so that it can provide a protection for the perovskite absorber against the environment, *e.g.* moisture ingress, and at the same time a barrier for volatile elements of the cell, *e.g.* effusion of organo-iodide components. Mechanical stability of the electrode and its interfaces should also be improved in order to pass stress tests such as damp heat or thermal cycling.

4 Mechanically stacked 4-terminal tandem solar cells

Summary

This chapter presents the integration of n-i-p semitransparent perovskite solar cells in mechanically stacked 4-terminal tandem solar cells. The challenges in reduction of the strong parasitic absorption and reflection losses are first discussed, including solutions with the introduction of optical coupling liquid, antireflective foils and less absorbing TCOs. Then, 4-terminal tandem measurements with >25% total efficiency are presented with a small area top cell. Finally, larger 1 cm^2 area top cells are integrated with similar size bottom cells to show >23% efficient fully integrated 1 cm^2 4-terminal tandem device.

4.1   Introduction

As soon as we had developed a perovskite solar cell with near-infrared transparency as presented in the previous chapter, the most straightforward way to assess its potential in a tandem configuration with silicon was the 4TT architecture. The different tandem architectures currently under research are presented in the introduction chapter of this thesis (see Section 1.3.3), where their advantages and disadvantages are also discussed. In the present chapter, we will focus on the mechanically stacked 4TT configuration, where both subcells are fabricated and characterized independently, thus reducing the constraints on mutual process compatibility. The chapter is divided in two main parts: the initial tests on this tandem configuration are first presented, showing the challenges and some simple solutions to parasitic absorption and

---

Parts of this chapter are based on published work. The sections reproduced in part or fully are marked with an asterisk ∗. Section 4.2 is partially based on a publication in *Solar Energy Materials and Solar Cells* and adapted with permission from [72]. Section 4.3 is partially based on a publication in *ACS Energy Letters*, adapted with permission from [76], and a conference proceeding [91].
The bottom cells used in Figure 4.4 were developed by Loris Barraud at CSEM especially for the 1 cm^2 area tandem devices.

reflection losses. Then, based on these initial observations, Section 4.3 shows the development of the 4TT toward high efficiencies, from measurements with small top cells to more realistic integrated larger area devices. For more detailed information on the characterization protocol or fabrication processes, the reader should refer to the experimental method in Annexe A.

4.2 Initial tests: parasitic absorption and reflection losses reduction *

In 2014, at the beginning of this thesis, mesoporous perovskite solar cells using compact and mesoporous TiO_2 layers were the most advanced cell structure [201]. Therefore, as already described in Section 3.2, our first semitransparent perovskite solar cells were based on this device structure. FTO coated glass substrates were initially used for their high thermal stability, necessary to maintain good electrical properties after TiO_2 sintering at 500°C. When first applying these newly developed NIR-transparent perovskite solar cells in a 4TT configuration, it became rapidly clear that the FTO was the main contributor to the top cell's sub-band gap parasitic absorption. A 4TT measurement consisted here of measuring the *J-V* parameters of the semitransparent perovskite cell, then measuring its EQE curve. This cell is then used as a filter to measure the EQE of the bottom cell as it would appear in a tandem configuration, with still an air gap between the top and bottom cells. As shown in Figure 4.1, the increased absorptance in the red and NIR spectral region due to larger free-carrier density in FTO (see Figure 4.1e) translates directly in the bottom cell's EQE by a loss of >1 mA/cm^2 compared to a measurement with a similar perovskite cell using a less absorbing ITO front electrode. We can however see that even with ITO, having lower free-carrier absorption, further improvements are still necessary to match the non-filtered reference silicon cell, as shown in Figure 4.1b. The bottom cell current can be further improved by reducing parasitic absorption losses in the front transparent electrode. Indeed the MoO_x buffer layer needed to protect the sensitive organic underlying layers from the rough sputtering conditions was found to contribute significantly to the parasitic absorption losses. This increased absorption after TCO deposition is explained with more details in Section 3.2.2. In brief, the argon (Ar) bombardment, plasma luminescence and temperature during TCO sputtering were found to reduce the metal oxide by increasing the oxygen vacancies density, which can act as absorbing optical centers. This increased parasitic absorption can be directly observed in the bottom cell EQE in a 4TT measurement, as shown in Figure 4.1b. This Figure clearly shows that the perovskite top cell without MoO_x buffer layer was more transparent in the wavelength range between 600 and 1000 nm. However, this top cell was also less efficient due to more intense sputter damage and degraded spiro-OMeTAD hole transporting layer, creating a trade-off between reduced sputter damage and increased parasitic absorption when introducing the MoO_x buffer layer.

IZO as front TCO was chosen for its good electrical and optical properties in its as-deposited state (see Section 3.2). The higher carrier mobility of IZO compared to ITO or FTO can be observed in Figure 4.1e, with clearly different absorptance spectra in the long wavelengths due to free-carrier-absorption. In the shorter wavelength range, IZO is however penalized by its
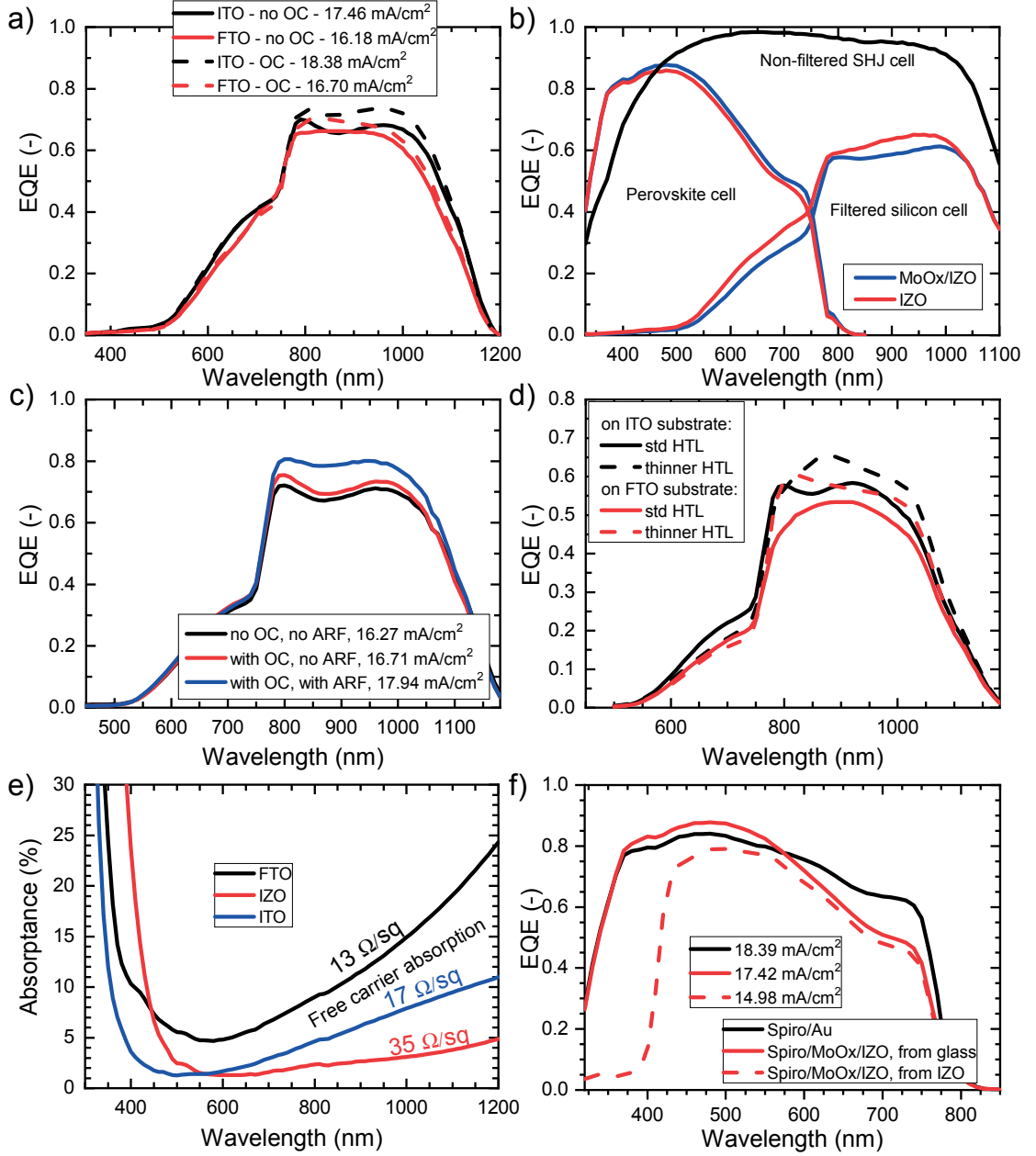
Figure 4.1 – a) EQE curves of silicon bottom cell filtered with a perovskite top cell grown on either an ITO or FTO substrate (OC stands for optical coupling, here canola oil); b) EQE spectra of a 4TT measurement showing the effect of the parasitic absorption losses in the MoO$_x$ buffer layer; c) EQE curves showing the impact of an optical coupling liquid and microtextured antireflective foil on the silicon bottom cell spectral response; d) EQE curves of a silicon bottom cell filtered with perovskite solar cells using thinner spiro-OMeTAD hole transporting layer (HTL); e) Absorptance spectra of FTO, IZO and ITO on glass substrates. Their sheet resistance are indicated on the curves for better comparison; f) EQE measurement of a semitransparent perovskite cell, illuminated either in substrate (through the IZO/MoO$_x$/spiro-OMeTAD electrode) or superstrate (through the glass).

narrower optical band gap. This issue is more important for monolithic tandem solar cell, as it will be discussed in the next chapter. Indeed in the 4TT configuration, the top cell illumination

orientation can be freely chosen to the more advantageous superstrate architecture (light enters the cell through the glass substrate). This situation reduces the constraints on the TCO optical band gap and on the short wavelengths transparency of the charge transporting layer, here spiro-OMeTAD, which is known to strongly absorb in the <400 nm wavelength range. Figure 4.1f illustrates these two situations with a semitransparent cell measured in substrate (from IZO) and superstrate (from glass) configurations. The charge transporting layers can however also contribute to the parasitic absorption losses in the longer wavelengths, mainly through their dopants, as shown in Figure 4.1d demonstrating the effect of thinning down the top cell's hole transporting layer (HTL) on the quantum efficiency response of the bottom cell. The improved bottom cell's response here can also be partially attributed to different reflectance, changing the interference pattern in the tandem device. Thinning down spiro-OMeTAD however leads to reduced electrical performance of the top cell, which largely outweigh the gain in the bottom cell for the total tandem efficiency.

Reflection losses were also found to be significant. In the presently investigated 4TT architecture, the two subcells are mechanically stacked on top of each other, leaving an air gap in between. The refractive index mismatch in the layer sequence TCO/Air/TCO (n=≈2/1/≈2) induces large reflection losses for the bottom cell. The introduction of an optical coupling layer between the subcells helped to further increase the bottom cell current as shown in Figure 4.1a&c , *e.g.* PDMS has n≈1.4, canola oil has n≈1.47. The reflection on the front glass surface can be reduced by either depositing an antireflective coating (*e.g.* LiF, magnesium fluoride (MgF_2), porous silicon dioxide (SiO_2)) or using a ARF (described further in experimental method Section A.4.3). This foil can be applied directly on the glass during the *J-V* and EQE measurement, helps to decrease the reflection and enhances light trapping for both the top and bottom cell. An illustration of its impact on the bottom cell response can be seen in Figure 4.1c and this technique was later on applied to all 4TT measurements.

From these preliminary observations, it is clear that the performance of the top perovskite cell needs to be improved, while keeping in mind the crucial importance of low parasitic absorption losses, in order for the tandem to outperform the silicon single junction cell.

4.3 Toward 1 cm^2 area integrated 4TT tandem device *

Figure 4.2a shows a schematic of the 4TT architecture, as well as the top cell orientation in superstrate configuration. All tandem results discussed in this Section will follow this arrangement and include optical coupling and ARF.

Using semitransparent mesoporous perovskite solar cells (see device schematic in Figure 1.3 of introduction) grown on FTO substrates, 4TT measurements reached efficiencies up to 18% [72]. As mesoporous cells require a TiO_2 scaffold layer annealed at 500°C, only FTO-coated substrates could be used, thanks to their thermal stability. ITO has a higher carrier mobility compared to FTO, and hence lower free carrier absorption in the long wavelengths spectral range. However, the conductivity of ITO drastically decreases after 500°C annealing. When still relying on the high-temperature sintered TiO_2 electron transporting layer, replacing FTO

Figure 4.2 – 4-terminal mechanically stacked tandem: a) Schematic drawing of the tandem stack with a NIR-transparent MAPbI$_3$ perovskite top cell illuminated through the glass substrate (superstrate configuration) and a silicon heterojunction bottom cell; b) and c) show the EQE spectra and *J-V* characteristics, respectively, of the mechanically stacked perovskite/SHJ tandem measurement with a 0.25 cm^2 top cell and 25.2% total efficiency. For more detailed information on the characterization protocol or fabrication processes, the reader should refer to the experimental method in Annexe A.4.4. Reproduced with permission [76]. Copyright 2016, American Chemical Society.

by ITO pushed the 4TT efficiency to 19.6%, thanks to its better transparency, and therefore lower parasitic absorption in the NIR spectral region. The development of a low-temperature-processed perovskite cell (described in Chapter 2) allowed us then to use ITO substrates, taking advantage of their better transparency, without degrading their electrical properties. These low-temperature cells were in n-i-p configuration using PEIE/PCBM as electron transporting layer and spiro-OMeTAD as hole transporting layer. The performance of these MAPbI$_3$ semitransparent perovskite cells could be raised up to 16.4% with an aperture area of 0.25 cm^2. By mechanically stacking this cell onto a 4 cm^2 silicon bottom cell, a 4TT measurement of 25.2% could be demonstrated experimentally. The EQE and *J-V* curves of this tandem measurement are shown in Figure 4.2. The perovskite absorber material was then modified toward slightly higher band gaps by introducing FA as a second cation and bromine as second halide,

	V_{oc}	J_{sc}	FF	Eff.	P_{mppt}
perovskite, 1.55 eV	1069	20.1	74.9	16.1	16.4
filtered silicon	693	15.98	79.5	8.8	
4TT					25.2
perovskite, 1.65 eV	1086	20	77.1	16.8	16.2
filtered silicon	695	17	79.8	9.4	
4TT					25.6
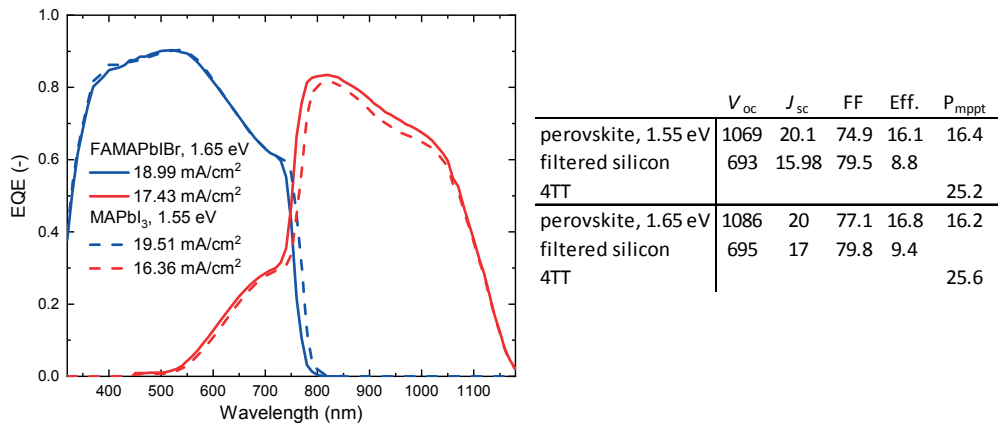
Figure 4.3 – EQE measurements of perovskite/silicon 4-terminal tandem cells, comparing two different perovskite compositions: FAMAPbI$_{3-x}$Br$_x$ and MAPbI$_3$. The FAMA-based cell was fabricated by Florent Sahli. For more detailed information on the characterization protocol or fabrication processes, the reader should refer to the experimental method in Annexe A.4.4.

increasing the band gap from 1.55 to 1.65 eV while keeping the top cell performance almost unchanged. The total 4TT measurement efficiency was then raised to 25.6%. This slight performance increase can be attributed to the additional current in the silicon bottom cell during the 4TT measurement, as shown in Figure 4.3. This clearly shows the necessity of moving to a larger top cell band gap for optimal tandem performance, which could be obtained by changing MAPbI$_3$ perovskite composition for a mixed-cation/halide perovskite material. This was largely the reason for the latest improvements of the 4TT efficiency record: for example, Duong et al. [78] used a quadruple cation (RbCsMAFA) perovskite absorber with 1.75 eV band gap yielding 26.4% tandem efficiency (0.16 cm^2 top cell area).

Nevertheless, these tandem measurements showed already an efficiency improvement of >3%$_{abs}$, as compared to the single-junction silicon heterojunction cells that were used as bottom cells and which had 1-sun efficiencies around 22%. The experimental demonstration of efficiencies beyond 25% with this tandem configuration also confirmed the potential of perovskite solar cells to boost the performance of high-efficiency silicon technology in tandem devices.

Demonstrating the same tandem device performance on >1 cm^2 cell area is the necessary next step toward a potential future industrialization. Therefore, after reaching >25% tandem efficiencies with small area top cells, our focus was redirected to the fabrication of efficient fully integrated tandem devices with both subcells having an aperture area of 1.03 cm^2 and being permanently attached to each other. We therefore further adapted the top cell to achieve high performance on 1 cm^2 area, which requires high uniformity in the deposition of all cell layers and high film quality, especially for the perovskite absorber. The spin coated PCBM electron transporting layer was thus replaced by a thin evaporated layer of C$_{60}$, allowing for better control on the layer thickness and pin-hole density difficult to achieve for <10 nm solution processed films. The perovskite composition was adapted to CsFAPbI$_{3-x}$Br$_x$, which, in our case, was key to fabricate high quality perovskite layers on larger areas. With these improvements, a 15.2% semitransparent top cell was fabricated and integrated on a SHJ bottom
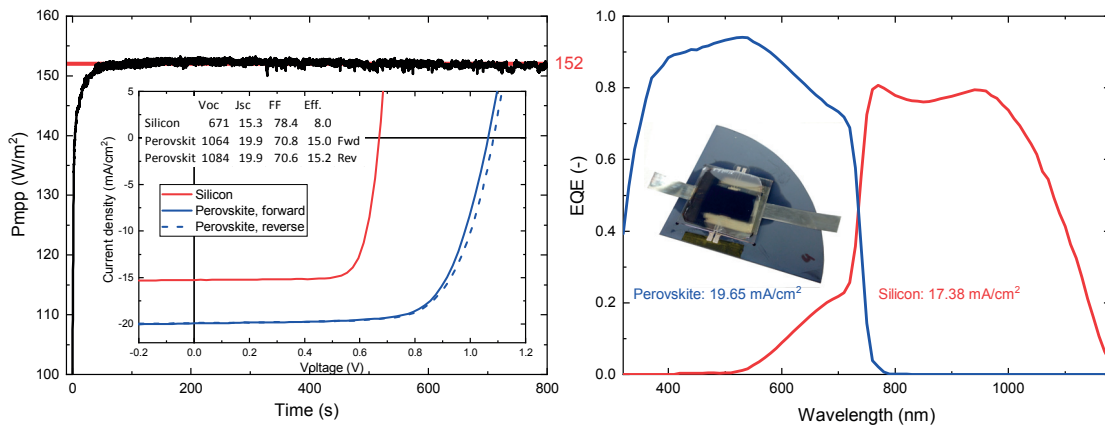
Figure 4.4 – Integrated mechanically stacked 4-terminal tandem device with 1.03 cm^2 aperture area in both sub-cells: A) *J-V* curves of top and bottom cells and maximum power point tracking curve of the CsFAPbIBr perovskite top cell. During the measurement of each sub cell, the other sub cell was kept at open circuit.

cell specifically designed with the same cell geometry and size. The two cells were optically coupled and glued together with polydimethylsiloxane (PDMS). This fully integrated mechanically stacked 4-terminal tandem device had an efficiency of 23.2%, as shown in Figure 4.4. The top cell was limited by a fill factor of ≈70% and the bottom cell mainly by the current, which was reduced by shadow losses due to the thick evaporated metal fingers used on the top cell back electrode. Those two losses are directly linked and might be drastically reduced by changing the metallization process from evaporation to screen printing. However, this technique requires a temperature-stable cell, which could be achieved with inverted p-i-n semitransparent perovskite cells as described in Chapter 3. However their performance at the time of writing this thesis were not sufficient to outperform the n-i-p top cells in 4TT devices. As presented in Chapter 3, 1 cm^2 area semitransparent n-i-p perovskite cells could be fabricated with >16% efficiency. However, after integration on the silicon cell with ribbons and PDMS, the cells usually lost some FF, which explains the 15.2% cell presented here (as measured in the integrated device). Further optimization of the integration methodology should help to reduce these losses.

4.4 General conclusions on the chapter

The potential of perovskite/silicon tandem solar cells was demonstrated with >25% total efficiency in a 4TT measurement with a small area perovskite top cell and >23% in a fully integrated 1 cm^2 area tandem device. Such tandem devices showed already excellent performance, especially in the blue spectral region where they outperform the SHJ single-junction cell, which itself suffers from parasitic absorption in the amorphous silicon layers. Light management and parasitic absorption are unarguably an essential topic for future development, which we showed by pointing out several issues in the choice of materials for the electrodes and charge transporting layers. Parasitic absorption losses are also an intrinsic disadvantage of the 4TT configuration as compared to monolithic tandem solar cells discussed in the next chapter, due to the additional TCO layers required to contact the rear side of the top cell and the front side of the bottom cell.

In terms of performance, the logical next goal is to reach >30% and reduce the efficiency gap with the III-V/Si mechanically stacked tandem devices, for which the record tops at 32.8% [14]. This should be practically possible, but still highly challenging, with further efficiency improvement of the perovskite top cell toward 20%, while keeping high near-infrared transparency and optical band gap closer to 1.7 eV. However, in order to stay relevant and directly comparable with the III-V technology, >1 cm^2 area devices should become the rule and not the exception.

For strategic reasons, after the demonstration of the potential in 4TT, our focus was redirected to the more industrially promising monolithic tandem solar cells, which are described in the next chapter.

5 Monolithically integrated 2-terminal tandem solar cells

Summary

This chapter presents the integration of perovskite solar cells in 2-terminal monolithically connected tandem solar cells with silicon heterojunction bottom cells. First the development of a TCO-based recombination layer is described and a flat n-i-p tandem with 21.2% efficiency is presented. Then, the important reflection losses and interference effects observed in all-flat devices are discussed, including solutions to these issues. The origins of parasitic absorption losses in monolithic tandem are then explained and, supported by optical simulations, new architectures and materials are investigated. Textured bottom silicon cells are then introduced: an attempt of planarization with LPCVD ZnO is first described with its inherent technical difficulties; then the development of a tandem device with the p-i-n top cell conformally coated onto the textured bottom cell is explained, leading to 25.24% certified power conversion efficiency, under maximum power point tracking. Finally, the up-scalability and light soaking stability of the developed textured tandems are shortly discussed with preliminary results. The chapter finishes with a proof-of-concept of a first perovskite/perovskite/silicon triple junction solar cell on textured wafers and a conclusion and perspectives section.

5.1   Introduction *

In the case of monolithic tandems, the top cell is directly processed on the bottom cell. This has the advantage of a reduced number of fabrication steps and fewer doped transparent conducting electrodes, resulting in lower manufacturing costs and less parasitic absorption. However, monolithic tandems require strict process compatibility, such that both top and bottom cell fabrication schemes have to be specifically adapted for monolithic tandem integration: i) both subcells have to be optimized to produce the same current at maximum power point, as the tandem current will be limited by the subcell with the lower current; ii) the perovskite cell may have to be processed at low temperatures for temperature-sensitive bottom cells, such as the SHJ solar cells, the silicon photovoltaic technology with currently the highest performance; iii) bottom cells with front surface texture are not compatible with solution-processing, which is typically used for the deposition of many layers during perovskite cell fabrication. This implies a current loss due to the lack of light trapping normally provided by the random pyramid texture of the silicon wafer; iv) the typically opaque rear electrode of perovskite cells has to be replaced by a conductive layer with high transparency throughout the visible and near-infrared spectrum; v) perovskite cells are usually much smaller than the industrially established silicon cells, which requires up-scaling of perovskite deposition processes or the development of efficient lab-scale silicon cells.

This chapter covers the results obtained during this thesis toward solving these problems: top cell integration, intermediate contact development, parasitic absorption reduction, reflection losses minimization by using fully textured wafers, up-scalability and demonstration of net efficiency gain compared to single junction cells.

5.2   Intermediate recombination layer: ITO, IZO*

In the case of a monolithic tandem, the device is connected to an external load by 2 terminals, one on the front of the tandem connecting the top cell front electrode and one on the rear connecting the back contact of the bottom cell. The two subcells are then connected in series through a recombination layer or tunnel junction: This feature is specific to this tandem architecture and critical for the device performance. In an ideally current-matched tandem cell, *i.e.* a tandem where both subcells are producing the same photogenerated current, an equal number of charge carriers are flowing from both subcells. For example, in a rear emitter device, the n-contact of the bottom cell is connected through the recombination layer to the p-contact of the top cell, allowing the electrons and holes generated respectively in the bottom and top cell to recombine. The intermediate contact must also be highly transparent (especially between 600 nm and 1200 nm), chemically stable and rely on simple up-scalable processes.

We initially chose to develop a recombination layer based on sputtered indium zinc oxide (IZO) due to its optimal electro-optical properties [161]. Furthermore, IZO has already been demonstrated to be an efficient intermediate contact in organic tandem solar cells [202]. The patterned intermediate recombination layer and top electrode were aligned, defining the
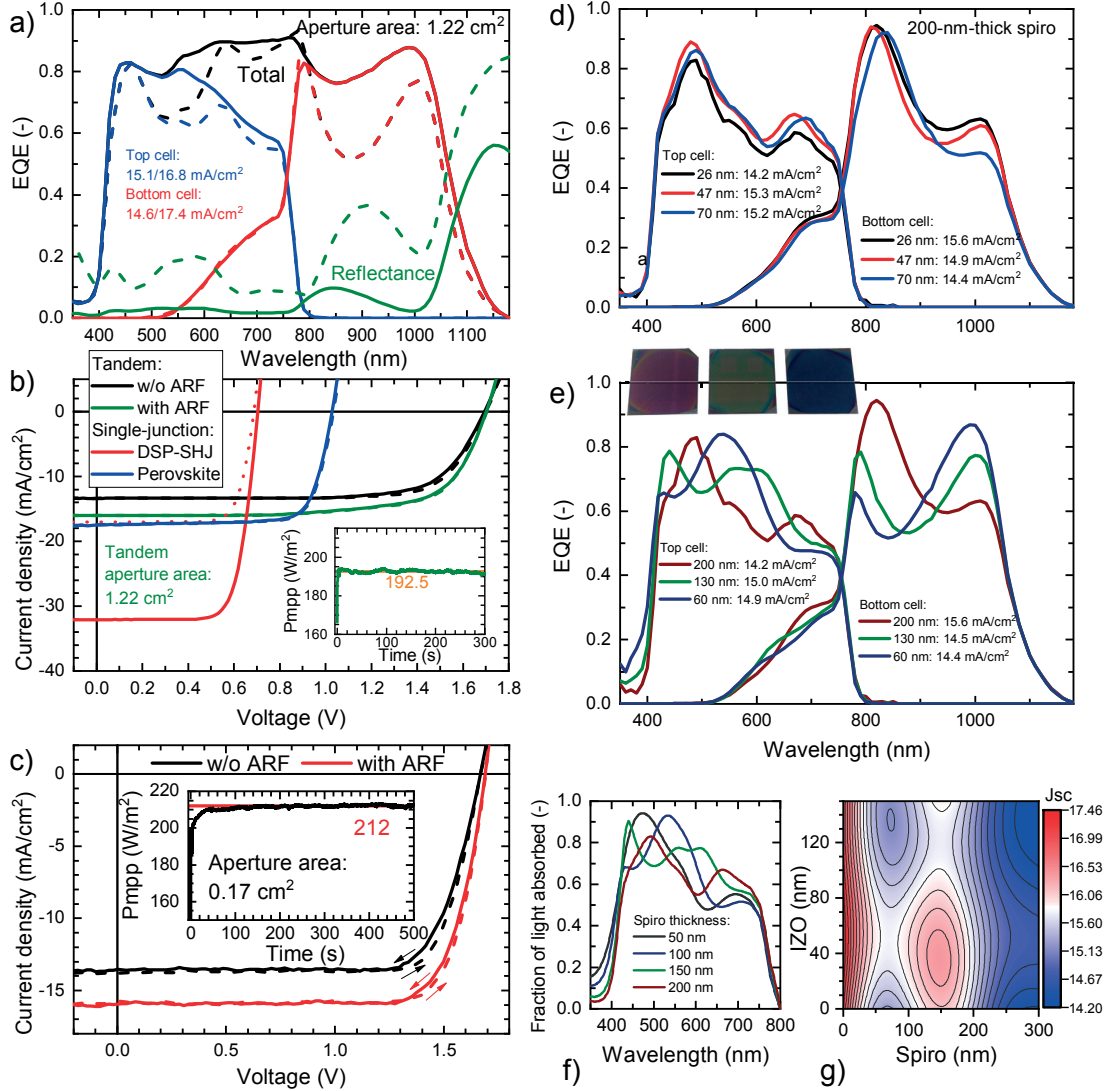
Figure 5.1 – a) EQE spectra of a perovskite/SHJ monolithic tandem with (solid lines) and without (dashed lines) ARF as well as the corresponding reflectance (green curves). The integrated J_{sc} for both top and bottom cells are given in the legend (without ARF/with ARF). b) *J-V* measurements of the best perovskite/SHJ monolithic tandem with 1.22 cm2 aperture area and of the single junction perovskite and double-side mirror polished (DSP)-SHJ cells. Reverse (solid lines) and forward (dashed lines) scans are shown for perovskite single-junction and tandem cells. The dotted red curve shows the *J-V* curve of the SHJ cell when illuminated at an intensity of 0.53 suns. c) *J-V* curves of the best perovskite/SHJ monolithic tandem with 0.17 cm^2 aperture area. The insets to panels b and c show the maximum power point tracking curves of the tandem cells. d) EQE measurements of monolithic tandems with 200 nm spiro-OMeTAD for three different IZO thicknesses and e) with 26 nm IZO intermediate recombination layer for three different spiro-OMeTAD thicknesses, measured without ARF foil. The inset pictures show the colors of the devices after spiro-OMeTAD deposition. f,g) Transfer matrix simulations showing how the interference pattern and current varies in the top cell in function of both IZO recombination layer and spiro-OMeTAD thicknesses. All perovskite absorbers in this Figure have a MAPbI$_3$ composition. Reproduced with permission [83]. Copyright 2016, American Chemical Society.

active area of the tandem solar cell. We fabricated monolithic tandem cells with a planar MAPbI$_3$ perovskite top cell in n-i-p configuration deposited at a temperature below 150°C

on an SHJ bottom cell, using DSP silicon wafers [83]. The choice of a polished bottom cell was dictated by the top cell processes, employing spin-coated charge transporting layers, *i.e.* spiro-OMeTAD and PCBM.

With an efficient and reliable semitransparent n-i-p perovskite solar cell and the IZO intermediate recombination layer, we could fabricate monolithic tandem solar cells with an efficiency as high as 19.5% in forward direction scan, with a V_{oc} of 1703 mV, *FF* of 70.9% and J_{sc} of 16.1 mA/cm^2. This cell was measured through a laser-cut mask with 1.22 cm^2 aperture area and showed a steady efficiency of 19.2%, when measured with a maximum power point tracking system. The complete set of results is detailed in Figure 5.1, and demonstrates that the tandem performance is better than those of both subcells. The small difference in J_{sc} between *J-V* (16.1 mA/cm^2) and EQE (16.8 mA/cm^2) measurements is due to the shadowing induced by the metal contact fingers, which cover 5% of the cell surface.

Efficiencies of up to 21.2% were reached on smaller tandem cells with an aperture area of 0.17 cm^2, as shown in Figure 5.1c. The cell also shows negligible hysteresis and J_{sc} is confirmed by EQE measurements. Compared to the cell with a larger area, we observe a gain in *FF* due to reduced current and series resistance.

During the second half of this thesis, we introduced a nanocrystalline silicon recombination junction as a replacement to the TCO recombination layer. This innovation was published by Sahli *et al.* [86] and helps to reduce parasitic absorption and internal reflection losses between the subcells. Its lower lateral conductivity in the nanocrystalline silicon (nc-Si:H) layers reduces the influence of shunt paths in the perovskite top cell, thus increasing the shunt resistance of the tandem and facilitating its up-scaling.

5.2.1 High-temperature stability of recombination layer *

Due to the sensitivity to process temperature above 200–300°C of SHJ cells, this type of bottom cell is not compatible with high-efficiency mesoporous perovskite top cells. Indeed, this perovskite cell architecture, which is at the origin of many recently certified single-junction efficiency records, is commonly based on a mesoporous TiO$_2$ scaffold layer, which typically requires a 500°C annealing step prior to perovskite absorber deposition. Incorporating this type of perovskite cell in a monolithic tandem therefore requires both the silicon bottom cell and intermediate recombination layer to be stable up to a temperature of 500°C. Most diffused-junction silicon solar cells could be designed to be compatible with a 500°C step, as they undergo typical diffusion/oxidation or firing steps close to 900°C. The commonly used indium tin oxide (ITO) or indium zinc oxide (IZO) is neither electrically nor optically stable upon annealing in an oxygen containing environment at 500°C and therefore is not compatible with the mesoporous perovskite top cell fabrication procedure. We have therefore developed a simple method to combine a mesoporous perovskite top cell with a homojunction silicon bottom cell, using a sputtered zinc tin oxide (ZTO) recombination layer. ZTO has previously been used as an electron transporting layer in organic optoelectronic devices [203, 204] and in thin-film transistors as the channel material [205, 206]. It was shown to be a promising indium-free n-type metal oxide with high electron mobility and transparency, as well as good
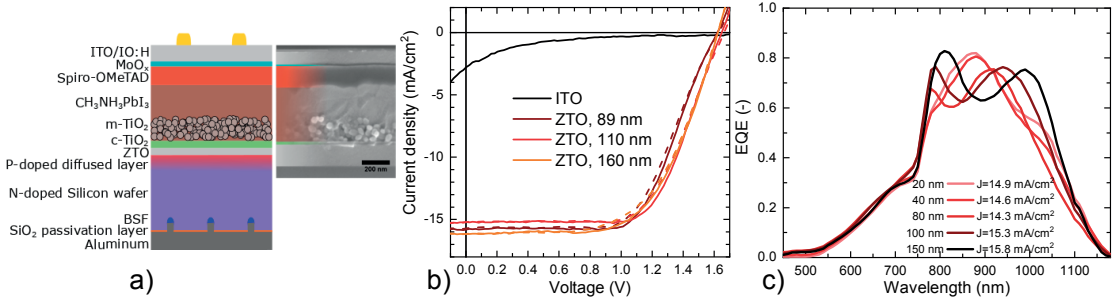
Figure 5.2 – Monolithic tandem cell structure with mesoporous MAPbI$_3$ perovskite top cell and homojunction silicon bottom cell. The SEM image shows a cross-section of a typical perovskite top cell. (Al-BSF Back Surface Field; mp-TiO$_2$ scaffold layer; compact titan dioxide (c-TiO$_2$) compact electron transporting layer; and spiro-OMeTAD hole transporting layer.) b) *J-V* curves of monolithic tandem cells with ITO or ZTO recombination layer. Dashed lines are for forward scans (J_{sc} to V_{oc}) and solid lines are for reverse scan (V_{oc} to J_{sc}); c) EQE curves of bottom cells in monolithic tandem devices with different ZTO recombination layer thicknesses. Reproduced with permission [84]. Copyright 2016, AIP Publishing.

temperature stability and mechanical integrity [207]. These properties qualify ZTO as an attractive candidate for the integration in monolithic tandem devices as an intermediate recombination layer. As shown in Figure 5.2, thanks to the thermal stability of optical and electrical properties up to 500°C, it can indeed be used effectively in a tandem solar cell as a recombination layer. As a proof-of-principle, we fabricated monolithic tandem cells with efficiencies up to 16%, with an aperture area of 1.43 cm^2. Figure 5.2c shows how the variation of the recombination layer thickness influences the optical interference pattern in the device. This device structure with diffused junction bottom cell and a mesoporous perovskite top cell was however then left aside, in order to focus fully on the low-temperature processed cells combining the sequential interdiffusion method for the top cell and silicon heterojunction bottom cells, seen as more promising on the long-term.

5.3   Reflection and parasitic absorption losses

5.3.1   Controlling the interference pattern *

The planar and non-scattering configuration of DSP wafer-based tandem devices results in strong optical interferences. This can clearly be identified in the EQE spectra, as shown in Figure 5.1a. Therefore, several strategies were investigated to reach the high performances presented in Figure 5.1c.

To increase the current of our devices, we applied microtextured anti-reflective foils (ARF) on the front side of the cells during characterization [208, 17]. As shown in Figure 5.1a, this strategy helps to drastically reduce reflection losses and to increase the current in the 1.22 cm^2-sized tandem cell by ≈10% in the top cell and by ≈16% in the bottom cell. Consequently, it passes from a bottom-limited to a top-limited situation. Previous studies on multijunction organic solar cells have shown that optical interferences can be tuned to maximize the light intensity in the absorber layers by changing the effective optical path length. This is usually

achieved by the insertion of an optical spacer [209, 210]. Motivated by these findings, we experimentally tested the effect of thickness variations in our devices. First, we varied the intermediate recombination layer thickness between ≈25 and 70 nm. The resulting EQE curves are shown in Figure 5.1d. We can observe a decrease in bottom cell current with increasing IZO thickness. The lower thicknesses lead to a situation where the perovskite top cell is current-limiting, whereas the highest thickness shifts the limitation to the bottom cell. An optimum situation with closely matching currents is therefore achieved with a 40 to 50 nm thick IZO layer. Similar results were obtained when using an ITO recombination junction. Then, the spiro-OMeTAD hole transporting layer thickness was varied. We choose to test this layer in particular because of its known high parasitic absorption, especially for wavelengths <400 nm, as it was discussed in Chapter 3.3.2. Reducing parasitic absorption in the hole transporting layer can then be achieved by either replacing spiro-OMeTAD by a more transparent material or by reducing its thickness and doping.

Figure 5.1e shows the resulting EQE spectra of tandem cells with spiro-OMeTAD layer thicknesses of ≈200, ≈130, and ≈60 nm. Interestingly, this thickness variation had a much stronger effect on the optical interference pattern compared with the IZO thickness variation. A small current gain (+0.3 mA/cm^2) can also be observed for wavelengths <400 nm, illustrating the improved transparency for thinner spiro-OMeTAD layers; however, sub-100 nm layers induced losses in V_{oc} and *FF* for both tandem and single-junctions cells, reducing the overall device performance.

To support these experimental results, we performed transfer matrix simulations of the tandem layer stack. The calculated absorptance spectra for several spiro-OMeTAD layer thicknesses are shown in Figure 5.1f. They accurately reproduce the interference patterns observed in the measured EQE spectra. Figure 5.1g shows the effect of varying simultaneously the thicknesses of the IZO recombination layer and the spiro-OMeTAD layer on the current generated in the top cell. The simulations agree well with the experimental results, showing that a ≈40 nm thick intermediate recombination layer and a 150 nm thick spiro-OMeTAD layer result in a local maximum for the top cell current. In these simulations, the maximum current is obviously obtained for a cell without spiro-OMeTAD layer, which would however result in drastically reduced overall device performance.

Reflection losses could be further reduced by using a textured SHJ bottom cell to more efficiently harvest infrared photons and further increase photocurrent. A rear texture could be implemented while keeping the front side flat to remain compatible with solution-processed top cells, as discussed in the next paragraph.

5.3.2   Bottom cell with rear-side texture for an enhanced infrared response *

As mentioned previously, monolithically integrated tandems are technically more challenging to realize because of strict process compatibility restrictions, also involving the requirement for a bottom cell with a sufficiently flat front surface for solution-processed top cells. Our first reported monolithic perovskite/SHJ tandem cell thus featured a DSP bottom cell and reached efficiencies of up to 19.2% for a cell area of 1.2 cm^2 [83]. A major limitation of this device
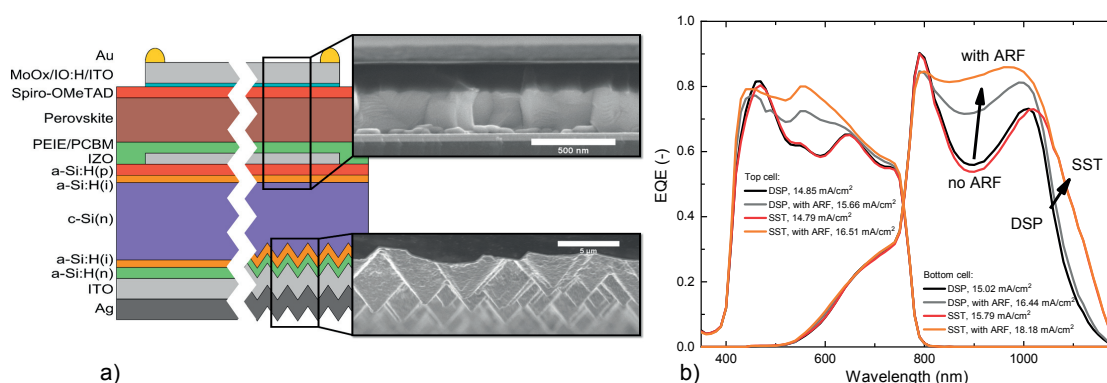
Figure 5.3 – a) Device schematic and SEM cross sectional images of monolithic tandem cells with flat front side and either flat (DSP) or textured rear side (SST). b) EQE curves of monolithic tandem cells on either DSP or SST bottom cells and with or without ARF. Reproduced with permission [76]. Copyright 2016, American Chemical Society.

was the low spectral response at the silicon band edge due to the polished SHJ rear side. We therefore then introduced a single-side textured (SST) SHJ bottom cell to enhance the bottom cell current. Figure 5.3a provides schematic drawings of monolithic tandems with DSP and SST bottom cells, the only difference being the textured rear side. To prepare SST bottom cells, the process was started with double-side polished silicon wafers, on which one side was first coated with a SiN_x dielectric mask. The texturization step was then carried out, followed by a cleaning and mask removal step in a diluted HF bath, resulting in a single-side textured wafer. The plasma enhanced chemical vapor deposition (PECVD) recipes for the amorphous silicon layers were then adapted to fit the front or rear surface finish.

The improvement in spectral response is illustrated by Figure 5.3b, showing a comparison EQE spectra for monolithic tandems with DSP and SST bottom cells. We can observe that the rear-side texture affects the EQE spectra only at wavelengths >1000 nm, as expected from the literature [69, 68], enhancing the bottom cell current density by 0.77 mA/cm^2 (without ARF). This design upgrade of our monolithic tandem enabled us to fabricate a cell with up to 20.5% initial steady-state efficiency under maximum power point tracking. The cell was measured with an aperture area of 1.43 cm^2, and an ARF was used to attenuate the interference pattern, increasing J_{sc} to 16.4 mA/cm^2 (from J-V scans). The device was then current-limited by the perovskite top cell, as shown by the tandem EQE curves in Figure 5.3b. To further improve tandem performance, the perovskite top cell will therefore need to generate a larger current. In addition, more advanced rear reflectors could be implemented to boost the bottom cell infrared current, using dielectric materials to enhance rear internal reflectance and reduce plasmonic absorption losses in the metallization [23, 211].

5.3.3 How to further reduce parasitic absorption and reflection losses? *

Light management is in any near-future research scenario unarguably an essential topic in perovskite/silicon tandem development. Because we used the same top cell for both 4-terminal (see Chapter 4) and 2-terminal (previous paragraph of this chapter) tandem cells,
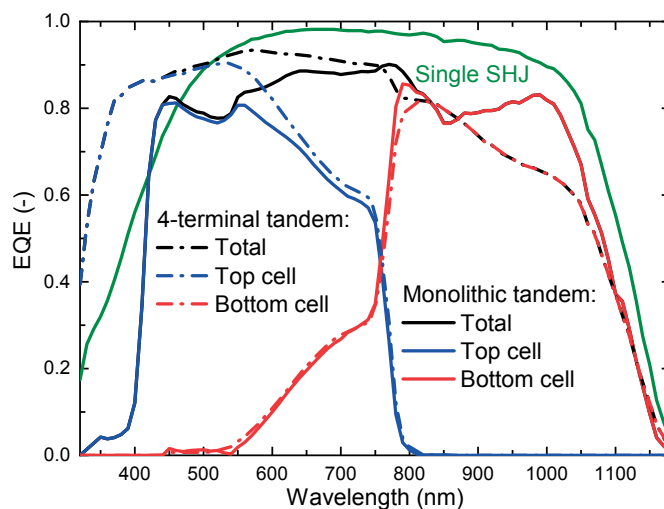
Figure 5.4 – Comparison of EQE spectra from the 25.2% mechanically stacked tandem, the 20.5% monolithic tandem with SST bottom cell, and a 22% single-junction SHJ cell, which was also used as bottom cell in the mechanically stacked tandem. These EQE measurements were conducted using an ARF. Reproduced with permission [76]. Copyright 2016, American Chemical Society.

we can directly compare the mechanically stacked and monolithic tandem cells in terms of their parasitic absorption and light management requirements. The so-far higher efficiency demonstrated with the mechanically stacked configuration is directly linked to better light trapping, no necessity for current matching, and a free choice in top cell illumination direction. In this context, in a monolithic tandem, the perovskite n-i-p top cell has to be illuminated through the spiro-OMeTAD layer, leading to severe parasitic absorption in the UV and visible spectrum. These losses become apparent from Figure 5.4, by comparing the spectral response in the <400 nm wavelength range of both tandem configurations. The mechanically stacked tandem shows excellent performance in this spectral region, even outperforming the SHJ single-junction cell, which itself suffers from parasitic absorption in the amorphous silicon layers.

Overall, the perovskite top cell in the mechanically-stacked configuration shows a 2.8 mA/cm^2 higher than that of the top cell in the monolithic tandem. By recovering about a third of these losses in the perovskite cell, the monolithic tandem would become current-limited by the bottom cell, even for a relatively thin perovskite cell. This clearly shows the necessity of moving to a larger top cell band gap for optimal monolithic tandem performance, which could be obtained by changing the standard MAPbI$_3$ composition for a mixed-cation/halide perovskite material, as discussed in Section 2.2.3.

The 4-terminal design of the mechanically stacked tandem, however, has a disadvantage: the presence of the additional transparent ITO contact in this configuration leads to a significant increase in parasitic absorption losses in the 850–1200 nm wavelength range due to free-carrier absorption [96]. As a result, the bottom cell current in the monolithic tandem, which requires only a very thin IZO intermediate recombination layer, is 1.2 mA/cm^2 higher. Further current gains in the bottom cell of monolithic tandems are expected by replacing IZO with a thin-film

silicon recombination layer, reducing the refractive index mismatch. This has been then demonstrated by Sahli *et al.* [86].

Interestingly, in the 550–800 nm spectral region, where free-carrier absorption in the transparent contacts is still negligibly small, the bottom cell current of both tandem configurations is nearly identical. This indicates that light transmission to the bottom cell is not affected by the absence or presence of a front-side texture in the wafer or whether the perovskite cell is separated from the SHJ cell by an optical coupling film or directly deposited on it.

The summed current of both subcells is 34.3 mA/cm^2 and 35.9 mA/cm^2 for the monolithic and mechanically stacked configuration, respectively, compared to 39.6 mA/cm^2 (without front-side metallization shadow losses) for the textured single-junction SHJ cell, which is used for the 4-terminal tandem measurements. This difference can partially be explained by parasitic absorption losses in the MoO$_x$ layer used in the tandem cell front electrode, which is induced by sputter damage during the TCO layer deposition. Such losses could be reduced by using the more resilient and transparent WO$_x$, as discussed in Section 3.3.1.

Reflection losses also contribute to the difference between tandem and SHJ single-junction EQE spectra. By replacing the rear-side textured wafer in the monolithic tandem with a double-side textured one, while keeping everything else unchanged, we could expect to gain $\approx$2.6 mA/cm^2, resulting in a summed current of >36.9 mA/cm^2. Such a double-side textured bottom cell requires the development of conformal perovskite cell deposition processes for highly textured substrates, which we discussed in Sections 2.3.2 and 3.2.3. This calculation however already shows that the parasitic absorption losses discussed above are more important than reflection losses for the monolithic tandem with single-side textured bottom cell and ARF. Considering the integration of monolithic tandems into glass-glass encapsulated
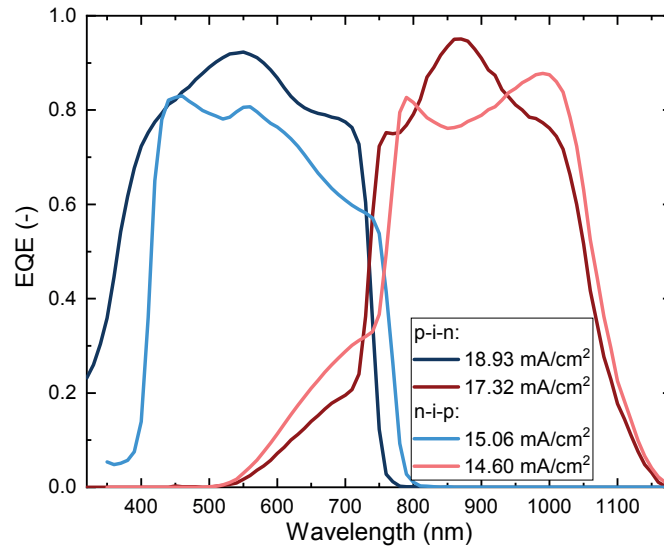
Figure 5.5 – EQE measurements of n-i-p and p-i-n monolithic tandem solar cells on DSP bottom cells. The layer stack of the n-i-p cell is: ARF/IZO/MoO$_x$/spiro-OMeTAD/MAPbI$_3$ perovskite/C$_{60}$/PEIE/ITO/SHJ bottom as published in [83]. The layer stack of the p-i-n cells is MgF$_2$/IZO/SnO$_2$/C$_{60}$/CsFAPbIBr perovskite/spiro-TTB/ITO/SHJ bottom.

modules, where the application of such an antireflective foil is expected to be less effective, the use of a double-side textured wafer would have a more pronounced effect on cell performance. As already introduced in Chapter 3, parasitic absorption losses can be reduced by using thin undoped evaporated charge transporting layers in the p-i-n cell configuration (see *e.g.* Figure 3.14). Figure 5.5 shows an experimental comparison of monolithic tandems on DSP wafers in either p-i-n or n-i-p configuration. These results show clearly the optical gains induced by inverting the device polarity, considering the charge transporting materials available. In p-i-n configuration, the current of the tandem cell was largely bottom limited, even if the top cell band gap was already blue-shifted compared to the absorber material used in the cell in n-i-p configuration. Using transfer matrix simulations, we can therefore now find optimization directions for a perovskite/silicon monolithic tandem in rear-emitter configuration with a p-i-n top cell. This includes a nc-Si:H tunnel junction [86] and a perovskite top cell with NiO_x as hole transporting layer and $C_{60}/SnO_2/IO:H$ as the front contact stack. In order to limit the complexity of the simulations presented here, all layers were considered to be flat (no surface roughness or texture). Complex refractive indices were either measured in-house or taken from literature [103, 212, 161, 213, 214, 215, 216]. The simulation results are shown in Figures 5.6 and 5.7.

The current of a monolithic tandem solar cell is limited by the subcell that generates the lowest current and the tandem voltage ideally is the sum of the subcells' voltages. Therefore, the optimal performance will be obtained when the top cell material is chosen such that it provides the highest voltage possible, while allowing the tandem cell to stay close to a current-matched situation [217]. Figure 5.7a illustrates a situation where the optical band gap of the top cell is increased without adjusting its thickness, leading quickly to a large current mismatch outside of the optimized region. Figure 5.7b shows the effect of varying the perovskite layer thickness
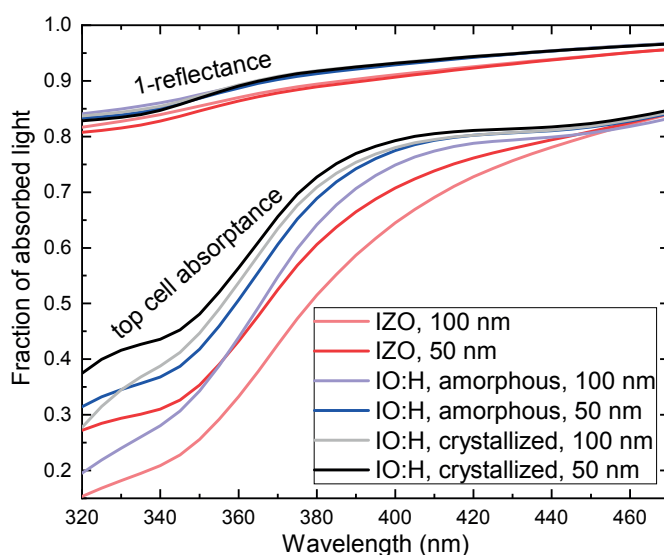
Figure 5.6 – Transfer matrix optical simulations of the top cell absorptance and reflectance in a flat monolithic tandem, showing the effect of the front TCO in the low-wavelengths spectral region. The cell is in p-i-n configuration as described in Reference [97]. Reproduced with permission [97]. Copyright 2018, American Chemical Society.

on the same tandem cell. As expected, this affects the top cell only for wavelengths $\lambda > 500$ nm, where the perovskite absorbs in the low-finesse thin-film interference regime [218]. Further research will therefore be necessary to develop thick perovskite layers (up to 1 μm) with still high optoelectronic quality. It is also evident from this data that, due to parasitic absorption losses and practical thickness constraints, the highest optical band gap which still allows for a current-matched situation is lower ($\approx$1.65-1.68 eV) compared to what would be expected from an ideal, loss-free, tandem cell ($\approx$1.75 eV) [219].

Parasitic absorption losses in a particular layer can be reduced by either tuning its material properties or by reducing its thickness. For the p-i-n perovskite cells described in Section 2.3.2, the C_{60} layer had a thickness of $\approx$20 nm. Figure 5.7c shows that in a monolithic tandem solar cell, reducing this thickness would drastically increase the spectral response of the top cell in the wavelength range <500 nm, which could translate to up to 1 mA/cm^2 gain in current in the perovskite cell. It was recently demonstrated that a C_{60} layer with thickness down to 1 nm is practically feasible without significant electrical losses [220].

A similar effect can be observed with the NiO_x layer, as shown in Figure 5.7d. However, thinning this layer increases the silicon bottom cell current, which seems to stem from a reduced reflection at the interfaces between the two subcells, as shown by the lowering of the reflection peak at around 800 nm.

Transparent conductive oxides (TCO) used for the front electrode and intermediate recombination layer are also a source of parasitic absorption. Figure 5.6 shows that proper choice and design of the front TCO can improve the response of the tandem in the full spectral range. Here, high-mobility TCOs were compared. Due to their already low free carrier absorption compared to more standard TCOs, the influence on the long wavelength range was minimal. However, their optical band gap and thicknesses influence the blue spectral response of the tandem. Optically, it is clearly beneficial to use a front TCO as thin as possible. This of course involves a trade-off with the electrical performance of the TCO electrode due to increased sheet resistance for thinner layers.

When a TCO is used as an intermediate recombination layer, lowering its charge carrier density to a minimum helps reduce parasitic absorption losses as well as internal reflection in the long wavelength range, as shown in Figure 5.7e. Changing the refractive index of this layer was found to have also an important effect on the interference pattern mainly in the bottom cell (Figure 5.7f). In the frame of these simulation conditions, a refractive index of 3 was found to be optimal, which is practically difficult to reach with the currently known contact materials. In the future, more complex optical structures could be considered to act as intermediate reflector for the photons with energies up to the perovskite absorption edge, with high transmittance for the photons in the silicon absorption window [221, 222].

In summary, optical simulations showed that the tandem optical performance should be improved by using fully textured bottom cells and conformal top cell coatings, which will enhance light trapping and minimize reflection losses. The top cell band gap should be adjusted to satisfy the current-matching requirement and maximise the voltage/current compromise. Finally, parasitic absorption losses should be minimised and can be controlled by a proper materials choice, deposition conditions, thickness and doping.
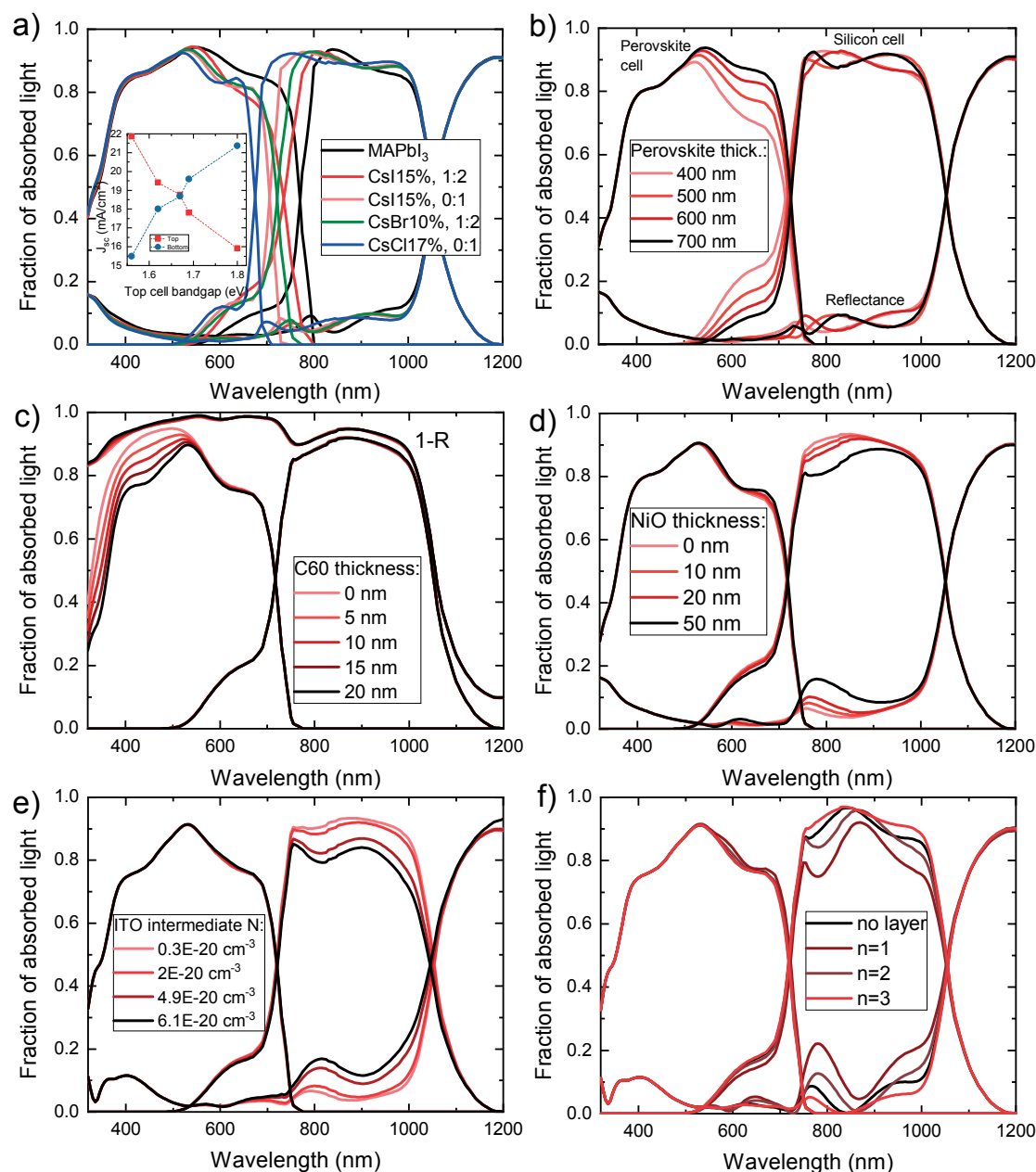
Figure 5.7 – Transfer-matrix modeling of perovskite/silicon heterojunction monolithic tandem solar cells with flat interfaces: a) Variation of the perovskite layer composition and band gap. The inset graph shows the simulated currents for the top and bottom cells when varying the top cell band gap without changing its thickness (580 nm); b) Perovskite absorber thickness variation with a CsBr10%-1:2 material; c) C_{60} thickness variation; d) NiO_x thickness variation; e) effect of varying the carrier concentration in the ITO layer between the silicon tunnel junction and the NiO_x; f) effect of varying the refractive index of a layer between the silicon tunnel junction and the NiO_x; The simulated tandem cell layer stack from back to front: Ag/a-Si:p/a-Si:i/c-Si/a-Si:i/a-Si:n/nc-Si:n/nc-Si:p/ITO/NiO_x/Perovskite/C_{60}/SnO_2/IO:H/MgF_2 (explained in more details in the Supplementary Information). Adapted with permission [97]. Copyright 2018, American Chemical Society.

5.4 Toward fully textured perovskite/silicon monolithic tandem solar cells

5.4.1 Statement of the problem

Absorber materials with indirect band gap, such as crystalline silicon, exhibit weak light absorption near their absorption edge. As a result, light trapping strategies have to be employed to increase the path length toward the theoretical limit given by the Yablonovitch formula of $4n^2$, with n being the refractive index of the absorber material. Texturing both interfaces of the silicon wafer is the most common strategy for crystalline silicon cells [223, 224]. From simulations and optical modelling, it is clear that a fully textured bottom cell would yield the highest current [212, 225], both by reduced reflection on the front surface (light can bounce several time on the surface, which increases its chance to enter the wafer) and by better light trapping of infrared light in the bottom cell. Also, the light path inside the wafer is extended due to the non-perpendicular entry from the pyramids faces, which increases the chances the light gets absorbed especially for photons with energies close to the band gap, normally weakly absorbed. A textured cell is therefore "optically thick" compared to a flat cell.

Figure 5.8 illustrates the problems encountered when a solution processed perovskite cell is deposited on a textured silicon substrate. The SEM cross-section images show that the perovskite absorber layer deposited by all-solution techniques, based on spin coating the precursor solution followed by an antisolvent dripping on the spinning substrate, is not conformal and tend to fill the valley of the pyramids and let their summit uncoated. Similar, the spin coated spiro-OMeTAD layer also does not cover the summit of the pyramids. This leads to a direct contact between the front TCO transparent electrode and the intermediate
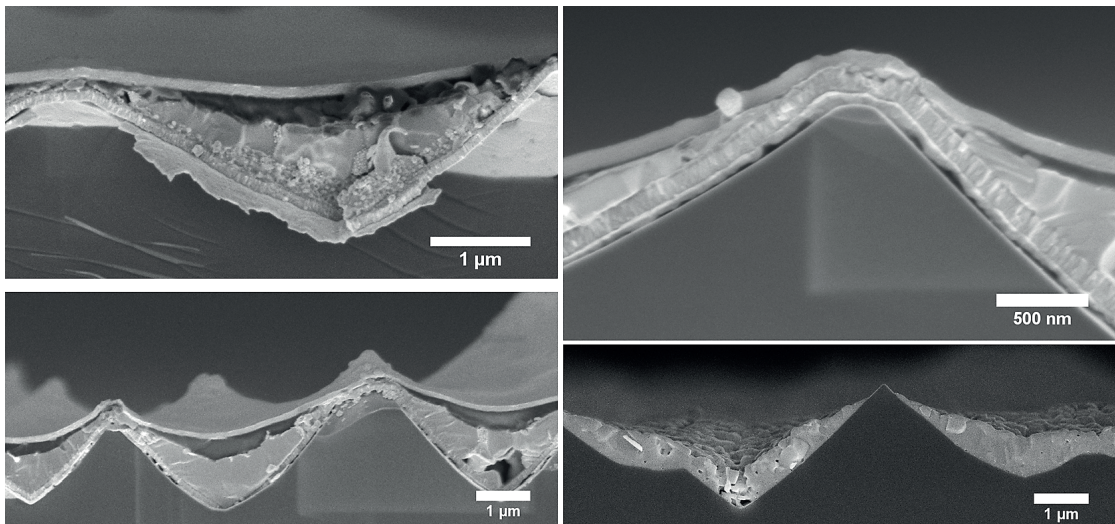
Figure 5.8 – Cross sectional SEM images of solution processed perovskite cells on textured silicon bottom cells, showing the non-conformality of the spin-coated layers, *i.e.* perovskite absorber layer, spiro-OMeTAD hole transporting layer and mp-TiO$_2$, and clear shunts by direct contact of front and intermediate TCO layers.

recombination layer, therefore shunting the top cell. Using solution processed perovskite and charge transporting layers on textured silicon wafers is therefore very challenging and would probably require the development of a new coating technique.

Note that atomically polished silicon wafers, as often used for perovskite/silicon monolithic tandem cells [83, 76, 82, 85], are rather expensive and would hinder the commercialization of this technology. However, the silicon industry has developed chemical processes to render a wafer sufficiently flat to become compatible with solution processed top cells. Therefore, the reason to use textured wafer is not so much industrial compatibility, but really better optical performance.

5.4.2 Buried planarization layer: LPCVD ZnO

A textured silicon cell is useful to reduce reflection losses and enhance light trapping of infrared light. But at the same time, solution processed perovskite cells require flat surfaces. An interesting solution to satisfy both of these constraints is to use a buried planarization layer on top of a double-side textured silicon bottom cell. Figure 5.9 gives a schematic of this configuration, which was simulated by Santbergen *et al.* [225]. From optical modelling results, they proposed that this layer should be highly transparent with low free-carrier absorption in the infrared, its thickness should be larger than the size of the pyramids in order to cover them fully (*i.e.* >10 μm), the refractive index should be around 2 and the conductivity can be kept low as no lateral conductivity is needed (nor desired). The simulations showed that a buried layer with these properties would allow an enhanced light absorption in the bottom cell as compared to a situation with a flat front surface.

The perfect candidate was therefore ZnO by LPCVD, as it was proven for thin-film silicon solar cells to be transparent, easily deposited in thick multi-micron layers, industrially deployable and up-scalable to square meters substrates [226, 227].
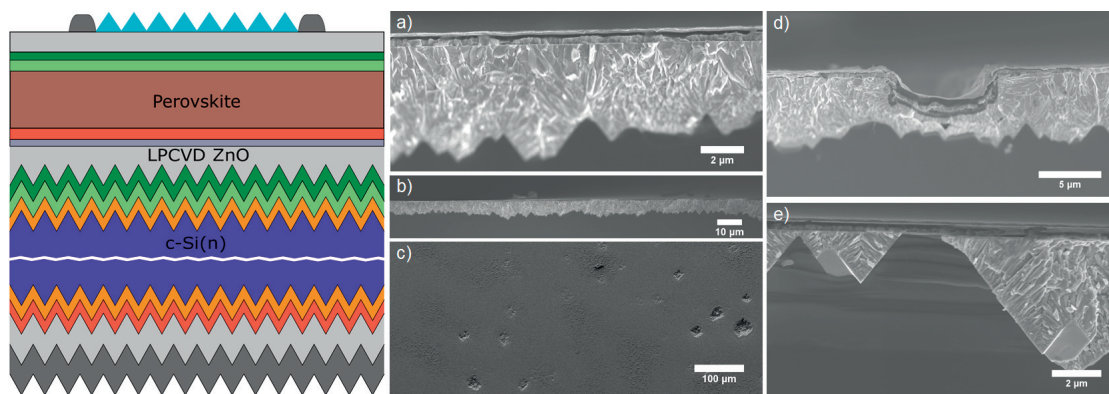
Figure 5.9 – Schematic layout of a monolithic tandem cell with buried planarization layer and flat top cell. a) & b) SEM images of textured silicon wafers planarized with a ZnO layer deposited by low-pressure chemical vapor deposition (LPCVD) and mechanical polishing. A full planar perovskite top cell can be seen on top of the ZnO layer. c) Surface defects due to the mechanical polishing, ripping off some ZnO regions. d) Cross-sectional view of such defect showing how the top cell tends to fill the hole and become shunted on the edges of the defect. e) Truncated silicon pyramid after a too long or too intense mechanical polishing.

5.4.2.1   ZnO and mechanical polishing

The idea consists of depositing a thick layer ($\approx$10-20 μm) of ZnO by LPCVD in order to entirely cover the pyramids of a silicon wafer. Then this layer can be mechanically polished with a chemical mechanical polishing (CMP) setup, which was custom built at EPFL/PV-Lab [228]. This technique was used to produce flat back reflectors for thin film silicon multijunction solar cells [229]. The perovskite top cell can finally be processed on the planarized surface similarly to flat glass substrates used for single-junction cells. The final device layout is schematically illustrated in Figure 5.9.

The ZnO layer deposition and CMP treatment are described in previous theses by Peter Cuony and Karin Söderström [228, 229]. The CMP step was taking about two hours per 2.5x2.5 cm^2 substrate. As shown in Figure 5.9a and b, the ZnO indeed covered entirely the silicon pyramids and the CMP method produced apparently flat surfaces on which a perovskite top cell could be deposited by solution processing techniques.

However, several important issues should be explained here. Due to the large thickness required for this application, often large amount of stress built up in the film, which often led to its delamination and pealing. Then, during the polishing, the slurry composition of silica particles and its concentration as well as the applied force had to be controlled carefully as their variation impacts the polishing rate. Particulates in the slurry solution were also ripping off some ZnO from the surface, creating holes in the planarization layer, as shown in Figure 5.9c. Figure 5.9d shows that such holes are catastrophic for the top cell formation. The duration of the polishing, the slurry concentration and the applied force dictates how much of the ZnO layer is polished. The ZnO thickness needed to be adapted to the size of the silicon pyramids and then the polishing time also adapted to avoid over-polishing the sample and destroying the SHJ bottom cell passivation layer by cutting the pyramids, as shown in Figure 5.9e with a truncated pyramid. As the thick ZnO layer was conductive, it had to be patterned in order to define the top cell active region. This constraint required one additional step: after the LPCVD and CMP processes, the active region was covered with a protective polymer layer (P70) and the ZnO on the remaining parts of the sample could be etched off in a HCl solution.

Finally, another important problem was the yield: at the end of the bottom cell preparation with the planarization layer, we had in average about 1 sample out of 10 initially that survived and that was seemingly ready for top cell deposition. And then this yield was often further reduced by the surface damages and holes shorting the top cell or truncated pyramids damaging the bottom cell. It was therefore extremely difficult to have a simply working tandem device. Although the initial idea seemed appealing and simple on its principle, it revealed itself tedious, time-consuming, and very difficult to reproduce. CMP was therefore not further considered.

5.4.2.2   Smooth ZnO recipe development and Ar plasma etching

Another method to obtain a planarization layer using LPCVD ZnO is to work on its deposition conditions. The idea here is to deposit a ZnO layer with already small and smooth features, no pyramids and relatively flat surface or with long waviness on silicon pyramids. The films
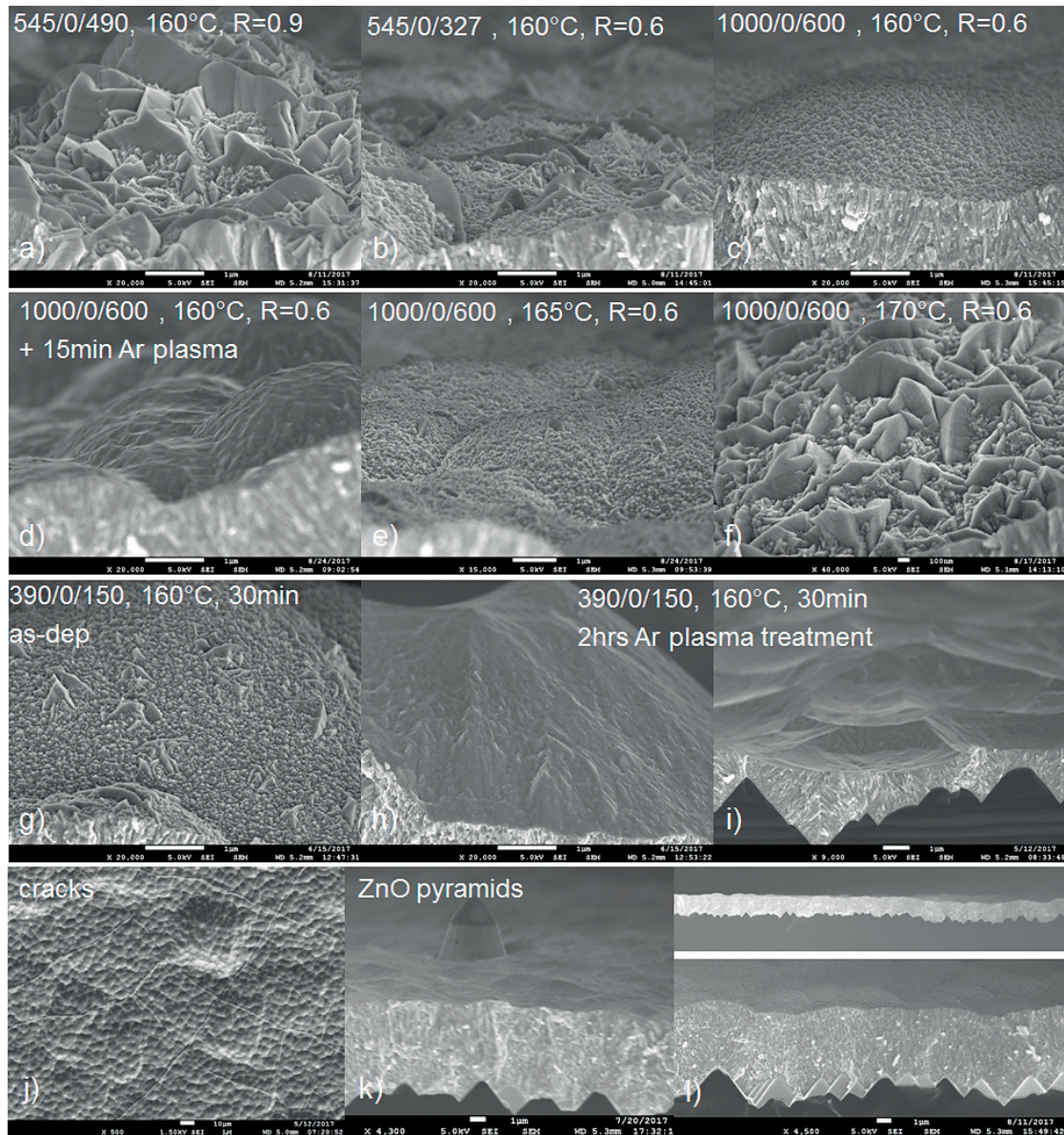
Figure 5.10 – SEM images of ZnO layer deposited by LPCVD. The deposition conditions are indicated in overlay on each image, with the DEZ/B_2H_6/H_2O flow rates (system's units), the deposition temperature and, if any, the post-treatment by Ar plasma.

should also be undoped to keep as high transparency as possible and an argon plasma post-treatment can be used to further smooth the remaining sharp surface features.

The deposition conditions of ZnO were largely studied in the past for thin-film silicon solar cells [230, 231, 232, 233, 229, 234, 235, 236]. Available parameters to be tuned include deposition temperature, water to diethyl zinc (DEZ) ratio, total gas flow rate, film thickness, substrate type and condition. Figure 5.10 shows SEM images of ZnO layers deposited on silicon wafers. If the water content is low compared to DEZ, the film tends to take a yellow color, losing its transparency. If in contrary the water content is too high, the ZnO grows with sharper and

larger pyramids. A good compromise was found with water/DEZ ratio around 0.6, as shown in Figure 5.10a and b. The remaining larger pyramids could be removed by increasing the total gas flow rates, as shown in Figure 5.10c and 15 minutes of Ar plasma were then enough to smooth the surface (Figure 5.10d). The deposition temperature had also an important role in the growth of pyramidal features. Figure 5.10e and f show that slightly increasing the temperature from 160°C by 5 to 10° was already sufficient to lose the conditions producing the small surface features. Lower temperatures led to stressed films, easily and rapidly cracking during the deposition or right after when the film was cooled down. The substrate choice was also important in the sense that controlling and knowing in advance the silicon pyramid size needed to adapt the thickness of the ZnO layer: the larger the pyramid size the thicker the ZnO layer must be. However, thicker films tend to crack and peal off more easily, especially with the developed smooth recipe giving the small surface features shown in Figure 5.10c. If the size of the pyramids was <3 μm, the ZnO can be grown, without cracking, thick enough to create an overlay that planarizes the textured silicon wafer, as shown in Figure 5.10l, however with still a remaining waviness. The silicon pyramid size was however found to be not all the time the same, with batch to batch variations between ≈2 μm and >10 μm height. This variation represents a serious difficulty for developing a reproducible ZnO recipe.

In conclusion, and similarly to the mechanical polishing method, the deposition of smooth planarizing ZnO layers was not so straightforward and the idea was put aside, in order to refocus our work force toward replacing all spin coated materials in the perovskite top cell with evaporated or sputtered materials, which are intrinsically conformal and compatible with textured surfaces, as shown in the next section.

5.4.3 >25% efficient fully textured monolithic tandem solar cells *

Fabricating monolithic tandem cells with textured silicon bottom cells requires a conformal deposition of the perovskite absorber. As shown in Figure 5.11a-e, a perovskite layer can be conformal on pyramids when deposited with the developed hybrid sequential method (as described in Chapter 2). The layers in this Figure were fabricated with CsI-PbI$_2$ as evaporated precursor, ITO as recombination layer and spiro-TTB as hole transporting layer. It can easily be observed that these perovskite layers contain many voids, cavities and defects, as well as a large roughness. Also when finishing the devices with a transparent electrode as described in Section 3.2.3, the V_{oc} was very low, around 680-700 mV which corresponds approximatively to a filtered silicon bottom cell (see Figure 5.12a-b) and indicates that the perovskite cell was mostly shunted. The reason for this behaviour was found by analysing a tandem cell in a TEM. Figure 5.12c-e shows STEM EDX images of textured tandem, with carbon indicated in red. Several important observations could be made from these measurements: 1) The perovskite layer was rough and non-continuous, with voids; 2) the C$_{60}$ layer could therefore penetrate in the perovskite layer and contact paths between the grains to the opposite contact, shunting the cell; 3) the spiro-TTB layer was found to be absent from most of the surface of the pyramids and to accumulate at their bottom, as shown in Figure 5.12e. We believe the spiro-TTB layer is dewetting during the annealing step necessary to form the perovskite absorber. This was

confirmed by a complementary experiment, shown in annexed Figure 5.13. These SEM top view images show that spiro-TTB is perfectly conformal on the ITO-coated silicon pyramids after evaporation, but dewets from the pyramid faces to slide in the valleys during annealing at 150°C. This obviously leaves most of the surface uncovered with the hole transporting layer of the top cell and was certainly the main responsible for the bad device performance shown in Figure 5.12a. Interestingly, this effect of dewetting was not problematic on flat devices, using the same layer stack and process sequence, as shown *e.g.* by the EQE measurement of a DSP p-i-n tandem cell in Figure 5.5 which had 20.5% efficiency.

Several changes had therefore to be made. We further developed our perovskite deposition method and, as discussed in Chapter 2, different Cs-containing precursors were investigated. CsBr was found to be the most promising and yield the most conformal and compact perovskite layer, without any apparent voids or pin-holes (see Section 2.2.3). The top cell band gap was also adjusted to around 1.6 eV in order to have high current in the top cell and approach the >20 mA/cm^2 current in the bottom cell already measured in Figure 5.12b. However, the main change was to replace the ITO recombination layer with a nc-Si:H recombination junction. This junction was developed in 2017 by Florent Sahli *et al.* [86] and showed high promises already on flat tandem devices, by increasing the device shunt resistance thanks to its low lateral conductivity. On textured wafers this silicon junction had the additional advantage that, on this material, spiro-TTB was not dewetting and stayed conformal after perovskite annealing. Also, the perovskite layer itself was found to become more compact and with lower roughness. Further development of the absorber layer could then be carried out, mainly by increasing its thickness, adapting the organo-halide solution concentration, the annealing conditions and optimizing its band gap for best current-matching conditions. These developments on the perovskite absorber layer were mostly carried out by Florent Sahli and are discussed with more details in reference [98].
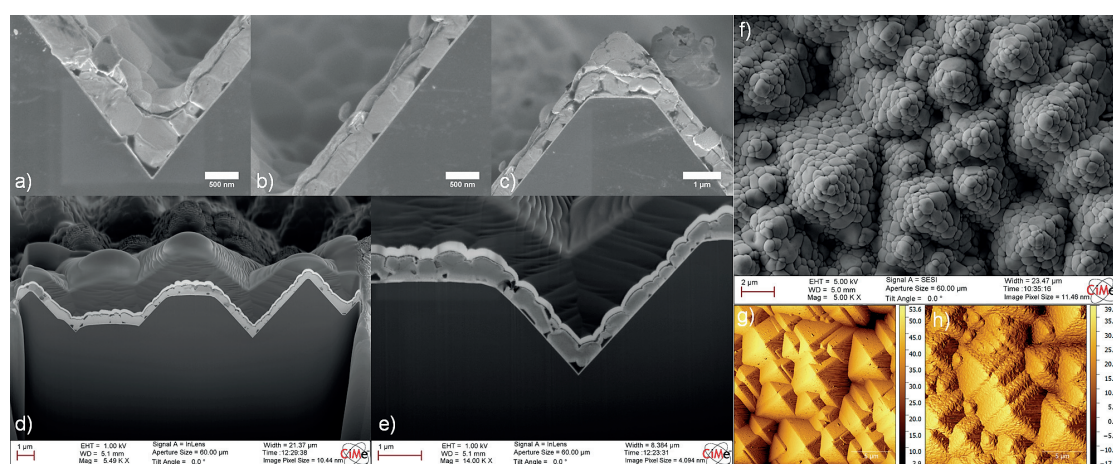
Figure 5.11 – a-c) Cross sectional SEM images of perovskite-silicon tandem on textured wafers; d-e) Focused ion beam (FIB) cross sectional images of textured monolithic tandems; f) SEM and h) AFM top view images of a perovskite-coated textured silicon wafers showing the grain morphology, as comparison to a bare silicon wafer in g). The perovskite absorber composition is CsFAPbIBr, here with CsI-15% precursor.
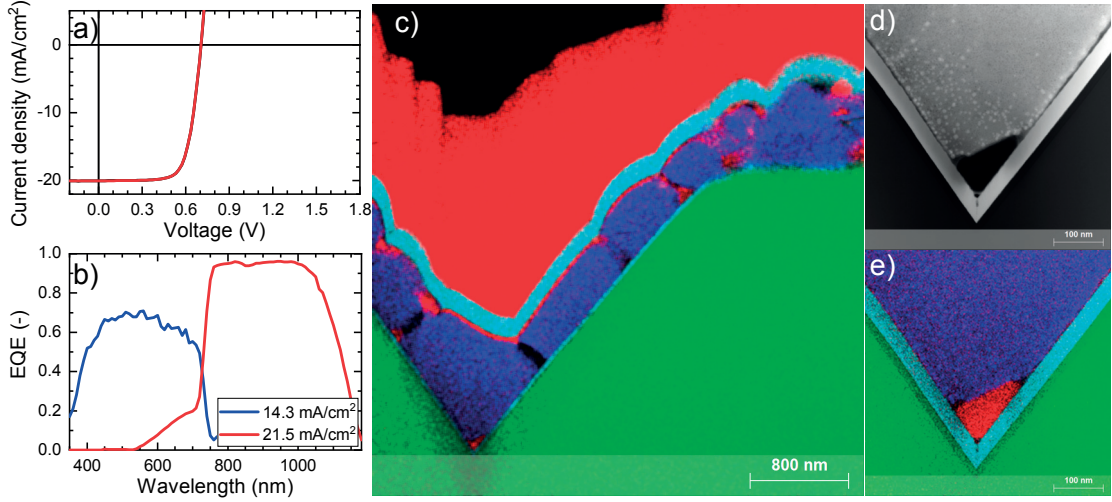
Figure 5.12 – a) *J-V* and b) EQE measurements of a textured monolithic tandem using ITO as recombination layer and thermally evaporated spiro-TTB as hole transporting layer in the p-i-n CsFAPbIBr perovskite top cell; c) STEM EDX analysis of the tandem measured in a), showing the dewetting of spiro-TTB from the silicon pyramids. The spiro-TTB was found to accumulate in the valley of the pyramids as shown with a STEM high-angle annular dark-field image in d) and a STEM EDX image in e). Si is shown in green, C in red, Pb in blue and In in cyan.

Following the implementation of an optimized perovskite absorber, an effective silicon recombination layer and improved charge transporting layers and electrode, a fully textured perovskite/silicon tandem solar cell could be fabricated with record efficiency of 25.24% under maximum power point tracking, independently certified by Fraunhofer ISE CalLab [98]. The main EQE and *J-V* characterization results are shown in Figure 5.14. Our in-house *J-V* measurements showed a reverse scan efficiency of up to 26.0% with V_{oc} of 1778 mV, *FF* of
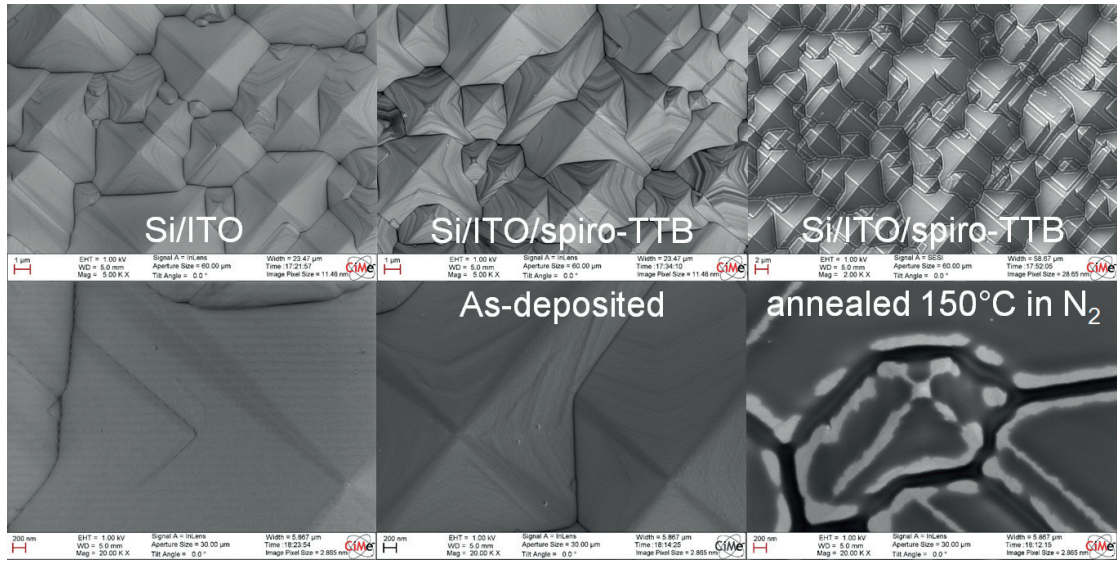
Figure 5.13 – SEM top view images showing the dewetting of spiro-TTB on ITO-coated textured Si wafers after annealing at 150°C.

74.8% and J_{sc} of 19.6 mA/cm^2 [98]. This new record represents an absolute increase of 1.6% on the previous perovskite/silicon monolithic tandem record [85], >3% increase compared to PV-lab SHJ baseline silicon cells, and similar performance as the state-of-the-art double side
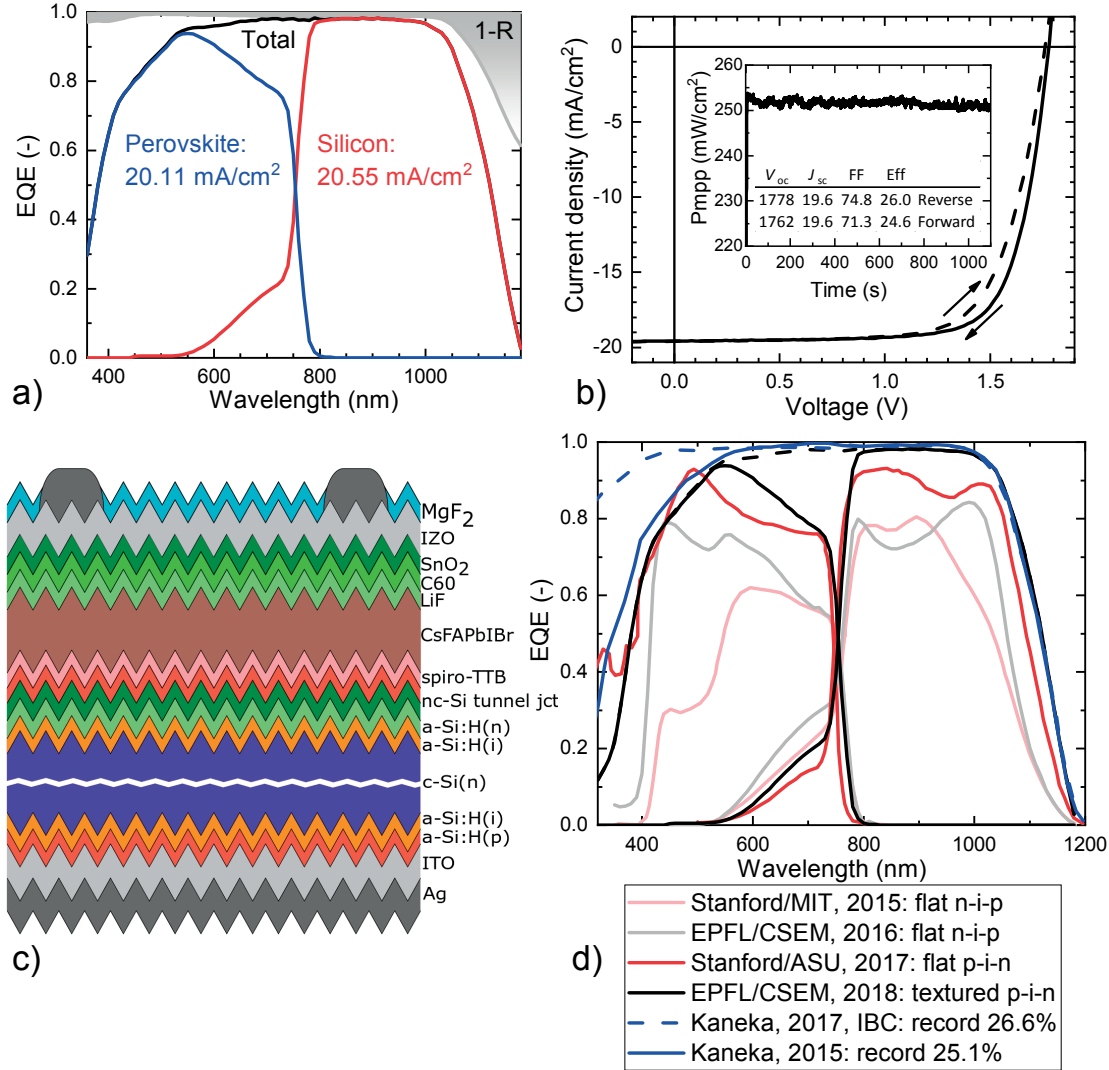
Figure 5.14 – a) EQE and b) *J-V* measurements of the record textured monolithic tandem solar cell. The inset in b) shows the maximum power point tracking of the cell for >1000 seconds and a table summarizing the *J-V* parameters in both scan directions (in-house measurements); c) schematic illustration of the textured monolithic tandem; d) EQE measurements comparing the four monolithic tandem cells holding or that held the record efficiency and the EQE of the best single junction SHJ cells from Kaneka with 26.6% and 25.1% efficiencies, respectively for back-contacted and top/rear contacted configurations. The data was extracted from references [6, 237, 98, 85, 83, 81]. This record device is the product of a close collaboration between Florent Sahli (FS) and the author of this thesis (JW). FS developed the silicon recombination junction and adapted it to the textured wafers. JW discovered the problem of dewetting of spiro-TTB (as shown in Figures 5.12 and 5.13), which was then solved by FS with the silicon junction. FS worked on the perovskite absorber growth on textured substrates, including the optimization of the PbI$_2$ thickness and organo-halide solution concentration. JW (together with Brett Kamino) developed the electron contact, including the transparent electrode (see Figure 3.4). JW and FS processed and characterized together the device batch including the record tandem cell.

contacted SHJ cells from Kaneka with 25.1% efficiency [237, 20].

Figure 5.14d shows the evolution of perovskite/silicon monolithic tandem solar cells in four years, passing from flat n-i-p device using high temperature processed mesoporous perovskite top cells [81], to flat low-temperature n-i-p planar perovskite cells [83] and then to the inverted polarity p-i-n but still on flat front surfaces [85], and finally on fully textured silicon wafers [98] (presented here). This comparative Figure shows clearly that a significant part of the efficiency evolution from 13.7% in 2015 [81] up to 25.2% in 2018 [98] is due to a better light management and increased current. When comparing the textured tandem cell to the best silicon single junction back-contacted cell from Kaneka with record efficiency of 26.6%, it becomes clear that the tandem cell is close to the optimum in the long wavelengths >700 nm, where both EQE curves overlap. In the short wavelengths <700 nm, the interdigitated back-contacted silicon cell has the advantage of lower parasitic absorption at the front, as it does not use any TCO or absorbing charge transporting layer such as used in the tandem cell. Comparing the back-contacted record cell to the record SHJ cell with top/rear contacts shows clearly this effect in the short wavelengths (see Figure 5.14d), significantly reducing the difference with our tandem cell. The difference in total current calculated from the difference of the back-contacted Kaneka EQE and our textured tandem total EQE curves amounts to 2.1 mA/cm^2, from which 1.92 mA/cm^2 is in the <700 nm spectral region. This difference is reduced to 0.97 mA/cm^2 when comparing to the top/rear contacted Kaneka cell. This current loss in the tandem cell could with further optimization still be lowered, mainly by thinning down the electron transporting layer and by using a more transparent TCO such as IZrO. Then, the current obtained from the J-V measurements could still be improved by replacing the evaporated silver metallization by a screen printed grid, using thinner fingers, and thus with reduced shadowing.

Therefore, it is safe to say that a textured tandem cell is close to an optimal optical system and further performance improvements should rather be expected from increased FF and V_{oc}. The holy grail, 30% efficiency, is therefore now practically possible: V_{oc} of 1875 mV, J_{sc} of 20 mA/cm^2 and FF of 80%. These values were individually already demonstrated: V_{oc} >1.2 V was shown for perovskite materials with similar band gap around 1.6 eV [238] but deposited by an all-solution processed method; the previous two record monolithic tandem devices already had FF of ≈79% [83, 85]; a J_{sc} of 20 mA/cm^2 is already demonstrated here with EQE measurements (Figure 5.14) and is within reach in J-V measurements.

5.4.4 Reflection, scattering and angular dependence

Figure 5.16f shows a comparison of reflectance spectra for monolithic tandems and a typical silicon heterojunction single junction cell. It is evident that devices with a flat front surface dramatically suffer from strong reflection losses with peaks up to 30% throughout the entire spectrum. These interference peaks can be lowered to around 10% when incorporating a microtextured antireflection foil. However, Figure 5.16f also shows that the best strategy to reduce reflection losses is to use silicon bottom cell with random pyramid textured front and back surfaces. The reflectance of a textured monolithic tandem is then even lower than the

reflection from a SHJ cell in the low-wavelengths (<500 nm) spectral region as well as in the near-infrared region (900-1100 nm). This can be attributed to the double antireflection coating effect provided by the IZO/MgF$_2$ front stack, and also to a large extent to the entire perovskite cell acting as a multiple layer antireflection stack for the silicon wafer.

This low reflectance is also explained by a close-to-ideal Lambertian scattering system, as shown in Figure 5.16b. The angular dependence of optoelectronic properties of the tandem device can then also be studied with angular dependent EQE measurements (see Figure 5.16c-e). During field operation, the light incidence angle changes constantly during the day and over the year, impacting the energy yield. These measurements suggest that, compared to tandem cells with flat front side, textured tandem devices should perform better in a photovoltaic system without active tracking. Interestingly, as shown in Figure 5.15, our experimental data correlates well with the simulation results published by Hörantner *et al.* [239], who concluded that, at high incidence angles, tandem cells would perform better than single SHJ cells. However, such specific implications for energy yield calculations should be taken with precaution and ideally also include the effect of an encapsulant and the glass cover present in a real module, which could be itself textured.

Overall, the reflection losses in a textured perovskite/silicon monolithic tandem cell can still be marginally reduced, most likely by better tuning the thicknesses in the front electrode stack. Parasitic absorption losses are however clearly more critical and have a far greater potential for improvement.

5.5   Light soaking stability test *

Stability has been a serious concern since the very beginning of the perovskite cell development. In the early 90s, Mitzi *et al.* did not pursue his work on perovskite materials for
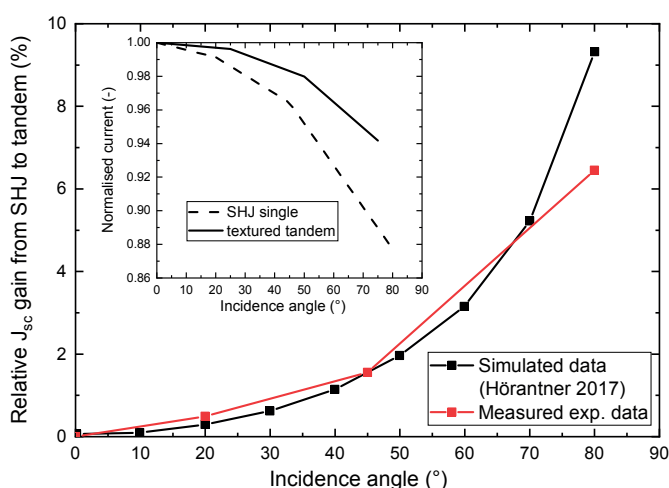
Figure 5.15 – Angular dependence of current generation: relative difference between a textured tandem cell and a SHJ single cell. The graph compares experimentally measured data on textured tandem cells similar to the record device and the simulation data published by Hörantner *et al.* [239].
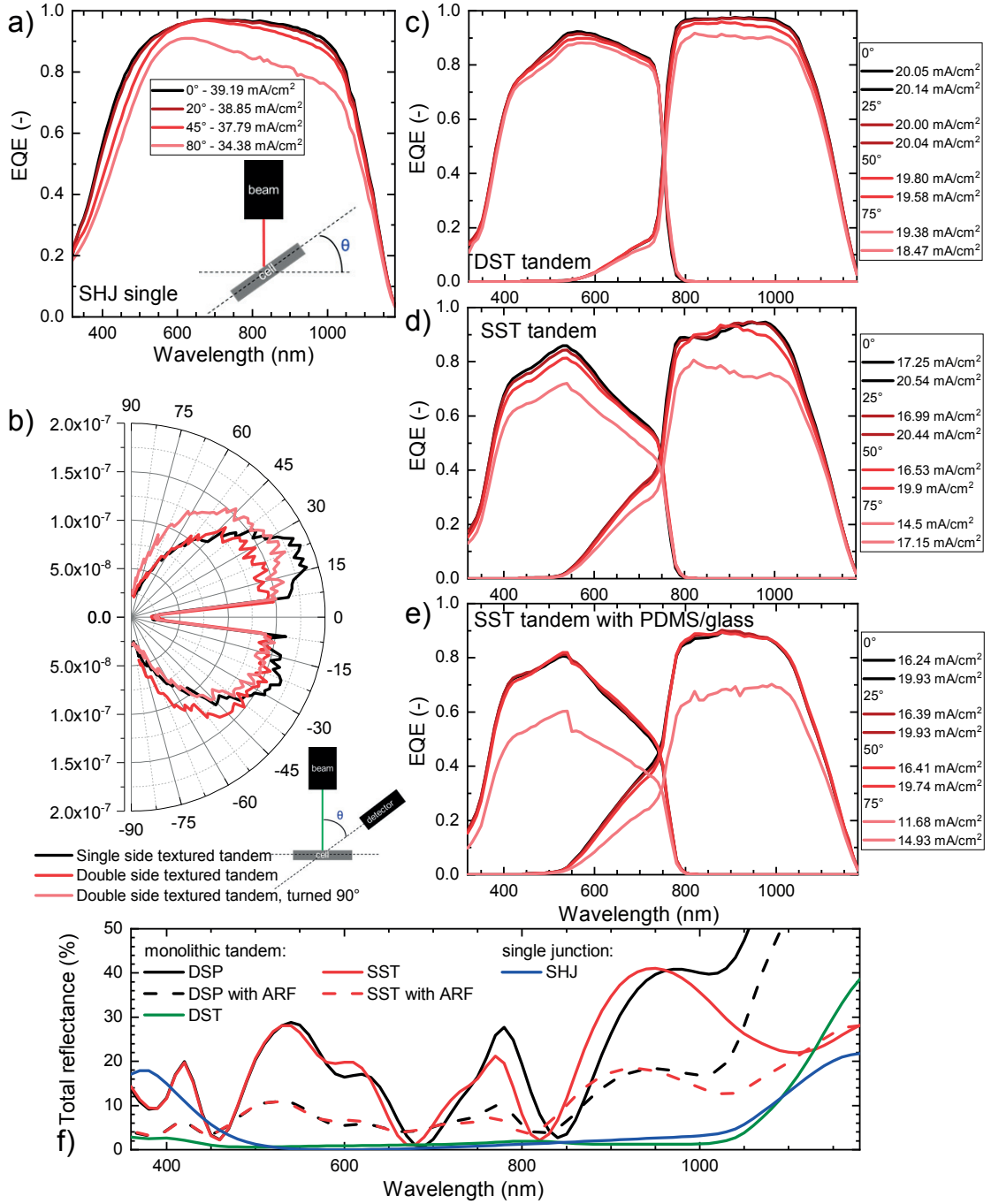
Figure 5.16 – Angular dependency of EQE measurements on a) single junction silicon SHJ cell and c)-e) monolithic tandem cells; b) angular resolved scattering of textured and flat tandems; f) comparison of reflectance measurements for double-side polished (DSP), single-side textured (SST) or double-side textured (DST) tandems, with or without microtextured antireflective foil.

photovoltaics exactly because of their poor stability [62]. Later on, the first solar cells with a perovskite absorber were stable for only a couple of minutes, at the time mainly because of the use of a liquid electrolyte [63]. However, in the last five years, tremendous progress
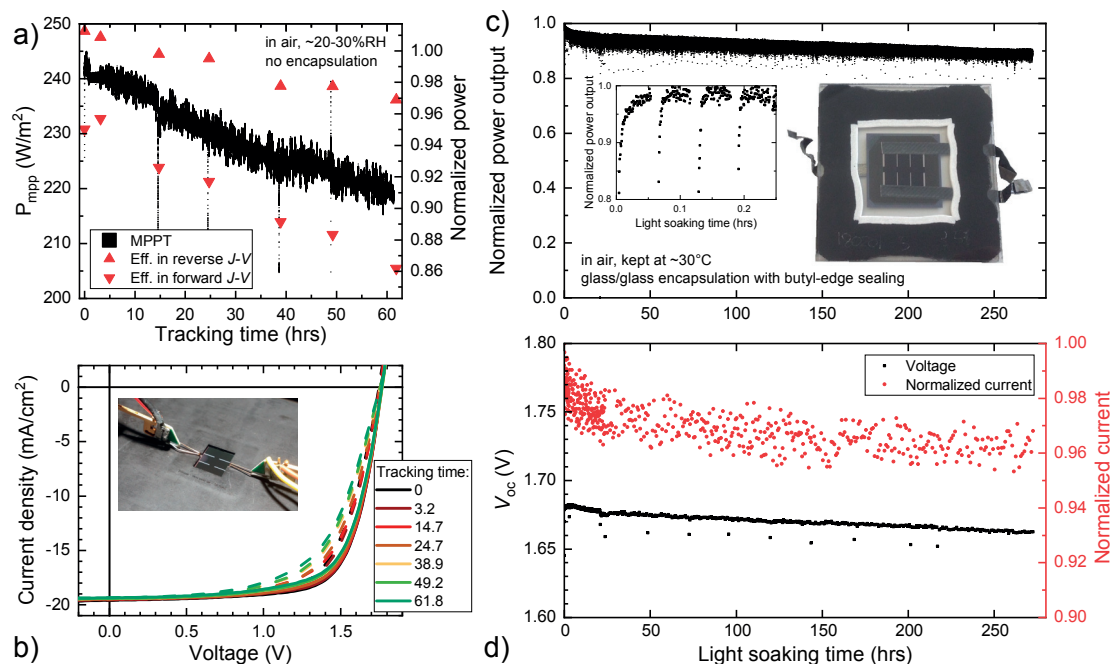
Figure 5.17 – Light soaking stability tests: a) textured monolithic tandem cell measured under maximum power point tracking in air without encapsulation, kept at 25°C, with regular *J-V* loop scans; b) the corresponding *J-V* curves at various moments during the experiment. The inset picture shows the cell and probes during the test; c) encapsulated textured monolithic tandem cell measured under maximum power point tracking for 270 hours in air and kept at 30°C; d) the corresponding *J-V* reverse scan parameters regularly measured during the experiment. Only the normalized current is given here as the cell was measured without mask and illumination intensity was not accurately known and controlled at the time of the experiment. The sourcemeter setup used to record the electrical parameters is described in Appendix C.

was achieved and more and more research groups have shown hundreds to thousands of hours of reliability data according to standardized degradation protocols. For market entry, perovskite/silicon tandem cells will have to pass reliability protocols according to the International Electrotechnical Commission (IEC) standards, including damp heat at 85°C/85% relative humidity, thermal cycling, and extended light soaking tests at 1 sun illumination. It should be noted that IEC tests only provide an indication of the chance of products to survive in the field. However, as long as the exact degradation mechanisms and the activation energies of theses mechanisms are neither known nor understood, it cannot be assumed that IEC tests are sufficient.

So far, in the literature, only single junction perovskite cells were tested for stability, including damp heat test for 1000 hours [85] and light soaking under different atmosphere [240].

We believe that tandem cells will have their own degradation mechanisms and therefore their stability might not be directly extrapolated from single junction cells data. We therefore tested directly the textured monolithic tandem cells under light soaking. In a first experiment, a non-encapsulated tandem device was measured under maximum power point tracking in air with 1 sun illumination intensity and without any UV blocking filters. As shown in Figure 5.17, the test lasted for 61 hours with regular *J-V* loop scans to record the evolution of all electrical

parameters. The cell had an initial efficiency of about 24%, which remained stable for about 6 hours. Then, the power linearly decreased to end up around 22% ($\approx$90% of initial power) after 61 hours. The hysteresis was found to increase during the experiment mostly due to a *FF* decreasing slightly more rapidly in the forward direction compared to the reverse. The exact interpretation of this phenomenon and its origin are still under discussion.

In a second phase, a monolithic tandem cell was encapsulated with a simple glass/glass scheme, including a butyl-edge sealant but no polymer lamination. The cell was placed in a class AAA light soaking chamber under $\approx$0.7 sun illumination intensity and 30°C constant temperature. The cell was kept at maximum power point with an in-house made Arduino-based sourcemeter (described in Appendix C). The setup was programmed to also regularly measure *J-V* scans in reverse direction, in order to precisely track the evolution of the main electrical parameters. As shown in Figure 5.17c, the power exponentially decayed during the first 20 hours and then linearly decreased to end up at $\approx$90% of its initial value after 270 hours. Figure 5.17 shows that J_{sc} follows the same trend with a clear exponential decay followed by a linear decrease to finish with 4% loss. The V_{oc} however first increased in the first few hours before also decreasing and losing about 20 mV after 270 hours. The cell has not seen any sudden failure but rather a constant decay without apparent stabilization. Further tests are currently ongoing to understand the reason for this decay. After this degradation period, the encapsulated cell was opened and brought in a FIB for cross-section imaging. It revealed that the evaporated silver metallization seemed to be unstable and migrating out through the MgF$_2$ layer. AgI was also found on the rear side metallization (apparent as black marks on the silver pad). This can be an indication that some iodine was leaving the perovskite absorber during the test.

A follow-up test was therefore started to compare evaporated to screen-printed Ag, and this time at 1 sun irradiation and 50°C. The test is ongoing at the time of writing this thesis. The encapsulation scheme will also be improved in collaboration with CSEM to include a polymer encapsulant that should offer a better protection to the cell from moisture ingress and UV light. Further experiments comparing tandem and single junction cells with same layer stack and composition should also help at understanding differences rising specifically from the tandem integration.

5.6   Large area textured tandems *

Most single junction perovskite solar cells, including the devices with record efficiencies [29], have been demonstrated on small active areas of typically <0.3 cm^2. A first up-scaling step for perovskite cells to 1 cm^2 area already necessitates dedicated work to carefully control film uniformity and reduce pinhole density. Chen *et al.* demonstrated one of the first 1 cm^2 perovskite solar cell with certified efficiency of 15% using a planar architecture [241]. They showed that by using a heavily doped NiMgLiO inorganic hole transporting layer with only 10–20 nm thickness, the shunt resistance of larger cells can be greatly reduced. This may be attributed to a lower pinhole density and fewer structural defects over the full device area.

For mesoporous cells, improving the perovskite layer quality was found to be the key for high efficiencies on larger cell areas. Li *et al.* developed a vacuum-assisted solution process to fabricate smooth and uniform perovskite layers [242]. They could demonstrate 20.5% efficiency (19.6% certified), with high uniformity of current generation over the 1 cm^2 cell area. Tan *et al.* recently also improved low temperature planar perovskite cells, filling the performance gap with the high-temperature mesoporous cells by showing 20.3% efficiency on 1 cm^2 area (19.5% certified) [243]. Here, reducing interface recombination on the TiO$_2$ layer was reached by chlorination. This low-temperature method is particularly interesting for tandem applications. Further up-scaling requires different approaches, depending on the application. A perovskite single-junction or top cell for a 4-terminal tandem with silicon bottom cell will be fabricated in the form of a thin-film module made by monolithically inter-connected segments. Laser-scribing techniques have recently been adapted for segment definition and interconnection in perovskite modules, leading to a rapid decrease in dead area, boosting aperture area efficiency [244, 245, 246].

The development of monolithic 2-terminal tandems so far mostly focused on aperture areas between 0.16 and 1.4 cm^2 [81, 82, 83, 76, 85]. Up-scaling of this tandem configuration to an industrial level requires different adaptations as compared to single-junction perovskite cells or 4-terminal tandems. This is mostly because 2-terminal tandem modules consist of wafer-size cells placed next to each other and interconnected by metal ribbons, and not of a single module-size substrate with interconnected segments. As a result, cell up-scaling is limited to the current industrial silicon cell size of 6 inches. However, additional requirements exist due to cost constraints, as the use of mechanically polished wafers, typically used for most monolithic perovskite/silicon tandem cells so far, is not an option. Scalable fabrication techniques that enable processing the perovskite top cell on fully textured wafers typically used in industry are thus required, such as sputtering, plasma-enhanced or low-pressure chemical vapour deposition, electrodeposition, or thermal evaporation, which was so far less relevant for the silicon photovoltaic industry but used, *e.g.* for organic light emitting diode manufacturing. In addition, to enable the integration of the technology in a silicon photovoltaic production line, a high throughput ($\approx$1 wafer per 1.5 s) and high yield ($\approx$98%) have to be targeted.

Low-temperature planar perovskite cells currently seem to be the most suitable option for 2-terminal tandem up-scaling, as they are compatible with silicon heterojunction bottom cells and can readily be made in either polarity, making them suitable for both n- and p-type silicon bottom cell technologies [82, 83]. For this device architecture, the perovskite layer can be deposited by thermal coevaporation of the precursors [247, 248], *e.g.* PbI$_2$, PbBr, CsI, MAI, FAI, or FABr. This approach is however still challenging, due to the difficulty of controlling accurately the evaporation rates of materials with significantly different volatility. A two-step interdiffusion technique, as developed during this thesis, might have advantages considering the integration in an in-line process, because the complex perovskite material formation can be separated in dedicated process steps: the lead halide compound can be thermally evaporated and then converted to the perovskite material by reaction with the organohalide precursors in the gas phase, using a chemical vapor deposition method [249, 146, 41]. Finally,
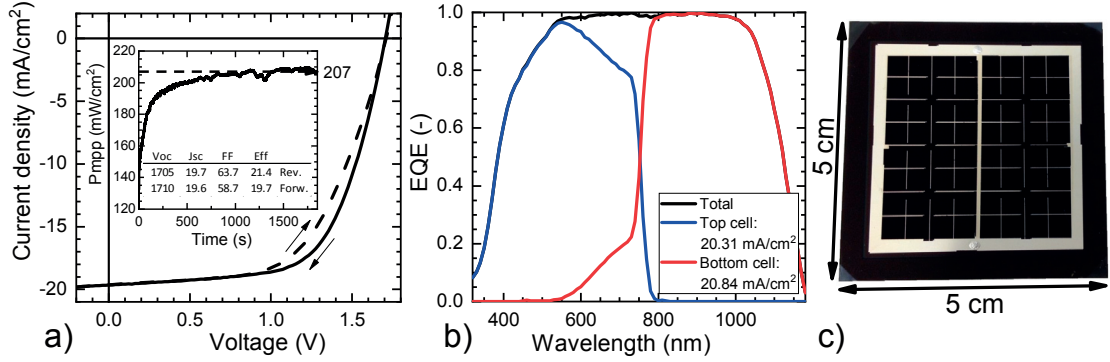
Figure 5.18 – a) *J-V* curves of a large textured perovskite/silicon monolithic tandem solar cells with 12.96 cm^2 aperture area. The inset shows the maximum power point tracking of the cell for >1800 seconds. b) EQE measurements of the large tandem cell, between the metal grid. A picture of the cell is shown in c) with the dimension indicating the size of the sample.

series resistance losses in monolithic tandems might be less challenging to mitigate compared to a single-junction thin-film module. The front contact can be made of a TCO and metallization, ultimately by screen printing with a low-temperature silver paste or electroplating as used in silicon heterojunction solar cells [250]. Internal interfacial resistances are here a major challenge, which requires further intense research.

The first academic larger sized monolithic tandem was demonstrated at EPFL/PV-lab by Sahli *et al.* [86], with 18% efficiency for 12.9 cm^2 aperture area. This was made with a n-i-p perovskite top cell and SST SHJ bottom cell.

Since then we could further improve the monolithic tandem solar cells performance with the introduction of textured rear emitter cells and Figure 5.18 shows a first demonstration of >20% efficient large area (12.9 cm^2) perovskite/silicon monolithic tandem. The cell was deposited on a 5x5 cm^2 silicon wafer with similar composition and device structure as the one used in Figure 5.14. As explained before, all layers were deposited by PECVD (for the silicon passivation layers), by sputtering (for the TCO and rear Ag), by thermal evaporation (for organic charge transporting layers and perovskite precursor) or by ALD (for the SnO$_2$ buffer). The only step that required a slight adaptation to the larger substrate size was the remaining spin coating step for the organo-halide solution, for which a pipette tip with larger opening was used in order to have a better coverage of the substrate as shown in Figure B.4.

As compared to the >25% record device, Figure 5.18a shows that J_{sc} was slightly lower due to larger shadowing from the metallization and that *FF* was the main limiting factor for the device performance. A direct improvement of *FF* will be possible by replacing the thermally evaporated Ag grid by a screen printed one, offering largely enhanced conductivity in the fingers, which can be made also thinner to reduce their impact on the current by shadowing. This will be further investigated by CSEM. Increasing the *FF* of this large cell from 65% to 75%, as demonstrated on 1.4 cm^2 area record cells, would directly improve its performance to >25% while keeping the other *J-V* parameters obtained in the reverse scan identical. This result is therefore very promising and shows that the processes demonstrated in this thesis are indeed up-scalable and >25% large area tandem cells are finally within reach.

5.7 Beyond tandems: perovskite/perovskite/silicon triple junction

High efficiency multijunction solar cells with over 2 subcells were so far only demonstrated with III-V materials [251, 252]. However, due to their high costs of fabrication, they can be used only in power generators for space satellites and terrestrial high-concentration systems. Thin-film silicon-based triple and quadruple junction solar cells were also demonstrated for low-cost applications but their efficiency remains modest and not competitive with single-junction cells [227, 253]. For non-concentrated light irradiation and triple junction cells, the record efficiency is held by Sharp with an InGaP/GaAs/InGaAs cell showing 37.9% efficiency. For Si-based multijunction solar cells, Fraunhofer ISE has made 2-terminal triple junction cells either by wafer bonding, with a GaInP/GaAs//Si showing 33.3% efficiency [254], or by monolithic growth, with a GaInP/GaAs/Si showing 19.7% efficiency. All-silicon triple junction cells can be made from amorphous and nanocrystalline thin-film silicon layers, a-Si/nc-Si/nc-Si, and the record stabilized efficiency tops at 14.0% [251].

Here, we present a perovskite-based triple junction solar cell, using a textured silicon hetero-junction bottom cell. The top and middle perovskite subcells were fabricated with the same process sequence as for the record tandem cell presented in the previous section. Figure 5.20a shows the schematic of the device layer stack. In this very first trial, the middle cell band gap was set around 1.55 eV by using 9% CsBr during the coevaporation with PbI_2 and pure FAI for the organo-halide spin coated solution. The top cell band gap was around 1.78 eV by increasing slightly the CsBr rate to about 16% and using pure FABr in solution. Also, the thickness of the top cell was slightly reduced to 250 nm of PbI_2 compared to 450 nm for the middle cell. Finally, the annealing temperature for the perovskite formation was 130°C for the top cell and 150°C for the middle cell.

Figure 5.20b and c show SEM and FIB cross-section images, respectively, of a triple junction cell. The middle and top cells are clearly visible, separated with the IZO recombination layer. All layers were conformal and both perovskite layers were compact without apparent pin-
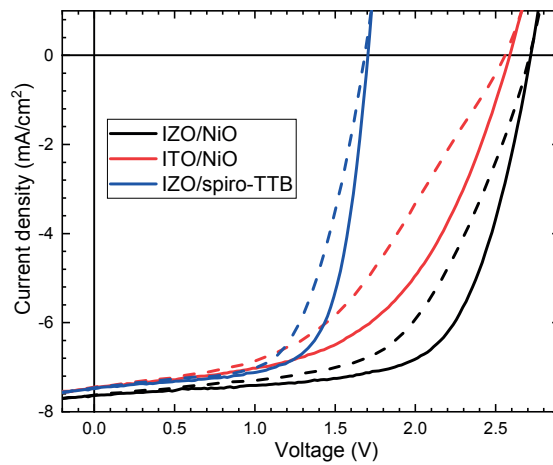
Figure 5.19 – *J-V* curves of triple junction solar cells with as recombination layer and hole transporting layer between the middle and top subcell either IZO/NiO, ITO/NiO or IZO/spiro-TTB.

V_{oc}	J_{sc}	FF	Eff	V_{mpp}	J_{mpp}	
mV	mA/cm^2	%	%	mV	mA/cm^2	
2688	7.7	68.0	14.0	2113	6.6	Reverse
2692	7.7	58.7	12.1	1905	6.4	Forward
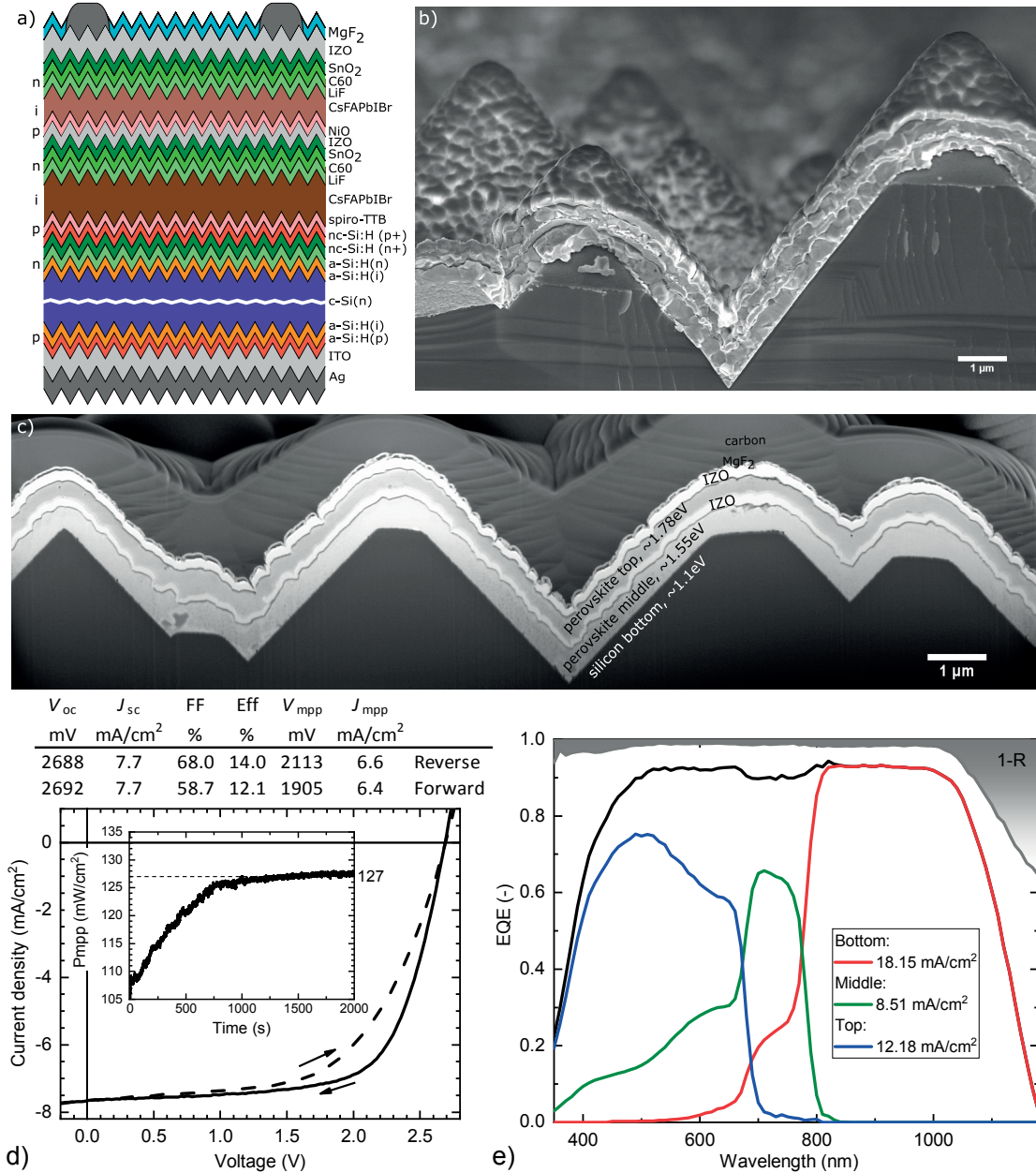
Figure 5.20 – a) Schematic of the layer stack of a perovskite/perovskite/silicon triple junction solar cell on a textured wafer; b) SEM and c) FIB cross-section images of a triple junction cell as schematized in a), showing clearly the two perovskite subcells separated by an IZO recombination layer; d) *J-V* curves and MPPT measurement of a triple junction cell with 1.4 cm^2 aperture area. The table inserted above the graph details the *J-V* parameters for both reverse and forward directions; e) EQE measurements of the triple junction cell, including the total response calculated by summing the subcells individual responses.

holes.

The junction between the bottom cell and the middle cell was made of the nc-Si:H recombination-junction also used for the tandem cells and spiro-TTB was directly evaporated onto these silicon layers. The junction between the middle and top cells had to be made with a TCO, here

IZO. Therefore, for the hole transporting layer in the top cell, spiro-TTB could not be used as it gave the same issue as for tandem cell, discussed in Section 5.4.3. Figure 5.19 shows that using spiro-TTB on top of IZO for the top cell resulted in a drastic loss of V_{oc} comparable to the top cell expected contribution, decreasing to close to 1.7 V, similar to a tandem cell. To solve this problem, NiO$_x$ was deposited by sputtering instead of spiro-TTB.

As shown in Figure 5.20d, this device structure was able to give up to 12.6% efficiency under maximum power point tracking and 14% under reverse J-V scan. The V_{oc} was close to 2.7 V and J_{sc} at 7.7 mA/cm^2. FF was depending on the scan direction but always below 70%. Figure 5.20e shows the EQE measurement of this triple junction cell. It is clear that the middle cell was limiting the total current. In the next phase of optimization, the total current will have to be better distributed among the subcells. The middle cell band gap needs to be lowered to around 1.4 eV and the top cell band gap increased around 1.9 eV. Then the fine-tuning of current distribution can be done by playing on their absorber layer thicknesses. The total EQE curve shows also that parasitic absorption losses will need to be reduced significantly. Overall, 13 mA/cm^2 current matched should be practically feasible with reasonable amount of further experimental work. The V_{oc} could also still be improved by at least 150 mV, with a longer-term practical potential for $\approx$3 V. In this early test, the NiO$_x$ layer could not be annealed at 200°C as required normally to improve its electronic properties, most likely resulting in V_{oc} losses. Other voltage losses could certainly be attributed to the recombination junction between the top and middle cells, which was here a non-optimized IZO layer, deposited with the same recipe as for the front electrode.

We can therefore clearly see that competing with all-III-V triple junction cells will be complicated in terms of efficiency, as 3 V * 13 mA/cm^2 * 77% makes just 30% efficient cells. A significant improvement in FF (>80%) as well as parasitic absorption reduction will therefore be necessary. But in terms of costs, the story might be different and this type of structure might allow some cost reduction in some applications such as solar-driven electrochemical reduction of CO$_2$ for the production of fuels and chemicals [255], or other applications requiring high voltage.

5.8   General conclusions on the chapter

In this chapter, the development of monolithic tandem solar cells was presented. The first tandems were fabricated in n-i-p configuration with double-side polished silicon bottom cells. The low temperature planar perovskite cells described in previous Chapters 2 and 3 were integrated in monolithic tandem cells using an intermediate recombination layer based on a TCO. ITO, IZO and ZTO were tested for this purpose. IZO showed the best device performance for low temperature devices with SHJ bottom cells whereas ZTO was found useful to allow the integration of high temperature TiO$_2$ scaffold layers in the perovskite top cell with a diffused-junction silicon bottom cell. Flat devices were found to produce strong interferences as shown in EQE measurements and strong reflection losses. ARF were used to reduce the impact of these interferences and reflection, and significantly boost the photogenerated current of the

tandem devices. With a planar n-i-p perovskite cell, a IZO recombination layer and a SHJ DSP bottom cell, the first perovskite/silicon monolithic tandem cell with >20% efficiency could be demonstrated with 0.17 cm^2 aperture area. This was shortly followed by the first >20% efficient tandem with >1 cm^2 area thanks to the introduction of a rear-side texture, enhancing the current in the bottom cell.

In order to decide how to continue the research and define the pathway to 25% efficiency, simulations and careful analysis of experimental data were carried out to define the materials to be replaced. Spiro-OMeTAD was quickly found to be the weakest link and new materials were investigated. It was only by inverting the polarity of the cell to p-i-n configuration that thin undoped charge transporting layers with reduced parasitic absorption losses could be integrated in perovskite cells and monolithic tandems.

Minimizing the reflection losses passes by using fully textured silicon solar cells, taking advantage of the double-bounce effect on the pyramids and enhanced light trapping. A first solution investigated involved the fabrication of a buried planarization layer based on a ZnO layer deposited by LPCVD. This approach revealed itself unsuccessful due to important technical difficulties. However, the development of p-i-n perovskite solar cells with evaporated charge transporting layers combined with an hybrid sequential deposition technique for the perovskite absorber allowed the use of fully textured silicon bottom cells with the goal of making conformally deposited top cells. This ambitious device structure made rapid progress: after some early investigations on morphology and wetting properties, it yielded record efficiencies >25% for the first time with perovskite/silicon monolithic tandem solar cells. The cells were mainly limited by low FF. Textured tandems were then used to carry out some preliminary experiments on light soaking stability, showing promising initial results, as well as up-scaling the device to 12.9 cm^2 with >20% efficiency. Finally, a first proof-of-concept triple junction solar cell could be demonstrated, showing high V_{oc} of ≈2.7 V and high potential for CO_2 electrochemical reduction.

In the near future, the road for tandem cells is paved and clear to >30% efficiency by fine-tuning the contacts, thinning down the charge transporting layers, optimizing the interfaces for best V_{oc} and *FF* and improving the perovskite absorber optoelectronic quality. The main challenge is clearly the material stability and device reliability, still largely under-investigated and misunderstood.

6 General conclusions and perspectives

This conclusion chapter summarizes the key achievements of this thesis toward the development of high efficiency perovskite/silicon tandem solar cells and presents perspectives for future research directions that could enable further performance enhancement, as well as better device reliability.

6.1   Conclusions

The perovskite solar cell research field has grown at an unprecedented pace during the last four years and tremendous progress was made. This offered many opportunities for the rapid development of perovskite/silicon tandem solar cells, toward high efficiencies >25% in both 4-terminal tandem and 2-terminal tandem architectures.

In order to reach such high performance, we had to develop a perovskite absorber with high optoelectronic quality and appropriately tuned optical band gap. We chose to use and develop an hybrid sequential deposition method, mixing thermal evaporation and solution processing, providing the possibility to deposit the perovskite layer on any substrate and charge transporting layer without the risk of damaging them with aggressive solvents. Planar low temperature cells could then be fabricated. The perovskite composition was modified along the way following discoveries coming from the perovskite community. CsFA-based perovskite compositions were adopted instead of the original MA-based material. This double-cation perovskite material allowed us to develop absorber layers with an optical band gap precisely tunable between 1.5 and 1.8 eV, which is crucial for current-matching optimization in monolithic tandem solar cells. The optical properties of these materials were also characterized, including complex refractive indices and absorption coefficients, helpful for optical simulations of multijunction solar cells.

The charge transporting layers were investigated and solution processed layers were replaced with thermally evaporated or sputtered ones, which is necessary for monolithic tandem integration. We therefore replaced the initial c-TiO$_2$ layer by first PCBM and then a thin evaporated C$_{60}$ layer as the electron contact. The replacement of the standard spiro-OMeTAD hole trans-

porting layer was significantly more difficult. It required to invert the polarity of the cell from n-i-p to p-i-n, in order to start the cell fabrication by a thermally evaporated undoped spiro-TTB or sputtered NiO_x and finish with the C_{60} electron contact on the other side of the absorber. These charge transporting layers are now thin, undoped and conformally deposited, and still allowed good device performance.

An important development step toward a functional perovskite/silicon tandem solar cell was the replacement of the standard opaque metal rear contact of perovskite solar cells with a broadband transparent electrode. Our investigations focused on TCO-based electrodes, and particularly on IZO, an amorphous high mobility TCO which does not require any post-deposition thermal treatment. For n-i-p perovskite cells, a transition metal oxide buffer layer was introduced to protect the sensitive hole transporting layer and perovskite absorber. This lead us to study the behaviour of these oxides when exposed to the sputtering plasma environment and discover a method based on a CO_2 plasma treatment to prevent and/or recover from the sputtering-induced damages. For p-i-n perovskite cells, an ALD-deposited SnO_2 layer was developed as buffer to protect the fullerene electron transporting layer.

Semitransparent perovskite cells were first applied in 4TT. Rapid progress could be made and over 25% efficiency was demonstrated in a measurement involving a small 0.25 cm^2 area top cell and a larger bottom cell. A tandem with 23.2% efficiency could be also demonstrated with a fully integrated device where both subcells had the same size of 1 cm^2. The research focus was then fully redirected to 2-terminal tandem cells.

The development of monolithically integrated tandem cells started with the development of the intermediate recombination layer. IZO was found to be well suited and allowed performance up to 21.2% efficiency in small area and 20.5% with 1 cm^2 area, which were at the time the first demonstration of over 20% perovskite/silicon tandem cells. These tandems were mainly limited by their optics and light management, as they were grown on bottom cells with a flat front surface, generating large reflection losses and strong optical interferences in the device. Our effort was therefore directed toward the integration on fully textured silicon bottom cells. This challenging task came to success after the development of a perovskite top cells with all evaporated charge transporting layers and the replacement of the TCO recombination layer by a nc-Si:H recombination junction. We could then demonstrate monolithic tandem cells with >25% efficiency at maximum power point, which was also independently certified by Fraunhofer ISE CalLab at 25.24%. Finally, first tests could be made toward larger tandem devices with 12.9 cm^2 aperture area and >20% efficiency. The light stability of tandem cells was tested with continuous light soaking and electrical characterization, showing promising first results. Also, the development of a robust monolithic tandem fabrication process allowed us to go a step further and make a first proof-of-concept of triple junction solar cells. These perovskite/perovskite/silicon multijunction solar cells showed conformal layers in both middle and top cells and decent performance around 12% with $V_{oc} \approx 2.7$ V.

6.2 Perspectives

To be viable for a silicon-based tandem PV product, the perovskite top cell is required to comply with the typical field warranty for PV panels, *i.e.* the power output should remain >80% after 25–30 years. In addition, tandem cells must be manufactured on industrial-scale wafers (typically 6 in.), with techniques and materials that add limited costs to the final product, which also concerns production throughput and yield. Stability, up-scalability, and cost-effectiveness are therefore the three most important keys for a possible commercialization. Between 4-terminal mechanically stacked and 2-terminal monolithically integrated tandems, we consider the 2-terminal the most interesting and promising architecture, with the highest potential for commercialization, thanks to the smaller number of layers compared to 4TT, enabling low production costs, high efficiency potential with limited parasitic absorption, and simpler implementation at the PV system level.

The costs of a PV installation is directly linked to the performance of the used cell technology, by saving area-related BOS costs. The path for tandem cells with beyond 30% efficiency is now clear and practically possible in the near future as discussed in Chapter 5. The challenge is to combine the state-of-the-art V_{oc} and *FF* demonstrated individually for single junction perovskite solar cells and implement them with the high current already demonstrated in textured tandems. Research should then focus on stabilizing wide band gap perovskite materials, reducing recombination paths through grain boundaries and interfaces passivation, improve charge extraction and reduce resistive losses in transparent electrodes and metallization.

Considering the cost calculation Table 1.2 presented in the introduction chapter, we can now make some rough estimations on the cost potential of the textured tandem cell presented in Chapter 5.4.3. Apart from the silicon bottom cell and the front TCO electrode, which are already part of a standard SHJ cell, 4 layers were added for the perovskite top cell: a hole transporting layer, the perovskite absorber, an electron transporting layer and the buffer layer. All materials were deposited with industrially already available and known techniques, *e.g.* magnetron sputtering, thermal evaporation, ALD (or spatial-ALD), therefore minimizing the investment costs on the development of new specific methods. These materials such as C_{60} or spiro-TTB are rather low cost and could still be replaced by other cheaper materials as already presented here, *e.g.* NiO_x instead of spiro-TTB. In terms of performance, we have used silicon bottom cells that had efficiencies around 22% as single junction. The absolute efficiency gain was therefore over 3% at the cell level. Considering the promising results for up-scaling (Section 5.6) and the recent industrial developments, with for example Oxford PV showing 6 inches tandem cells, we can reasonably assume a similar gain at the module level (still to be confirmed). We can then estimate manufacturing costs just below 40 €cts per additional watt of output power, leading to around 5 €cts/Wp area related BOS cost saving for a typical roof top installation. Further increasing the cell performance to over 30% efficiency and/or using cheaper materials would obviously further increase the cost saving and render this tandem concept even more economically attractive.

The main challenges for commercialization are however not efficiency or up-scalability. The main concerns are about materials toxicity, material stability and device reliability:

Chapter 6. General conclusions and perspectives

The silicon PV industry is moving to lead-free soldering, which is expected to gradually become the leading technology for interconnections over the next decade [11]. The industrial development of perovskite/silicon tandem cells can therefore be expected to also follow this trend and anticipate future more strict regulations. Research toward lead-free, or lead-less perovskite solar cells has therefore already started, although device efficiencies still lie far behind those of state-of-the-art lead-containing compounds.

Material and device stability are the biggest challenge of any perovskite-based solar cells. Perovskite/silicon tandem solar cells must show the same reliability and trust level as all other silicon-based PV technologies, with 30 years industrial warranty on photovoltaic modules. The perovskite solar cell stability already improved massively from the few minutes in 2009 to several months at the present state-of-the-art. However, there are still issues in materials' intrinsic instability with *e.g.* phase segregation under illumination or their sensitivity to extrinsic environmental conditions such as humidity, temperature variation or heat. So far, perovskite solar cells were typically tested with non-standard reliability testing. Future research should aim at studying these cells with industrially accepted degradation protocols, understanding the related degradation mechanisms and develop new perovskite specific standard tests. Through a deep understanding of the degradation origin, the device stability can then be improved by modifying accordingly the absorber material composition, the contacts materials and their interfaces, paving the way for industrially-viable perovskite-silicon tandem cells with operational lifetimes >30 years.

Perovskite will certainly continue to surprise us. Considering the amazing development of the field of perovskite solar cells and perovskite-based tandem in the last 5 years, we can sincerely hope for a successful future for this technology, which could lead to virtually unlimited clean energy at affordable cost, to power our daily life from utility scale, building-integrated systems, to wearable electronics and mass transportation.

A Experimental details

A.1 Perovskite cell fabrication

A.1.1 Mesoporous n-i-p opaque cells

Mesoporous perovskite solar cells were used in references [72] and [84]. A compact titan dioxide (c-TiO$_2$) layer with a thickness of 20 nm was sputtered on a cleaned, laser-patterned fluorine doped tin oxide (FTO) substrate (Solaronix TCO22-15), followed by a 300-nm-thick mesoporous titan dioxide (mp-TiO$_2$) deposited by spin coating. The TiO$_2$-coated substrate was then annealed at 500°C for 15 min. The $CH_3NH_3PbI_3$ perovskite absorber layer was deposited following the procedure described by Jeon et al [201]. A 1.2 M solution of lead iodide (PbI$_2$) and methylammonium iodide, CH_3NH_3I (MAI) at a molar ratio of 1:1 was prepared at 60°C in a 7:3 v/v γ-butyrolactone/dimethyl sulfoxide mixture. This solution was then spin coated at room temperature on the mp-TiO$_2$/c-TiO$_2$/FTO/glass substrates at 1000 rpm for 15 s followed by 5000 rpm for 30 s. Ten seconds before the end of the second spin coating step, toluene was dripped on the rotating sample. The sample was then annealed at 100°C for 10 min. The spiro-OMeTAD solution (72.3 mg/ml, 2,2',7,7'-Tetrakis-(N,N-di-4-methoxyphenylamino)-9,9'-spirobifluorenes (spiro-OMeTAD) (Merck), 28.8 μl/ml 4-tert-butylpyridine (Sigma-Aldrich), 17.5 μl/ml stock solution of 520 mg/ml lithium bis (trifluoromethylsulfonyl) imide (Sigma-Aldrich) in acetonitrile, dissolved in chlorobenzene) was finally spin coated at 4000 rpm for 30 s. The opaque cells were finally metallized with ≈70 nm of gold, deposited by thermal evaporation at ≈ 5×10^{-6} mbar base pressure.

A.1.2 Planar n-i-p opaque cells

Planar n-i-p perovskite cells were used in references [83, 76, 96]. 15 Ω/□ ITO-coated glass substrates (Kintec) were first cleaned with a 10-15 min UV-ozone treatment. Then a polyethyleneimine (PEIE) (Mw 70'000, 80% ethoxylated solution, Sigma-Aldrich, diluted to 0.05% w/w in DI water) layer and a 20-nm-thick phenyl-C61-butyric-acid-methyl-ester (PCBM) (99.5%, Solenne) layer were spin coated at 5000 rpm during 60 s and 3000 rpm during 30 s, respectively. The substrates

were annealed at 150°C for 10 min between PEIE and PCBM and at 70°C for 10 min after PCBM, in a nitrogen (N_2)-filled glovebox. Then a 150-nm-thick lead iodide (PbI_2) layer was thermally evaporated at a rate of 1 Å/s in a Lesker mini-spectros system, with substrate temperature of 80°C and a base pressure of 1.5×10^{-6} torr. The PbI_2 layer was transformed to the final perovskite phase by spin coating a 50 mg/ml solution of methylammonium iodide (MAI, Dyesol) in isopropanol, containing 24.8 μl/ml 2-methoxyethanol [83], or pure ethanol [76]. The substrate was set in rotation and only after speed stabilization the solution was dripped on the rotating substrate (spin and drop method). The film was then annealed on a hotplate inside a nitrogen-filled glovebox at 100-120°C for 30 min. A spiro-OMeTAD solution in chlorobenzene (72.3 mg/ml, 2,2',7,7'-Tetrakis-(N,N-di-4-methoxyphenylamino)-9,9'-spirobifluorenes (spiro-OMeTAD) (Lumtec), 28.8 μl/ml 4-tert-butylpyridine (TCI), 17.5 μl/ml stock solution of 520 mg/ml lithium bis trifluoromethylsulfonyl imide (Sigma-Aldrich) in acetonitrile) was then spin coated at 4000 rpm for 30 s. The opaque cells were finally metallized with ≈70 nm of gold, deposited by thermal evaporation at $\approx 5 \times 10^{-6}$ mbar base pressure.

A.1.3 Near-infrared transparent n-i-p cells

To fabricate semitransparent perovskite cells in n-i-p configuration, the cells were fabricated with the same sequence as described above for either mesoporous or planar cells, and stopping after the spiro-OMeTAD spin coating. Then, instead of the gold metallization, 10-15 nm of molybdenum oxide (stoichiometric MoO_3 or WO_3 powder, 99.9995% Alfa Aesar, at a base pressure of $3-5 \times 10^{-6}$ mbar and rate of 0.2-1 Å/s) was thermally evaporated as protective buffer layer, using Mo box boats. This was followed by the transparent conductive oxide (TCO) deposition by RF magnetron sputtering. Several TCO were used in this thesis: indium zinc oxide (IZO) (IZO, 4-inches target, composition 90 wt% In_2O_3 and 10 wt% ZnO, in Leybold Univex or home-made "Lebowski"), hydrogenated indium oxide (IO:H, in MRCII), indium tin oxide (ITO, in MRCII), zinc tin oxide (ZTO, in Oerlikon Clusterline). The MoO_x/TCO stack was deposited through a shadow mask. Then a metal (Au or Ag) frame was thermally evaporated around the active area to enhance carrier extraction.

For the work in reference [72], IZO was deposited by RF magnetron sputtering at 60 W (0.76 W/cm^2) with a working pressure of 2.1×10^{-3} mbar using pure argon gas. The chamber base pressure was at 5.5×10^{-6} mbar, the substrate temperature at 60°C and the sample-target distance at 13 cm.

For the work in references [76] and [84], a 110-nm-thick IO:H/ITO bilayer was deposited sequentially in the same chamber without breaking the vacuum. The IO:H film was prepared by using an In_2O_3 target and introducing H_2O vapor in the Ar/O_2 flux to incorporate hydrogen in the layer [256].

For the fabrication of monolithic tandem solar cells, the process flow is the same as the single junction perovskite cells, by just replacing the glass/ITO substrate with the silicon bottom cell as described below.

A.1.4 Planar p-i-n opaque cells

As described and used for example in reference [97], planar p-i-n perovskite cells were grown in superstrate configuration on 15 $\Omega/\square$ ITO-coated glass substrates (Kintec). The hole contact was either 17 nm of 2,2',7,7'-Tetra(N,N -di-p -tolyl)amino-9,9-spirobifluorene (spiro-TTB) (spiro-TTB, Lumtec >99%), thermally evaporated in an alumina crucible, or 20 nm of sputtered nickel oxide. In both cases, the perovskite layer was formed using a sequential 2-step hybrid deposition method, consisting of first thermally co-evaporating a Cs-halide compound and PbI_2. The evaporation rate of PbI_2 was fixed at 1 Å/s and the Cs-halide rate was then adjusted to obtain the desired Cs content. This rate is indicated in the manuscript as a percentage of the PbI_2 rate, *i.e.* CsI15% corresponds to a rate of 0.15 Å/s, co-evaporated with a 1 Å/s rate of PbI_2. The PbI_2 thickness was set to 180 nm for the CsI and CsBr samples and 160 nm for the CsCl samples. The Cs halides were purchased from Abcr and had purities >99%. The CsX-PbI_2 layer was then transformed to the final perovskite layer by spin coating a 0.445M ethanol solution of formamidinium iodide (FAI) and/or formamidinium bromide (FABr) (Dyesol), with specific molar ratio given throughout the thesis, *i.e.* 1:2 corresponds to a mixture of 1 mol of FAI for 2 mol of FABr. The solution was spin coated inside a nitrogen-filled glovebox. Then the samples were taken in air and annealed on a hotplate at 150 °C for 25 min. The cells were finished with the electron contact consisting of a thermally evaporated bilayer of 20 nm of C_{60} (>99.95%, NanoC) and 5 nm of TmPyPB (1,3,5-Tri[(3-pyridyl) -phen-3-yl]benzene, >99%, Lumtec), followed by 110 nm of thermally evaporated silver.

A.1.5 Near-infrared transparent p-i-n cells

After the C_{60} deposition, the samples were transferred to an ALD chamber (Oxford Instrument), where ≈10 nm of SnO_2 were grown from TDMSASn and H_2O precursors. The main controlled parameters were the purge time, the number of cycles and the temperature. A TCO was subsequently deposited on the SnO_2 layer to make the transparent electrode, similarly to the n-i-p cells. Finally, a Ag metal grid was thermally evaporated and covered with an evaporated antireflective coating of MgF_2.

A.2 Silicon cell fabrication

A.2.1 Silicon heterojunction solar cells

As presented in references [72] or [76], the silicon bottom cells used for mechanically stacked 4-terminal tandem measurements were amorphous silicon/crystalline silicon heterojunction solar cells (SHJ), fabricated with n-type-doped crystalline silicon float-zone wafers (resistivity of 1-5 Ohm; thickness ≈300 μm). After standard double-side texturization in a KOH-based solution, the wafers were passivated and carrier-selective contacts were created by deposition of intrinsic and doped hydrogenated amorphous silicon layers by PECVD. The cells were then finished with ITO deposition and metallization with full-area silver on the rear-side and

screen-printed silver grid on the front-side to define 4-cm^2-sized cells.

For monolithic tandem solar cells as presented in references [83] or [76], the silicon bottom cells were double-side mirror polished (DSP), single-side textured (SST) or double-side textured (DST). For DSP cells, we used double-side mirror polished, n-type doped, crystalline silicon float-zone wafers with a (100) surface orientation, a resistivity of 1-5 Ohm.cm and a thickness of 260-300 μm. After a 60 s dip in hydrofluoric acid (5% aqueous solution) to strip off the native oxide layer at the surface, the wafer surfaces were passivated and carrier-selective contacts were created by deposition of intrinsic and doped (n or p) hydrogenated amorphous silicon layers. For this we used our standard PECVD process, which we adapted for polished wafers. For SST cells, the process was also started with DSP silicon wafers. But then one side was first coated with a dielectric mask and a standard KOH texturization step was then carried out, followed by a cleaning and mask removal step in a diluted HF bath, resulting in a single-side textured wafer. The PECVD recipes for the amorphous silicon layers were then adapted to fit the front or rear surface finish. The prepared 4-inch wafers were then coated with ITO and Ag by sputtering on the rear side in full area, followed by laser cutting to 2.5×2.5 cm^2 samples. Finally, the intermediate recombination layer was made of a sputtered IZO layer, deposited at room temperature with 100 W sputter power at 1 μbar of pure argon, through a shadow mask defining the active area of the cells on which the front top electrode will later be aligned. This TCO layer was deposited directly on the p-type amorphous silicon emitter layer. The perovskite top cell was then grown on the recombination layer, following exactly the same process as for the single junction cells.

The TCO recombination layer was later replaced by a nanocrystalline silicon tunnel junction, as demonstrated by F. Sahli *et al.* [86].

For monolithic tandem solar cells presented in Chapter 5, fully textured silicon bottom cells were prepared using n-type-doped crystalline silicon float-zone wafers, standard double-side texturization in a KOH-based solution and standard passivation and carrier-selective contact deposition. The bottom cells used for fully-textured tandems were in the rear-emitter configuration and all using a nanocrystalline silicon tunnel junction, without TCO as intermediate contact, if not specified otherwise. The rear side ITO/Ag stack was patterned (in contrast to the front emitter bottom cells previously described), centered on 2.5×2.5 cm^2 samples and aligned with the front side transparent contact finishing the cell on top of the perovskite top cell.

A.2.2 Low-pressure chemical vapor deposition (LPCVD)

LPCVD was used to deposit zinc oxide (ZnO) layers, in an attempt to planarize the surface of a textured silicon wafer (see Chapter 5.4). The system had three gas entries: diethylzinc (DEZ, $Zn(C_2H_5)_2$), H_2O and diborane as dopant (B_2H_6). The samples were placed on an aluminum plate, which was held at a constant temperature (*i.e.* 170 °C). All gas fluxes and substrate temperature could be controlled. The used parameters are indicated in the discussion in the related Section of Chapter 5.4.

A.3 Thin film characterization

Thin films were deposited on SCHOTT AF32 glass substrates, if not otherwise stated.

A.3.1 UV-visible spectrophotometry

A PerkinElmer Lambda 950 spectrophotometer was used to determine total and diffuse reflectance and transmittance of thin-films on glass substrate and reflectance of silicon wafers or tandem cells. The absorptance was calculated as: $A(\lambda) = 100\% - TT(\lambda) - TR(\lambda)$. The setup was equipped with a 150-mm InGaAs integrating sphere. All measurements were carried out at room temperature in ambient air.

A.3.2 Variable-angle spectroscopic ellipsometry (VASE)

VASE was mainly used to obtain complex refractive indices of perovskite materials as presented in references [103, 97]. VASE measurements were carried out with a Horiba Jobin Yvon UVISEL iHR320 ellipsometer under incident angles of 50, 60 and 70° for photon energies between 0.6 and 4 eV with 50 meV increment. The ellipsometric models for the complex refractive index were developed using three substrate types to decouple intrinsic properties from substrate dependent artefacts: glass, double-side polished silicon and oxidized silicon. Surface roughness was measured by atomic force microscopy and integrated into the models. Reflectance and transmittance data were acquired using the UV-vis spectrophotometer. All measurements were carried out at room temperature in ambient air.

A.3.3 Fourier-transform photocurrent spectroscopy (FTPS)

FTPS was carried out on a Thermo Nicolet 8700 FTIR spectrophotometer equipped with an external 100 W halogen light source. The measurements were carried out on full solar cell stacks. All measurements were carried out at room temperature in ambient air. More information can be found in reference [33, 104].

A.3.4 Photothermal deflection spectroscopy (PDS)

PDS measurements were performed by immersing a perovskite layer deposited on a glass substrate in a FluorinertTM FC-72 temperature-sensitive liquid. More information can be found in reference [33, 104].

A.3.5 X-ray diffraction (XRD)

As presented in reference [97], XRD measurements were carried out in an Empyrean diffractometer (Panalytical) equipped with a PIXcel-1D detector. The diffraction patterns were

measured using a Cu Kα radiation (wavelength of 1.54Å). The measurements were carried out in ambient air.

A.3.6 Transparent conducting oxide (TCO) characterization

The film thickness was determined with a step profiler (AmBios XP-2). The sheet resistance (R_{sq}) was measured with a four-point-probe setup. Electrical conductivity, carrier Hall mobility and carrier density were obtained from Hall-effect measurements in the van der Pauw configuration on an Ecopia HMS-5000 system at room temperature, ambient air and in the dark. For these measurements, the TCO layers were deposited on glass substrates and placed close to the devices during the deposition, acting as witness sample.

A.3.7 Microscopy techniques

Atomic force microscopy was used to determine the surface roughness of perovskite layers, using a Bruker Dimension Edge atomic force microscope.
The SEM images were acquired using a JEOL JSM-7500TFE SEM at an accelerating voltage of 5 kV and using a working distance of 5 mm.
For TEM, cross sections of perovskite cells were prepared using the conventional focused ion beam lift-off technique, which was performed on a Zeiss Nvision 40 FIB/SEM workstation. The lamellae were then transferred quickly (<2 min in air) to a high-resolution transmission electron microscope (either FEI Tecnai Osiris or an image and probe Cs-corrected FEI Titan Themis microscope) operated at 200 kV. More details on the TEM/EDX characterization of perovskite cells can be found in a previous publication [102]. The Cs/Pb atomic ratio was estimated from EDX spectra using the Cliff-Lorimer method (using the Pb L and Cs K edges, with all the other elements deconvoluted).

A.4 Solar cell characterization

A.4.1 External quantum efficiency

An external quantum efficiency (EQE) is defined as the ratio of the number of photogenerated and collected carriers over the number of incident photons at a specific wavelength. This measurement helps to quantify the optical performance of a solar cell and its wavelength dependent absorption and carrier collection capability. EQE spectra were measured with a custom made spectral response setup equipped with a white halogen lamp, a Horiba micro HR grating monochromator and lock-in amplifiers. The setup allowed measuring EQE in a spectral range from 310 nm to 1190 nm. The influence of chopper frequency, voltage bias and white light bias was tested for mesoporous perovskite cells and shown in Figure A.1. Accordingly, the chopper frequency was fixed at 10 Hz for TiO$_2$-based mesoporous cells, due to their slow response time. For fullerene-based planar perovskite cells, the chopper frequency

was set at 232 Hz, as this type of cell was not sensitive to the chopper frequency. The J_{sc} was determined from EQE measurements by convolution of the EQE spectra with the AM1.5g solar spectrum. The single junction perovskite cells were measured without any backreflector, white light bias or voltage bias, if not otherwise specified.

In the case of monolithic tandem solar cells, light bias and voltage bias were used in order to gain access to the contribution of each subcell. As the two subcellsare connected in series, the current generated by the tandem device is limited to the lowest photogenerated current of the two subcells. Therefore, to measure the EQE curve of the perovskite top cell, the tandem device was illuminated with infrared light (using an IR filter at 830 nm), which was saturating the silicon bottom cell. Blue light was used in the same principle to measure the EQE of the silicon bottom cell. The exact spectra of the light bias used throughout this thesis can be found in a previous thesis by Karin Söderström [229], p.33. Voltage bias were applied during measurements: 0.9-1V during the measurement of the bottom cell and 0.6-0.7 V during the measurement of the top cell. The effects of light and electrical biases as well as frequency were carefully tested. For example that they had no significant effect on one of our early monolithic tandem cell [83]. This effect was regularly tested every time a new type of cell was measured for the first time.

A.4.2 Current-voltage measurements

J-V measurements provide probably the most important set of information in the development of a photovoltaic device, as they allow to assess its performance. *J-V* characteristics were acquired with a class-AAA WACOM continuous light solar simulator, using a halogen and a xenon lamp to match the AM1.5g irradiance spectrum and 1000 W/m^2 irradiation intensity. Fitting the *J-V* curves allowed to extract the open circuit voltage (V_{oc}), the short circuit current density (J_{sc}), the fill factor (*FF*), the series resistance (Roc), the shunt resistance (Rsc), the voltage, current and power at maximum power point (V_{mpp},J_{mpp},P_{mpp}) (see Figure A.2a). All cells were measured through laser cut shadow mask, defining the illumination area and therefore the device area. Single junction cells were measured with a black background to minimize back reflection, especially important for semitransparent solar cells. Wafer-based cells were measured on a temperature controlled chuck, acting as back contact, and four-point kelvin probes were used for the front contacts. The temperature was fixed at 25°C and all measurements were carried out in ambient air, without encapsulation, if not stated otherwise. Illumination intensity dependent measurements were carried out using neutral density filters placed between the cell and the sun simulator.

Due to the slow response and often hysteretic behavior of perovskite-based solar cells (see hysteresis illustration in Figure A.2a), the *J-V* scan parameters, such as delay between two measurements, the integration time at each point, the number of point in a voltage interval, the starting voltage and ending voltage, were carefully chosen and readapted for all cell types. For example, mesoporous TiO$_2$-based perovskite solar cells had very slow response and the observed hysteresis was very sensitive to scan speed variations. They were therefore scanned at around 33 mV/s. In contrast, planar fullerene-based perovskite cells had a faster response
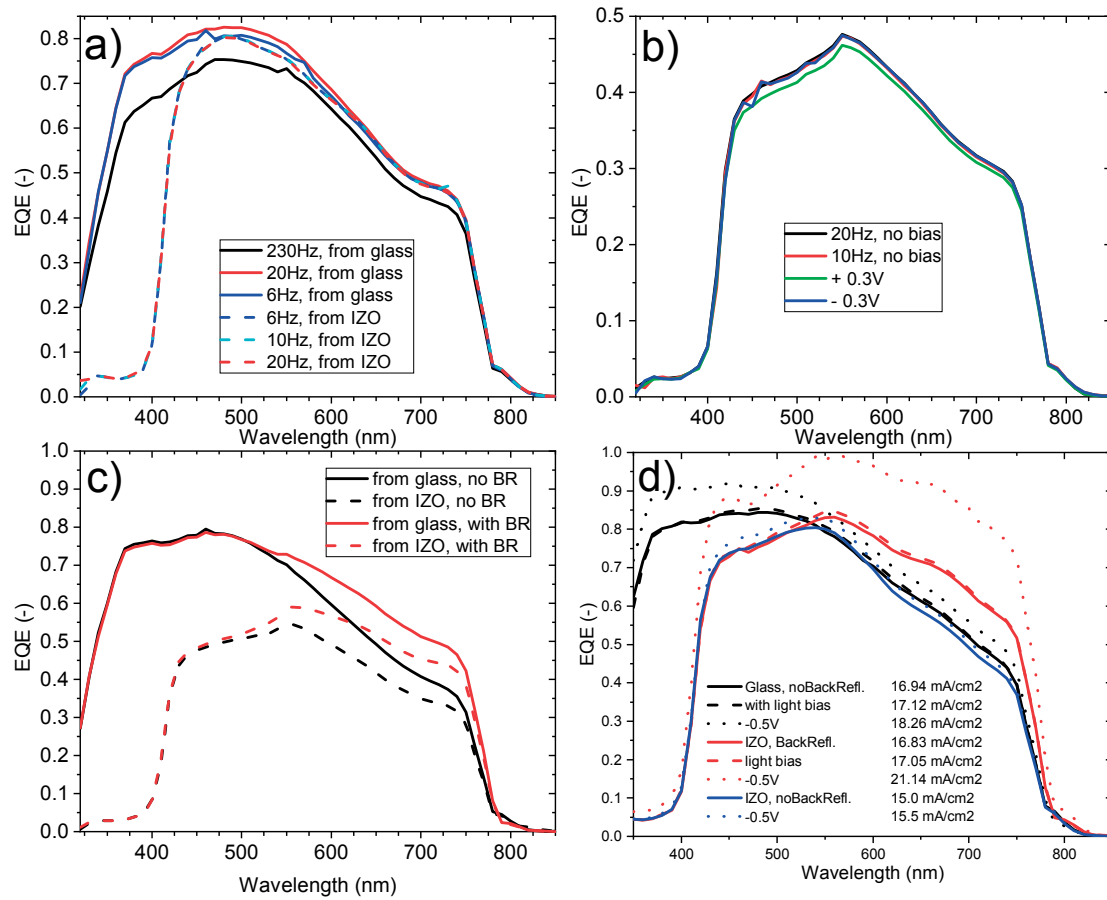
Figure A.1 – External quantum efficiency (EQE) spectra. (a) Effect of chopper frequency on EQE of a semitransparent cell with MoO_x 10 nm/IZO 60 W rear electrode. (b) Effect of voltage bias on a semitransparent cell with MoO_x 35 nm/IZO 150 W rear electrode. (c) Effect of attaching a white, diffusive back reflector on the rear side of a semitransparent cell with MoO_x 35 nm/IZO 60 W rear electrode. (d) Effect of white light bias and back reflector on the EQE of a semitransparent cell with IZO rear electrode.

time and were less sensitive to sweep parameters. They were usually scanned at 100 mV/s. For all perovskite-based cells, the hysteresis was systematically checked by scanning the cell both in reverse (V_{oc} to J_{sc}) and forward (J_{sc} to V_{oc}) directions, in a loop scan without turning off the light and without additional delay. Finally, the slow response of perovskite cells can also be observed by a significant change of J-V parameters in several consecutive scans. Therefore we usually also actively tracked the maximum power point for several hundreds of seconds until the power output stabilized. A MPPT algorithm was written and integrated in our sun simulator LabVIEW software. It was based on a three-point weight MPPT algorithm [257], which was chosen to avoid oscillation problems often seen with perturbe-and-observe algorithms [258], with Figure A.2b showing a typical oscillation example on a mesoporous perovskite cell.
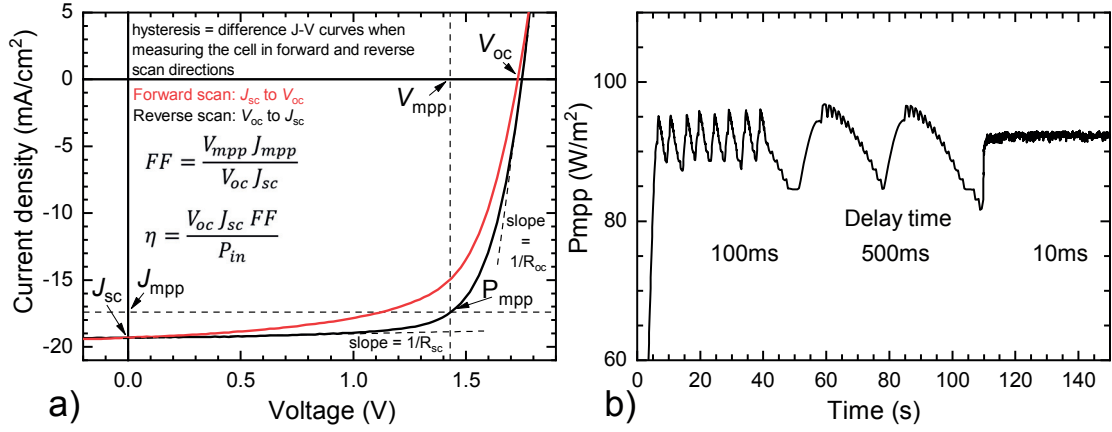
Figure A.2 – MPPT measurement of a mesoporous perovskite solar cells with a perturbe-and-observe algorithm, showing oscillations linked to chosen time parameters.

A.4.3 Microtextured antireflective foils and antireflective coatings

Microtextured antireflective foils were fabricated in-house by Xavier Niquille. The procedure was described in detail in previous publications and theses [259, 208, 229]. During this thesis, replicates of silicon random pyramids and of cube-corner structures as shown in Figure A.3 were used, fabricated on PEN flexible foils with Ormostamp resin. The foils were applied on the solar cells with canola oil as optical coupling liquid.
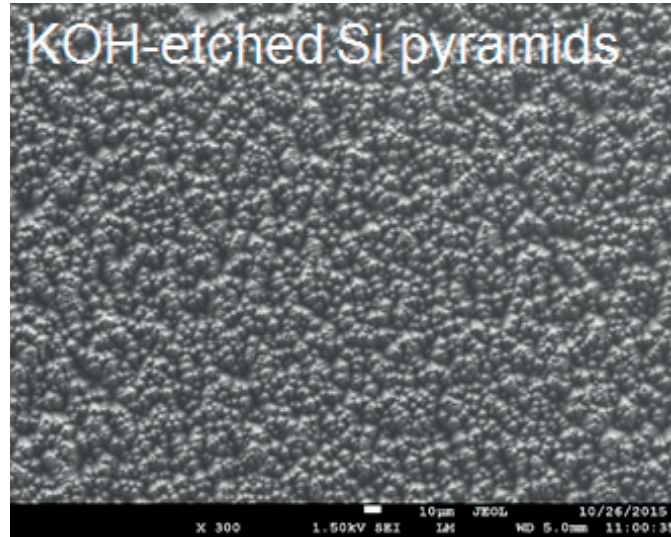
Figure A.3 – SEM topview images of microtextured antireflective foils with Si pyramids.

A.4.4 Mechanically-stacked 4-terminal tandem measurements

When the perovskite cell had a significantly slower size (*i.e.* ≈0.25 cm^2) compared to the silicon cell (*i.e.* 4 cm^2), we defined the tandem as a mechanically stacked 4TT measurement, and

not device, which was kept for the case where both sub cells had the same size and were integrated (see below). As presented in references [72, 76], 4TT measurements consisted on first measuring the *J-V* and EQE characteristics of the near-infrared transparent perovskite cell as a single-junction. Then, the EQE of a SHJ bottom cell (4 cm^2) was measured through the perovskite cell, acting as filter. The EQE beam size was 1×2 mm^2, therefore smaller than the active area of the perovskite cell and small than the Ag fingers spacing on the silicon cell. This measurement provided a J_{sc} value that was then multiplied by a shadowing factor, in order to be closer to a realistic situation where the top cell would also be larger and have a metal grid that we assume to be the same as the one of the bottom cell. This shadowing factor was therefore defined as the ratio of the silicon cell J_{sc} including the front metal grid and the silicon cell J_{sc} without metal grid. The obtained corrected J_{sc} was then corresponding to the current that would be generated in the bottom cell and was then used to measure the *J-V* characteristics of the bottom cell. The illumination intensity of the sun simulator was adjusted with neutral density filters to match the measured J_{sc}, which allowed to measure the V_{oc} and *FF* accurately. The tandem total efficiency was then calculated by summing the measured individual performance of both the near-infrared transparent perovskite top cell and the filtered silicon bottom cell. The validity of this protocol was confirmed by using larger area perovskite cell dummy filters and measuring the current of the bottom cell directly. Also using neutral density filters yield identical results as when using a long-wave pass filter, which was tested both on silicon heterojunction (SHJ) cells and passivated emitter with rear locally diffused (PERL) cells, as shown in Figure A.4.

For integrated mechanically stacked 4-terminal tandem devices, the two sub cells had the same size and geometry. The top and bottom cells were specifically designed to have 1.03 cm^2 aperture area, with both metal finger grid aligned. The contacts were made with metal ribbon and
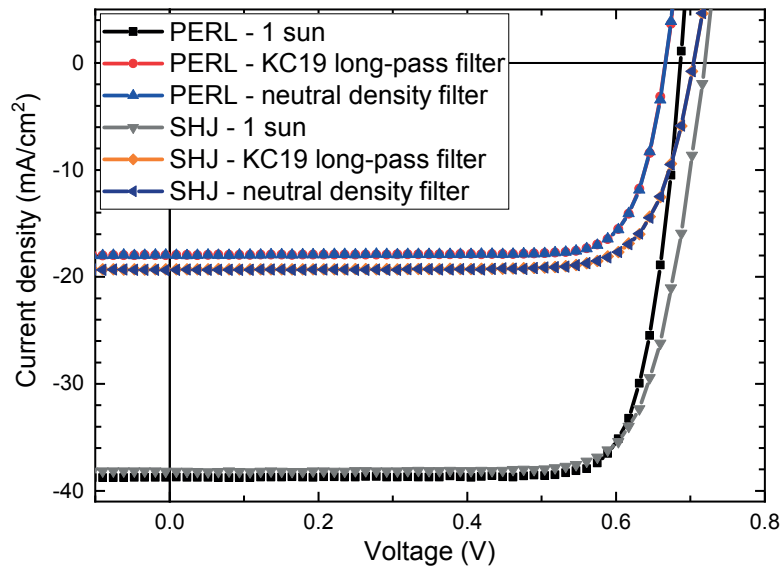
Figure A.4 – J-V curves of silicon heterojunction (SHJ) or passivated emitter rear locally diffused (PERL) solar cells when using either a long-pass filter or neutral density filter, showing a perfect superposition for these two cases.

the top cell was glued to the bottom cell with PDMS, which was also acting as optical coupling layer. *J-V* and EQE characteristics could then be directly measured on the device for both sub cells. This integrated device configuration with larger cell areas is a more realistic demonstration of a real 4-terminal tandem system, whereas the above-discussed measurement with dissimilar cell sizes should be seen as a demonstration of the efficiency potential.

B Additional experimental data
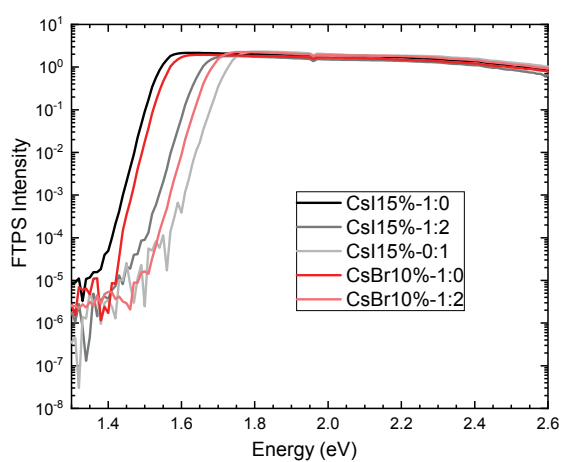
Figure B.1 – FTPS measurements of perovskite solar cells with various compositions indicated in the legend with their experimental conditions. Reproduced with permission [97]. Copyright 2018, American Chemical Society.

Appendix B. Additional experimental data

Table B.1 – Best *J-V* parameters for all investigated cell compositions from section 2.2.3 and their corresponding EQE-extracted short circuit current and optical band gap.

	Cell type	Composition	Eg (EQE) eV	J_{sc} (EQE) mA/cm^2	ARF? -	Ap. area cm^2	scan dir. -	V_{oc} mV	J_{sc} mA/cm^2	FF %	Eff. %	P_{mpp} mW/cm^2
n-i-p semitransparent	4	CsBr10%-1:0	1.56	19.13	no	0.25	reverse	1025	19.40	78.5	15.6	15.5
	4	CsBr10%-1:0	1.55	20.62	yes	0.25	reverse	1031	21.11	78.7	17.1	16.7
	4	CsBr10%-2:1	1.61	18.91	no	1.03	reverse	1052	19.40	76.2	15.5	15.7
	4	CsBr10%-2:1	1.61	19.84	yes	1.03	reverse	1079	20.20	75.9	16.6	
	4	CsBr10%-1:2	1.68	16.96	no	0.25	reverse	1126	16.81	77.5	14.7	14.5
	4	CsBr10%-0:1	1.74	15.28	no	0.25	reverse	1144	15.35	75.4	13.2	13.2
	4	CsI15%-1:2	1.64	17.96	no	0.25	reverse	1111	18.10	73.5	14.8	14.5
	4	CsI15%-0:1	1.70	16.72	no	0.25	reverse	1164	16.55	72.1	13.9	12.9
	1	CsBr10%-1:0	1.53	22.16	no	0.25	forward	1005	21.69	60.7	13.2	13.2
	1	CsBr10%-1:2	1.65	19.00	no	0.25	reverse	1082	18.74	75.0	15.2	15.0
	1	CsBr10%-0:1	1.72	17.47	no	0.25	forward	1088	15.69	69.6	11.9	11.6
	3	CsBr10%-0:1	1.73	16.03	no	0.25	reverse	1085	15.72	80.0	13.6	13.2
p-i-n opaque	1	CsI15%-1:0	1.51	22.14	no	0.25	forward	851	17.15	54.3	7.9	
	1	CsI15%-1:2	1.62	19.77	no	0.25	forward	1049	19.63	75.5	15.6	14.7
	1	CsI15%-0:1	1.69	18.01	no	0.25	forward	1107	18.09	74.1	14.8	14.6
	1	CsCl8%-1:3	1.70	18.17	no	0.25	reverse	1086	18.05	72.4	14.2	
	2	CsCl8%-0:1	1.75	16.11	no	0.25	forward	1053	15.99	76.1	12.8	13.4
	1	CsCl12%-1:3	1.72	17.45	no	0.25	forward	1104	17.07	76.8	14.5	13.9
	1	CsCl12%-0:1	1.77	16.48	no	0.25	reverse	1131	16.18	74.6	13.7	13.0
	2	CsCl17%-0:1	1.80	15.40	no	0.25	forward	1150	15.03	67.8	11.7	11.0
	2	CsCl17%-0:1	1.79	16.36	yes	0.25	forward	1113	15.74	72.0	12.6	12.0

1 p-i-n: ITO/spiro-TTB/Perovskite/C$_{60}$/TmPyPB/Ag

2 p-i-n: ITO/NiO/Perovskite/C$_{60}$/TmPyPB/Ag

3 p-i-n: ITO/NiO/Perovskite/LiF/C$_{60}$/TmPyPB/Ag

4 n-i-p: ITO/LiF/C$_{60}$/Perovskite/spiro-OMeTAD/MoO$_x$/IO:H/ITO
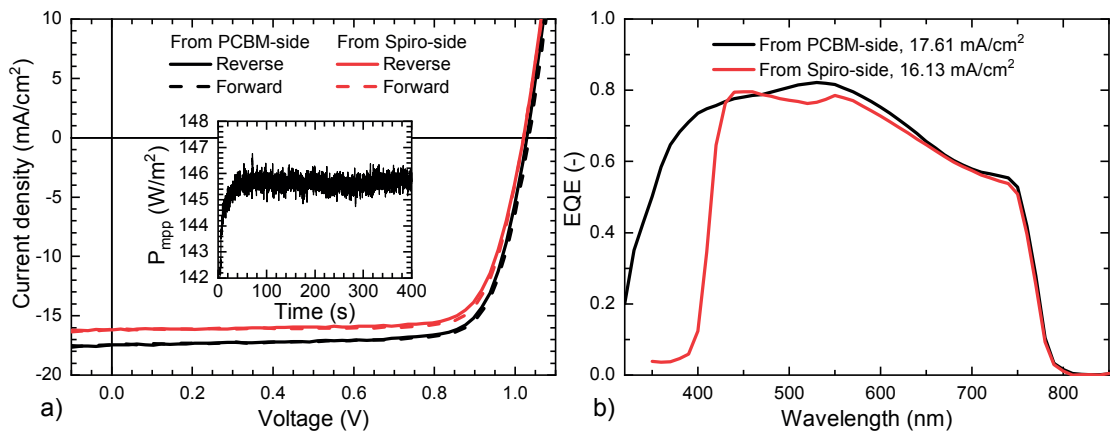
Figure B.2 – a) *J-V* and b) EQE measurements of a low-temperature processed semitransparent perovskite solar cell with the same layer stack as used for the top cell in the monolithic tandem device but deposited on ITO-coated glass substrates, measured in both substrate and superstrate configurations, indicated, respectively, by "From spiro-side" and "From PCBM-side". The inset shows a maximum power point tracking measurement of the cell. Reproduced with permission [83]. Copyright 2016, American Chemical Society.
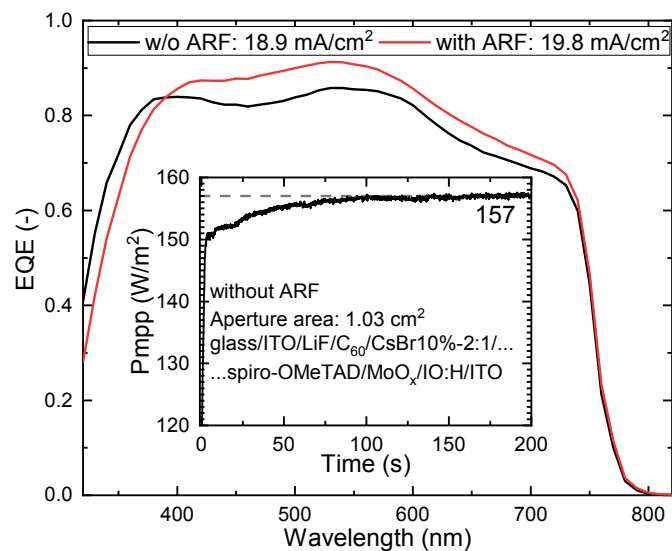
Figure B.3 – EQE curves of the best large semitransparent n-i-p perovskite cell, with and without ARF. The inset shows the maximum power point tracking of the cell without ARF.
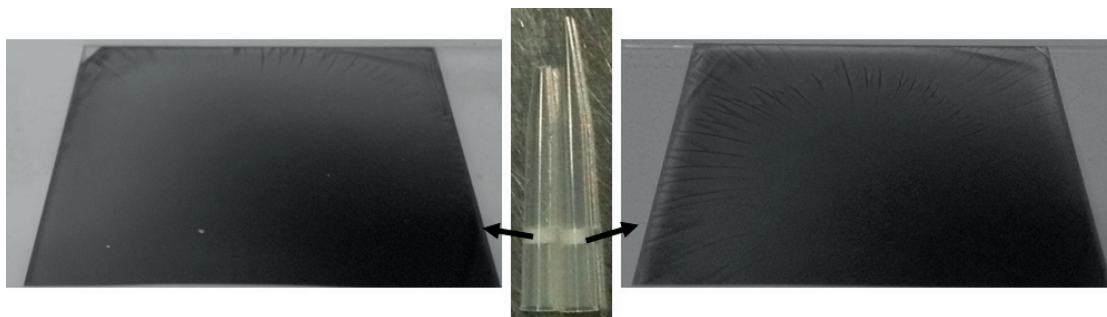
Figure B.4 – Pictures of 5x5 cm^2 area textured silicon wafer coated with a perovskite cell, showing the effect of the opening size of the dispersing tip used for the organo-halide solution. This tip opening trick was made available to the author by Dr. Soo-Jin Moon, while she was working on up-scaling solution processed perovskite cells to larger modules.

C Labview and Python applications written during the thesis

All source codes can be made available upon request to the author.

Labview-based MPPT

In order to measure a stabilized power output and be less prone to discussion around hysteresis in perovskite solar cells, I had to implement a maximum power point tracking (MPPT) system in our sun simulator software. The MPPT software is shown in Figure C.1, showing the front and backend of the Labview program. Here only the 3-point weight algorithm is shown as this was the most adapted to perovskite cells, and so the most used throughout this thesis. More standard Perturn & Observe algorithms were however also coded for comparison. It allowed to observe live the evolution of the maximum power and voltage and current at maximum power point, as well as to change live some parameters such as the voltage step or delay time. This software is used on a daily basis by all members of the perovskite group.

Data analysis Python software

The study of solar cells can generate a large amount of data. I therefore started from the beginning of my thesis to program several piece of code allowing to faster treat, analyze and summarize the raw data generated by J-V and EQE. After having started with Mathematica, I then migrated the code to Python in order to include a graphical user interface and make the software more easy to use for people not familiar with programming. The Figure C.2 shows what the user can see and do with this software, including a main window from which pop-up windows allows access to the specific softwares for each characterization technique. At the time of writing this thesis, the software is capable of analyzing J-V, MPPT, EQE, spectrophotometry, QSSPC, Hall effect, photoluminescence and ellipsometry data, as well as transfer matrix modeling for optical optimization of complex thin film multilayer stacks. The software is now used by over 10 people in the group in a daily basis to minimize the time spent on otherwise time-consuming data processing tasks.
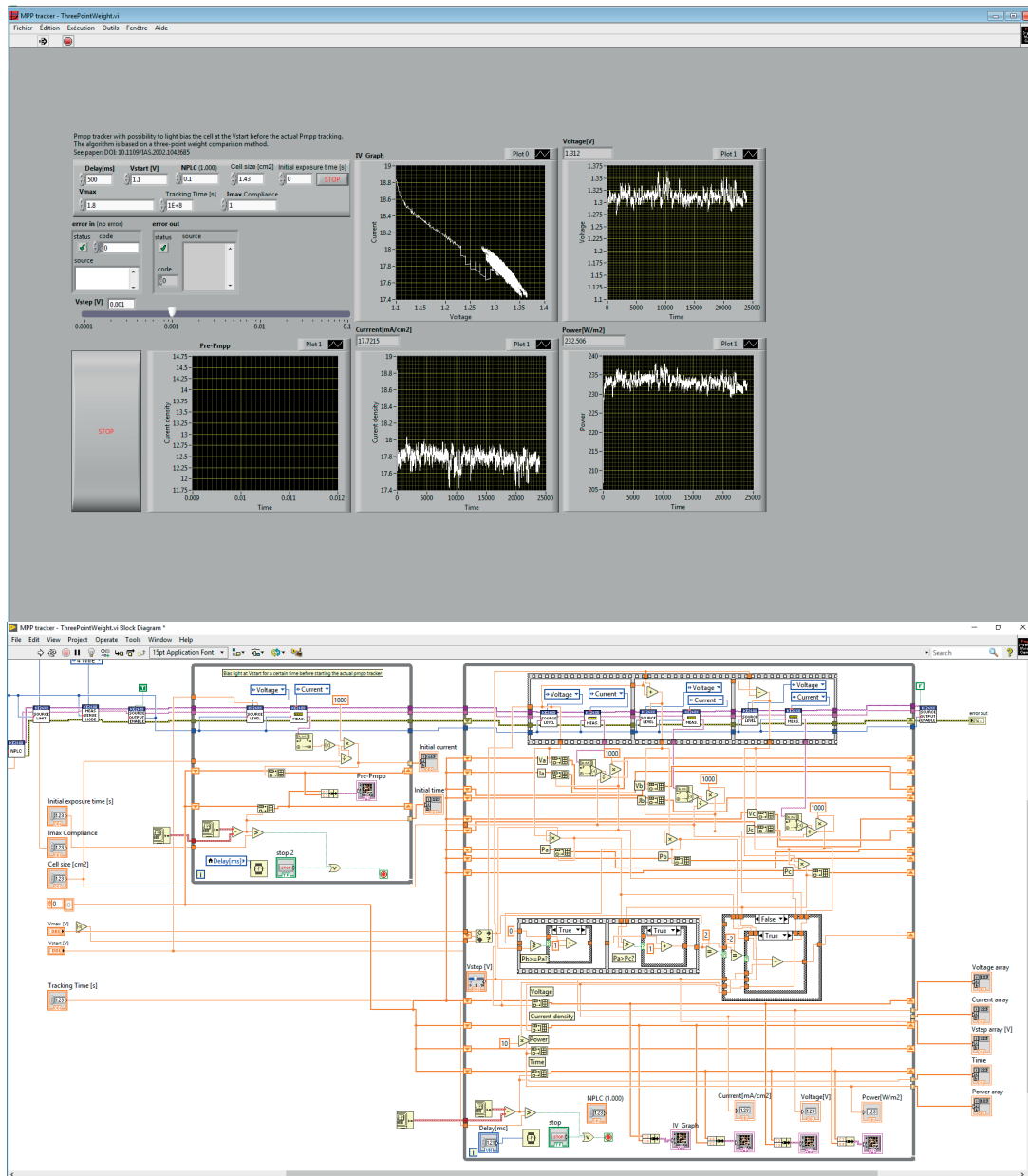
Figure C.1 – Front and backend of the Labview-based maximum power point tracking system implemented on the IV Malibu sun simulator and based on a three-point-weight algorithm.

Arduino-based sourcemeter with Python GUI: The Sourcuino

Together with Jonas Geissbuehler, we fabricated a sourcemeter based on an Arduino Uno and PCB board. The system was designed to be cheap (<100 CHF including all components), easily transportable (reduced it to fit the size of the Arduino board), and able to measure without significant noise small cells with around 1 cm^2 area. I designed and coded the graphical user interface with Python, taking particular attention for user-friendlyness, as the software and
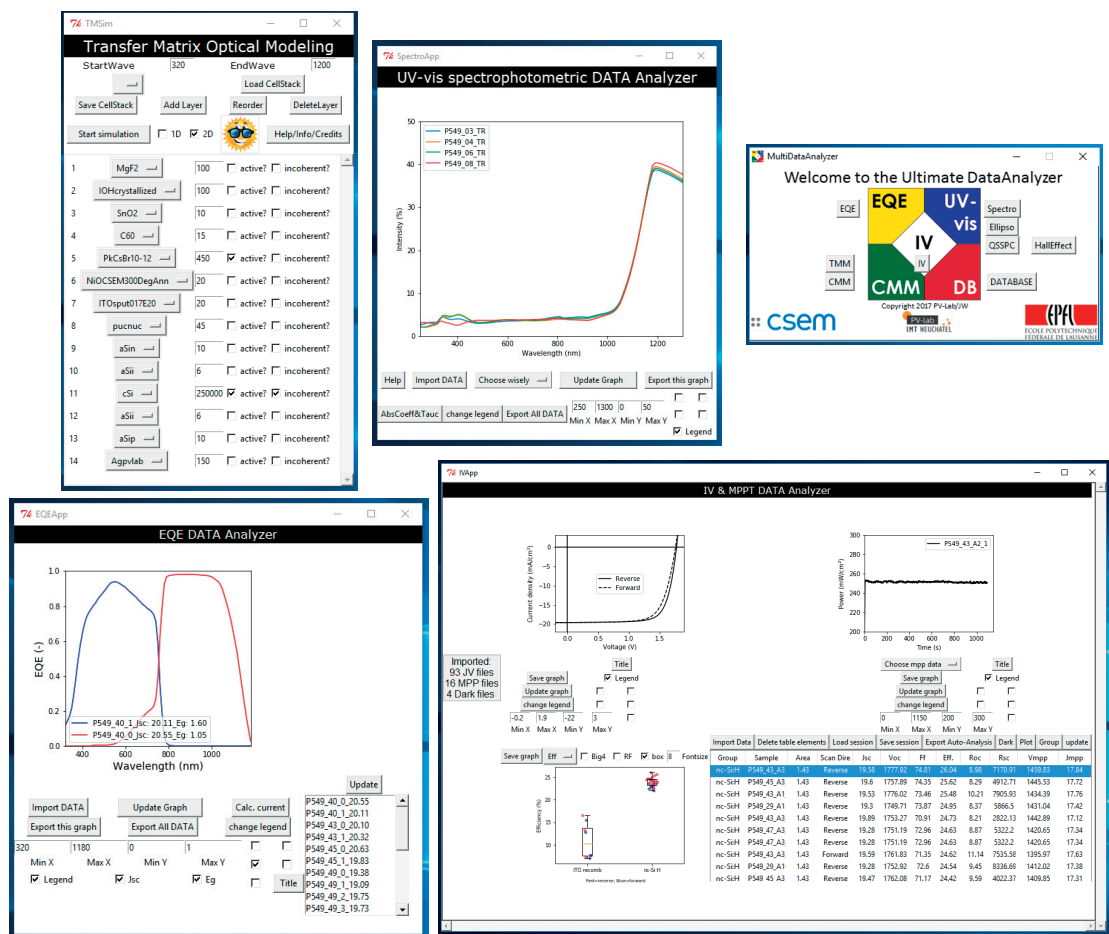
Figure C.2 – Overview of the graphical user interfaces of the Data Analysis software written in Python.

setup are meant to be used for both exhibitions, presentations for young students, and also for solar cell long-term degradation. To this end, the software has a function to alternate MPP tracking and J-V curve scanning with user-defined parameters (shown in Figure C.3). The setup can handle two devices in parallel and was used for the stability testing of perovskite/silicon tandem solar cells under light soaking with continuous MPPT and regular automatized *J-V* scans (see chapter 5).

Sheet: /
File: sourcunio_pcb_Gen2_1.sch

Title: Sourcuino   J. Werner & J.Geissbühler

| Size: A4 | Date: 2017-03-26 | **Rev: GEN2** |
| KiCad E.D.A. eeschema 4.0.1-stable | | Id: 1/1 |
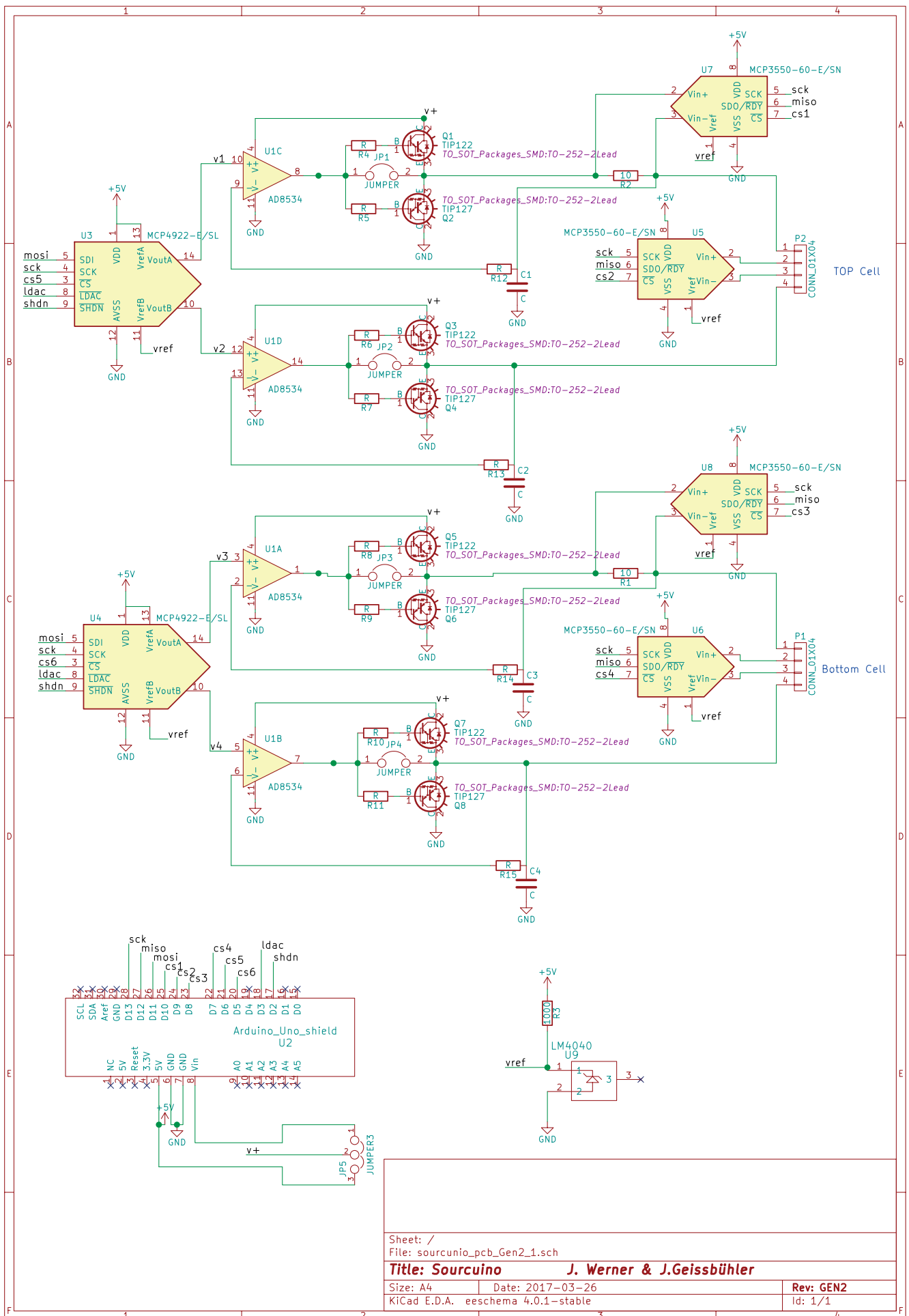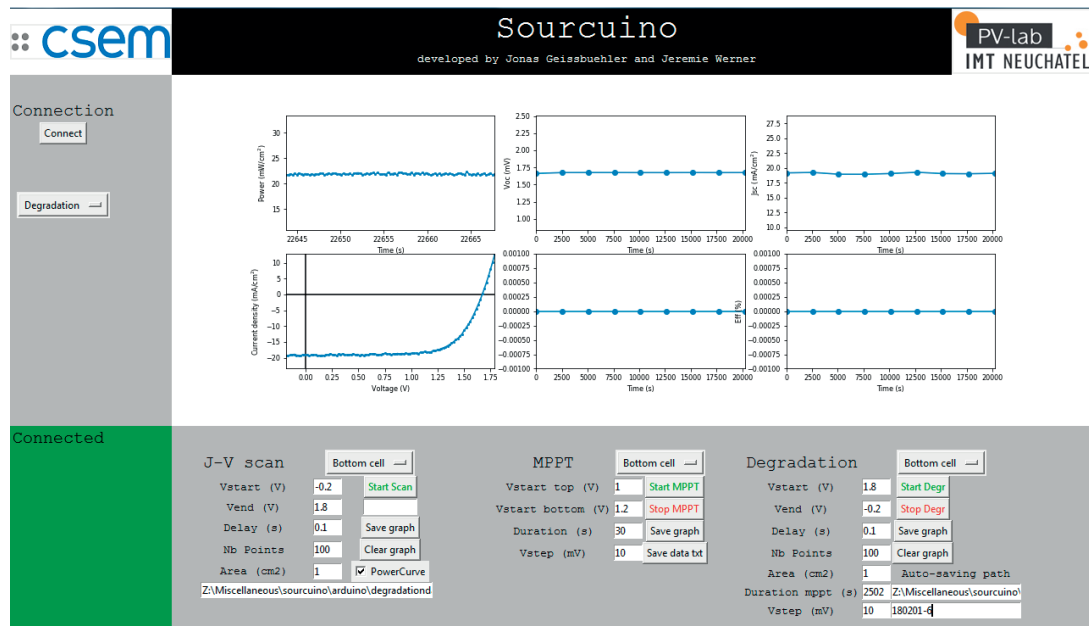
Figure C.3 – Graphical user interface view of the Sourcuino in "Degradation" configuration.

Glossary

FF fill factor.

J_{mpp} current density at maximum power point.

J_{sc} short circuit current density.

P_{mpp} power at maximum power point.

R_{sq} sheet resistance.

V_{mpp} voltage at maximum power point.

V_{oc} open circuit voltage.

J-V current density/voltage.

4TT 4-terminal tandem.

AFM atomic force microscope.

Al-BSF aluminum back surface field.

ALD atomic layer deposition.

Ar argon.

ARF microtextured antireflective foil.

BOS balance of system.

C$_{60}$ Buckminsterfullerene.

c-Si crystalline silicon.

c-TiO$_2$ compact titan dioxide.

CMP chemical mechanical polishing.

CO$_2$ carbon dioxide.

Glossary

Cs cesium.

CsBr cesium bromide.

CsCl cesium chloride.

CSEM Swiss Center for Electronics and Microtechnology.

CsI cesium iodide.

CVD chemical vapor deposition.

DEZ diethyl zinc.

DMF N, N-dimethylformamide.

DMSO dimethylsulphoxide.

DSP double-side mirror polished.

DST double-side textured.

E$_g$ optical bandgap.

EDX energy-dispersive X-ray spectroscopy.

EQE external quantum efficiency.

FA formamidinium, $[R_2N - CH = NR_2]^+$.

FABr formamidinium bromide.

FAI formamidinium iodide.

FIB focused ion beam.

FTO fluorine doped tin oxide.

FTPS Fourier-transform photocurrent spectroscopy.

HTL hole transporting layer.

IO:H hydrogenated indium oxide.

ITO indium tin oxide.

IZO indium zinc oxide.

IZrO indium zirconium oxide.

LCOE levelized cost of electricity.

LiF lithium fluoride.

LPCVD low-pressure chemical vapor deposition.

MA methylammonium, CH_3NH_3.

MAI methylammonium iodide, CH_3NH_3I.

MAPbI$_3$ methylammonium lead triiodide.

MgF$_2$ magnesium fluoride.

MoO$_3$ stoichiometric molybdenum oxide.

MoO$_x$ molybdenum oxide.

mp-TiO$_2$ mesoporous titan dioxide.

MPPT maximum power point tracking.

N$_2$ nitrogen.

nc-Si:H nanocrystalline silicon.

NiO$_x$ nickel oxide.

NIR near-infrared .

NPB N,N' -Bis(naphthalen-1-yl)-N,N' -bis(phenyl)-benzidine.

O$_2$ oxygen.

PbI$_2$ lead iodide.

PCBM phenyl-C61-butyric-acid-methyl-ester.

PDMS polydimethylsiloxane.

PDS photothermal deflection spectroscopy.

PECVD plasma enhanced chemical vapor deposition.

PEDOT:PSS poly(3,4-ethylenedioxythiophene)-poly(styrenesulfonate).

PEIE polyethyleneimine.

PERC passivated emitter rear contact.

PL photoluminescence.

PTAA poly(triarylamine).

SEM scanning electron microscope.

SHJ amorphous-silicon/crystalline-silicon heterojunction solar cell.

SiO$_2$ silicon dioxide.

SnO$_2$ tin oxide.

spiro-OMeTAD 2,2',7,7'-Tetrakis-(N,N-di-4-methoxyphenylamino)-9,9'-spirobifluorenes.

spiro-TTB 2,2',7,7'-Tetra(N,N -di-p -tolyl)amino-9,9-spirobifluorene.

SST single-side textured.

TCO transparent conductive oxide.

TEM transmission electron microscope.

TiO$_2$ titan dioxide.

TMO transition metal oxide.

TmPyPB 1,3,5-Tri[(3-pyridyl) -phen-3-yl]benzene.

V$_2$O$_5$ vanadium pentoxide.

VASE variable-angle spectroscopic ellipsometry.

WO$_3$ stoichiometric tungsten oxide.

WO$_x$ tungsten oxide.

XPS x-ray photoelectron spectroscopy.

XRD x-ray diffraction.

ZnO zinc oxide.

ZTO zinc tin oxide.

Bibliography

[1] Jérémie Werner, Bjoern Niesen, and Christophe Ballif. Perovskite/Silicon Tandem Solar Cells: Marriage of Convenience or True Love Story? - An Overview. *Advanced Materials Interfaces*, 5(1):1700731, jan 2018.

[2] International Energy Agency. World Energy Outlook 2017. Technical report, 2017.

[3] Swiss Federal Office of Energy SFOE. Energy Consumption in Switzerland 2016. Technical Report June, 2017.

[4] Sunpower. X-Series Residential Solar Panels SunPower Residential Solar Panels Engineered for Peace of Mind X-Series. 2016.

[5] IEC standard 61215. IEC International Standard for design qualification and type approval of PV modules, IEC 61215:2016. In *International Electrotechnical Commission*, 2016.

[6] Kunta Yoshikawa, Wataru Yoshida, Toru Irie, Hayato Kawasaki, Katsunori Konishi, Hirotaka Ishibashi, Tsuyoshi Asatani, Daisuke Adachi, Masanori Kanematsu, Hisashi Uzu, and Kenji Yamamoto. Exceeding conversion efficiency of 26% by heterojunction interdigitated back contact solar cell with thin film Si technology. *Solar Energy Materials and Solar Cells*, (June), 2017.

[7] NREL Efficiency Chart. NREL Efficiency Chart, 2017.

[8] Louise C. Hirst and Nicholas J. Ekins-Daukes. Fundamental losses in solar cells. *Prog. Photovolt: Res. Appl.*, 19(August 2010):286–293, 2011.

[9] William Shockley and Hans J. Queisser. Detailed balance limit of efficiency of p-n junction solar cells. *Journal of Applied Physics*, 32(3):510–519, 1961.

[10] W. Shockley and W. T. Read. Statistics of the Recombination of Holes and Electrons. *Physical Review*, 87(46):835–842, 1952.

[11] ITRPV. International Technology Roadmap for Photovoltaic— 2016 Results. Technical report, 2017.

Bibliography

[12] World Economic Forum. Renewable Infrastructure Investment Handbook: A Guide for Institutional Investors. Technical Report December, 2016.

[13] Christiana B Honsberg, Richard C Corkish, and Stephen P Bremner. A new generalized detailed balance formulation to calculate solar cell efficiency limits. *Georgia Institute of Technology*, 1:3, 2001.

[14] Stephanie Essig, Christophe Allebé, Timothy Remo, John F. Geisz, Myles A. Steiner, Kelsey Horowitz, Loris Barraud, J. Scott Ward, Manuel Schnabel, Antoine Descoeudres, David L. Young, Michael Woodhouse, Matthieu Despeisse, Christophe Ballif, and Adele Tamboli. Raising the one-sun conversion efficiency of III-V/Si solar cells to 32.8% for two junctions and 35.9% for three junctions. *Nature Energy*, 2(9), 2017.

[15] David C. Bobela, Lynn Gedvilas, Michael Woodhouse, Kelsey A. W. Horowitz, and Paul A. Basore. Economic competitiveness of III-V on silicon tandem one-sun photovoltaic solar modules in favorable future scenarios. *Prog. Photovolt: Res. Appl.*, 25:41–48, 2017.

[16] T. Söderström, F. J. Haug, X. Niquille, V. Terrazzoni, and C. Ballif. Asymmetric intermediate reflector for tandem micromorph thin film silicon solar cells. *Applied Physics Letters*, 94(6):1–4, 2009.

[17] Jan Willem Schuttauf, Grégory Bugnon, Michael Stuckelberger, Simon Hänni, Mathieu Boccard, Matthieu Despeisse, Franz Josef Haug, Fanny Meillaud, and Christophe Ballif. Thin-film silicon triple-junction solar cells on highly transparent front electrodes with stabilized efficiencies up to 12.8%. *IEEE Journal of Photovoltaics*, 4(3):757–762, 2014.

[18] Corsin Battaglia, Andres Cuevas, and Stefaan De Wolf. High-efficiency Crystalline Silicon Solar Cells: Status and Perspectives. *Energy & Environmental Science*, 9:1552–1576, 2016.

[19] F Fertig, R Lantzsch, A Mohr, M Schaper, M Bartzsch, D Wissen, F Kersten, A Mette, S Peters, A Eidner, J Cieslak, K Duncker, M Junghänel, E Jarzembowski, M Kauert, D Meißner, B Reiche, S Geißler, S Hörnlein, C Klenke, L Niebergall, A Schönmann, A Weihrauch, F Stenzel, A Hofmann, T Rudolph, A Schwabedissen, M Gundermann, M Fischer, J W Müller, and D J W Jeong. Mass production of p-type Cz silicon solar cells approaching average stable conversion efficiencies of 22%. In *7th International Conference on Silicon Photovoltaics, SiliconPV 2017*. Elsevier Ltd, 2017.

[20] Kunta Yoshikawa, Hayato Kawasaki, Wataru Yoshida, Toru Irie, Katsunori Konishi, Kunihiro Nakano, Toshihiko Uto, Daisuke Adachi, Masanori Kanematsu, Hisashi Uzu, and Kenji Yamamoto. Silicon heterojunction solar cell with interdigitated back contacts for a photoconversion efficiency over 26%. *Nature Energy*, 2(March):17032, 2017.

[21] Armin Richter, Martin Hermle, and Stefan W. Glunz. Reassessment of the limiting efficiency for crystalline silicon solar cells. *IEEE Journal of Photovoltaics*, 3(4):1184–1191, 2013.

[22] Mikio Taguchi, Ayumu Yano, Satoshi Tohoda, Kenta Matsuyama, Yuya Nakamura, Takeshi Nishiwaki, Kazunori Fujita, and Eiji Maruyama. 24.7% Record efficiency HIT solar cell on thin silicon wafer. *IEEE Journal of Photovoltaics*, 4(1):96–99, 2014.

[23] Zachary C. Holman, Antoine Descoeudres, Stefaan De Wolf, and Christophe Ballif. Record Infrared Internal Quantum Efficiency in Silicon Heterojunction Solar Cells With Dielectric/Metal Rear Reflectors. *IEEE Journal of Photovoltaics*, 3(4):1243–1249, 2013.

[24] Michelle Vaisman, Shizhao Fan, Kevin Nay Yaung, Emmett Perl, Diego Martín-Martín, Zhengshan J. Yu, Mehdi Leilaeioun, Zachary C. Holman, and Minjoo L. Lee. 15.3%-Efficient GaAsP Solar Cells on GaP/Si Templates. *ACS Energy Letters*, 2(8):1911–1918, aug 2017.

[25] Martin A. Green and Anita Wing-Yi Ho-Baillie. Perovskite Solar Cells: The Birth of a New Era in Photovoltaics. *ACS Energy Letters*, 2:822–830, 2017.

[26] Juan-Pablo Correa-Baena, Michael Saliba, Tonio Buonassisi, Michael Grätzel, Antonio Abate, Wolfgang Tress, and Anders Hagfeldt. Promises and challenges of perovskite solar cells. *Science*, 358(6364):739–744, 2017.

[27] Seong Sik Shin, Eun Joo Yeom, Woon Seok Yang, Seyoon Hur, Min Gyu Kim, Jino Im, Jangwon Seo, Jun Hong Noh, and Sang Il Seok. Colloidally prepared La-doped BaSnO3 electrodes for efficient , photostable perovskite solar cells. *Science*, 6620(March), 2017.

[28] Meng Zhang, Jae Sung Yun, Qingshan Ma, Jianghui Zheng, Cho-Fai Jonathan Lau, Xiaofan Deng, Jincheol Kim, Dohyung Kim, Jan Seidel, Martin A. Green, Shujuan Huang, and Anita Wing-Yi Ho-Baillie. High Efficiency Rubidium Incorporated Perovskite Solar Cells by Gas Quenching. *ACS Energy Letters*, 2:438–444, 2017.

[29] M. Saliba, T. Matsui, K. Domanski, J.-Y. Seo, A. Ummadisingu, S. M. Zakeeruddin, J.-P. Correa-Baena, W. R. Tress, A. Abate, A. Hagfeldt, and M. Gratzel. Incorporation of rubidium cations into perovskite solar cells improves photovoltaic performance. *Science*, 2016.

[30] Hairen Tan, Ankit Jain, Oleksandr Voznyy, Xinzheng Lan, F. Pelayo García de Arquer, James Z. Fan, Rafael Quintero-Bermudez, Mingjian Yuan, Bo Zhang, Yicheng Zhao, Fengjia Fan, Peicheng Li, Li Na Quan, Yongbiao Zhao, Zheng-Hong Lu, Zhenyu Yang, Sjoerd Hoogland, and Edward H. Sargent. SI - Efficient and stable solution-processed planar perovskite solar cells via contact passivation. *Science*, (February), 2017.

[31] Kyung Taek Cho, Sanghyun Paek, G. Grancini, Cristina Roldán Carmona, Peng Gao, Yong Hui Lee, and Mohammad Khaja Nazeeruddin. SI - Highly efficient perovskite solar cells with a compositional engineered perovskite/hole transporting material interface. *Energy Environ. Sci.*, 85:1–3, 2017.

Bibliography

[32] Mojtaba Abdi-Jalebi, Zahra Andaji-Garmaroudi, Stefania Cacovich, Camille Stavrakas, Bertrand Philippe, Johannes M Richter, Mejd Alsari, Edward P Booker, Eline M Hutter, Andrew J Pearson, Samuele Lilliu, Tom J Savenije, Håkan Rensmo, Giorgio Divitini, Caterina Ducati, Richard H Friend, and Samuel D Stranks. Maximizing and stabilizing luminescence from halide perovskites with potassium passivation. *Nature*, 555(7697):497–501, mar 2018.

[33] Stefaan De Wolf, Jakub Holovsky, Soo-Jin Moon, Philipp Löper, Bjoern Niesen, Martin Ledinsky, Franz-Josef Haug, Jun-Ho Yum, and Christophe Ballif. Organometallic Halide Perovskites: Sharp Optical Absorption Edge and Its Relation to Photovoltaic Performance. *The Journal of Physical Chemistry Letters*, 5(6):1035–1039, mar 2014.

[34] Eva Lisa Unger, Lukas Kegelmann, Klara Suchan, David Sörell, Lars Korte, and Steve Albrecht. Roadmap and roadblocks for the band gap tunability of metal halide perovskites. *J. Mater. Chem. A*, 5:11401–11409, 2017.

[35] Wolfgang Tress. Perovskite Solar Cells on the Way to Their Radiative Efficiency Limit - Insights Into a Success Story of High Open-Circuit Voltage and Low Recombination. *Advanced Energy Materials*, 7(14):1602358, jul 2017.

[36] Samuel D Stranks, Giles E Eperon, Giulia Grancini, Christopher Menelaou, Marcelo J P Alcocer, Tomas Leijtens, Laura M Herz, Annamaria Petrozza, and Henry J Snaith. Electron-Hole Diffusion Lengths Exceeding 1 Micrometer in an Organometal Trihalide Perovskite Absorber. *Science*, 342(6156):341–344, oct 2013.

[37] Luis M. Pazos-Outón, Monika Szumilo, Robin Lamboll, Johannes M. Richter, Micaela Crespo-quesada, Mojtaba Abdi-Jalebi, Harry J. Beeson, Milan Vrucinic, Mejd Alsari, Henry J. Snaith, Bruno Ehrler, Richard H. Friend, and Felix Deschler. Photon recycling in lead iodide perovskite solar cells. *Science*, 351(6280):1430–1434, 2016.

[38] Marina Monteiro Lunardi, Anita Wing Yi Ho-Baillie, Juan Pablo Alvarez-Gaitan, Stephen Moore, and Richard Corkish. A life cycle assessment of perovskite/silicon tandem solar cells. *Progress in Photovoltaics: Research and Applications*, 25(8):679–695, aug 2017.

[39] Ilke Celik, Zhaoning Song, Alexander J. Cimaroli, Yanfa Yan, Michael J. Heben, and Defne Apul. Life Cycle Assessment (LCA) of perovskite PV cells projected from lab to fab. *Solar Energy Materials and Solar Cells*, 156:157–169, 2016.

[40] Spencer T. Williams, Adharsh Rajagopal, Chu Chen Chueh, and Alex K Y Jen. Current Challenges and Prospective Research for Upscaling Hybrid Perovskite Photovoltaics. *Journal of Physical Chemistry Letters*, 7(5):811–819, 2016.

[41] Matthew R. Leyden, Yan Jiang, and Yabing Qi. Chemical Vapor Deposition Grown Formamidinium Perovskite Solar Modules with High Steady State Power and Thermal Stability. *Journal of Materials Chemistry A*, 4(13125), 2016.

[42] Ibraheem Almansouri, Anita Ho-Baillie, Stephen P. Bremner, and Martin A. Green. Supercharging Silicon Solar Cell Performance by Means of Multijunction Concept. *IEEE Journal of Photovoltaics*, 5(3):968–976, 2015.

[43] Anthony L. Lentine, Gregory N. Nielson, Murat Okandan, Jose Luis Cruz-Campa, and Anna Tauke-Pedretti. Voltage matching and optimal cell compositions for microsystem-enabled photovoltaic modules. *IEEE Journal of Photovoltaics*, 4(6):1593–1602, 2014.

[44] Rune Strandberg. Spectral and temperature sensitivity of area de-coupled tandem modules. In *Proceedings of the 42nd IEEE Photovoltaic Specialist Conference*, New Orleans, 2015.

[45] Hisashi Uzu, Mitsuru Ichikawa, Masashi Hino, Kunihiro Nakano, Tomomi Meguro, José Luis Hernández, Seon Kim, Nam-gyu Park, and Kenji Yamamoto. High efficiency solar cells combining a perovskite and a silicon heterojunction solar cells via an optical splitting system. *Applied Physics Letters*, 106(013506), 2015.

[46] Kenji Yamamoto, Daisuke Adachi, Hisashi Uzu, Mitsuru Ichikawa, Toru Terashita, Tomomi Meguro, Naoaki Nakanishi, Masashi Yoshimi, and José Luis Hernández. High-efficiency heterojunction crystalline Si solar cell and optical splitting structure fabricated by applying thin-film Si technology. *Japanese Journal of Applied Physics*, 54(8S1):08KD15, aug 2015.

[47] Rui Sheng, Anita W. Y. Ho-Baillie, Shujuan Huang, Mark Keevers, Xiaojing Hao, Liangcong Jiang, Yi-Bing Cheng, and Martin a. Green. Four-Terminal Tandem Solar Cells Using CH3NH3PbBr3 by Spectrum Splitting. *The Journal of Physical Chemistry Letters*, 6(19):3931–3934, 2015.

[48] Yan Li, Hongwei Hu, Bingbing Chen, Teddy Salim, Jing Zhang, Jianning Ding, Ningyi Yuan, and Yeng Ming Lam. Reflective perovskite solar cells for efficient tandem applications. *J. Mater. Chem. C*, 5:134–139, 2017.

[49] Zhengshan J Yu, Kathryn C Fisher, Brian M Wheelwright, Roger P Angel, and Zachary C Holman. PVMirror : A New Concept for Tandem Solar Cells and Hybrid Solar Converters. *IEEE Journal of Photovoltaics*, pages 1–9, 2015.

[50] Thomas P. White, Niraj N. Lal, and Kylie R. Catchpole. Tandem Solar Cells Based on High-Efficiency c-Si Bottom cells: top cell requirements for > 30 % Efficiency. *IEEE Journal of Photovoltaics*, 4(1):208–214, 2014.

[51] Niraj N Lal, Thomas P White, and Kylie R Catchpole. Optics and Light Trapping for Tandem Solar Cells on Silicon. *IEEE Journal of Photovoltaics*, 4(6):1380–1386, 2014.

[52] Ibraheem Almansouri, Anita Ho-Baillie, and Martin A Green. Ultimate efficiency limit of single-junction perovskite and dual-junction perovskite / silicon two- terminal devices. *Japanese Journal of Applied Physics*, 54, 2015.

Bibliography

[53] Fan Fu, Stefano Pisoni, Thomas P Weiss, Thomas Feurer, Aneliia Wäckerlin, Peter Fuchs, Shiro Nishiwaki, Lukas Zortea, Ayodhya N Tiwari, and Stephan Buecheler. Compositionally Graded Absorber for Efficient and Stable Near-Infrared-Transparent Perovskite Solar Cells. *Advanced Science*, page 1700675, jan 2018.

[54] Fan Fu, Thomas Feurer, Thomas Paul Weiss, Stefano Pisoni, Enrico Avancini, Christian Andres, Stephan Buecheler, and Ayodhya N Tiwari. High-efficiency inverted semi-transparent planar perovskite solar cells in substrate configuration. *Nature Energy*, 2(16190), 2016.

[55] Heping Shen, The Duong, Jun Peng, Daniel Jacobs, Nandi Wu, Junbo Gong, Yiliang Wu, Siva Krishna Karuturi, Xiao Fu, Klaus Weber, Xudong Xiao, Thomas P. White, and Kylie Catchpole. Mechanically-stacked perovskite/CIGS tandem solar cells with efficiency of 23.9% and reduced oxygen sensitivity. *Energy & Environmental Science*, 11(2):394–406, 2018.

[56] Teodor Todorov, Talia Gershon, Oki Gunawan, Charles Sturdevant, and Supratik Guha. Perovskite-kesterite monolithic tandem solar cells with high open-circuit voltage. *Applied Physics Letters*, 105(17):173902, oct 2014.

[57] Yao Liu, Lawrence A. Renna, Monojit Bag, Zachariah A. Page, Paul Y. Kim, Jaewon Choi, Todd Emrick, Dhandapani Venkataraman, and Thomas P. Russell. High Efficiency Tandem Thin-Perovskite/Polymer Solar Cells with a Graded Recombination Layer. *ACS Applied Materials & Interfaces*, 8(11):7070–7076, 2016.

[58] Dewei Zhao, Changlei Wang, Zhaoning Song, Yue Yu, Cong Chen, Xingzhong Zhao, Kai Zhu, and Yanfa Yan. Four-Terminal All-Perovskite Tandem Solar Cells Achieving Power Conversion Efficiencies Exceeding 23%. *ACS Energy Letters*, pages 305–306, jan 2018.

[59] Dewei Zhao, Yue Yu, Changlei Wang, Weiqiang Liao, Niraj Shrestha, Corey R. Grice, Alexander J. Cimaroli, Lei Guan, Randy J. Ellingson, Kai Zhu, Xingzhong Zhao, Ren-Gen Xiong, and Yanfa Yan. Low-bandgap mixed tin–lead iodide perovskite absorbers with long carrier lifetimes for all-perovskite tandem solar cells. *Nature Energy*, 2(March):17018, 2017.

[60] Giles E Eperon, Tomas Leijtens, Kevin A Bush, R. Prasanna, Thomas Green, J. T.-W. Wang, D. P. McMeekin, George Volonakis, Rebecca L Milot, R. May, A. Palmstrom, Daniel J Slotcavage, R. A. Belisle, Jay B Patel, Elizabeth S Parrott, Rebecca J Sutton, Wen Ma, Farhad Moghadam, Bert Conings, Aslihan Babayigit, H.-G. Boyen, S. Bent, Feliciano Giustino, Laura M Herz, Michael B Johnston, M. D. McGehee, and Henry J Snaith. Perovskite-perovskite tandem photovoltaics with optimized band gaps. *Science*, 354(6314):861–865, 2016.

[61] Zhibin Yang, Adharsh Rajagopal, Chu Chen Chueh, Sae Byeok Jo, Bo Liu, Ting Zhao, and Alex K Y Jen. Stable Low-Bandgap Pb-Sn Binary Perovskites for Tandem Solar Cells. *Advanced Materials*, 28(40):8990–8997, 2016.

132

[62] D. B. Mitzi, C. a. Feild, W. T. a. Harrison, and a. M. Guloy. Conducting tin halides with a layered organic-based perovskite structure. *Nature*, 369(6480):467–469, 1994.

[63] Akihiro Kojima, Kenjiro Teshima, Yasuo Shirai, and Tsutomu Miyasaka. Organometal halide perovskites as visible-light sensitizers for photovoltaic cells. *Journal of the American Chemical Society*, 131(17):6050–1, may 2009.

[64] Michael M Lee, Joël Teuscher, Tsutomu Miyasaka, Takurou N Murakami, and Henry J Snaith. Efficient Hybrid Solar Cells Based on Meso-Superstructured Organometal Halide Perovskites. *Science*, 338(6107):643–647, nov 2012.

[65] Mingzhen Liu, Michael B Johnston, and Henry J Snaith. Efficient planar heterojunction perovskite solar cells by vapour deposition. *Nature*, 501(7467):395–8, sep 2013.

[66] Henry J. Snaith. Perovskites : The Emergence of a New Era for Low-Cost , High-Efficiency Solar Cells. *The Journal of Physical Chemistry Letters*, 4:3623–3630, 2013.

[67] Philipp Löper, Bjoern Niesen, Soo-Jin Moon, Silvia Martin de Nicolas, Jakub Holovsky, Zdenek Remes, Martin Ledinsky, Franz-Josef Haug, Jun-Ho Yum, Stefaan De Wolf, and Christophe Ballif. Organic–Inorganic Halide Perovskites: Perspectives for Silicon-Based Tandem Solar Cells. *IEEE Journal of Photovoltaics*, 4(6):1545–1551, nov 2014.

[68] Bennett W. Schneider, Niraj N. Lal, Simeon Baker-Finch, and Thomas P. White. Pyramidal surface textures for light trapping and antireflection in perovskite-on-silicon tandem solar cells. *Optics Express*, 22(S6):A1422, aug 2014.

[69] Steve Albrecht, Michael Saliba, Juan-Pablo Correa-Baena, Klaus Jäger, Lars Korte, Anders Hagfeldt, Michael Grätzel, and Bernd Rech. Towards optical optimization of planar monolithic perovskite/silicon-heterojunction tandem solar cells. *Journal of Optics*, 18(6):064012, 2016.

[70] Philipp Löper, Soo-Jin Moon, Sílvia Martín de Nicolas, Bjoern Niesen, Martin Ledinsky, Sylvain Nicolay, Julien Bailat, Jun-Ho Yum, Stefaan De Wolf, and Christophe Ballif. Organic–inorganic halide perovskite/crystalline silicon four-terminal tandem solar cells. *Phys. Chem. Chem. Phys.*, 17:1619–1629, 2015.

[71] Colin D Bailie, M Greyson Christoforo, Jonathan P Mailoa, Andrea R Bowring, Eva L Unger, William H Nguyen, Julian Burschka, Norman Pellet, Jungwoo Z. Lee, Michael Grätzel, Rommel Noufi, Tonio Buonassisi, Alberto Salleo, and Michael D. McGehee. Semi-transparent perovskite solar cells for tandems with silicon and CIGS. *Energy Environ. Sci.*, 8:956–963, 2014.

[72] Jérémie Werner, Guy Dubuis, Arnaud Walter, Philipp Löper, Soo-Jin Moon, Sylvain Nicolay, Monica Morales-Masis, Stefaan De Wolf, Bjoern Niesen, and Christophe Ballif. Sputtered rear electrode with broadband transparency for perovskite solar cells. *Solar Energy Materials and Solar Cells*, 141:407–413, 2015.

Bibliography

[73] D. P. McMeekin, G. Sadoughi, W. Rehman, G. E. Eperon, M. Saliba, M. T. Horantner, A. Haghighirad, N. Sakai, L. Korte, B. Rech, M. B. Johnston, L. M. Herz, and H. J. Snaith. A mixed-cation lead mixed-halide perovskite absorber for tandem solar cells. *Science*, 351(6269):151–155, jan 2016.

[74] The Duong, Niraj Lal, Dale Grant, Daniel Jacobs, Peiting Zheng, Shakir Rahman, Heping Shen, Matthew Stocks, Andrew Blakers, Klaus Weber, Thomas P White, and Kylie R Catchpole. Semitransparent Perovskite Solar Cell With Sputtered Front and Rear Electrodes for a Four-Terminal Tandem. *IEEE Journal of Photovoltaics*, pages 1–9, 2016.

[75] Bo Chen, Yang Bai, Zhengshan Yu, Tao Li, Xiaopeng Zheng, Qingfeng Dong, Liang Shen, Mathieu Boccard, Alexei Gruverman, Zachary Holman, and Jinsong Huang. Efficient Semitransparent Perovskite Solar Cells for 23.0%-Efficiency Perovskite/Silicon Four-Terminal Tandem Cells. *Advanced Energy Materials*, 6(19):1601128, oct 2016.

[76] Jérémie Werner, Loris Barraud, Arnaud Walter, Matthias Bräuninger, Florent Sahli, Davide Sacchetto, Nicolas Tétreault, Bertrand Paviet-Salomon, S.-J. Soo-Jin Moon, Christophe Allebé, Matthieu Despeisse, Sylvain Nicolay, Stefaan De Wolf, Bjoern Niesen, and Christophe Ballif. Efficient Near-Infrared-Transparent Perovskite Solar Cells Enabling Direct Comparison of 4-Terminal and Monolithic Perovskite/Silicon Tandem Cells. *ACS Energy Letters*, 1(2):474–480, 2016.

[77] Jun Peng, The Duong, Xianzhong Zhou, Heping Shen, Yiliang Wu, Hemant Kumar Mulmudi, Yimao Wan, Dingyong Zhong, Juntao Li, Takuya Tsuzuki, Klaus J Weber, Kylie R Catchpole, and Thomas P White. Efficient Indium-Doped TiO x Electron Transport Layers for High-Performance Perovskite Solar Cells and Perovskite-Silicon Tandems. *Advanced Energy Materials*, 7:1601768, 2017.

[78] The Duong, YiLiang Wu, Heping Shen, Jun Peng, Xiao Fu, Daniel Jacobs, Er-Chien Wang, Teng Choon Kho, Kean Chern Fong, Matthew Stocks, Evan Franklin, Andrew Blakers, Ngwe Zin, Keith McIntosh, Wei Li, Yi-Bing Cheng, Thomas P. White, Klaus Weber, and Kylie Catchpole. Rubidium Multication Perovskite with Optimized Bandgap for Perovskite-Silicon Tandem with over 26% Efficiency. *Advanced Energy Materials*, 1700228:1–11, 2017.

[79] Manoj Jaysankar, Weiming Qiu, Maarten van Eerden, Tom Aernouts, Robert Gehlhaar, Maarten Debucquoy, Ulrich W. Paetzold, and Jef Poortmans. Four-Terminal Perovskite/Silicon Multijunction Solar Modules. *Advanced Energy Materials*, 7(15):1602807, aug 2017.

[80] César Omar Ramírez Quiroz, Yilei Shen, Michael Salvador, Karen Forberich, Nadine Schrenker, George D. Spyropoulos, Thomas Heumüller, Benjamin Wilkinson, Thomas Kirchartz, Erdmann Spiecker, Pierre J. Verlinden, Xueling Zhang, Martin A. Green, Anita Ho-Baillie, and Christoph J Brabec. Balancing electrical and optical losses for efficient 4-terminal Si–perovskite solar cells with solution processed percolation electrodes. *Journal of Materials Chemistry A*, 6(8):3583–3592, 2018.

[81] Jonathan P. Mailoa, Colin D. Bailie, Eric C. Johlin, Eric T. Hoke, Austin J. Akey, William H. Nguyen, Michael D. McGehee, and Tonio Buonassisi. A 2-terminal perovskite/silicon multijunction solar cell enabled by a silicon tunnel junction. *Applied Physics Letters*, 106:121105, 2015.

[82] Steve Albrecht, Michael Saliba, Juan Pablo Correa Baena, Felix Lang, Lukas Kegelmann, Mathias Mews, Ludmilla Steier, Antonio Abate, Jörg Rappich, Lars Korte, Rutger Schlatmann, Mohammad Khaja Nazeeruddin, Anders Hagfeldt, Michael Grätzel, and Bernd Rech. Monolithic perovskite/silicon-heterojunction tandem solar cells processed at low temperature. *Energy & Environmental Science*, 9(1):1–6, 2016.

[83] Jérémie Werner, Ching-Hsun Weng, Arnaud Walter, Luc Fesquet, Johannes Peter Seif, Stefaan De Wolf, Bjoern Niesen, and Christophe Ballif. Efficient Monolithic Perovskite/Silicon Tandem Solar Cell with Cell Area >1 cm 2. *The Journal of Physical Chemistry Letters*, 7(1):161–166, jan 2016.

[84] Jérémie Werner, Arnaud Walter, Esteban Rucavado, S.-J. Soo-Jin Moon, Davide Sacchetto, Michael Rienaecker, Robby Peibst, Rolf Brendel, Xavier Niquille, S. De Wolf, Philipp Löper, Monica Morales-Masis, Sylvain Nicolay, Bjoern Niesen, Christophe Ballif, Stefaan De Wolf, Philipp Löper, Monica Morales-Masis, Sylvain Nicolay, Bjoern Niesen, and Christophe Ballif. Zinc tin oxide as high-temperature stable recombination layer for mesoscopic perovskite/silicon monolithic tandem solar cells. *Applied Physics Letters*, 109(23):233902, 2016.

[85] Kevin A. Bush, Axel F. Palmstrom, Zhengshan (Jason) Yu, Mathieu Boccard, Rongrong Cheacharoen, Jonathan P. Mailoa, David P. McMeekin, Robert L. Z. Hoye, Colin D. Bailie, Tomas Leijtens, Ian Marius Peters, Maxmillian C. Minichetti, Nicholas Rolston, Rohit Prasanna, Sarah S.E. Sofia, Duncan Harwood, Wen Ma, Farhad Moghadam, Henry J. Snaith, Tonio Buonassisi, Zachary C. Holman, Stacey F. Bent, and Michael D. McGehee. 23.6%-efficient monolithic perovskite/silicon tandem solar cells with improved stability. *Nature Energy*, 2(4):17009, feb 2017.

[86] Florent Sahli, Brett A. Kamino, Jérémie Werner, Matthias Bräuninger, Bertrand Paviet-Salomon, Loris Barraud, Raphaël Monnard, Johannes Peter Seif, Andrea Tomasi, Quentin Jeangros, Aïcha Hessler-Wyser, Stefaan De Wolf, Matthieu Despeisse, Sylvain Nicolay, Bjoern Niesen, and Christophe Ballif. Improved Optics in Monolithic Perovskite/Silicon Tandem Solar Cells with a Nanocrystalline Silicon Recombination Junction. *Advanced Energy Materials*, (1701609):1701609, oct 2017.

[87] YiLiang Wu, Di Yan, Jun Peng, The Duong, Yimao Wan, Sieu Pheng Phang, Heping Shen, Nandi Wu, Chog Barugkin, Xiao Fu, Sachin Surve, Dale Grant, Daniel Walter, Thomas P. White, Kylie R. Catchpole, and Klaus J. Weber. Monolithic perovskite/silicon-homojunction tandem solar cell with over 22% efficiency. *Energy & Environmental Science*, 10(11):2472–2479, 2017.

Bibliography

[88] Manoj Jaysankar, Miha Filipič, Bartosz Zielinski, Raphael Schmager, Wenya Song, Weiming Qiu, Ulrich W. Paetzold, Tom Aernouts, Maarten Debucquoy, Robert Gehlhaar, and Jeff Poortmans. Perovskite–silicon tandem solar modules with optimised light harvesting. *Energy & Environmental Science*, 2018.

[89] Michael Saliba, Taisuke Matsui, Ji-Youn Seo, Konrad Domanski, Juan-Pablo Correa-Baena, Nazeeruddin Mohammad K., Shaik M Zakeeruddin, Wolfgang Tress, Antonio Abate, Anders Hagfeldt, and Michael Gratzel. Cesium-containing Triple Cation Perovskite Solar Cells: Improved Stability, Reproducibility and High Efficiency. *Energy Environ. Sci.*, 9:1989–1997, 2016.

[90] Kevin A. Bush, Colin D. Bailie, Ye Chen, Tomas Leijtens, Andrea R. Bowring, Farhad Moghadam, and Michael D. McGehee. Thermal and Environmental Stability of Semi-Transparent Perovskite Solar Cells for Tandems Enabled by a Sputtered ITO Electrode. *Advanced Materials*, 28:3937–3943, 2016.

[91] Jérémie Werner, Florent Sahli, Brett Kamino, Davide Sacchetto, Matthias Bräuninger, Arnaud Walter, Soo-jin Moon, Loris Barraud, Bertrand Paviet-salomon, Jonas Geissbuehler, Christophe Allebé, Raphäel Monnard, Stefaan De Wolf, Matthieu Despeisse, Sylvain Nicolay, Bjoern Niesen, and Christophe Ballif. Perovskite / Silicon Tandem Solar Cells : Challenges Towards High- Efficiency in 4-Terminal and Monolithic Devices. In *IEEE-pvsc conference proceedings, Washington DC*, Washington D.C., 2017.

[92] Zhaoning Song, Chad L. McElvany, Adam B. Phillips, Ilke Celik, Patrick W. Krantz, Suneth Chandana Watthage, Geethika Kaushalya Liyanage, Defne Apul, and Michael J. Heben. A technoeconomic analysis of perovskite solar module manufacturing with low-cost materials and techniques. *Energy & Environmental Science*, 10(6):1297–1305, 2017.

[93] I. M. Peters, S. Sofia, J. Mailoa, and T. Buonassisi. Techno-economic analysis of tandem photovoltaic systems. *RSC Advances*, 6(71):66911–66923, 2016.

[94] Nathan L. Chang, Anita Wing Yi Ho-Baillie, Paul A. Basore, Trevor L. Young, Rhett Evans, and Renate J. Egan. A manufacturing cost estimation method with uncertainty analysis and its application to perovskite on glass photovoltaic modules. *Progress in Photovoltaics: Research and Applications*, 25(5):390–405, 2017.

[95] Nancy M. Haegel, Robert Margolis, Tonio Buonassisi, David Feldman, Armin Froitzheim, Raffi Garabedian, Martin Green, Stefan Glunz, Hans-Martin Henning, Burkhard Holder, Izumi Kaizuka, Benjamin Kroposki, Koji Matsubara, Shigeru Niki, Keiichiro Sakurai, Roland A. Schindler, Michael Woodhouse, and Sarah Kurtz. Terawatt-scale photovoltaics: Trajectories and challenges. *Science*, 356(6334):141–143, 2017.

[96] Jérémie Werner, Jonas Geissbuehler, Ali Dabirian, Sylvain Nicolay, Monica Morales Masis, Stefaan De Wolf, Björn Niesen, Christophe Ballif, J. Geissbühler, Ali Dabirian,

Sylvain Nicolay, M. Morales-Masis, S.D. Wolf, Björn Niesen, and Christophe Ballif. Parasitic absorption reduction in metal oxide-based transparent electrodes: application in perovskite solar cells. *ACS Applied Materials & Interfaces*, 8(27):17260–17267, 2016.

[97] Jérémie Werner, Gizem Nogay, Florent Sahli, Terry Chien-Jen Yang, Matthias Bräuninger, Gabriel Christmann, Arnaud Walter, Brett A. Kamino, Peter Fiala, Philipp Löper, Sylvain Nicolay, Quentin Jeangros, Bjoern Niesen, and Christophe Ballif. Complex Refractive Indices of Cesium–Formamidinium-Based Mixed-Halide Perovskites with Optical Band Gaps from 1.5 to 1.8 eV. *ACS Energy Letters*, 3(3):742–747, mar 2018.

[98] Florent Sahli, Jérémie Werner, Brett A. Kamino, Matthias Bräuninger, Raphaël Monnard, Bertrand Paviet-salomon, Loris Barraud, Laura Ding, Juan J. Diaz Leon, Davide Sacchetto, Gianluca Cattaneo, Mathieu Boccard, Matthieu Despeisse, Sylvain Nicolay, Quentin Jeangros, Bjoern Niesen, and Christophe Ballif. Fully Textured Monolithic Perovskite/Silicon Tandem Solar Cells with 25.2% Power Conversion Efficiency. *in press, Nature Materials*, 2018.

[99] Jonas Geissbühler, Jérémie Werner, Silvia Martin de Nicolas, Loris Barraud, Aïcha Hessler-Wyser, Matthieu Despeisse, Sylvain Nicolay, Andrea Tomasi, Bjoern Niesen, Stefaan De Wolf, and Christophe Ballif. 22.5% Efficient Silicon Heterojunction Solar Cell With Molybdenum Oxide Hole Collector. *Applied Physics Letters*, 107(8):081601, 2015.

[100] Stephanie Essig, Julie Dréon, Esteban Rucavado, Mathias Mews, Takashi Koida, Mathieu Boccard, Jérémie Werner, Jonas Geissbühler, Philipp Löper, Monica Morales-Masis, Lars Korte, Stefaan De Wolf, and Christophe Ballif. Toward Annealing-Stable Molybdenum-Oxide-Based Hole-Selective Contacts For Silicon Photovoltaics. *Solar RRL*, 1700227:1700227, 2018.

[101] Dávid Forgács, Lidón Gil-Escrig, Daniel Pérez-Del-Rey, Cristina Momblona, Jérémie Werner, Bjoern Niesen, Christophe Ballif, Michele Sessolo, H.J. Henk J. Bolink, L. Gil-Escrig, D. Pérez-Del-Rey, Cristina Momblona, Jérémie Werner, Bjoern Niesen, Christophe Ballif, Michele Sessolo, and H.J. Henk J. Bolink. Efficient Monolithic Perovskite/Perovskite Tandem Solar Cells. *Advanced Energy Materials*, 7(8):1602121, 2017.

[102] Q. Jeangros, M. Duchamp, J. Werner, M. Kruth, R.E. Dunin-Borkowski, B. Niesen, C. Ballif, and A. Hessler-Wyser. In Situ TEM Analysis of Organic-Inorganic Metal-Halide Perovskite Solar Cells under Electrical Bias. *Nano Letters*, 16(11), 2016.

[103] Philipp Löper, Michael Stuckelberger, Bjoern Niesen, Jérémie Werner, Miha Filipič, Soo-jin Moon, Jun-ho Yum, Marko Topič, Stefaan De Wolf, and Christophe Ballif. Complex Refractive Index Spectra of CH 3 NH 3 PbI 3 Perovskite Thin Films Determined by Spectroscopic Ellipsometry and Spectrophotometry. *The Journal of Physical Chemistry Letters*, 6(1):66–71, jan 2015.

[104] Jakub Holovský, Stefaan De Wolf, Jérémie Werner, Zdeněk Remeš, Martin Müller, Neda Neykova, Martin Ledinský, Ladislava Černá, Pavel Hrzina, Philipp Löper, Bjoern Niesen,

and Christophe Ballif. Photocurrent Spectroscopy of Perovskite Layers and Solar Cells: A Sensitive Probe of Material Degradation. *The Journal of Physical Chemistry Letters*, 8(4):838–843, feb 2017.

[105] M. Stuckelberger, T. Nietzold, G.N. Hall, B. West, J. Werner, B. Niesen, C. Ballif, V. Rose, D.P. Fenning, and M.I. Bertoni. Charge Collection in Hybrid Perovskite Solar Cells: Relation to the Nanoscale Elemental Distribution. *IEEE Journal of Photovoltaics*, 7(2), 2017.

[106] Zhaoning Song, Jérémie Werner, Niraj Shrestha, Florent Sahli, Stefaan De Wolf, Björn Niesen, Suneth C. Watthage, Adam B. Phillips, Christophe Ballif, Randy J. Ellingson, and Michael J. Heben. Probing Photocurrent Nonuniformities in the Subcells of Monolithic Perovskite/Silicon Tandem Solar Cells. *The Journal of Physical Chemistry Letters*, 7(24):5114–5120, dec 2016.

[107] M. Mundus, B. Venkataramanachar, R. Gehlhaar, M. Kohlstädt, B. Niesen, W. Qiu, J.P. Herterich, F. Sahli, M. Bräuninger, J. Werner, J. Hohl-Ebinger, G. Uytterhoeven, U. Würfel, C. Ballif, M.C. Schubert, W. Warta, and S.W. Glunz. Spectrally resolved nonlinearity and temperature dependence of perovskite solar cells. *Solar Energy Materials and Solar Cells*, 172, 2017.

[108] Zhaoning Song, Jeremie Werner, Suneth C. Watthage, Florent Sahli, Niraj Shrestha, Stefaan De Wolf, Bjorn Niesen, Adam B. Phillips, Christophe Ballif, Randy J. Ellingson, and Michael J. Heben. Imaging the Spatial Evolution of Degradation in Perovskite/Si Tandem Solar Cells After Exposure to Humid Air. *IEEE Journal of Photovoltaics*, 7(6):1563–1568, nov 2017.

[109] Genevieve N. Hall, Michael Stuckelberger, Tara Nietzold, Jessi Hartman, Ji Sang Park, Jérémie Werner, Bjoern Niesen, Marvin L. Cummings, Volker Rose, Christophe Ballif, Maria K. Chan, David P. Fenning, and Mariana I. Bertoni. The Role of Water in the Reversible Optoelectronic Degradation of Hybrid Perovskites at Low Pressure. *Journal of Physical Chemistry C*, 121(46):25659–25665, 2017.

[110] Rundong Fan, Yuan Huang, Ligang Wang, Liang Li, Guanhaojie Zheng, and Huanping Zhou. The Progress of Interface Design in Perovskite-Based Solar Cells. *Advanced Energy Materials*, 6(17):1–32, 2016.

[111] Jong H. Kim, Chu-Chen Chueh, Spencer T. Williams, and Alex K.-Y. Jen. Room-temperature, solution-processable organic electron extraction layer for high-performance planar heterojunction perovskite solar cells. *Nanoscale*, 7:17343–17349, 2015.

[112] Chen Tao, Stefanie Neutzner, Letizia Colella, Sergio Marras, Ajay Ram Srimath Kandada, Marina Gandini, Michele De Bastiani, Giuseppina Pace, Liberato Manna, Mario Caironi, Chiara Bertarelli, and Annamaria Petrozza. 17.6% Stabilized Efficiency in

Low-Temperature Processed Planar Perovskite Solar Cells. *Energy Environ. Sci.*, 8:8–10, 2015.

[113] Elham Halvani Anaraki, Ahmad Kermanpur, Ludmilla Steier, Konrad Domanski, Taisuke Matsui, Wolfgang Tress, Michael Saliba, Antonio Abate, Michael Grä, Anders Hagfeldt, and Juan-Pablo Correa-Baena. Highly efficient and stable planar perovskite solar cells by solution-processed tin oxide. *Energy Environ. Sci.*, 3128(9):3128–3134, 2016.

[114] Laura Calio, Samrana Kazim, Michael Graetzel, and Shahzada Ahmad. Hole-Transport Materials for Perovskite Solar Cells. *Angewandte Chemie - International Edition*, 55(47):14522–14545, 2016.

[115] Ramireddy Rajeswari, Madoori Mrinalini, Seelam Prasanthkumar, and Lingamallu Giribabu. Emerging of Inorganic Hole Transporting Materials For Perovskite Solar Cells. *Chemical Record*, 17:1–20, 2017.

[116] Zhengshan (Jason) Yu, Mehdi Leilaeioun, and Zachary Holman. Selecting tandem partners for silicon solar cells. *Nature Energy*, 1(11):16137, sep 2016.

[117] Giles E. Eperon, Samuel D. Stranks, Christopher Menelaou, Michael B. Johnston, Laura M. Herz, and Henry J. Snaith. Formamidinium lead trihalide: a broadly tunable perovskite for efficient planar heterojunction solar cells. *Energy & Environmental Science*, 7(3):982, 2014.

[118] Bruno Brunetti, Carmen Cavallo, Andrea Ciccioli, Guido Gigli, and Alessandro Latini. On the Thermal and Thermodynamic (In)Stability of Methylammonium Lead Halide Perovskites. *Scientific Reports*, 6(August):31896, 2016.

[119] Eric T Hoke, Daniel J Slotcavage, Emma R Dohner, Andrea R Bowring, Hemamala I Karunadasa, and Michael D McGehee. Reversible photo-induced trap formation in mixed-halide hybrid perovskites for photovoltaics. *Chemical Science*, 6(1):613–617, 2015.

[120] Daniel J. Slotcavage, Hemamala I. Karunadasa, and Michael D. McGehee. Light-Induced Phase Segregation in Halide-Perovskite Absorbers. *ACS Energy Letters*, 1(6):1199–1205, dec 2016.

[121] Alex J. Barker, Aditya Sadhanala, Felix Deschler, Marina Gandini, Satyaprasad P. Senanayak, Phoebe M. Pearce, Edoardo Mosconi, Andrew J. Pearson, Yue Wu, Ajay Ram Srimath Kandada, Tomas Leijtens, Filippo De Angelis, Siân E. Dutton, Annamaria Petrozza, and Richard H. Friend. Defect-Assisted Photoinduced Halide Segregation in Mixed-Halide Perovskite Thin Films. *ACS Energy Letters*, 2:1416–1424, may 2017.

[122] Rachel Ellen Beal, Daniel J Slotcavage, Tomas Leijtens, Andrea Ruth Bowring, Rebecca A Belisle, William H Nguyen, George F. Burkhard, Eric T Hoke, and Michael D McGehee. Cesium Lead Halide Perovskites with Improved Stability for Tandem Solar Cells. *The Journal of Physical Chemistry Letters*, 7(5):746–751, mar 2016.

Bibliography

[123] Waqar Ahmad, Jahangeer Khan, Guangda Niu, and Jiang Tang. Inorganic CsPbI3 Perovskite-Based Solar Cells: A Choice for a Tandem Device. *Solar RRL*, 2017.

[124] Lyubov A. Frolova, Denis V. Anokhin, Alexey A. Piryazev, Sergey Yu. Luchkin, Nadezhda N. Dremova, Keith J. Stevenson, and Pavel A. Troshin. Highly Efficient All-Inorganic Planar Heterojunction Perovskite Solar Cells Produced by Thermal Coevaporation of CsI and PbI2. *The Journal of Physical Chemistry Letters*, 8:67–72, 2017.

[125] Yuze Lin, Bo Chen, Fuwen Zhao, Xiaopeng Zheng, Yehao Deng, Yuchuan Shao, Yanjun Fang, Yang Bai, Chunru Wang, and Jinsong Huang. Matching Charge Extraction Contact for Wide-Bandgap Perovskite Solar Cells. *Advanced Materials*, 2017.

[126] M. Bonnet-Eymard, M. Boccard, G. Bugnon, F. Sculati-Meillaud, M. Despeisse, and C. Ballif. Optimized short-circuit current mismatch in multi-junction solar cells. *Solar Energy Materials and Solar Cells*, 117:120–125, 2013.

[127] Kira L. Gardner, Jeffrey G. Tait, Tamara Merckx, Weiming Qiu, Ulrich W. Paetzold, Lucinda Kootstra, Manoj Jaysankar, Robert Gehlhaar, David Cheyns, Paul Heremans, and Jef Poortmans. Nonhazardous Solvent Systems for Processing Perovskite Photovoltaics. *Advanced Energy Materials*, 6(14):1600386, jul 2016.

[128] Julian Burschka, Norman Pellet, Soo-Jin Moon, Robin Humphry-Baker, Peng Gao, Mohammad K Nazeeruddin, and Michael Grätzel. Sequential deposition as a route to high-performance perovskite-sensitized solar cells. *Nature*, 499(7458):316–9, jul 2013.

[129] Fan Fu, Lukas Kranz, Songhak Yoon, Johannes Löckinger, Timo Jäger, Julian Perrenoud, Thomas Feurer, Christina Gretener, Stephan Buecheler, and Ayodhya N. Tiwari. Controlled growth of PbI2 nanoplates for rapid preparation of CH3NH3PbI3 in planar perovskite solar cells. *physica status solidi (a)*, 212(12):2708–2717, dec 2015.

[130] Esma Ugur, Arif D. Sheikh, Rahim Munir, Jafar I. Khan, Dounya Barrit, Aram Amassian, and Frédéric Laquai. Improved Morphology and Efficiency of n-i-p Planar Perovskite Solar Cells by Processing with Glycol Ether Additives. *ACS Energy Letters*, 2(9):1960–1968, 2017.

[131] Xing Zhao and Nam-Gyu Park. Stability Issues on Perovskite Solar Cells. *Photonics*, 2(4):1139–1151, 2015.

[132] A.B. Djurišić, F.Z. Liu, H.W. Tam, M.K. Wong, A. Ng, C. Surya, W. Chen, and Z.B. He. Perovskite solar cells - An overview of critical issues. *Progress in Quantum Electronics*, 53:1–37, may 2017.

[133] Bert Conings, Jeroen Drijkoningen, Nicolas Gauquelin, Aslihan Babayigit, Jan D'Haen, Lien D'Olieslaeger, Anitha Ethirajan, Jo Verbeeck, Jean Manca, Edoardo Mosconi, Filippo De Angelis, and Hans-Gerd Boyen. Intrinsic Thermal Instability of Methylammonium Lead Trihalide Perovskite. *Advanced Energy Materials*, 5(15):1500477, aug 2015.

[134] Tomas Leijtens, Kevin Bush, Rongrong Cheacharoen, Rachel Beal, Andrea Bowring, and Michael D. McGehee. Towards enabling stable lead halide perovskite solar cells; interplay between structural, environmental, and thermal stability. *J. Mater. Chem. A*, pages 1–18, 2017.

[135] Weiming Qiu, Aniruddha Ray, Manoj Jaysankar, Tamara Merckx, Joao P. Bastos, David Cheyns, Robert Gehlhaar, Jef Poortmans, and Paul Heremans. An Interdiffusion Method for Highly Performing Cesium/Formamidinium Double Cation Perovskites. *Advanced Functional Materials*, 27(28):1700920, jul 2017.

[136] Jiahao Huang, Pan Xu, Jian Liu, and Xiao-Zeng You. Sequential Introduction of Cations Deriving Large-Grain Cs x FA 1- x PbI 3 Thin Film for Planar Hybrid Solar Cells: Insight into Phase-Segregation and Thermal-Healing Behavior. *Small*, 13(10):1603225, mar 2017.

[137] Mahesh K. Gangishetty, Robert W. J. Scott, and Timothy L. Kelly. Effect of relative humidity on crystal growth, device performance and hysteresis in planar heterojunction perovskite solar cells. *Nanoscale*, 8(12):6300–6307, 2016.

[138] Maarten van Eerden, Manoj Jaysankar, Afshin Hadipour, Tamara Merckx, John J. Schermer, Tom Aernouts, Jef Poortmans, and Ulrich W. Paetzold. Optical Analysis of Planar Multicrystalline Perovskite Solar Cells. *Advanced Optical Materials*, 5(18):1700151, sep 2017.

[139] J. A. Guerra, A. Tejada, L. Korte, L. Kegelmann, J. A. Töfflinger, S. Albrecht, B. Rech, and R. Weingärtner. Determination of the complex refractive index and optical bandgap of CH3NH3PbI3 thin films. *Journal of Applied Physics*, 121(17):173104, may 2017.

[140] Naresh Kumar Kumawat, Madhvendra Nath Tripathi, Umesh Waghmare, and Dinesh Kabra. Structural, Optical, and Electronic Properties of Wide Bandgap Perovskites: Experimental and Theoretical Investigations. *The Journal of Physical Chemistry A*, 120(22):3917–3923, 2016.

[141] Chang-Wen Chen, Sheng-Yi Hsiao, Chien-Yu Chen, Hao-Wei Kang, Zheng-Yu Huang, and Hao-Wu Lin. Optical properties of organometal halide perovskite thin films and general device structure design rules for perovskite single and tandem solar cells. *Journal of Materials Chemistry A*, 3(17):9152–9159, 2015.

[142] Jixian Xu, Andrei Buin, Alexander H. Ip, Wei Li, Oleksandr Voznyy, Riccardo Comin, Mingjian Yuan, Seokmin Jeon, Zhijun Ning, Jeffrey J. McDowell, Pongsakorn Kanjanaboos, Jon-Paul Sun, Xinzheng Lan, Li Na Quan, Dong Ha Kim, Ian G. Hill, Peter Maksymovych, and Edward H. Sargent. Perovskite–fullerene hybrid materials suppress hysteresis in planar diodes. *Nature Communications*, 6(1):7081, dec 2015.

[143] Yanjun Fang, Cheng Bi, Dong Wang, and Jinsong Huang. The Functions of Fullerenes in Hybrid Perovskite Solar Cells. *ACS Energy Letters*, 2(4):782–794, apr 2017.

[144] Rebecca A. Belisle, Pratham Jain, Rohit Prasanna, Tomas Leijtens, and Michael D. McGehee. Minimal Effect of the Hole-Transport Material Ionization Potential on the Open-Circuit Voltage of Perovskite Solar Cells. *ACS Energy Letters*, 1(3):556–560, 2016.

[145] Wei-Hung Lee, Chien-Yu Chen, Chia-Shuo Li, Sheng-Yi Hsiao, Wei-Lun Tsai, Min-Jie Huang, Chien-Hong Cheng, Chih-I Wu, and Hao-Wu Lin. Boosting thin-film perovskite solar cell efficiency through vacuum-deposited sub-nanometer small-molecule electron interfacial layers. *Nano Energy*, 38(April):66–71, aug 2017.

[146] Apostolos Ioakeimidis, Christos Christodoulou, Martha Lux-Steiner, and Konstantinos Fostiropoulos. Effect of PbI2 deposition rate on two-step PVD/CVD all-vacuum prepared perovskite. *Journal of Solid State Chemistry*, 244:20–24, 2016.

[147] Yan Jiang, Matthew R. Leyden, Longbin Qiu, Shenghao Wang, Luis K. Ono, Zhifang Wu, Emilio J. Juarez-Perez, and Yabing Qi. Combination of Hybrid CVD and Cation Exchange for Upscaling Cs-Substituted Mixed Cation Perovskite Solar Cells with High Efficiency and Stability. *Advanced Functional Materials*, 28(1):1703835, jan 2018.

[148] Giulia Longo, Cristina Momblona, Maria Grazia I. La Placa, Lidon Gil-Escrig, Michele Sessolo, and Henk J Bolink. Fully Vacuum Processed Wide Bandgap Mixed Halide Perovskite Solar Cells. *ACS Energy Letters*, 3:214–219, 2017.

[149] Zhirong Zhang, Meicheng Li, Wenjian Liu, Xiaopeng Yue, Peng Cui, and Dong Wei. CH3NH3PbI3 converted from reactive magnetron sputtered PbO for large area perovskite solar cells. *Solar Energy Materials and Solar Cells*, 163(July 2016):250–254, 2017.

[150] Jonas Geissbühler. *Advanced Architectures and Processing for High-Efficiency Silicon Heterojunction Solar Cells PAR*. Phd thesis, Ecole Polytechnique Fédérale de Lausanne, 2015.

[151] Monica Morales-masis, Stefaan De Wolf, Rachel Woods-robinson, Joel W Ager, and Prof C Ballif. Transparent Electrodes for Efficient Optoelectronics. *Advanced Electronic Materials*, (1600529), 2017.

[152] Fei Guo, Hamed Azimi, Yi Hou, Thomas Przybilla, Mengyao Hu, Carina Bronnbauer, Stefan Langner, Erdmann Spiecker, Karen Forberich, and Christoph J Brabec. High-performance semitransparent perovskite solar cells with solution-processed silver nanowires as top electrodes. *Nanoscale*, 7(5):1642–1649, dec 2015.

[153] Jihoon Ahn, Hyewon Hwang, Sunho Jeong, and Jooho Moon. Metal-Nanowire-Electrode-Based Perovskite Solar Cells: Challenging Issues and New Opportunities. *Advanced Energy Materials*, 7(15):1602751, aug 2017.

[154] Yuichi Kato, Luis K. Ono, Michael V. Lee, Shenghao Wang, Sonia R. Raga, and Yabing Qi. Silver Iodide Formation in Methyl Ammonium Lead Iodide Perovskite Solar Cells with Silver Top Electrodes. *Advanced Materials Interfaces*, 2(13):2–7, 2015.

[155] Felix Lang, Marc a. Gluba, Steve Albrecht, Jörg Rappich, Lars Korte, Bernd Rech, and Norbert H. Nickel. Perovskite Solar Cells with Large-Area CVD-Graphene for Tandem Solar Cells. *The Journal of Physical Chemistry Letters*, 6:2745–2750, 2015.

[156] Peng You, Zhike Liu, Qidong Tai, Shenghua Liu, and Feng Yan. Efficient Semitransparent Perovskite Solar Cells with Graphene Electrodes. *Advanced Materials*, 27(24):3632–3638, jun 2015.

[157] Hiroyuki Kanda, Abdullah Uzum, Hitoshi Nishino, Tomokazu Umeyama, Hiroshi Imahori, Yasuaki Ishikawa, Yukiharu Uraoka, and Seigo Ito. Interface Optoelectronics Engineering for Mechanical-Stacked Tandem Solar Cells Based on Perovskite and Silicon. *ACS Applied Materials & Interfaces*, 8:33553–33561, 2016.

[158] Yang (Michael) Yang, Qi Chen, Yao-Tsung Hsieh, Tze-Bin Song, Nicholas De Marco, Huanping Zhou, and Yang Yang. Multilayer Transparent Top Electrode for Solution Processed Perovskite/Cu(In,Ga)(Se,S) 2 Four Terminal Tandem Solar Cells. *ACS Nano*, 9(7):7714–7721, jul 2015.

[159] Burag Yaglioglu, Yen-Jung Huang, Hyo-Young Yeom, and David C. Paine. A study of amorphous and crystalline phases in In2O3–10 wt.% ZnO thin films deposited by DC magnetron sputtering. *Thin Solid Films*, 496(1):89–94, feb 2006.

[160] N. Ito, Y. Sato, P.K. Song, A. Kaijio, K. Inoue, and Y. Shigesato. Electrical and optical properties of amorphous indium zinc oxide films. *Thin Solid Films*, 496(1):99–103, feb 2006.

[161] Monica Morales-masis, Silvia Martin De Nicolas, Jakub Holovsky, Stefaan De Wolf, and Christophe Ballif. Low-Temperature High-Mobility Amorphous IZO for Silicon Heterojunction Solar Cells. *IEEE Journal of Photovoltaics*, 5(5):1340–1347, 2015.

[162] Yasmina Dkhissi, Fuzhi Huang, Sergey Rubanov, Manda Xiao, Udo Bach, Leone Spiccia, Rachel A Caruso, and Yi-Bing Cheng. Low temperature processing of fl exible planar perovskite solar cells with ef fi ciency over 10 %. *Journal of Power Sources*, 278:325–331, 2015.

[163] Yue Long Li, Do Young Lee, Su Ryun Min, Han Na Cho, Jongsung Kim, and Chee Won Chung. Effect of Oxygen Concentration on Properties of Indium Zinc Oxide Thin Films for Flexible Dye-Sensitized Solar Cell. *Japanese Journal of Applied Physics*, 47(8):6896–6899, aug 2008.

[164] Jong-gul Doh, Jin Sup Hong, R Vittal, Man Gu Kang, Nam-gyu Park, and Kang-jin Kim. Enhancement of Photocurrent and Photovoltage of Dye-Sensitized Solar Cells with TiO2 Film Deposited on Indium Zinc Oxide Substrate. *Chem. Mater.*, 16(3):493–497, 2004.

[165] H. Schmidt, H. Flugge, T. Winkler, T. Bulow, T. Riedl, and W. Kowalsky. Efficient semi-transparent inverted organic solar cells with indium tin oxide top electrode. *Applied Physics Letters*, 94(24):243302, 2009.

[166] Thomas Welzel and Klaus Ellmer. Negative oxygen ion formation in reactive magnetron sputtering processes for transparent conductive oxides. *Journal of Vacuum Science & Technology A*, 30(2012):061306, 2012.

[167] Wolfgang Tress and Olle Inganäs. Simple experimental test to distinguish extraction and injection barriers at the electrodes of (organic) solar cells with S-shaped current–voltage characteristics. *Solar Energy Materials and Solar Cells*, 117:599–603, oct 2013.

[168] A. Wagenpfahl, D. Rauh, M. Binder, C. Deibel, and V. Dyakonov. S-shaped current-voltage characteristics of organic solar devices. *Physical Review B*, 82(11):115306, sep 2010.

[169] Jens Meyer, Sami Hamwi, Michael Kröger, Wolfgang Kowalsky, Thomas Riedl, and Antoine Kahn. Transition Metal Oxides for Organic Electronics: Energetics, Device Physics and Applications. *Advanced Materials*, 24(40):5408–5427, oct 2012.

[170] Corsin Battaglia, Xingtian Yin, Maxwell Zheng, Ian D Sharp, Teresa Chen, Stephen Mcdonnell, Angelica Azcatl, Carlo Carraro, Biwu Ma, Roya Maboudian, Robert M Wallace, and Ali Javey. Hole selective MoOx contact for silicon solar cells. *Nano letters*, 14:967–971, 2014.

[171] Yixin Zhao and Kai Zhu. Solution Chemistry Engineering toward High-Efficiency Perovskite Solar Cells. *The Journal of Physical Chemistry Letters*, 5(23):4175–4186, dec 2014.

[172] Zach M Beiley, M Greyson Christoforo, Paul Gratia, Andrea R Bowring, Petra Eberspacher, George Y Margulis, Clément Cabanetos, Pierre M Beaujuge, Alberto Salleo, and Michael D McGehee. Semi-Transparent Polymer Solar Cells with Excellent Sub-Bandgap Transmission for Third Generation Photovoltaics. *Advanced Materials*, 25(48):7020–7026, dec 2013.

[173] Yuanhang Cheng, Qing-Dan Yang, Jingyang Xiao, Qifan Xue, Ho-Wa Li, Zhiqiang Guan, Hin-Lap Yip, and Sai-Wing Tsang. Decomposition of Organometal Halide Perovskite Films on Zinc Oxide Nanoparticles. *ACS Applied Materials & Interfaces*, 7(36):19986–19993, 2015.

[174] K.O. Brinkmann, J. Zhao, N. Pourdavoud, T. Becker, T. Hu, S. Olthof, K. Meerholz, L. Hoffmann, T. Gahlmann, R. Heiderhoff, M. F. Oszajca, N. A. Luechinger, D. Rogalla, Y. Chen, B. Cheng, and T Riedl. Suppressed decomposition of organometal halide perovskites by impermeable electron-extraction layers in inverted solar cells. *Nature Communications*, 8:13938, 2017.

[175] J. Zhao, K. O. Brinkmann, T. Hu, N. Pourdavoud, T. Becker, T. Gahlmann, R. Heiderhoff, A. Polywka, P. Görrn, Y. Chen, B. Cheng, and T. Riedl. Self-Encapsulating Thermostable and Air-Resilient Semitransparent Perovskite Solar Cells. *Advanced Energy Materials*, 7(14):1602599, jul 2017.

[176] Irfan Irfan and Yongli Gao. Effects of exposure and air annealing on MoOx thin films. *Journal of Photonics for Energy*, 2:021213, 2012.

[177] Zheng Zhang, Yan Xiao, Huai Xin Wei, Guo Fu Ma, Steffen Duhm, Yan Qing Li, and Jian Xin Tang. Impact of oxygen vacancy on energy-level alignment at MoOx/organic interfaces. *Applied Physics Express*, 6, 2013.

[178] Shih-Yuan Lin, Ying-Chung Chen, Chih-Ming Wang, Po-Tsung Hsieh, and Shun-Chou Shih. Post-annealing effect upon optical properties of electron beam evaporated molybdenum oxide thin films. *Applied Surface Science*, 255(6):3868–3874, 2009.

[179] A. Siokou, G. Leftheriotis, S. Papaefthimiou, and P. Yianoulis. Effect of the tungsten and molybdenum oxidation states on the thermal coloration of amorphous WO3 and MoO3 films. *Surface Science*, 482-485:294–299, 2001.

[180] G. Leftheriotis, S. Papaefthimiou, P. Yianoulis, and a. Siokou. Effect of the tungsten oxidation states in the thermal coloration and bleaching of amorphous WO3 films. *Thin Solid Films*, 384:298–306, 2001.

[181] T. H. Fleisch. An XPS study of the UV reduction and photochromism of MoO3 and WO3. *The Journal of Chemical Physics*, 76(2):780, 1982.

[182] Xiao Bo Shi, Mei Feng Xu, Dong Ying Zhou, Zhao Kui Wang, and Liang Sheng Liao. Improved cation valence state in molybdenum oxides by ultraviolet-ozone treatments and its applications in organic light-emitting diodes. *Applied Physics Letters*, 102, 2013.

[183] Joo Hyung Kim, You Jong Lee, Yoon Sung Jang, Jin Nyoung Jang, Doo Hyun Kim, Byung Chul Song, Dong Hyeok Lee, Soon Nam Kwon, and MunPyo Hong. The effect of Ar plasma bombardment upon physical property of tungsten oxide thin film in inverted top-emitting organic light-emitting diodes. *Organic Electronics*, 12(2):285–290, feb 2011.

[184] Xiaoliang Liu, Shijuan Yi, Chenggong Wang, Irfan Irfan, and Yongli Gao. Effect of oxygen plasma treatment on air exposed MoOx thin film. *Organic Electronics*, 15(5):977–983, 2014.

[185] T J Tate and Mino Green. lon implantation effects in polycrystalline W03 thin films. *Journal of Applied Physics*, pages 3509–3511, 1991.

[186] F. Y. Xie, L. Gong, X. Liu, Y. T. Tao, W. H. Zhang, S. H. Chen, H. Meng, and J. Chen. XPS studies on surface reduction of tungsten oxide nanowire film by Ar + bombardment. *Journal of Electron Spectroscopy and Related Phenomena*, 185(3-4):112–118, 2012.

[187] T. J. Driscoll, L. D. McCormick, and W. C. Lederer. Altered layer formation and sputtering yields for 5 keV Ar+ bombardment of MoO3 and WO3. *Surface Science*, 187(2-3):539–558, 1987.

[188] Naveen Kumar Elumalai, Chellappan Vijila, Rajan Jose, Ashraf Uddin, and Seeram Ramakrishna. Metal oxide semiconducting interfacial layers for photovoltaic and photocatalytic applications. *Materials for Renewable and Sustainable Energy*, 4(3):11, 2015.

[189] Richard J. Colton, Alberto M. Guzman, and J. Wayne Rabalais. Photochromism and electrochromism in amorphous transition metal oxide films. *Accounts of Chemical Research*, 11(4):170–176, 1978.

[190] Tao He and Jiannian Yao. Photochromism of molybdenum oxide. *Journal of Photochemistry and Photobiology C: Photochemistry Reviews*, 4(2):125–143, 2003.

[191] J. Scarminio, a. Lourenço, and a. Gorenstein. Electrochromism and photochromism in amorphous molybdenum oxide films. *Thin Solid Films*, 302:66–70, 1997.

[192] Binayak Dasgupta, Yi Ren, Lai Mun Wong, Lingyu Kong, Eng Soon Tok, Wai Kin Chim, and Sing Yang Chiam. Detrimental Effects of Oxygen Vacancies in Electrochromic Molybdenum Oxide. *The Journal of Physical Chemistry C*, 119(19):10592–10601, may 2015.

[193] Fan Fu, Thomas Feurer, Timo Jäger, Enrico Avancini, Benjamin Bissig, Songhak Yoon, Stephan Buecheler, and Ayodhya N. Tiwari. Low-temperature-processed efficient semi-transparent planar perovskite solar cells for bifacial and tandem applications. *Nature Communications*, 6(November):8932, 2015.

[194] Benedicte Demaurex, Stefaan De Wolf, Antoine Descoeudres, Zachary Charles Holman, and Christophe Ballif. Damage at hydrogenated amorphous/crystalline silicon interfaces by indium tin oxide overlayer sputtering. *Applied Physics Letters*, 101(17):171604, 2012.

[195] Xichang Bao, Qianqian Zhu, Ting Wang, Jing Guo, Chunpeng Yang, Donghong Yu, Ning Wang, Weichao Chen, and Renqiang Yang. Simple O2 Plasma Processed V2O5 as an Anode Buffer Layer for High-Performance Polymer Solar Cells. *ACS Applied Materials & Interfaces*, 7(14):7613–7618, 2015.

[196] L D Lopez-Carreno, G Benitez, L Viscido, J M Heras, F Yubero, J P Espinos, and a R Gonzalez-Elipe. Oxidation of molybdenum surfaces by reactive oxygen plasma and O2(+) bombardment: an Auger and XPS study. *Surface and Interface Analysis*, 26(4):235–241, 1998.

[197] Joonyoup Kim, C. K. Suman, Seunguk Noh, and Changhee Lee. Surface treatment of molybdenum oxide for performance improvement of organic light emitting diodes. *Displays*, 31(3):139–142, 2010.

[198] Jens Meyer, Thomas Winkler, Sami Hamwi, Stephan Schmale, Hans-Hermann Johannes, Thomas Weimann, Peter Hinze, Wolfgang Kowalsky, and Thomas Riedl. Transparent Inverted Organic Light-Emitting Diodes with a Tungsten Oxide Buffer Layer. *Advanced Materials*, 20(20):3839–3843, oct 2008.

[199] Peter Vanysek. Electrochemical series. In M. Haynes, editor, *CRC Handbook of Chemistry and Physics, 91th ed.* CRC Press, 2010.

[200] Nam Joong Jeon, Jun Hong Noh, Woon Seok Yang, Young Chan Kim, Seungchan Ryu, Jangwon Seo, and Sang Il Seok. Compositional engineering of perovskite materials for high-performance solar cells. *Nature*, 517(7535):476–480, 2015.

[201] Nam Joong Jeon, Jun Hong Noh, Young Chan Kim, Woon Seok Yang, Seungchan Ryu, and Sang Il Seok. Solvent engineering for high-performance inorganic–organic hybrid perovskite solar cells. *Nature Materials*, 13(9):897–903, sep 2014.

[202] Bong Joon Lee, Hyo Jung Kim, Won I. Jeong, and Jang J. Kim. A transparent conducting oxide as an efficient middle electrode for flexible organic tandem solar cells. *Solar Energy Materials and Solar Cells*, 94(3):542–546, 2010.

[203] Than Zaw Oo, R. Devi Chandra, Natalia Yantara, Rajiv Ramanujam Prabhakar, Lydia H. Wong, Nripan Mathews, and Subodh G. Mhaisalkar. Zinc Tin Oxide (ZTO) electron transporting buffer layer in inverted organic solar cell. *Organic Electronics: physics, materials, applications*, 13(5):870–874, 2012.

[204] Monica Morales-Masis, Fabien Dauzou, Quentin Jeangros, Ali Dabirian, Herbert Lifka, Rainald Gierth, Manfred Ruske, Date Moet, Aïcha Hessler-Wyser, and Christophe Ballif. An Indium-Free Anode for Large-Area Flexible OLEDs: Defect-Free Transparent Conductive Zinc Tin Oxide. *Advanced Functional Materials*, 26(3):384–392, 2016.

[205] H. Q. Chiang, J. F. Wager, R. L. Hoffman, J. Jeong, and D. a. Keszler. High mobility transparent thin-film transistors with amorphous zinc tin oxide channel layer. *Applied Physics Letters*, 86(1):13–16, 2005.

[206] M K Jayaraj, K J Saji, K Nomura, T Kamiya, and H Hosono. Optical and electrical properties of amorphous zinc tin oxide thin films examined for thin film transistor application. *Journal of Vacuum Science & Technology B*, 26(2):495–501, 2008.

[207] Fabien Dauzou, Piet C.P. Bouten, Ali Dabirian, Yves Leterrier, Christophe Ballif, and Monica Morales-Masis. Mechanical integrity of hybrid indium-free electrodes for flexible devices. *Organic Electronics*, 35:136–141, 2016.

[208] Carolin Ulbrich, Andreas Gerber, Ko Hermans, Andreas Lambertz, and Uwe Rau. Analysis of short circuit current gains by an anti-reflective textured cover on silicon thin film solar cells. *Progress in Photovoltaics: Research and Applications*, 21:1672–1681, 2013.

[209] Afshin Hadipour, Bert de Boer, and Paul W M Blom. Solution-processed organic tandem solar cells with embedded optical spacers. *Journal of Applied Physics*, 102(7):074506, 2007.

[210] Jan Gilot, Ionut Barbu, Martijn M. Wienk, and Rene a. J. Janssen. The use of ZnO as optical spacer in polymer solar cells: Theoretical and experimental study. *Applied Physics Letters*, 91(11):113520, 2007.

147

Bibliography

[211] Ali Dabirian, Silvia Martin de Nicolas, Bjoern Niesen, Aïcha Hessler-Wyser, Stefaan De Wolf, Monica Morales-Masis, and Christophe Ballif. Tuning the Optoelectronic Properties of ZnO:Al by Addition of Silica for Light Trapping in High-Efficiency Crystalline Si Solar Cells. *Advanced Materials Interfaces*, 3(3):1500462, feb 2016.

[212] Miha Filipič, Philipp Löper, Bjoern Niesen, Stefaan De Wolf, Janez Krč, Christophe Ballif, and Marko Topič. CH3NH3PbI3 perovskite / silicon tandem solar cells: characterization based optical simulations. *Optics Express*, 23(7):A263, apr 2015.

[213] Martin A. Green. Self-consistent optical parameters of intrinsic silicon at 300 K including temperature coefficients. *Solar Energy Materials and Solar Cells*, 92(11):1305–1310, 2008.

[214] B. Macco, Y. Wu, D. Vanhemel, and W. M.M. Kessels. High mobility In2O3: H transparent conductive oxides prepared by atomic layer deposition and solid phase crystallization. *Physica Status Solidi - Rapid Research Letters*, 8(12):987–990, 2014.

[215] Zachary C. Holman, Miha Filipič, Antoine Descoeudres, Stefaan De Wolf, Franc Smole, Marko Topič, and Christophe Ballif. Infrared light management in high-efficiency silicon heterojunction and rear-passivated solar cells. *Journal of Applied Physics*, 113(1):033107–1–13, 2013.

[216] Jesus M. Siqueiros, Roberto Machorro, and Luis E. Regalado. Determination of the optical constants of MgF2 and ZnS from spectrophotometric measurements and the classical oscillator method. *Applied Optics*, 27(12):2549–2553, 1988.

[217] Klaus Jäger, Lars Korte, Bernd Rech, and Steve Albrecht. Numerical optical optimization of monolithic planar perovskite-silicon tandem solar cells with regular and inverted device architectures. *Optics Express*, 25(12):A473, 2017.

[218] Qianqian Lin, Ardalan Armin, Ravi Chandra Raju Nagiri, Paul L. Burn, and Paul Meredith. Electro-optics of perovskite solar cells. *Nature Photonics*, 9(2):106–112, feb 2015.

[219] M. H. Futscher and B. Ehrler. Efficiency Limit of Perovskite/Si Tandem Solar Cells. *ACS Energy Letters*, 1:863–868, 2016.

[220] Dianyi Liu, Qiong Wang, Christopher J. Traverse, Chenchen Yang, Margaret Young, Padmanaban S. Kuttipillai, Sophia Y. Lunt, Thomas W. Hamann, and Richard R. Lunt. Impact of Ultrathin C 60 on Perovskite Photovoltaic Devices. *ACS Nano*, 12(1):876–883, jan 2018.

[221] Bjoern Niesen, Nicolas Blondiaux, Mathieu Boccard, Michael Stuckelberger, Raphaël Pugin, Emmanuel Scolan, Fanny Meillaud, Franz-Josef Haug, Aïcha Hessler-Wyser, and Christophe Ballif. Self-patterned nanoparticle layers for vertical interconnects: application in tandem solar cells. *Nano letters*, 14(9):5085–91, sep 2014.

[222] Augusto Martins, Ben Hur Viana Borges, Juntao Li, Thomas F. Krauss, and Emiliano R. Martins. Photonic Intermediate Structures for Perovskite/c-Silicon Four Terminal Tandem Solar Cells. *IEEE Journal of Photovoltaics*, 7(5):1190–1196, 2017.

[223] Patrick Campbell and Martin A. Green. Light trapping properties of pyramidally textured surfaces. *Journal of Applied Physics*, 62(1):243–249, 1987.

[224] Zachary Holman and Mathieu Boccard. Light management in silicon solar cells. In Angèle Reinders, Pierre Verlinden, Wilfried van Sark, and Alexandre Freundlich, editors, *Photovoltaic Solar Energy: From Fundamentals to Applications, First Edition*, chapter 3.7, pages 136–149. John Wiley & Sons, Ltd., 2017.

[225] Rudi Santbergen, Ryota Mishima, Tomomi Meguro, Masashi Hino, Hisashi Uzu, Johan Blanker, Kenji Yamamoto, and Miro Zeman. Minimizing optical losses in monolithic perovskite/c-Si tandem solar cells with a flat top cell. *Optics Express*, 24(18):A1288, sep 2016.

[226] Daniel Messerschmidt. *Advanced LPCVD ZnO - Challenges in Application for Thin Film Solar Cells and Modules.* PhD thesis, Université de Neuchâtel, 2014.

[227] X. Multone, L. Fesquet, D. Borrello, D. Romang, G. Choong, E. Vallat-Sauvain, M. Charrière, a. Billet, J.-F. Boucher, J. Steinhauser, J.-B. Orhan, R. Monnard, J.-P. Cardoso, G. Charitat, B. Dehbozorgi, N. Guillot, G. Monteduro, M. Marmelo, R. Semenzi, S. Benagli, and J. Meier. Triple-junction amorphous/microcrystalline silicon solar cells: Towards industrially viable thin film solar technology. *Solar Energy Materials and Solar Cells*, 140:388–395, 2015.

[228] P Cuony. *Optical Layers for Thin-film Silicon Solar Cells.* Phd thesis, EPFL, 2011.

[229] Karin Söderström. *Coupling light into thin silicon layers for high-efficiency solar cells.* Phd thesis, EPFL, 2013.

[230] S. Nicolay, M. Benkhaira, L. Ding, J. Escarre, G. Bugnon, F. Meillaud, and C. Ballif. Control of CVD-deposited ZnO films properties through water/DEZ ratio: Decoupling of electrode morphology and electrical characteristics. *Solar Energy Materials and Solar Cells*, 105:46–52, oct 2012.

[231] Lorenzo Fanni. *Explaining Morphological and Electrical Features of Boron- doped Zinc Oxide to Tailor New Electrodes for Photovoltaics.* PhD thesis, Ecole Polytechnique Fédérale de Lausanne, 2016.

[232] L. Ding, L. Fanni, D. Messerschmidt, S. Zabihzadeh, M. Morales Masis, S. Nicolay, and C. Ballif. Tailoring the surface morphology of zinc oxide films for high-performance micromorph solar cells. *Solar Energy Materials and Solar Cells*, 128:378–385, sep 2014.

[233] Laura Ding. *Low-Pressure Chemical Vapor Deposited Zinc Oxide Films : Toward Decoupled Opto-Electrical and Morphological Properties for More Efficient Electrodes.* Phd thesis, EPFL, 2013.

[234] Housei Akazawa. Argon plasma treatment of transparent conductive zno films. *Applied Physics Express*, 2(081601), 2009.

Bibliography

[235] O. Caglar, P. Carroy, P.A. Losio, and I. Sinicco. Nanocrystalline zinc oxide for surface morphology control in thin-film silicon solar cells. *Solar Energy Materials and Solar Cells*, 144:55–62, jan 2016.

[236] Lorenzo Fanni, A. Brian Aebersold, Monica Morales-Masis, Duncan T L Alexander, Aïcha Hessler-Wyser, Sylvain Nicolay, Cécile Hébert, and Christophe Ballif. Increasing Polycrystalline Zinc Oxide Grain Size by Control of Film Preferential Orientation. *Crystal Growth & Design*, 15(12):5886–5891, dec 2015.

[237] Daisuke Adachi, José Luis Hernández, and Kenji Yamamoto. Impact of carrier recombination on fill factor for large area heterojunction crystalline silicon solar cell with 25.1% efficiency. *Applied Physics Letters*, 107(23):233506, 2015.

[238] Juan-Pablo Correa-Baena, Wolfgang Tress, Konrad Domanski, Elham Halvani Anaraki, Silver-Hamill Turren-Cruz, Bart Roose, Pablo P. Boix, Michael Grätzel, Michael Saliba, Antonio Abate, Anders Hagfeldt, S. M. Zakeeruddin, U. Steiner, M. Grätzel, A. Abate, and M. K. Nazeeruddin. Identifying and suppressing interfacial recombination to achieve high open-circuit voltage in perovskite solar cells. *Energy & Environmental Science*, 1:556–560, 2017.

[239] Maximilian Tobias Hörantner and Henry J. Snaith. Predicting and optimising the energy yield of perovskite-on-silicon tandem solar cells under real world conditions. *Energy & Environmental Science*, 10(9):1983–1993, 2017.

[240] Konrad Domanski, Essa A. Alharbi, Anders Hagfeldt, Michael Grätzel, and Wolfgang Tress. Systematic investigation of the impact of operation conditions on the degradation behaviour of perovskite solar cells. *Nature Energy*, 3(1):61–67, jan 2018.

[241] Wei Chen, Yongzhen Wu, Youfeng Yue, Jian Liu, Wenjun Zhang, Xudong Yang, Han Chen, Enbing Bi, Islam Ashraful, Michael Grätzel, and Liyuan Han. Efficient and stable large-area perovskite solar cells with inorganic charge extraction layers. *Science*, 350(6263):944–948, 2015.

[242] Xiong Li, Dongqin Bi, Chenyi Yi, J.-D. Decoppet, Jingshan Luo, Shaik Mohammed Zakeeruddin, Anders Hagfeldt, and M. Gratzel. A vacuum flash-assisted solution process for high-efficiency large-area perovskite solar cells. *Science*, 353(6294):58–62, jul 2016.

[243] Hairen Tan, Ankit Jain, Oleksandr Voznyy, Xinzheng Lan, F. Pelayo García de Arquer, James Z. Fan, Rafael Quintero-Bermudez, Mingjian Yuan, Bo Zhang, Yicheng Zhao, Fengjia Fan, Peicheng Li, Li Na Quan, Yongbiao Zhao, Zheng-Hong Lu, Zhenyu Yang, Sjoerd Hoogland, and Edward H. Sargent. Efficient and stable solution-processed planar perovskite solar cells via contact passivation. *Science*, 355(6326):722–726, feb 2017.

[244] Soo-Jin Moon, Jun-Ho Yum, Linus Lofgren, Arnaud Walter, Laurent Sansonnens, Mustapha Benkhaira, Sylvain Nicolay, Julien Bailat, and Christophe Ballif. Laser-Scribing Patterning for the Production of Organometallic Halide Perovskite Solar Modules. *IEEE Journal of Photovoltaics*, 5(4):1087–1092, jul 2015.

[245] George D. Spyropoulos, César Omar Ramirez Quiroz, Michael Salvador, Yi Hou, Nicola Gasparini, Peter Schweizer, Jens Adams, Peter Kubis, Ning Li, Erdmann Spiecker, Tayebeh Ameri, Hans-Joachim Egelhaaf, and Christoph J. Brabec. Organic and perovskite solar modules innovated by adhesive top electrode and depth-resolved laser patterning. *Energy & Environmental Science*, 9(2302):13–15, 2016.

[246] L Rakocevic, R Gehlhaar, T Merckx, W Qui, U W Paetzold, H Fledderus, and J Poortmans. Interconnection Optimization for Highly Efficient Perovskite Modules. *IEEE Journal of Photovoltaics*, 7(1):404–408, 2016.

[247] Cristina Momblona, Lidón Gil-Escrig, Enrico Bandiello, Eline M. Hutter, Michele Sessolo, Kay Lederer, Jan Blochwitz-Nimoth, and Henk J. Bolink. Efficient vacuum deposited p-i-n and n-i-p perovskite solar cells employing doped charge transport layers. *Energy Environ. Sci.*, 9(11):3456–3463, 2016.

[248] Lidón Gil-Escrig, Cristina Momblona, Dávid Forgács, Sara Pla, Fernando Fernández-Lázaro, Michele Sessolo, Ángela Sastre-Santos, and Henk J. Bolink. Interface engineering in efficient vacuum deposited perovskite solar cells. *Organic Electronics*, 37:396–401, 2016.

[249] Annie Ng, Zhiwei Ren, Qian Shen, Sin-Hang Cheung, Huseyin Cem Gokkaya, Shu Kong So, aleksandra B. Djurisic, Yangyang Wan, Xiaojun Wu, and Charles Surya. Crystal Engineering for Low Defect Density and High Efficiency Hybrid Chemical Vapor Deposition Grown Perovskite Solar Cells. *ACS Applied Materials & Interfaces*, 8(48):32805–32814, 2016.

[250] Jonas Geissbühler, Stefaan De Wolf, Antonin Faes, Nicolas Badel, Quentin Jeangros, Andrea Tomasi, Loris Barraud, Antoine Descoeudres, Matthieu Despeisse, and Christophe Ballif. Silicon heterojunction solar cells with copper - plated grid electrodes : Status and comparison with silver thick - film techniques. *IEEE Journal of Photovoltaics*, 4(4), 2014.

[251] Martin A. Green, Yoshihiro Hishikawa, Ewan D. Dunlop, Dean H. Levi, Jochen Hohl-Ebinger, and Anita W.Y. Ho-Baillie. Solar cell efficiency tables (version 51). *Progress in Photovoltaic Research and applications*, 26:3–12, 2018.

[252] Romain Cariou, Jan Benick, Paul Beutel, Nasser Razek, Christoph Fl, Martin Hermle, David Lackner, Stefan W Glunz, Senior Member, Andreas W Bett, Markus Wimplinger, and Frank Dimroth. Monolithic Two-Terminal III–V//Si Triple-Junction Solar Cells With 30.2% Efficiency Under 1-Sun AM1.5g. *IEEE Journal of Photovoltaics*, pages 1–7, 2016.

[253] Jan-Willem Schüttauf, Bjoern Niesen, Linus Löfgren, Maximilien Bonnet-Eymard, Michael Stuckelberger, Simon Hänni, Mathieu Boccard, Grégory Bugnon, Matthieu Despeisse, Franz-Josef Haug, Fanny Meillaud, and Christophe Ballif. Amorphous silicon–germanium for triple and quadruple junction thin-film silicon based solar cells. *Solar Energy Materials and Solar Cells*, 133:163–169, 2015.

Bibliography

[254] Romain Cariou, Jan Benick, Frank Feldmann, Oliver Höhn, Hubert Hauser, Paul Beutel, Nasser Razek, Markus Wimplinger, Benedikt Bläsi, David Lackner, Martin Hermle, Gerald Siefer, Stefan W. Glunz, Andreas W. Bett, and Frank Dimroth. III–V-on-silicon solar cells reaching 33% photoconversion efficiency in two-terminal configuration. *Nature Energy*, apr 2018.

[255] Marcel Schreier, Florent Héroguel, Ludmilla Steier, Shahzada Ahmad, Jeremy S. Luterbacher, Matthew T. Mayer, Jingshan Luo, and Michael Grätzel. Solar conversion of CO2 to CO using Earth-abundant electrocatalysts prepared by atomic layer modification of CuO. *Nature Energy*, 2(7):17087, 2017.

[256] L. Barraud, Z. C. Holman, N. Badel, P. Reiss, a. Descoeudres, C. Battaglia, S. De Wolf, and C. Ballif. Hydrogen-doped indium oxide/indium tin oxide bilayers for high-efficiency silicon heterojunction solar cells. *Solar Energy Materials and Solar Cells*, 115:151–156, 2013.

[257] Ying-tung Hsiao and China-hong Chen. Maximum power tracking for photovoltaic power system. *Conference Record of the 37th 2002 IEEE Industry Applications Conference*, 2:1035–1040, 2002.

[258] Norman Pellet. *Investigations on hybrid organic-inorganic perovskites for high performance solar cells.* PhD thesis, Ecole Polytechnique Fédérale de Lausanne, 2017.

[259] Jordi Escarré, Karin Söderström, Matthieu Despeisse, Sylvain Nicolay, Corsin Battaglia, Gregory Bugnon, Laura Ding, Fanny Meillaud, Franz Josef Haug, and Christophe Ballif. Geometric light trapping for high efficiency thin film silicon solar cells. *Solar Energy Materials and Solar Cells*, 98:185–190, 2012.

Publication list

Peer-reviewed journal contributions

Publications as first author

1 J. Werner, G. Dubuis, A. Walter, P. Löper, S-J. Moon, S. Nicolay, M. Morales-Masis, S. De Wolf, B. Niesen and C. Ballif, "*Sputtered rear electrode with broadband transparency for perovskite solar cells,*" Solar Energy Materials and Solar Cells, vol. **141**, pp. 407-413, 2015.

2 J. Werner, C-H. Weng, A. Walter, L. Fesquet, J. P. Seif, S. De Wolf, B. Niesen and C. Ballif, "*Efficient Monolithic Perovskite/Silicon Tandem Solar Cell with Cell Area > 1cm^2,*" Journal of Physical Chemistry Letters, vol. **7**, pp. 161-166, 2016.

3 J. Werner, J. Geissbühler, A. Dabirian, S. Nicolay, M. Morales-Masis, S. De Wolf, B. Niesen, and C. Ballif, "*Parasitic absorption reduction in metal oxide-based transparent electrodes: application in perovskite solar cells,*" ACS Applied Materials & Interfaces, vol. **8** (27), pp. 17260–17267, 2016.

4 J. Werner, L. Barraud, A. Walter, M. Bräuninger, F. Sahli, D. Sacchetto, N. Tétreault, B. Paviet-Salomon, S-J. Moon, C. Allebé, M. Despeisse, S. Nicolay, S. De Wolf, B. Niesen, C. Ballif, "*Efficient Near-Infrared-Transparent Perovskite Solar Cells Enabling Direct Comparison of 4-Terminal and Monolithic Perovskite/Silicon Tandem Cells,*" ACS Energy Letters, vol. **1**, pp. 474-480, 2016.

5 J. Werner, A. Walter, E. Rucavado, S-J. Moon, D. Sacchetto, M. Rienaecker, R. Peibst, R. Brendel, X. Niquille, S. De Wolf, P. Löper, M. Morales-Masis, S. Nicolay, B. Niesen, C. Ballif, "*Zinc tin oxide as high-temperature stable recombination layer for mesoscopic perovskite/silicon monolithic tandem solar cells,*" Applied Physics Letters, vol. **109**, 233902, 2016.

6 J. Werner, B. Niesen, C. Ballif, "*Perovskite/silicon tandem solar cells: marriage of con-*

venience or true love story? - An overview," Advanced Materials Interfaces, vol. **5**, 1, 1700731, 2017.

7 J. Werner, G. Nogay, F. Sahli, T. C.-J. Yang, M. Bräuninger, G. Christmann, A. Walter, B. A. Kamino, P. Fiala, P. Löper, S. Nicolay, Q. Jeangros, B. Niesen, C. Ballif, "*Complex Refractive Indices of Cesium–Formamidinium-Based Mixed-Halide Perovskites with Optical Band Gaps from 1.5 to 1.8 eV*," ACS Energy Letters, vol. **3**, pp. 742-747, 2018.

8 F. Sahli*, J. Werner*, B. A. Kamino, M. Bräuninger, R. Monnard, B. Paviet-salomon, L. Barraud, L. Ding, J.J. Diaz Leon, D. Sacchetto, G. Cattaneo, M. Despeisse, M. Boccard, S. Nicolay, Q. Jeangros, B. Niesen, C. Ballif, "*Fully Textured Monolithic Perovskite/Silicon Tandem Solar Cells with 25.2% Power Conversion Efficiency*," in press, Nature Materials, 2018.

9 J. Werner, F. Sahli, D. Ren, J. Luo, F. Fu, J.J. Diaz Leon, A. Walter, B. A. Kamino, B. Niesen, M. Graetzel, S. Nicolay, Q. Jeangros, C. Ballif, "*Textured Perovskite/Perovskite/Silicon Monolithic Triple Junction Solar Cells with Open-circuit Voltage up to 2.69 V*," submitted, 2018.

Publications as co-author

1 P. Löper, M. Stuckelberger, B. Niesen, J. Werner, M. Filipic, S-J. Moon, J-H. Yum, M. Topic, S. De Wolf, and C. Ballif, "*Complex refractive index spectra of CH3NH3PbI3 perovskite thin films determined by spectroscopic ellipsometry and spectrophotometry*," The Journal of Physical Chemistry Letters, vol. **6**, p. 66-71, 2015.

2 J. Geissbühler, J. Werner, S. Martin de Nicolas, L. Barraud, A. Hessler-Wyser, M. De-speisse, S. Nicolay, B. Niesen, S. De Wolf, and C. Ballif, "*Molybdenum oxide is an efficient hole collector in silicon heterojunction solar cells*," Applied Physics Letter, vol. **107**, 081601, 2015.

3 J. Holovsky, S. De Wolf, J. Werner, Z. Remes, M. Müller, N. Neykova, M. Ledinsky, L. Cerna, P. Hrzina, P. Löper, B. Niesen, C. Ballif, "*Photocurrent Spectroscopy of Perovskite Layers and Solar Cells: A Sensitive Probe of Material Degradation*," The Journal of Physical Chemistry Letters, vol. **8**, pp. 838-843, 2017.

4 Q. Jeangros, M. Duchamp, J. Werner, M. Kruth, R. E. Dunin-Borkowski, B. Niesen, C. Ballif, A. Hessler-Wyser, "*In Situ TEM Analysis of Organic-Inorganic Metal-Halide Perovskite Solar Cells under Electrical Bias*," Nano Letters, vol. **16** (11), 2016.

5 D. Forgacs, L. Gil-Escrig, D. Pérez-Del-Rey, C. Momblona, J. Werner, B. Niesen, C. Ballif, M. Sessolo, H. J. Bolink, "*Efficient Monolithic Perovskite/Perovskite Tandem Solar Cells*," Advanced Energy Materials, 1602121, 2017.

6 M. Stuckelberger, T. Nietzold, G. N. Hall, B. West, J. Werner, B. Niesen, C. Ballif, V. Rose, D. P. Fenning, M. I. Bertoni, "*Charge collection in hybrid perovskite solar cells: Relation*

to the nanoscale elemental distribution," IEEE Journal of Photovoltaics, vol. **7** (2), pp. 590-597, 2017.

7   Z. Song, J. Werner, N. Shrestha, F. Sahli, S. De Wolf, B. Niesen, S. C. Watthage, A. B. Philips, C. Ballif, R. J. Ellingson, M. J. Heben, "*Probing Photocurrent Nonuniformities in the Subcells of Monolithic Perovskite/Silicon Tandem Solar Cells,*" The Journal of Physical Chemistry Letters, vol. **7** (24), pp. 5114-5120, 2016.

8   M. Mundus. B. Venkataramanachar, R. Gehlhaar, M. Kohlstädt, B. Niesen, W. Qiu, J. P. Herterich, F. Sahli, M. Bräuninger, J. Werner, J. Hohl-Ebinger, G. Uytterhoeven, U. Würfel, C. Ballif, W. Warta, S. W. Glunz, "*Spectrally Resolved Nonlinearity and Temperature Dependence of Perovskite Solar Cells,*" Solar Energy Materials and Solar Cells, vol. **172**, pp. 66-73, 2017.

9   Z. Song, J. Werner, S. C. Watthage, F. Sahli, N. Shrestha, S. De Wolf, B. Niesen, A. B. Phillips, C. Ballif, R. J. Ellingson, M. J. Heben, "*Imaging the Spatial Evolution of Degradation in Perovskite/Si Tandem Solar Cells after Exposure to Humid Air,*" IEEE Journal of Photovoltaics, vol. **7**, 6, pp. 1563-1568, 2017.

10 G. Hall, M. Stuckelberger, T. Nietzold, J. Hartman, J. S. Park, J. Werner, B. Niesen, M. L. Cummings, V. Rose, C. Ballif, M. K. Chan, D. P. Fenning, M. I. Bertoni, "*The Role of Water in the Reversible Optoelectronic Degradation of Hybrid Perovskites at Low Pressure,*" Journal of Physical Chemistry C, vol. **121**, 46, pp. 25659-25665, 2017.

11 F. Sahli, B. A. Kamino, J. Werner, M. Bräuninger, B. Paviet-Salomon, L. Barraud, R. Monnard, J. P. Seif, A. Tomasi, Q. Jeangros, A. Hessler-Wyser, S. De Wolf, M. Despeisse, S. Nicolay, B. Niesen, C. Ballif, "*Improved Optics in Monolithic Perovskite/Silicon Tandem Solar Cells with a Nanocrystalline Silicon Recombination Junction,*" Advanced Energy Materials, 1701609, 2017.

12 S. Essig, J. Dréon, E. Rucavado, M. Mews, T. Koida, M. Boccard, J. Werner, J. Geissbühler, P. Löper, M. Morales-Masis, L. Korte, S. De Wolf, C. Ballif, "*Toward Annealing-Stable Molybdenum-Oxide-Based Hole-Selective Contacts For Silicon Photovoltaics,*" Solar RRL, 1700227, 2018.

13 S. Altazin, L. Stepanova, J. Werner, B. Niesen, C. Ballif, B. Ruhstaller, "*Design of Perovskite/Crystalline-Silicon Tandem Solar Cells,*" Optics Express, vol. **26**, 10, 2018.

14 E. Rucavado, F. Landucci, J. Werner, M. Doebeli, Q. Jeangros, A. Hessler-Wysser, C. Ballif, M. Morales-Masis, "*Ultra-transparent and highly-conductive Zr-doped indium oxide: carrier transport and potential for perovskite/silicon tandem solar cells,*" in preparation, 2018.

Conference contributions as first author

Oral presentations

1 J. Werner, S-J. Moon, P. Löper, A. Walter, L. Fesquet, M. Filipic, C-H. Weng, L. Löfgren, J. Bailat, M. Topic, M. Morales-Masis, R. Peibst, R. Brendel, S. Nicolay, S. De Wolf, B. Niesen and C. Ballif **(P)**, "*Towards ultra-high efficient photovoltaics with perovskite/crystalline silicon tandem devices*," Keynote plenary presentation at 31st EU-PVSEC, Hamburg, Germany, 14-18 September 2015.

2 J. Werner **(P)**, C-H. Weng, A. Walter, L. Fesquet, J. Peter Seif, N. Tetreault, P. Löper, S-J. Moon, S. Nicolay, S. De Wolf, B. Niesen and C. Ballif, "*Perovskite/crystalline silicon tandem solar cells: light management and performance optimization*," Symposium EE3, MRS Spring Meeting, Phoenix, 2016. Award: Symposium EE3 Best Oral Contribution.

3 J. Werner **(P)**, F. Sahli, B. Kamino, D. Sacchetto, M. Bräuninger, A. Walter, S-J. Moon, L. Barraud, B. Paviet-Salomon, J. Geissbuehler, C. Allebé, R. Monnard, S. De Wolf, M. Despeisse, S. Nicolay, B. Niesen, C. Ballif, "*Perovskite/Silicon Tandem Solar Cells: Challenges Towards High-Efficiency in 4-Terminal and Monolithic Devices*," Area 6, Si-Based Tandems: Battle Royale, IEEE pvsc 44, Washington DC, USA, 2017. Award: Best Student Paper Award Area 6.

Conference proceedings

1 J. Werner, S-J. Moon, P. Löper, A. Walter, L. Fesquet, M. Filipic, C-H. Weng, L. Löfgren, J. Bailat, M. Topic, M. Morales-Masis, R. Peibst, R. Brendel, S. Nicolay, S. De Wolf, B. Niesen and C. Ballif, "*Towards ultra-high efficient photovoltaics with perovskite/crystalline silicon tandem devices*," Keynote plenary presentation at 31st EU-PVSEC, Proceedings, Hamburg, Germany, 14-18 September 2015.

2 J. Werner, F. Sahli, B. Kamino, D. Sacchetto, M. Bräuninger, A. Walter, S-J. Moon, L. Barraud, B. Paviet-Salomon, J. Geissbuehler, C. Allebé, R. Monnard, S. De Wolf, M. Despeisse, S. Nicolay, B. Niesen, C. Ballif, "*Perovskite/Silicon Tandem Solar Cells: Challenges Towards High-Efficiency in 4-Terminal and Monolithic Devices*," Area 6, Si-Based Tandems: Battle Royale, IEEE pvsc 44, Washington DC, USA, 2017.

Poster presentation

1 J. Werner, G. Dubuis, A. Walter, P. Löper, S-J. Moon, S. Nicolay, M. Morales-Masis, S. De Wolf, B. Niesen and C. Ballif, "*Broadband transparent sputtered indium zinc oxide electrode for perovskite solar cells*," presented at the Hybrid and Organic Photovoltaics Conference, Rome, Italy, May 10-13th, 2015.

2 J. Werner, C-H. Weng, A. Walter, S-J. Moon, P. Löper, S. De Wolf, S. Nicolay, B. Niesen

and C. Ballif, "*Perovskite/C-Si tandem solar cells: How to enhance a silicon solar cell performance!,*" 1st International Conference on Perovskite Solar Cells and Optoelectronics, Lausanne, Switzerland, 27-29 September 2015

3 J. Werner, F. Sahli, M. Bräuninger, A. Walter, B. Kamino, R. Monnard, B. Paviet-Salomon, L. Barraud, C. Allebé, D. Sacchetto, M. Despeisse, S-J. Moon, S. Nicolay, B. Niesen, C. Ballif, "*High-efficiency 4-terminal and monolithic perovskite/silicon tandem devices,*" presented at the Hybrid and Organic Photovoltaics Conference, Lausanne, Switzerland, May 2017.

Acknowledgements

During the four exceptional years I spent at PV-Lab, I have met incredible and amazing people and I would like to thank them all for their wonderful contributions to this thesis, which made it successful at both professional and personal levels.

I would like to start these acknowledgements by thanking my thesis director, Christophe Ballif, for sharing his passion for PV and renewable energies, for challenging and pushing me, and for making this laboratory a very enjoyable and stimulating place to work.

The second person I would like to thank was maybe the most important person I could count on in a daily basis: my thesis co-director Björn Niesen. Thank you for all the things you taught me, including diplomacy (which I'm still learning ;)) and for the faithful every day motivation you managed to communicate to the group. Thank you for your good spirit, leading to a great team work experience, where your legendary patience and calm often counterbalanced my ardour and impatience.

I acknowledge Prof. Frank Nüesch, Dr. Sam Stranks, Dr. Benjamin Strahm and Dr. Stefano Mischler for their involvement in the thesis jury and for their precious time spent at reading my work.

A special big MERCI to the technical team: Cédric, Lionel, Aymeric, Nathanaël, Joël, Sylvain, Xavier. Sans vous, rien ne fonctionnerait dans le labo (ou pas pour longtemps). Merci pour votre soutien sans faille, même quand on casse tout, et pour votre ingéniosité sans limite pour trouver des solutions à tous nos soucis techniques.

Un grand merci à Mary-Claude pour son soutien dans les tâches administratives pour lesquels je n'ai pas toujours été très doué et à Karine dans la dernière ligne droite pour l'organisation des soutenances.

Thanks to Silvia, Niels, Luc, Johannes, Bertrand, Loris, Raphaël and Guillaume for the continuous supply of silicon bottom cells, whatever the crazy demands we had.

Merci à mes cher collègues de bureau, Xavier et Sylvain, Arnaud et Jordan, pour les discussions très diverses, rarement très scientifiques, souvent sportives ou politiques, mais toujours passionnées et passionantes, ainsi que les très nombreux moments de franches rigolades.

Acknowledgements

Jérémie WERNER   Swiss citizen, born in 1989
Chemin de Bel-Air 1   ch.linkedin.com/in/jwerner15/
2000 Neuchâtel   jeremie.werner@alumni.epfl.ch
CH-Suisse

OrcID: *https://orcid.org/0000-0003-4997-9945*
Google Scholar ID:
https://scholar.google.ch/citations?user=jmWy_EcAAAAJ&hl=fr&authuser=1

EDUCATION

PhD in Materials Science and Engineering,   2014-2018
PV-lab, EPFL, Neuchâtel: *Perovskite/Silicon Tandem Solar Cells*

Master in Materials Science and Engineering   2012-2014
Ecole Polytechnique Fédérale de Lausanne (EPFL), Switzerland
Orientation: Materials for microelectronics and Microtechnology

- Fall semester research project in Ceramics Laboratory (LC), supervised by Prof. Nava Setter: *Processing and characterization of epitaxial rhombohedral PZT thin films deposited by pulsed laser deposition.*
- Spring semester research project in Semiconductor materials laboratory (LMSC), Prof. A. Fontcuberta i Morral: *Characterization of silicon nanowires array solar cells.*
- Master's thesis at Holst Centre/TNO, Eindhoven, supervised by Prof. Paul Muralt, EPFL, and Dr. Juliane Tripathi, Holst Centre/TNO: *Deposition of functional layers by atmospheric plasma printing. Microplasma printing technology.*

Bachelor in Materials Science and Engineering   2009-2012
Ecole Polytechnique Fédérale de Lausanne (EPFL), Switzerland

- *Academic year abroad, Erasmus, at **Imperial College, London***   *2011-2012*
  Award: Imperial College International Diploma, first class honours

Military service as saxophonist in the military music, Aarau and Bern   07-11.2008

High school, option physic and applications of mathematics   2004-2008
College St-Michel, Fribourg

SCIENTIFIC CONTRIBUTIONS DURING PHD THESIS

7 peer-reviewed journal articles as first author, including 1 review paper
13 peer-reviewed journal articles as co-author
2 conference proceeding as first author
2 orals presentations at international conferences, both awarded for Best student contribution of the symposium
3 poster presentations at international conferences

KNOWLEDGE

MS-Office, LaTex, Mathematica, ImageJ, Matlab, PC1D
Programming languages: Python, Arduino, Labview, C,

INTERESTS

Thin films technology, photovoltaics, plasma processing, materials for energy applications
Trail running, hiking

LANGUAGES

French (Mother tongue), *English* (Professional working proficiency)